UNIVERSITÀ
DEGLI STUDI
DI PADOVA

Sede Amministrativa: Università degli Studi di Padova
Dipartimento di Ingegneria Civile, Edile e Ambientale

SCUOLA DI DOTTORATO DI RICERCA IN: Scienze dell'Ingegneria Civile e Ambientale
CICLO XXVI

SPACE-TIME EXTREMES OF SEA WAVE STATES:

FIELD, ANALYTICAL AND NUMERICAL INVESTIGATIONS

Direttore della Scuola: Ch.mo Prof. Stefano Lanzoni
Supervisore: Ch.mo Prof. Piero Ruol
Co-supervisore: Dott. Alvise Benetazzo (ISMAR-CNR)

Dottorando: Francesco Barbariol

To Sabrina and Benedetta.

Abstract

Evaluation of wave extremes occurring in short-crested sea states is the research topic of this doctoral thesis. Short-crestedness is the typical condition in sea storms. In fact, engineering practice and reports from people working offshore (e.g. on fixed platforms or routing ships) are raising questions on the adequacy of conventional wave statistics for the prediction of extremes during short-crested storm conditions. Indeed, wave statistics has been traditionally derived from time measurements, i.e. at a fixed point. Recently, experimental evidence has proved that the maximum sea surface elevation occurring at a fixed point of the sea is smaller than the maximum occurring over a surrounding area. Hence, unless the space dynamics of wave groups is fully included inside the area, the measured maximum at a point or over a smaller area underestimates the actual maximum. To overcome this fact, during the last decade stochastic models to calculate maxima of Gaussian multidimensional random fields, i.e. Piterbarg's theorem and Adler and Taylor's Euler Characteristic approach, have been applied to wave statistics. According to these theories, we should be able to estimate the expected maxima that can occur over an area (space) during a short-crested sea state of given duration (time), giving an explanation to the experimental evidence.

The aim of this doctoral thesis is to investigate and discuss these recently applied stochastic models, in order to contribute changing the paradigm of wave analysis: from time to space-time domain. Thus, we worked on multiple fronts with multiple approaches. Field campaigns allowed us to validate stochastic models and to propose a data analysis procedure to char-

acterize sea states at a given location with respect to space-time wave extremes. Analytical and numerical approaches served us to give possible solutions to the well-recognized lack of directional wave spectra, i.e. the input of the multidimensional stochastic models. Indeed, we propose closed formulae to calculate the input spectral parameters in a context of idealized sea states and we develop an ad hoc version of the SWAN (Simulating WAves Nearshore) model, called SWAN-ST (SWAN Space-Time), to allow space-time extreme analysis to be performed on realistic domains. Moreover, analytical and numerical model outputs were used to investigate the dependence of wave extremes upon specific physical parameters governing wind wave mechanics (i.e. wind speed, fetch length, ambient current speed and bottom slope). Finally, we tested the numerical modeling of space-time extremes on realistic domains by running a 3 years hindcast of on the Mediterranean Sea.

Sommario

Il tema di ricerca di questa tesi è la valutazione degli estremi di moto ondoso che si possono verificare in stati di mare a creste corte. Questa è infatti la condizione tipica durante le tempeste marine. La pratica ingegneristica e l'esperienza di chi opera nel settore off-shore (e.g. su piattaforme o navi), stanno sollevando interrogativi circa l'adeguatezza della statistica d'onda convenzionale per quanto riguarda la stima degli estremi durante condizioni di mare a creste corte in tempesta. Infatti, la statistica delle onde è stata tradizionalmente ricavata da misure temporali, cioè ottenute in un punto fisso. Recentemente, è stata provata l'evidenza sperimentale secondo cui la massima elevazione di superficie che si verifica in un punto del mare è minore della massima elevazione che si verifica su un area circostante. Perciò, a meno che la dinamica spaziale di un gruppo d'onda sia completamente inclusa all'interno dell'area, il massimo misurato ad un punto o su un area più piccola sottostima il massimo effettivo. Per ovviare a ciò, nella scorsa decade sono stati applicati alla statistica del moto ondoso alcuni modelli stocastici per la stima dei massimi di campi multidimensionali Gaussiani, ovvero il teorema di Piterbarg e l'approccio alle caratteristiche di Eulero di Adler e Taylor. In base a queste teorie, siamo in grado di stimare i massimi attesi che si possono verificare su un area (spazio) durante uno stato di mare a creste corte di una data durata (tempo), fornendo così una spiegazione dell'evidenza sperimentale.

Lo scopo di questa tesi dottorale è quello di investigare e discutere questi modelli stocastici di recente applicazione al fine di contribuire ad un cambio di paradigma nell'analisi del moto ondoso: dal dominio del tempo al dominio dello spazio-tempo.

Quindi, ci siamo concentrati su diversi fronti utilizzando approcci differenti. Campagne di misura ci hanno consentito di validare i modelli stocastici e di proporre una procedura di analisi dei dati volta a caratterizzare gli stati di mare in un sito, relativamente agli estremi nel dominio spazio-tempo. Approcci analitici e approcci numerici ci sono invece serviti per fornire possibili soluzioni al ben noto problema della mancanza di spettri direzionali d'onda, ovvero gli input del modelli stocastici multidimensionali. Infatti, abbiamo proposto delle formule chiuse per calcolare i parametri spettrali di input in un contesto di stati di mare concettualizzati e abbiamo sviluppato una versione ad hoc del modello numerico SWAN (Simulating WAves Nearshore), chiamata SWAN-ST (SWAN Space-Time) per permettere l'analisi degli estremi nel dominio spazio-tempo su domini realistici. Inoltre, i risultati ottenuti da questi approcci analitici e numerici sono stati utilizzati per studiare la dipendenza degli estremi di moto ondoso da parametri fisici specifici che governano la meccanica delle onde da vento, ovvero la velocità del vento, la lunghezza del fetch, la presenza di una corrente e la pendenza del fondo. Infine, abbiamo testato la possibilità di modellare numericamente gli estremi spazio-tempo su domini realistici, simulando 3 anni di eventi sul mare Mediterraneo.

Contents

Part I

Introduction

Chapter 1

Extreme waves

1.1 Introduction

1.1.1 Observations

During the last decades, scientific community has devoted many efforts in trying to accurately measure, model and predict extreme sea wave conditions. In fact, the standard statistical model of ocean waves, i.e. based on the linear or second-order random phase/amplitude wave model, has been widely employed with success to accurately predict wave spectra, wave statistics and wave kinematics in ordinary conditions. Nevertheless, it is not able to explain some extreme wave measurements and accidents occurring to offshore structures, e.g. fixed platforms and ships (Forristall, 2005). As an example, the famous "Gorm wave" and "New Year (or Draupner) wave" (Figure 1.1) had a crest to significant wave height ratio of 2.2 and 1.54, respectively, whereas the standard wave model predicted a maximum value of 1.25. Collections of such extreme events, either measured or indirectly witnessed by the damages on structures and by the sinking of ships (Figure 1.2) can be found for example in (Sand et al., 1990; Skourup et al., 1997; Socquet-Juglard, 2005; Forristall, 2007; Dysthe et al., 2008; Forristall, 2011; Cavaleri et al., 2012). In addition, during the European project MaxWave (Rosenthal and Lehner, 2008) several accidents occurred to ships and offshore platforms were analyzed to improve the understanding of physical processes underlying extreme waves generation.

To explain these "freak wave" events, part of the scientific community focused on the physical mechanism of their generation and on higher order, i.e. strongly non-linear, wave models (Osborne et al., 2000; Onorato et al., 2001, 2002). Wave tank experiments, field measurements and numerical modeling

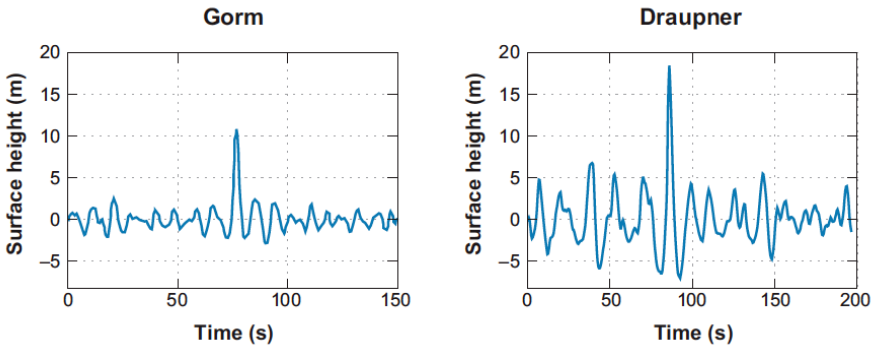

Figure 1.1: Extremely high waves unexplainable resorting to the standard wave model (predicted maximum crest to significant wave height ratio, 1.25). Left: the "Gorm Wave" recorded in the North Sea on November 17, 1984 (crest to significant wave height ratio, 2.2). Right: the "New Year wave", recorded at the Draupner platform in the North Sea on January 1, 1995 (crest to significant wave height ratio, 1.54). Picture from (Dysthe et al., 2008)

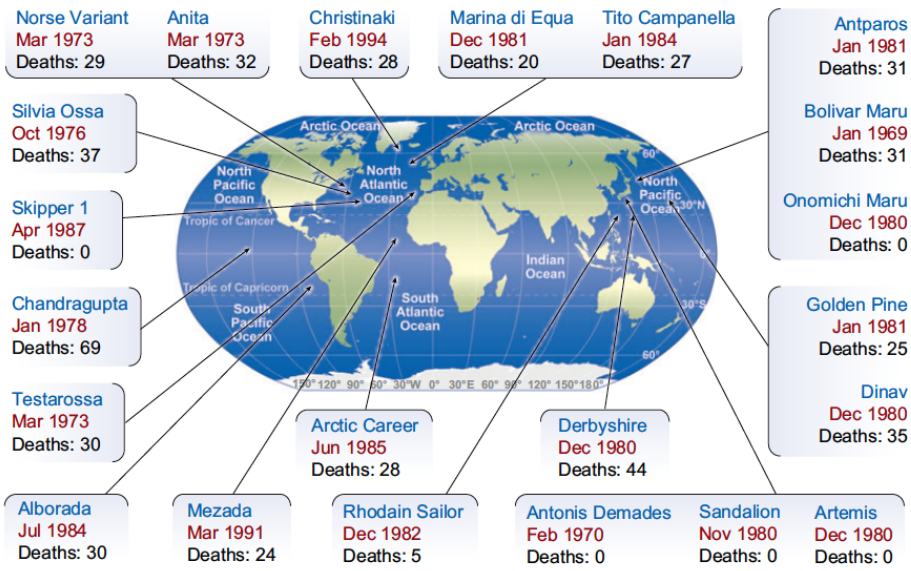

Figure 1.2: Locations of 22 supercarriers sinkings after collision with extremely high waves, between 1969 and 1994. Picture from (Kharif and Pelinovsky, 2003).

(e.g. using the Nonlinear Schroedinger equations) individuated the spatial focusing due to current induced refraction, the dispersive focusing and the nonlinear focusing, i.e. the so called Benjamin-Feir instability, as the main factors that contribute to the genesis of an extremely high wave (Dysthe et al., 2008). Nevertheless, research on these topics is still ongoing and far from a closure of the problem.

A different theoretical approach is based on the belief that such extreme wave events are not outliers of the standard wave model, but have to be considered either elements of another population or elements of a more numerous Gaussian (i.e. linear) or second-order sample. For this reason, Forristall (2005) stated that new statistics able to model and predict also extremely high waves is nowadays more needed than new physics of waves and strongly non-linear models. To confirm it, in a review on oceanic rogue waves (i.e. unexpectedly high waves) Dysthe et al. (2008) concluded that a wave statistics based on a second-order wave model is sufficient to explain the most of the measured rogue waves. Additionally, results of MaxWave project were in agreement with this conclusion (Rosenthal and Lehner, 2008). Despite this, Forristall (2005, 2007) prove that even a second-order wave statistics is ineffective to interpret, for example, damages occurred to the decks and structures of some platforms in the Gulf of Mexico during hurricanes Ivan, Katrina and Rita.

To summarize, except for a few rare events, e.g. the New Year wave of Figure 1.1, measurements of extreme waves are well modeled by the standard second-order wave model, but the most of damages occurred to offshore structures and sinking of routing ships have not yet found a satisfactory explanation. A possible motivation to this fact will be detailed in the next Section.

1.1.2 Time vs space-time: experimental evidence

Traditionally the sea surface elevation has been measured by using 0D instruments, i.e. recording the time series of the sea surface displacement η from a reference level at a single fixed point. For several decades, data recorded from wave gauges, ultrasonic instruments and buoys represented the only wave measurements available. Thus, wave statistical models have been validated against wave data gathered at fixed points, with time t as the only independent variable, i.e. $\eta = \eta(t)$. Nevertheless, sea surface elevation is a variable evolving over a 2D space $\mathbf{x} = (x, y)$, i.e. $\eta = \eta(\mathbf{x}, t)$ (Holthuijsen, 2007).

Since the 80s, the computing capabilities allowed to retrieve 2D maps of the sea-surface elevation $\eta(\mathbf{x}, t)$, thanks to image sequences recorded using

stereo-photogrammetry (Shemdin et al., 1988; Banner et al., 1989). After that, radar mounted on ships and platforms and Synthetic Aperture Radar (SAR) or Interferometric SAR (ISAR) mounted on satellites widened the possibility of retrieving portions of the sea surface in time, with different spatial scales and accuracies (Dankert et al., 2003). Hence, remote sensing the wave field over an area during a storm or estimating it indirectly by the damages occurred, for example, to the deck of a platform (Forristall, 2006), some authors suggested that the standard model underestimates the actual maxima.

The change of the domain of observation from time to space-time revealed that the maximum sea surface elevation recorded over an area of the sea surface during a given duration sea state is greater than that obtained at single fixed points inside the area. This evidence was found among the others by Forristall (2006) while studying the problem of the air gap below the deck of drilling platforms. Fedele et al. (2013) deployed a stereo-photogrammetric system, i.e. WASS (Wave Acquisition Stereo System, (Benetazzo, 2006)) on the CNR-ISMAR oceanographic tower "Acqua Alta", 8 miles off the Venice coast in the northern Adriatic Sea. During field campaigns in 2009 and 2010 they measured the sea surface elevations over different size areas during sea states. They proved that the maximum sea surface elevation $\overline{\eta}_{ST}$ increases with the area. Socquet-Juglard et al. (2005) and Forristall (2005) verified the same evidence by numerically simulating short-crestes sea states. Forristall (2011) observed this fact on a wave tank experiment. Besides these, European project MaxWave concluded that extending analysis to space domain results in much more individual waves observed, hence the standard model criteria for extreme waves have to be overcome (Rosenthal and Lehner, 2008).

1.1.3 New statistics in space-time domain

Currently, the underestimation of the actual wave maxima by point measurements is accepted and acknowledged by the ocean community, but as an experimental evidence rather than as a consolidated and widespread paradigm of analysis. This is due to the lack, until recently, of robust enough statistical theories able to model the distribution of sea surface elevation maxima over the space-time domain. The problem is that there is no mathematical definition of a wave in space. In fact, even an analogous of wave period is difficult to be defined in space, unless an arbitrary direction is prescribed. Nevertheless, when space domain is considered, the geometry of the waves must be accounted for (Baxevani and Rychlik, 2006). That is, short-crestedness and directional wave characteristics have to be calculated, e.g. wavelength and wave crest.

Stochastic theories to evaluate maxima of multidimensional Gaussian random fields were developed by Piterbarg (1996) and Adler and Taylor (2007). They followed different approaches and reached similar results that allowed to estimate the exceedance probability distribution functions (EDFs) of maxima of random fields in $\mathbb{R}^n$, provided that the sample is numerous and the threshold considered sufficiently high. Besides EDFs, these theories allow to estimate the expected maximum of the random field. Recently, Piterbarg's theorem and Adler and Taylor Euler Characteristics approach have been applied to ocean wave statistics, reasonably assuming that the sea surface can be modeled as a Gaussian random surface either in $\mathbb{R}^1$, i.e. in time, in $\mathbb{R}^2$, i.e. over the 2D-space, or in $\mathbb{R}^3$, i.e. over the 2D-space and time. Krogstad et al. (2004) chose the Piterbarg's approach and applied it straightforwardly to ocean wave analysis. They also corrected the linear estimate of maxima to the second-order according to the Tayfun quadratic equation (Tayfun, 1980). Hence, according to the definition of Socquet-Juglard et al. (2005) in the followings we will talk of Piterbarg's model in a linear context and of Tayfun-Piterbarg's model in a second-order non-linear context. Fedele (2012) instead focused on the approach of Adler and Taylor and developed a method, hereafter called Fedele's method, that differs from the Piterbarg's model mainly because it accounts for the occurrence of maxima even at the boundaries of the space-time domain, as it could happen when the area of analysis is smaller than the characteristic space dimension of the waves. For this reason, Fedele's methods holds for areas of any given size, while Piterbarg's theorem only for areas with side greater than the mean wavelength of the sea state. To meet this fact, Forristall (2005) developed an approximation that allows to apply Piterbarg's model also on smaller areas. Also Fedele's method results can be corrected to the second-order applying Tayfun quadratic equation (Tayfun, 1980). The details of these stochastic methods will be described and discussed in Chapter 3.

1.2 Motivations and aims

Including Piterbarg and Fedele's stochastic models into wave statistics could significantly increase the reliability of extreme wave predictions. Applicability of these models is constrained by the availability of directional wave spectra. In fact, since they synthesize the wave field space-time features, they are the basis of extreme wave prediction. Directional wave spectra are generally obtained by measuring the time evolving 2D wave field with directional buoys, arrays of wave gauges, stereo-photogrammetry, radars or satellites SAR and ISAR. Then, measurements are post-processed using de-

terministic or stochastic techniques to get the directional spectrum. Some of the instrumentations cited are relatively expensive and difficult to deploy and maintain in an open sea environment or in orbit around the Earth. At present, one of the most promising sources of directional spectra are spectral numerical wave models, despite the limitations of modeling and the unavoidable errors introduced by numerics. For these reasons, directional spectra are rarely available and, when available, periods of coverage of the data are usually limited by the duration of projects and studies.

Beside this, space-time stochastic models have been not yet robustly validated against space-time measurements of sea states. Piterbarg's theorem model results have been compared to numerical simulated maximum sea surface elevations (Forristall, 2005, 2007; Krogstad et al., 2004; Socquet-Juglard et al., 2005) and to wave tank experiments maxima (Forristall, 2011).

Moreover, due to the pure statistical character of these models and to their limited application until now, the relationship between maximum sea surface elevation over an area and physical parameters governing wind wave mechanics has not been yet investigated.

In this context, we were motivated to give a contribution aimed at filling these gaps. Primary, we intended to compare stochastical space-time extremes against stereo-photogrammetric WASS measurements, in order to validate these models and discuss their application to realistic measured sea states. Then, we wanted to propose possible solutions to the lack of directional spectra. To this end, we resorted to the analytical spectral formulation of idealized sea states, i.e. Pierson-Moskowitz and JONSWAP spectra, and to numerical spectral wave modeling. We were also aimed at investigating and discussing the dependence of stochastic space-time sea surface maxima upon specific physical parameters, such as wind speed and fetch length, the presence of an ambient current and bottom steepness. Finally, we intended to test the capability of performing space-time extreme analysis in realistic conditions by means of numerical modeling.

1.3 General overview

Apart from the present, i.e. **Introduction (Part I)**, this doctoral thesis is composed of two more Parts. In the next, i.e. second, Part, we will define the **Theoretical Background (Part II)** we want the reader to be acknowledged of before going into the core of the results obtained. This theoretical basis is common to all the results presented in the following Part. In particular, the basic assumptions of the random wave model and the spectral representation of short-crested sea states will be presented (Chapter

2). Then, we will illustrate the techniques used to obtain the directional wave spectrum that is the starting point of our successive analysis. After that, we will face with the representation of idealized, i.e. simplified under some hypotheses, and realistic sea states. In this contexts, the analytical and numerical tools we employed are presented. Once these bases have been given, we will illustrate the stochastic methods to model space-time wave extremes of sea states, i.e. the Piterbarg's theorem and the Fedele's method based on the Adler and Taylor's Euler Characteristics approach (Chapter 3). We will also present Forristall's approximation, holding for small areas relative to the mean wavelength and the Tayfun second-order correction to account for non-linearities in the sea states. These methods will be used in the rest of the thesis to obtain the expected wave space-time extremes of short-crested sea states, object of investigations. The physical mechanism limiting results of the stochastic models, i.e. wave-breaking, will be mentioned before closing the second Part.

The third Part collects the **Results (Part III)** we scored during the doctoral school program, inherent with the topic of the thesis. Results are structured in order to be gathered according to the methodology employed, namely, field results (Chapter 4 and 5), analytical results (Chapter 6) and numerical results (Chapter 7). Field campaigns allowed us to validate the stochastic models of Piterbarg and Fedele (using stereo-photogrammetric wave measurements) and to investigate space-time extremes dependence upon space domain size and probability distributions (using directional buoy wave measurements). Analyical and numerical results were achieved with a dual purpose. On the one hand, we tried to solve the difficulty of applying space-time extremes stochastic models due to the well-recognized lack of directional wave spectra. Indeed, using analytical methods in the context of idealized sea states we derived closed formulae for the models inputs (i.e. mean wavenumber vector, mean wave period, space-time and space-space irregularity parameters) that depend upon physical parameters only, e.g. wind speed and fetch length. In the context of realistic sea states, we took advantage of spectral numerical wave modeling to allow space-time extreme analysis to be performed on geophysical domains. To do that, we developed an ad hoc version of the SWAN model (Simulating WAves Nearshore, (Booij et al., 1999)) devoted to the calculation of stochastic models inputs. On the other hand, analytical and numerical methodologies were used to meet stochastically obtained space-time results with physical parameters governing the mechanics of waves, i.e. wind speed, fetch length, ambient current speed and bottom steepness. Numerical modeling was also used to perform a 3 years (2008-2010) hindcast of Mediterranean Sea states and space-time extremes. Doing so, we proved the possibility of using numerical models for space-time

extremes prediction in realistic conditions.

Part II

Theoretical background

Chapter 2

Spectral representation of short-crested sea states

2.1 Random wave model

Short-crested sea states are herein represented by the two-dimensional random-phase/amplitude model. According to this model, sea surface elevation evolving in time t over 2D space $\mathbf{x} = (x, y)$, i.e. $\eta(\mathbf{x}, t)$, is a random variable as well as amplitude a and phase ϕ. In particular, amplitude is Rayleigh distributed and phase is uniformly distributed over $[0; 2\pi]$. Angular frequency σ and direction θ, hence wave-number vector $\mathbf{k}$, are arbitrarily discretized in the spectral domain (σ, θ) in order to accurately approximate the continuous energy spectrum $E(\sigma, \theta)$.

In this context, the random wavy surface is represented by the sum of a large number MN of harmonics [1]:

$$\eta(\mathbf{x}, t) = \sum_{m=1}^{M} \sum_{n=1}^{N} a_{m,n} \cos\left(\mathbf{k}_{m,n} \cdot \mathbf{x} - \sigma_m t + \phi_{m,n}\right) \tag{2.1}$$

where $\mathbf{k}_{m,n} \cdot \mathbf{x} = k_m(x \cos\theta_n + y \sin\theta_n)$, being k the magnitude of $\mathbf{k}$. For each harmonic component $(m = 1, ..., M)$ the relationship between frequency σ_m and wavenumber k_m is defined by the linear dispersion relationship (d: water depth and g gravitational acceleration):

$$\sigma_m^2 = g k_m \tanh k_m d \tag{2.2}$$

[1] Herein, an harmonic wave is a cosine wave with single amplitude, frequency and wavenumber: $h(t) = a \cos(\mathbf{k} \cdot \mathbf{x} - \sigma t + \phi)$.

The random-phase/amplitude model (2.1) represents a Gaussian sea state, i.e. a space-time portion of the sea with Gaussian distributed sea surface elevations $\eta(\mathbf{x}, t)$, that is stationary in time t and homogeneous over space $\mathbf{x}$. This linear process has been widely used with success to model mild slope short-crested random waves in deep waters (Holthuijsen, 2007).

2.2 Directional spectrum

The distribution of sea wave energy over frequencies σ and directions θ is provided by the directional energy density spectrum $E(\sigma, \theta)$ (unit: $\mathrm{Nm^{-1}Hz^{-1}rad^{-1}}$). The directional variance density spectrum $S(\sigma, \theta)$ [2] (unit: $\mathrm{m^2Hz^{-1}rad^{-1}}$) is proportional to $E(\sigma, \theta)$ through water density ρ and gravitational acceleration g

$$S(\sigma, \theta) = E(\sigma, \theta)/(\rho g) \tag{2.3}$$

The directional spectrum $S(\sigma, \theta)$ is conventionally [3] decomposed as follows:

$$S(\sigma, \theta) = S(\sigma)D(\sigma, \theta) \tag{2.4}$$

where:

- $S(\sigma)$ is the one-sided variance density spectrum or frequency spectrum,

$$S(\sigma) = \int_0^{2\pi} S(\sigma, \theta)d\theta \tag{2.5}$$

- $D(\sigma, \theta)$ is the directional spreading function, i.e. a function that models the spreading of wave energy/variance at each frequency σ over directions θ.

$D(\sigma, \theta)$ satisfies the two following properties:

- $D(\sigma, \theta)$ is a non-negative function of θ;
- $\int_0^{2\pi} D(\sigma, \theta)d\theta = 1$

[2] Since the relationship between σ and k is assumed to be governed by (2.2), the directional spectrum $S(\sigma, \theta)$ could be alternatively written as $S(k, \theta)$ or $S(\mathbf{k})$.

[3] The spectral decomposition (2.4) is conventional in a time domain approach, since it separates the unknown part of the spectrum to be modeled, i.e. $D(\sigma, \theta)$, from the most reliable part, i.e. $S(\sigma)$.

To simplify the directional spreading function, it is assumed to be dependent only upon θ, i.e. $D(\sigma, \theta) = D(\theta)$.

Wave extremes in the space-time domain depend upon the directional spectrum $S(\sigma, \theta)$ which is the basis for prediction through stochastic models like Piterbarg's theorem and Fedele's method. In fact, directional spectrum synthesizes the space-time features of the wave field. Hence, spectral parameters of $S(\sigma, \theta)$ are used to implement the cited models. These spectral parameters will be presented in the followings.

Unfortunately, directional spectra are rarely available in the practice because they require advanced techniques and expensive instrumentations to be measured. Recently, satellites radar imaging (SAR, ISAR) as well as stereo-photogrammetric imaging (Benetazzo et al., 2012) have increased the availability of directional spectra but a directional spectral representation of the sea states is not yet the standard in the ocean waves community, especially among design engineers. Alternatively, directional spectra could be obtained resorting to analytical spectral functions, in the context of idealized sea states, i.e. simplified under specific assumptions. However nowadays, the most promising "source" of directional spectra is numerical spectral modeling. In fact, despite the unavoidable approximations and errors introduced by numerics, numerical models can provide directional spectra with considerable detail both in space and time, accounting for realistic domains and forcings. Analytical spectral functions and numerical modeling will be illustrated in the following sections.

2.2.1 Spectral parameters

Spectral parameters required for the implementation of Piterbarg's theorem and Fedele's method can be expressed in terms of the moments of the directional spectrum $S(\sigma, \theta)$ (Fedele, 2012):

$$m_{ijl} = \int_0^{2\pi} \int_0^{\infty} k_x^i k_y^j \sigma^l S(\sigma, \theta) d\sigma d\theta \tag{2.6}$$

being $k_x = k \cos\theta$ and $k_y = k \sin\theta$ the components of the wavenumber vector $\mathbf{k}$.

Preliminary, we rotate the axes of the reference frame until positive x-axis corresponds to the mean wave direction $\overline{\theta}$ [4]. Then, following Baxevani and

[4]This common practice in ocean engineering ensures that spatial partial derivatives of the sea surface $\eta(\mathbf{x}, t)$ are uncorrelated and hence independent in a statistical sense. The rotation has to be chosen in order that the variance of the surface gradient is maximum along, for example, x direction (Baxevani and Rychlik, 2006).

Rychlik (2006), spectral parameters can be written as

$$\begin{aligned} &\overline{T} = 2\pi\sqrt{\frac{m_{000}}{m_{002}}}, \quad \overline{L}_x = 2\pi\sqrt{\frac{m_{000}}{m_{200}}}, \quad \overline{L}_y = 2\pi\sqrt{\frac{m_{000}}{m_{020}}} \\ &\alpha_{xt} = \frac{m_{101}}{\sqrt{m_{200}m_{002}}}, \quad \alpha_{yt} = \frac{m_{011}}{\sqrt{m_{020}m_{002}}}, \quad \alpha_{xy} = \frac{m_{110}}{\sqrt{m_{020}m_{200}}} \end{aligned} \tag{2.7}$$

Here, $\overline{T}$ is the mean wave period, $\overline{L}_x$ and $\overline{L}_y$ are the mean wavelength components in the $x-y$ reference frame. In the chosen reference frame, i.e. x-axis corresponding to mean wave direction, $\overline{L}_x$ becomes the mean wavelength and $\overline{L}_y$ the mean crest length [5]. α_{xt}, α_{yt} and α_{xy} are irregularity parameters that express the correlation between space and space, or space and time derivatives of $\eta(\mathbf{x}, t)$.

While the physical meaning of $\overline{T}$, $\overline{L}_x$ and $\overline{L}_y$ is straightforward, the role of irregularity parameters α_{xt}, α_{yt} and α_{xy} needs explanation. According to Baxevani and Rychlik (2006), these parameters characterize the kinematics of the wave field and play an important role in the distribution of high crests. They represent the ratio between the principal and the drift velocity of the wave field and assume values within [-1,1]. So, if a wave field is simply drifting in time along a principal direction, e.g. x, the absolute value of the corresponding parameter α_{xt} approaches unity. If a wave field results from two wave fields moving along positive x and y axes, then α_{xt} and α_{yt} are null, but not α_{xy}. In such crossed sea conditions, the waves are higher than in the case of drifting along x. Irregularity parameters express how much organized is the wave motion of the random field. The more it is organized, the smaller is the number of waves one has to expect in the space-time domain or on its boundary. In fact, they act as reducing factors in the formulae of the average number of waves (see Chapter 3). Hence, the probability of exceedence of a certain threshold decreases.

The degree of short-crestedness of a sea state can be evaluated by using the following parameter, once again resorting to the moments of the directional spectrum (Baxevani et al., 2003):

$$\gamma_s = \sqrt{\frac{m_{020}}{m_{200}}} \tag{2.8}$$

It approaches 0 for a long-crested sea state, while it tends to 1 the more the sea state is short-crested.

[5] Since $\overline{L}_x$ and $\overline{L}_y$ are calculated from second order moments in k_x and k_y, $\arctan \overline{L}_x/\overline{L}_y$ is not equal to the mean wave propagation direction, that is obtained from first order moment components, i.e. $\overline{\theta} = \arctan(m_{010}/m_{100})$.

2.2.2 Directional wave spectrum calculation

Given the importance of getting reliable directional wave spectra as input for space-time stochastic models, we recall here some systems to estimate such spectra from observations. Directional spectra can be measured using:

- single-point systems: they record simultaneously 3 wave properties at a fixed location. The most widely used are:
  - the heave-pitch-roll buoy, measuring rotations about the 3 buoy axes;
  - the directional waverider buoy, measuring the vertical displacement, i.e. surface elevation, and the two component of the horizontal displacement;
  - the two-components current meter, associated with a pressure or a surface-elevation probe.
- arrays of probes: they are composed of several fixed location sensors recording simultaneous time series of the surface elevation, pressure or other wave properties.
- remote sensing systems: such as radars or stereo-photogrammetric systems, they take pictures of the sea surface over space and time.

Data gathered by the listed instrumentations have to be processed to obtain the directional spectrum. For single-point systems and arrays of gauges, resorting to the spectral decomposition (2.4), $S(\sigma, \theta)$ is estimated by combining a Fourier transform of the time varying sea surface elevation, aimed at calculating $S(\sigma)$, with deterministic or stochastic techniques to calculate the directional spreading function $D(\sigma, \theta)$. In case of remote sensing systems, $S(\sigma, \theta)$ can be derived by the two-dimensional wavenumber spectrum $S(k_x, k_y)$, according to

$$S(\sigma, \theta) = \frac{\sigma}{c c_g} S(k_x, k_y) \tag{2.9}$$

where $S(k_x, k_y)$ is obtained by Fourier transforming the sea surface elevation field, while c and c_g are wave phase celerity and wave group celerity, respectively.

In Chapters 4 and 5 (Part III) we will calculate directional spectra gathered from a stereo-photogrammetric system (WASS) and from a directional waverider buoy, respectively. Besides what written above, to calculate $S(\sigma, \theta)$ from stereo-photogrammetric measurements in one of the field test reported

we extracted a set of virtual gauges from the reconstructed 3D maps of sea surface elevations. Therefore, we used one of the techniques typically used for array of gauges, instead of Fourier transforming the wave the sea surface elevation field. In all the cases analyzed, we applied stochastic techniques, since we are only interested in the directional spectrum calculation and not in the knowledge of the phases distribution (Benoit et al., 1997).

Stochastic methods

Stochastic techniques for directional spectrum calculation proceed in two steps (Benoit et al., 1997):

1. *perform spectral analysis of the recorded time-series, by computing the cross-spectral density functions between each pair of signals.*

   Assume J sensors are employed: they are located in $\mathbf{x}_j$ and their signals $P_j(t)$ are recorded over a time T, at a sampling rate $1/\Delta t$. The analysis of the correlation between each pair of signals is performed in the frequency domain, by estimating the cross-spectral densities G_{ij} between each couple $(P_i; P_j)$. Following the Wiener-Kintchine theorem, the cross-spectral densities G_{ij} and the cross-correlation functions $R_{ij}(\tau)$ are a Fourier transform pair [6]:

   $$G_{ij}(\sigma) = \int_{-\infty}^{+\infty} R_{ij}(\tau) e^{-i\sigma t} d\tau \tag{2.11}$$

   where

   $$R_{ij}(\tau) = \lim_{T\to\infty} \frac{1}{T} \int_0^{+T} P_i(t) P_j(t+\tau) dt \tag{2.12}$$

   In the practice, the cross-spectra G_{ij} are estimated from the discretely sampled and finite duration time-series, by digital procedures based on the Fast Fourier Transform. In the same way, a Fourier pair (physical-wavenumber spaces) exists between the cross-spectral density function $G(\mathbf{r}, \sigma)$ measured at two locations separated by $\mathbf{r} = \mathbf{x}_i - \mathbf{x}_j$ and the directional spectrum $S(\mathbf{k}, \sigma)$:

   $$G(\mathbf{r}, \sigma) = \int_{\mathbf{k}} S(\mathbf{k}, \sigma) e^{-i\vec{k}\cdot\mathbf{r}} d\mathbf{k} \tag{2.13}$$

[6] The Fourier transform of a function $x(t)$ is

$$X(\sigma) = \int_{-\infty}^{+\infty} x(t) e^{-i\sigma t} dt \tag{2.10}$$

Since G_{ij} and G_{ji} are complex conjugate quantities, the cross-spectra are evaluated only for $i \leq j$. For a J probes system, the total number of (complex) cross-spectra to compute is $J(J+1)/2$. But one can note that:

- J are auto-spectra ($i = j$), real quantities;
- $J(J-1)/2$ are actual cross-spectra ($i < j$), whose real parts C_{ij} are called "coincident spectral density functions" or "co-spectra", while their imaginary parts Q_{ij} are called "quadrature spectral density functions" or "quad-spectra".

2. *determine the directional spectrum (or the directional spreading function $D(\sigma, \theta)$) by inverting the relationship between the cross-spectra and the directional spectrum.*

   Under the assumptions fixed above, the relationship between the cross power spectrum and the wavenumber-frequency spectrum $S(\mathbf{k}, \sigma)$ for a pair of wave properties was introduced by Isobe et al. (1984):

$$G_{ij}(\sigma) = \int_{\mathbf{k}} H_i(\mathbf{k}, \sigma) H_j^*(\mathbf{k}, \sigma) e^{-i\mathbf{k}(\mathbf{x}_j - \mathbf{x}_i)} S(\mathbf{k}, \sigma) d\mathbf{k} \quad (i = 1, ..., J; i < j) \tag{2.14}$$

   H_i and H_j^* [7] are transfer functions between the surface elavation signal and other wave signals (pressure, velocity and slope of the surface). For the surface elevation, they are trivially equal to 1 and eq. (2.13) is resorted. The wave-number $\mathbf{k}$ is related to frequency through the dispersion relation (2.2) and so, according to (2.9), (2.14) can be rewritten in terms of the directional spectrum $S(\sigma, \theta)$ as:

$$G_{ij}(\sigma) = \int_0^{2\pi} H_i(\sigma, \theta) H_j^*(\sigma, \theta) e^{-i\mathbf{k}(\mathbf{x}_j - \mathbf{x}_i)} S(\sigma, \theta) d\theta \quad (i = 1, ..., J; i < j) \tag{2.15}$$

   or in terms of the directional spreading function $D(\sigma, \theta)$, exploiting (2.4):

$$G_{ij}(\sigma) = S(\sigma) \int_0^{2\pi} H_i(\sigma, \theta) H_j^*(\sigma, \theta) e^{-i\mathbf{k}(\mathbf{x}_j - \mathbf{x}_i)} D(\sigma, \theta) d\theta \quad (i = 1, ..., J; i < j) \tag{2.16}$$

The core of the directional wave analysis is the solution of the integral system of equations (2.16), that is, finding a function $D(\sigma, \theta)$ continuous over $[0; 2\pi]$ at each frequency, from a finite and limited number of equations given

[7] The symbol * stands for the complex conjugation.

by cross-spectra. Variance density spectrum $S(\sigma)$ is obtained by performing Welch's method with 50% overlapping and Hanning windowing (Bendat and Piersol, 2011). If an infinite number of wave signals were simultaneously recorded, the directional spectrum could be uniquely determined.

In the followings, a brief illustration of the chosen techniques (i.e., EMEP and WFS) is reported, while a more complete description of them and of the other techniques available can be found, for example, in (Benoit et al., 1997):

- *WFSM: Weighted Fourier Series Method (Longuet-Higgins et al., 1963)*

  It is an easy-implementation computational efficient method, though it is not one of the more accurate. The method basically consists in calculating an approximation of the directional spreading function $D(\sigma, \theta)$ using a Fourier Series truncated at order K:

$$D(\sigma, \theta) = \frac{a_0}{2\pi} + \frac{1}{\pi} \sum_{n=1}^{K} (a_n \cos n\theta + b_n \sin n\theta) \tag{2.17}$$

  where

$$a_n = \int_0^{2\pi} D(\sigma, \theta) \cos n\theta d\theta \qquad b_n = \int_0^{2\pi} D(\sigma, \theta) \sin n\theta d\theta \tag{2.18}$$

  and $a_0 = 1$. To avoid the occurrence of negative values of the directional spreading function Longuet-Higgins et al. (1963) introduced a weighting function $W_K(\theta)$

$$W_K(\theta) = R_K \left(\cos \frac{\theta}{2} \right)^{2K} \tag{2.19}$$

  where R_K is the normalization coefficient chosen such that $\int_0^{2\pi} W_K(\theta) d\theta = 1$

$$R_K = \frac{2^{2K-1}(K!)^2}{\pi(2K)!} \tag{2.20}$$

  $W_K(\theta)$ has a Fourier series decomposition with coefficients a_k^K. Convolving the truncated Fourier series and the weighting function gives

$$\begin{aligned} D_{WFS}(\sigma, \theta) &= \int_0^{2\pi} W_K(\theta - \theta') D(\sigma, \theta') d\theta' = 1 \\ &= \frac{1}{2\pi} + \frac{1}{\pi} \sum_{n=1}^{K} a_k^K (a_n \cos n\theta + b_n \sin n\theta) \end{aligned} \tag{2.21}$$

  For a single point measuring device acquiring the sea surface elevation and the horizontal displacements, e.g. a directional waverider buoy,

K=2 and

$$W_2(\theta) = \frac{1}{2\pi} + \frac{1}{\pi}\left[\frac{2}{3}\cos\theta + \frac{1}{6}\cos 2\theta\right] \tag{2.22}$$

$$D_{WFS}(\sigma,\theta) = \frac{1}{2\pi} + \frac{2}{3\pi}\left(a_1\cos\theta + b_1\sin\theta\right) + \frac{1}{6\pi}\left(a_2\cos 2\theta + b_2\sin 2\theta\right) \tag{2.23}$$

$$\begin{aligned} a_1(f) &= \frac{Q_{12}}{\sqrt{C_{11}(C_{22}+C_{33})}} & a_2(f) &= \frac{C_{22}-C_{33}}{C_{22}+C_{33}} \\ b_1(f) &= \frac{Q_{13}}{\sqrt{C_{11}(C_{22}+C_{33})}} & b_2(f) &= \frac{2C_{23}}{C_{22}+C_{33}} \end{aligned} \tag{2.24}$$

- *EMEP: Extended Maximum Entropy Method (Hashimoto et al., 1994).*

  It basically consists in determining the directional spreading function by maximizing an entropy function and accounting for errors. For a detailed description of the method, see (Hashimoto et al., 1994). Computation time is highly variable depending on how easily the iterative computation finds the solution. Low spectral energies at low and high frequencies can cause problems with the solution and slow the computation. In these cases the computation may need to be successively over-relaxed to achieve a converging solution. The authors concluded that:

  - the EMEP can be applied to handle arbitrary-mixed instrument array measurements;
  - when the EMEP is applied to three-quantity measurements, it yields the same estimate as the MEP (Maximum Entropy Principle) and has higher resolution than the EMLM (Extended Maximum Likelihood Method);
  - when the EMEP is applied to more than three arbitrary-mixed instrument array measurements, it yields almost the same estimate as the BDM (Bayesian Direct Method, i.e. the more accurate method) and has the highest resolution among other existing methods.

2.3 Idealized sea states: analytical spectral formulations

The analysis of complex realistic problems is usually made by resorting to simplified idealized conditions. Idealized sea states strictly holds under the

hypothesis of a constant wind blowing perpendicularly off a long and straight coastline over deep waters. Nevertheless, often they are employed even if the founding hypothesis does not strictly hold, because idealized conditions allow to disentangle the roles of different forcings, highlighting the governing physical processes at the expenses of minor ones.

In these conditions, sea state wave parameters, i.e. significant wave height H_s and peak wave period T_p, and the variance density spectrum $S(\sigma)$ are determined by the wind speed U, the fetch length F and the time since the wind started to blow D. Resorting to the concept of equivalent fetch of a wave component, i.e. the length of the fetch such that the wind has the same time to transfer energy to the wave component, only wind speed U and fetch length F are required to describe the sea state. In this context, universal relationship for wave parameters have been observed and universal spectral shapes have been proposed. For example in fully-developed conditions, when fetch length is not relevant, significant wave height H_s and peak period T_p depend only upon wind speed and dimensionless H_s and T_p are universal constant. In fact, the use of dimensionless quantities allows to generalize observations making them independent from the scale of observation.

2.3.1 Completely developed sea states: the Pierson-Moskowitz spectrum

The first variance density spectral shape $S(\sigma)$ considered is the fully-developed spectrum observed by Pierson and Moskowitz (1964). It is a one parameter spectrum that can be expressed as a function of either wind speed U, modal frequency σ_m or significant wave height H_s. If wind speed U is the parameter of the spectrum, then

$$S(\sigma) = Ag^2\sigma^{-5}e^{-B(g/U/\sigma)^4} \tag{2.25}$$

where $A = 0.0081$ is the Phillips constant and $B = 0.74$.

In the following we will use the modal frequency dependent spectral shape: to highlight dependence on modal frequency, we can resort to one of the universal relationship observed, i.e. $\sigma_m = 0.87(g/U)$ [8] (Ochi, 2005) obtaining

$$S(\sigma) = Ag^2\sigma^{-5}e^{-P(\sigma/\sigma_m)^{-4}} \tag{2.26}$$

[8] In fully developed conditions sea state depends only upon the wind speed U, i.e. fetch length is not relevant and waters are deep. In such conditions, Pierson and Moskowitz (1964) found a dimensionless modal period $gT_m/U = 7.14$, yielding to $\sigma_m = 0.87(g/U)$. Here, U is measured 19.5 m above sea level. To account for 10 m wind speed U_{10}, assuming $U_{19.5} = 1.075U_{10}$, dimensionless modal period becomes $gT_m/U_{10} = 7.69$ and $\sigma_m = 0.82(g/U_{10})$ (Holthuijsen, 2007)

being $P = 5/4$.

Alternatively, Pierson Moskowitz spectrum can be written as a function of the significant wave height H_s, taking advantage of another universal relationship observed for a fully developed sea state, i.e. $H_s = 0.21(U^2/g)$ [9] (Ochi, 2005)

$$S(\sigma) = Ag^2\sigma^{-5}e^{-Q(g/H_s)^2/\sigma^4} \tag{2.27}$$

where $Q = 0.032$.

2.3.2 Generating sea states: the JONSWAP spectrum

Pierson-Moskowitz spectrum provides good fittings to fully-developed seas data. For younger fetch-limited seas, i.e. with fetch length shorter than the equivalent fetch length, the JONSWAP spectrum was proposed by Hasselmann et al. (1973). The high and low frequency tails of spectra observed during JONSWAP (JOint North Sea WAves Project) project have the same shape of those of Pierson-Moskowitz spectra, but JONSWAP peaks are sharper. Hence, JONSWAP frequency spectrum is expressed as a scaled Pierson-Moskowitz spectrum, multiplied by a peak-enhancement function

$$G(\sigma) = \gamma^{\exp\left[-\frac{1}{2}\left(\frac{\sigma/\sigma_m - 1}{\beta}\right)^2\right]} \tag{2.28}$$

where β is a peak-width parameter ($\beta = \beta_a = 0.07$ for $\sigma \leq \sigma_m$ and $\beta = \beta_b = 0.09$ for $\sigma > \sigma_m$). The scaling is provided by the A_J parameter. JONSWAP frequency spectrum is therefore (Holthuijsen, 2007)

$$S(\sigma) = A_J g^2\sigma^{-5}e^{-P(\sigma/\sigma_m)^{-4}}\gamma^{\exp\left[-\frac{1}{2}\left(\frac{\sigma/\sigma_m - 1}{\beta}\right)^2\right]} \tag{2.29}$$

Parameters of JONSWAP spectrum evolve as the sea-state evolves. In particular for a constant wind speed, A_J, γ and σ_m decrease with fetch length F (Figure 2.1). As the sea state tends to fully developed conditions, $A_J \to A = 0.0081$, $\gamma \to 1$ and the dimensionless modal frequency $\nu = (\sigma_m/2\pi)U/g \to 0.13$. These are typical values of Pierson-Moskowitz spectrum parameters. Several authors proposed to model the dependence of JONSWAP parameters upon ν by using power laws (Hasselmann et al., 1973, 1976; Mitsuyasu et al., 1980; Lewis and Allos, 1990; Young, 1999). Different coefficients for power laws were obtained from large data sets analyses, including JONSWAP project data set. Some discrepancies emerged among the

[9] In fully developed conditions Pierson and Moskowitz (1964) found a dimensionless significant wave height $gH_s/U^2 = 0.21$, yielding to $H_s = 0.21(U^2/g)$. To account for 10 m wind speed U_{10} in place of 19.5 m wind speed, assuming $U_{19.5} = 1.075U_{10}$, dimensionless H_s becomes $H_s = 0.24(U_{10}^2/g)$ (Holthuijsen, 2007)

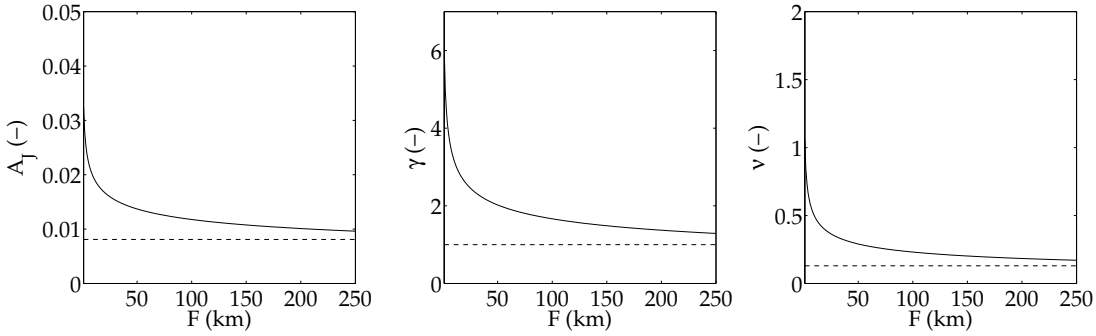

Figure 2.1: Parameters of the JONSWAP spectrum as a function of fetch length F (solid lines), according to Lewis and Allos (1990). Wind speed $U = 15$ m/s and F values are chosen in order to keep $\overline{F}$ between 0 and 10^4, drawing upon (Lewis and Allos, 1990). Left panel: scaling parameter A_J. Central panel: peak-enhancement factor γ. Right panel: dimensionless modal frequency $\nu = (\sigma_m/2\pi)U/g$. Dashed lines represent parameters values of the Pierson-Moskowitz spectrum (fully developed conditions): $A = 0.0081$ (left panel), $\gamma = 1$ (central panel), $\nu = 0.13$ (right panel).

cited studied (Young, 1999). Hence, we choose to model evolution of JONSWAP parameters according to the power laws of Lewis and Allos (1990), since they assume Pierson-Moskowitz shape as correct, thus taking into account the transition to fully developed conditions:

$$\begin{aligned} A_J &= 0.032\nu^{0.67} \\ \gamma &= 5.87\nu^{0.86} \\ \overline{F} &= 47.4\nu^{-3.03} \end{aligned} \tag{2.30}$$

where $\overline{F} = Fg/U^2$ is dimensionless fetch. According to (2.30) and to the definitions of dimensionless modal frequency ν and fetch length $\overline{F}$, JONSWAP parameters can be expressed as a function of wind speed U and fetch length F:

$$\begin{aligned} A_J &= 0.032\left(\overline{F}/47.4\right)^{-0.67/3.03} = 0.045\left(F/U^2\right)^{-0.22} \\ \gamma &= 5.87\left(\overline{F}/47.4\right)^{-0.86/3.03} = 9.18\left(F/U^2\right)^{-0.28} \\ \sigma_m &= 2\pi g/U(\overline{F}/47.4)^{-1/3.03} = 16.5(FU)^{-0.33} \end{aligned} \tag{2.31}$$

Typically, $A_J = [0.0081, 0.032]$, $\gamma = [1, 7]$ with a mean value of 3.3, $\sigma_m > 0.13g/U$.

2.3.3 Directional distribution function

The analytic formulations of the directional spectrum $S(\sigma, \theta)$ we will use in the rest of the thesis are the easiest to be manipulated since we chose a directional distribution function that does not depend on the frequency σ:

$$S(\sigma, \theta) = S(\sigma)D(\sigma, \theta) = S(\sigma)D(\theta) \tag{2.32}$$

We considered the $\cos^2$ directional distribution function (Ochi, 2005). This directional distribution depends on the direction θ only and has directional spreading equal to 31.5°, therefore it can be reasonably employed to represent short-crested wind sea states (Holthuijsen, 2007):

$$D(\theta) = \frac{2}{\pi}\cos(\theta - \theta_p)^2, \qquad -\pi/2 \leq (\theta - \theta_p) \leq \pi/2 \tag{2.33}$$

θ_p being peak wave direction. To simplify further the analyses, we will assume peak wave direction $\theta_p = 0$, i.e. propagation along x axis of a cartesian reference frame.

2.4 Realistic sea states: spectral numerical wave modeling

Idealized conditions described above are generally used under the cited hypotheses, i.e. simple domains and constant winds. In fact, when an accurate prediction of wave parameters (in space and time) is required in presence of complex domains and rapidly changing winds (in space and time) idealized conditions can be used only to get a first estimate of wave sea states. The alternative approach is to integrate the wave energy evolution equation:

$$\frac{dS(\sigma, \theta)}{dt} = \frac{\partial S(\sigma, \theta)}{\partial t} + \mathbf{c}_g \cdot \nabla S(\sigma, \theta) = F(\sigma, \theta) \tag{2.34}$$

Eq. (2.34) can be integrated either on the wave rays, i.e. following a Lagrangian approach, or locally on the nodes of a discretized spatial domain, i.e. following a Eulerian approach. Due to the non-linear character of the processes involved and accounted for in the source term $F(\sigma, \theta)$ [10], the Eulerian approach has been preferred and advanced spectral numerical wave modeling, i.e. second and third generation models, are therefore based on it.

[10] Since the source term $F(\sigma, \theta)$ depends on all the components of the directional spectrum $S(\sigma, \theta)$, the solution of the evolution equation (2.34) for a spectral component at a prediction point along a ray requires the knowledge of the energy associated to the other components of the spectrum, that are obviously unknown. For this reason the Lagrangian approach has been abandoned (Holthuijsen, 2007).

2.4.1 The wave action balance equation

Modern spectral numerical wave models solve the wave action density balance equation, that will be presented and described in this section. Wave action density is $N(\sigma,\theta) = S(\sigma,\theta)/\sigma$, σ being relative wave frequency, i.e. the angular frequency in a system moving with the current (if present). The reason for this change of variable, i.e. from energy density to action density, is the possibility of including the effects of wave-current interaction into eq. (2.34). In fact, including them into an energy density based equation implies adding extra terms representing the effects of the work done by the current against the radiation stresses. Instead, wave action density equation, though identical to wave energy density equation, does not require extra terms because wave action density $N(\sigma,\theta)$ is conserved in presence of an ambient current. Basically, wave action density equation can be obtained, exactly as done for wave energy density equation, by balancing the wave action of one spectral component (σ,θ) traveling through a $\Delta x\Delta y$ cell during a time interval Δt: *change of wave action = net import + local generation*. To account for some wave propagation processes, e.g. shoaling, refraction and others, also the net import of wave action inside a spectral cell $\Delta\sigma\Delta\theta$ must be considered. After the three contributions have been made explicit (for details on how the equation is obtained see for example (Holthuijsen, 2007)), the equation in its more general form, i.e. holding both in coastal and oceanic waters [11], reads:

$$\frac{\partial N(\sigma,\theta)}{\partial t}+\frac{\partial c_{g,x}N(\sigma,\theta)}{\partial x}+\frac{\partial c_{g,y}N(\sigma,\theta)}{\partial y}+\frac{\partial c_{g,\theta}N(\sigma,\theta)}{\partial \theta}+\frac{\partial c_{g,\sigma}N(\sigma,\theta)}{\partial \sigma} = \frac{F(\sigma,\theta)}{\sigma} \tag{2.36}$$

The same equation can be written in the geographical (λ,ϕ) domain. Herein, we will focus on the equation written above in the cartesian domain (x,y), aware that the same considerations hold also for the equation in the geo-

[11] The equation herein reported holds both in coastal and oceanic waters. In oceanic, i.e. deep and far from coasts, waters, a simpler form of the equation can be derived. It is written for energy density $S(\sigma,\theta)$ since, generally, in oceanic waters the effect of wave-current interactions is negligible. Moreover, the group celerity, i.e. the speed at which energy (action) is transported, does not depend on x and y, hence it can be taken out of the derivatives. Only propagation in the physical domain (x,y) is accounted for. Hence, processes of refraction, diffraction and shoaling are not modeled. Finally, the source term does not account for processes like bottom friction, triad wave-wave interactions and depth-induced wave breaking. The resulting equation is exactly equal to the evolution equation (2.34)

$$\frac{\partial S(\sigma,\theta)}{\partial t} + c_{g,x}\frac{\partial S(\sigma,\theta)}{\partial x} + c_{g,y}\frac{\partial S(\sigma,\theta)}{\partial y} = F(\sigma,\theta) \tag{2.35}$$

graphical domain.

The first term of eq. (2.36) accounts for the temporal variation of wave action density. The second and the third terms represent wave propagation in the physical space (x, y), while fourth and fifth ones represent wave propagation in the spectral space (σ, θ). The right-hand side term, i.e. $F(\sigma, \theta)$, is the source term, collecting the contributions of various processes of generation, dissipation and transfer of energy over the spectral components. Generation is due to wind. Dissipation is caused by whitecapping, depth-induced breaking and bottom friction. Transfer of energy over the spectral components is due to non-linear wave-wave interactions in deep waters (quadruplets) and in intermediate/shallow waters (triplets). Dynamic processes occurring during wave propagation, e.g. refraction, diffraction, shoaling (depth-induced) and wave-current interactions, are represented by the left-hand side terms of eq. (2.36). Refraction due to depth variations and diffraction, though the latter not properly modeled [12], are accounted for in the fourth term. In fact, the rotation induced by these processes to spectral components in the physical space corresponds to propagation along θ in the spectral space, with speed $c_{g,\theta}$. In the followings we will focus on shoaling and wave-current interaction, which are two of the processes investigated in Part III. They are typical intermediate/shallow water processes and, though their causes are different, they share some common characteristics.

Shoaling

Depth-induced shoaling is the process of steepening of an harmonic wave, occurring when its phase speed decreases approaching shallower waters. It is mainly governed by the group speed c_g, since balancing energy transport $P = Ec_g$ between two different depth sections (2: deep waters, 1: onshore), i.e. $(Ec_g)_2 = (Ec_g)_1$, implies that

$$\frac{H_2}{H_1} = \sqrt{\frac{c_{g,1}}{c_{g,2}}} \tag{2.37}$$

being $E = 1/8\rho g H^2$ the energy of an harmonic wave with height H. Hence, the effect of shoaling on an harmonic wave approaching the coastline over a flat sloping bottom is to slow down the wave speed and to increase the amplitude [13]. This process is known as "energy bunching", namely the hor-

[12] Diffraction is not properly modeled because the diffraction-induced turning rate $c_{\theta,diff}$, formulated for an harmonic wave, is modeled in an approximate form for irregular waves.

[13] Actually, in a first phase of the propagation towards the coastline, the group speed increases before decreasing. Hence, looking at eq. (2.40), initially the amplitude of an

izontal compacting of energy. On the contrary, frequency can be considered constant during shoaling.

The effect of shoaling on a spectrum can be investigated by looking at the shoaling effect on each spectral component. Hence, energy globally increases since the amplitude of the harmonics composing the spectrum increases. Mean frequency changes, because low frequency components are more affected by shoaling with respect to high frequency components. In fact, deep waters waves are dispersive, so longer low frequency components travel faster than higher frequency components. Therefore, a down-shifting on the mean frequency is usually observed on the spectrum while waves propagate towards shallower waters. In wave action density equation (2.36), shoaling is accounted for in the second and third terms, where the group speed variation acts. To highlight the effect of shoaling eq. (2.36) have to be written in absence of other processes, i.e. no wind generation, dissipation or energy transfer:

$$\frac{\partial N(\sigma,\theta)}{\partial t} + \frac{\partial c_{g,x} N(\sigma,\theta)}{\partial x} + \frac{\partial c_{g,y} N(\sigma,\theta)}{\partial y} = 0 \tag{2.38}$$

Assuming a 1D domain and stationary conditions, shoaling can be easily studied. In fact:

$$\frac{\partial c_{g,x} N(\sigma,\theta)}{\partial x} = 0 \tag{2.39}$$

which means that for each spectral component:

$$c_{g,x} N(\sigma,\theta) = \text{const} \tag{2.40}$$

Wave-current interaction

The presence of an ambient time and/or space varying current modifies the propagation of waves. It interacts with waves by exchanging energy (work done by the current against the radiation stresses) and by bodily moving its medium of propagation with varying speed. In the following, we will briefly discuss which are the effects of current on waves and how they are accounted for in the wave action balance equation (2.36). A more complete dissertation on this topic can be found in (Holthuijsen, 2007), for example.

Primarily, we must distinguish among the cases of constant and variable current speed. In fact in the former case, an harmonic wave propagating on a moving medium is only bodily transported by the current without changing wave height, frequency nor direction. Hence, in a moving frame of reference whose moving speed is that of the current, i.e. V, kinematics of linear wave

harmonic decreases.

is retained. Accordingly, linear dispersion relationship (2.2) for an harmonic wave does not change, assuming σ is the relative frequency. The absolute frequency ω, i.e. absolute with respect to a fixed frame of reference, is expressed by the Doppler-shifted dispersion relationship, accounting for current speed V:

$$\omega = \sigma + \mathbf{k} \cdot \mathbf{V} \tag{2.41}$$

where $\mathbf{k} \cdot \mathbf{V}$ represents the Doppler shift. Neither ω changes if current speed is constant. However, the presence of an ambient current, even if constant, modifies the magnitude and direction (in the absolute reference frame) of the energy transport. As a matter of fact, group speed $\mathbf{c}_g$ in the absolute reference frame is (subscript a stands for absolute, subscript r for relative):

$$\mathbf{c}_{g,a} = \mathbf{c}_{g,r} + \mathbf{V} \tag{2.42}$$

On the contrary, the presence of an ambient current that is variable in space and/or time causes also:

- changes in height, due to energy bunching, refraction and transfer of energy between current and waves;
- changes in frequency, due to current-induced frequency shifting (in the reference frame moving with wave action (or wave energy) speed);
- changes in direction, due to refraction.

Studying the wave-current interactions, Phillips (1977) obtained the relationship between relative phase speed of an harmonic wave in a moving medium c and in still waters c_0 (hereinafter, subscript 0 will indicate that physical parameters are in still waters). Resorting to the wave numbers conservation principle in stationary conditions [14], he obtained:

$$\frac{c}{c_0} = \frac{1}{2} + \frac{1}{2}\left(1 + \frac{4V}{c_0}\right)^{0.5} \tag{2.44}$$

Eq. (2.44) shows that the phenomenon of a wave entering a moving medium is governed by the ratio V/c_0. It shows also that part of the right-hand side

[14] Eq. (2.44) was obtained starting from the principle of wave conservation. $\partial\mathbf{k}/\partial t + \nabla\omega = 0$. In 1D stationary conditions, it gives: ω =const. Hence, absolute frequency is maintained between still and moving (with speed V) waters. According to eq. (2.42), since $\omega = kc$ it follows that $k(c + V) = k_0 c_0$ and in deep waters the following quadratic equation in c/c_0 is obtained,

$$\frac{c^2}{c_0^2} = \frac{c}{c_0} + \frac{V}{c_0} \tag{2.43}$$

whose solution is eq. (2.44)

term vanishes when $V = -1/4c_0$. In other words, when an opposing current has speed equal to one fourth of the wave phase speed, waves can't propagate through the current field. Actually, they break before that limit (Phillips, 1977).

Concerning change in wave height, energy bunching and transfer of energy are readily accounted for in the wave action balance equation by using the actual propagation velocity of wave energy, i.e. $\mathbf{c}_g$, and by substituting wave energy balance with wave action balance, respectively. Consider an harmonic wave with height H_0 that passes from still waters, i.e. with current speed $V_0 = 0$, to a current field with constant speed V. Wave energy is not conserved in presence of a current, hence we have to balance the transport of wave action N between a section in still waters and a section in moving waters: $(Nc_g)_0 = (N(c_g + V))$ implies that (Phillips, 1977):

$$\frac{H}{H_0} = \frac{c_0}{\sqrt{c(c+2V)}} \tag{2.45}$$

where deep waters have been assumed for the sake of simplicity ($\sigma = g/(2c_g)$ and $c_g = c/2$). Eq. (2.45) models how wave height is modified by an ambient current. If this is a following current, i.e. $V > 0$, eq. (2.44) shows that phase speed is increased and hence, according to eq. (2.45) wave height is reduced. If waves are propagating against the current, i.e. $V < 0$, from (2.44) follows that phase speed is slowed down and consequently according to (2.45) wave height increases.

In a frame of reference moving with wave action speed, relative frequency σ evolves in presence of an ambient current. The rate of change is $c_\sigma = d\sigma/dt$. Calling n and m the directions respectively parallel and orthogonal to the wave propagation direction, i.e. normal to the crest:

$$c_\sigma = \frac{\partial \sigma}{\partial d}\left(\frac{\partial d}{\partial t} + \mathbf{V}\cdot\nabla d\right) - c_g\mathbf{k}\cdot\frac{\partial \mathbf{V}}{\partial n} \tag{2.46}$$

c_σ is the velocity of frequency shifting, that is due to a time variation of water depth (first term between brackets), to the effect of a current bodily moving the wave over a horizontally varying bottom (second term in brackets) and to the effect of a wave moving with horizontally varying current (last term of the right-hand side).

Current-induced refraction is the change of wave direction due to the presence of an ambient current. Its rate of change $c_{\theta,curr}$ sums to those ones due to depth-induced refraction $c_{\theta,depth}$ and diffraction $c_{\theta,diff}$, and is expressed by:

$$c_{\theta,curr} = -\frac{\mathbf{k}}{k}\frac{\partial \mathbf{V}}{\partial m} \tag{2.47}$$

Thus, it only acts in presence of a current that is variable along the wave crest direction m.

2.4.2 The Simulating WAves Nearshore (SWAN) model

To solve the wave action density balance equation on complex domains and accounting for all the cited processes of wave generation, propagation and dissipation, numerical techniques are required. To this end, several numerical models have been developed, e.g. WAVEWATCH (Tolman, 1999), WAM (The WAMDI Group, 1988; Günther et al., 1992), TOMAWAC (Benoit et al., 1996), MIKE21-SW (Sorensen et al., 2004) and SWAN (Booij et al., 1999) among others. They share the most of the features and they mainly differ for the numerical scheme used to solve eq. (2.36) (e.g. finite differences, finite elements or finite volumes) and for the formulations of the source terms adopted. These models are also known as "spectral wave models" since they assume a spectral representation of sea states. Alternatively, they are called "phase-averaging models" since they predict average or integral properties of the sea state, instead of resolving each single waves, as done by the "phase-resolving models". In fact, the spectral approach takes into account the amplitudes but not the phases (Young, 1999).

We chose to employ the Simulating WAves Nearshore model (SWAN, (Booij et al., 1999; The SWAN Team, 2011)), Cycle III version 40.85. As opposed to other spectral wave models, SWAN has been optimized to be performant in the nearshore areas of the seas. In fact, in these regions geographical space must be discretized in order to catch the bottom variability and the small scale processes that the latter can cause (e.g. depth-induced breaking, refraction, shoaling). Hence, the resolution of the grids is allowed to reach very low values, until 10-100 m of cell side. A model with such resolution cannot simultaneously satisfy Courant criterion [15] and guarantee a reasonable computational efforts, therefore SWAN is based on an implicit finite difference numerical scheme that is unconditionally stable [16] (Holthuijsen, 2007). Nevertheless, the integration of the source terms is not so stable, because some of these require an explicit scheme. Hence, differently from

[15] Courant criterion (Holthuijsen, 2007) requires that an explicit numerical scheme satisfy the following condition to prevent numerical instabilities: during a time step Δt wave energy must not travel more than a cell side Δx, i.e. $\Delta t < \Delta x / c_{g,x}$ (analogously for Δy). It follows that if Δx is small enough to catch the bottom variability, Δt is forced to be small too. For example, a 0.04 Hz wave on a coastal region (5 m deep) discretized using 100 m side cells, requires a 15 s time step to be modeled.

[16] Though stable under condition, e.g. Courant criterion, explicit schemes are often preferred with respect to implicit schemes, because the former are more robust and can be solved directly without solving implicit equations.

other models, SWAN applies a limiter to wave action change, to avoid the development of numerical instabilities.

Grids can be expressed in SWAN by using Cartesian or spherical coordinates and they can be both rectangular or curvilinear. Boundary conditions are fully absorbing for wave energy leaving the open boundaries or reaching the coastlines and needs to be prescribed for wave energy entering the computational domain. The directional spectral space can be discretized in order to cover the whole range of directions, i.e. $\theta = [0°\text{-}359°]$, or alternatively only a sector, i.e. $\theta_{min} \leq \theta \leq \theta_{max}$. Frequencies are defined with logarithmic distribution between a minimum and a maximum cut-off frequency, i.e. $\sigma_{min} \leq \sigma \leq \sigma_{max}$ Outside this prognostic range, the diagnostic tails are imposed, i.e. 0 for $\sigma < \sigma_{min}$ and σ^{-m} $(m = 4, 5)$ for $\sigma > \sigma_{max}$. The latter tail is needed to compute integral wave parameters [17] and to calculate the non-linear wave-wave interactions at high frequencies.

SWAN models the processes characterizing wave propagation, such as shoaling, refraction and wave-current interaction. These are represented in the left-hand side of wave action balance equation (2.36). Additionally, the processes of generation, dissipation and transfer of wave energy are included and represented in the right-hand side of eq. (2.36), i.e. in the source term $F(\sigma, \theta)$. The formulations adopted by SWAN for these processes are the same as those of WAM model, i.e. WAM Cycle III (The WAMDI Group, 1988) and WAM Cycle IV (Günther et al., 1992). Additionally, as a model devoted to nearshore areas, SWAN includes depth-induced breaking, bottom friction and triad wave-wave interactions in intermediate/shallow waters. For a detailed illustration of the formulations adopted and available with SWAN, see (The SWAN Team, 2011).

[17] The integral parameters of the spectrum are calculated from the moments of the directional spectrum $S(\sigma, \theta)$. The latter are obtained according to eq. (2.6) by integrating frequency between 0 and ∞. Hence, a diagnostic tail on high frequencies is needed to extend integration over the maximum cut-off frequency σ_{max}.

Chapter 3

Stochastic models for space-time extremes estimate

Stochastic models for wave extreme estimation in the space-time domain are herein illustrated. We will start from the firstly developed model, based on Piterbarg's theorem (Piterbarg, 1996; Krogstad et al., 2004). Then we will consider an approximation of Piterbarg's theorem holding for small areas, i.e. whose side is shorter than a wavelength, due to Forristall (Forristall, 2006). After that, we will expose Fedele's method (Fedele, 2012) based on the Adler and Taylor's Euler Characteristics approach (Adler, 1981; Adler and Taylor, 2007). Hence, the second-order non-linear correction of maximum sea surface elevations, based on the Tayfun quadratic equation (Tayfun, 1980), will be presented. Finally, we will discuss wave breaking, i.e. the physical mechanism that limits the stochastic estimated maxima.

3.1 Piterbarg's theorem

Piterbarg's Theorem (Piterbarg, 1996) states the asymptotic extremal distributions for homogeneous Gaussian fields in $\mathbb{R}^n$. We take $n = 3$, assuming the stochastic variable is the space-time varying sea surface elevation $\zeta(\mathbf{x}, t) = \eta(\mathbf{x}, t)/\sigma_\eta$, here normalized on the standard deviation of $\eta(\mathbf{x}, t)$, i.e. σ_η . The distribution of maxima depends on the size of the space-time volume $V \subset \mathbb{R}^3$ and on the size of an average wave W

$$|V| = XYD \qquad |W| = \overline{L}_x \overline{L}_y \overline{T}(1 - \alpha_{xt}^2 - \alpha_{xt}^2)^{-1/2} \tag{3.1}$$

Here, X and Y are area sides, D is sea state duration, $\overline{L}_x$ is mean wavelength, $\overline{L}_y$ is mean crest length, $\overline{T}$ is mean wave period, α_{xt} and α_{yt} account for the

correlation between space and time derivatives of $\eta(\mathbf{x}, t)$ (see Section 2.2.1). The equivalent number of waves within V is therefore (Krogstad et al., 2004)

$$N = 2\pi \frac{|V|}{|W|} = 2\pi \frac{XYD}{\overline{L}_x \overline{L}_y \overline{T}} \sqrt{1 - \alpha_{xt}^2 - \alpha_{yt}^2} \tag{3.2}$$

Assuming a sample of N waves with parent statistics of this kind:

$$N h_N^2 e^{-h_N^2/2} = 1 \tag{3.3}$$

h_N represents the maximum among N, i.e. the threshold exceeded once over N in the sample. A good enough approximation to h_N is

$$h_N \sim \sqrt{2 \ln N + 2 \ln(2 \ln N)} \tag{3.4}$$

Taking threshold $s >> \sigma_\eta$, Piterbarg's theorem define the cumulative distribution function of the maximum sea surface elevation ζ_{ST} over space and time

$$Pr(\zeta_{ST} \leq s) \sim \exp\left(\frac{(s^2 - 1)}{h_N^2} \exp\left(-\frac{1}{2}(s^2 - h_N^2)\right)\right) \tag{3.5}$$

For large N, (3.5) tends asympotically to the Gumbel distribution (Gumbel, 1958)

$$G(\zeta_{ST} \leq s) = \exp\left(-\exp\left(-(h_N - 2/h_N)(s - h_N)\right)\right) \tag{3.6}$$

Hence, the expected maximum sea surface height $\overline{\zeta}_{ST}$ over an area and during a time interval (space-time domain) is obtained as the expected value of the Gumbel distribution (3.6) (Krogstad et al., 2004)

$$\overline{\zeta}_{ST} = \overline{\eta}_{ST}/\sigma_\eta = h_N + \frac{\gamma}{h_N - 2/h_N} \tag{3.7}$$

being $\gamma \sim 0.5772$ the Euler-Mascheroni constant.

The expected maximum at a fixed point $\overline{\zeta}_T$ (time domain) stems from a Rayleigh parent statistics, thus it can be obtained combining

$$\overline{\zeta}_T = \overline{\eta}_T/\sigma_\eta = h_N + \frac{\gamma}{h_N} \tag{3.8}$$

with $h_N = \sqrt{2 \ln N}$, where the average number of waves $N = D/\overline{T}$ (time domain).

To consistently compare results of Piterbarg's theorem with results of Fedele's method that are normalized on the significant wave height H_s, the expected maximum over the space-time $\overline{\zeta}_{ST}$ and the expected maximum over time $\overline{\zeta}_T$ are rewritten as:

$$\overline{\xi}_{ST} = \overline{\zeta}_{ST}/4 \qquad \overline{\xi}_T = \overline{\zeta}_T/4 \tag{3.9}$$

in the approximation of a narrow-banded process, in which $H_s = 4\sigma_\eta$ holds. Hence, results hold when $\overline{\eta}_{ST} >> H_s/4$.

3.2 Forristall's approximation for small areas

Forristall found empirically that for small areas, i.e. whose side is smaller than a wavelength, a good fit to simulated maximum surface elevations versus area size can be achieved using the following average number of waves (Forristall, 2006)

$$N = 2\frac{X}{\overline{L}_x}\frac{D}{\overline{T}} \tag{3.10}$$

Thus, for small areas, the equivalent number of waves is proportional to the side of the area X, rather than to the area. This is due to the fact that the maximum is likely to occur on the side of the area when this is small with respect to the average size of the waves, i.e. $\overline{L}_x\overline{L}_y$.

In the following analysis, when $A \leq L_x L_y$ results of Piterbarg's theorem will be replaced by those obtained using Forristall's approximation, i.e. maxima over space and time (3.7) will be calculated using (3.10) in place of (3.2).

3.3 Fedele's method

Assume $\eta(\mathbf{x}, t)$ is a homogeneous (in space) and stationary (in time) Gaussian random field, e.g. the sea surface elevation in deep waters with a low sea severity. The excursion set $U_{\Omega,h}$ is the subset of the space-time volume Ω (with zero mean and standard deviation σ_η) such that the threshold h is exceeded by $\eta(\mathbf{x}, t)$

$$U_{\Omega,h} = \{(\mathbf{x}, t) \in \Omega : \eta(\mathbf{x}, t) > h\}$$

The Euler Characteristic EC of this set is a topological invariant counting the number of connected volumetric components minus the number of holes plus the number of hollows in the set. Hence, if the threshold h is high, i.e. $h >> \sigma_\eta$, EC counts the local maxima of the sea surface. Adler (1981) and Adler and Taylor (2007) have shown that the probability that the maximum exceeds a given high threshold $h >> \sigma_\eta$ is well approximated by the expected Euler Characteristic EC of the excursion set:

$$P(\max(\eta) > h|\Omega) = \mathbb{E}[EC(U_{\Omega,h})] \tag{3.11}$$

The maximum could exceed the threshold inside the volume V, at one of the sides of the volume, i.e. over S, or along the perimeter, i.e. along P. Hence, resorting to Euler Characteristics, the probability (3.11) is splitted among

three contributions

$$P(\max(\eta) > h|\Omega) = P(\max(\eta) > h|V) + P(\max(\eta) > h|S) + P(\max(\eta) > h|P) \tag{3.12}$$

The average number of 3D waves inside the volume has been defined by Fedele (2012), following Adler and Taylor (2007), as

$$M_3 = 2\pi \frac{D}{\overline{T}} \frac{X}{\overline{L}_x} \frac{Y}{\overline{L}_y} \sqrt{1-\alpha} \tag{3.13}$$

where $\alpha = \alpha_{xt}^2 + \alpha_{yt}^2 + \alpha_{xy}^2 - 2\alpha_{xt}\alpha_{yt}\alpha_{xy}$. The average number of 2D waves on the sides of the volume is (Fedele, 2012)

$$M_2 = \sqrt{2\pi} \left(\frac{XD}{\overline{TL}_x} \sqrt{1-\alpha_{xt}^2} + \frac{YD}{\overline{TL}_y} \sqrt{1-\alpha_{yt}^2} + \frac{XY}{\overline{L}_x \overline{L}_y} \sqrt{1-\alpha_{xy}^2} \right) \tag{3.14}$$

Along the perimeter of the volume, the average number of 1D waves is (Fedele, 2012)

$$M_1 = \frac{D}{\overline{T}} + \frac{X}{\overline{L}_x} + \frac{Y}{\overline{L}_y} \tag{3.15}$$

Though, since we are interested in comparing space-time contribution against time contribution, we will consider the average number of 1D waves as $M_1 = \frac{D}{\overline{T}}$. Spectral parameters involved in the previous formulae have been introduced and presented in Section 2.2.1, equation (2.7).

Given a sea state with sea severity H_s, the probabilities of exceedance (Fedele, 2012) of 3D, 2D and 1D waves are respectively

$$\begin{aligned} P_V(h|H_s) &= [16(h/H_s)^2 - 1]P(h|H_s) \\ P_S(h|H_s) &= 4(h/H_s)P(h|H_s) \\ P_P(h|H_s) &= P(h|H_s) \end{aligned} \tag{3.16}$$

where $P(h|H_s) = \exp\left(-8\frac{h^2}{H_s^2}\right)$ is the Rayleigh exceedence distribution function, holding in time domain under the narrow-banded process hypothesis.

Assuming stochastic independence among waves, according to Fedele (2012) the exceedance distribution of the maximum (3.12) can be written as

$$P(\max(\eta) > h|\Omega) = M_3 P_V(h|H_s) + M_2 P_S(h|H_s) + M_1 P_P(h|H_s) \tag{3.17}$$

Hence, the expected maximum sea surface height over an area A and during an interval D follows from Gumbel asymptotics (Gumbel, 1958)

$$\overline{\xi}_{ST} = \overline{\eta}_{ST}/H_s = h_N + \frac{\gamma}{16h_N - \frac{(32M_3h_N + 4M_2)}{(16M_3h_N^2 + 4M_2h_N + M_1)}} \tag{3.18}$$

where h_N is calculated from the parent statistics

$$(16M_3h_N^2 + 4M_2h_N + M_1)\exp(-8h_N^2) = 1. \tag{3.19}$$

The expected maximum sea surface height at a fixed point is recovered imposing $X = Y = 0$ in the previous equations:

$$\overline{\xi}_T = \overline{\eta}_T/H_s = h_N + \frac{\gamma}{16h_N} \tag{3.20}$$

where $h_N = \sqrt{\ln \frac{D/\overline{T}}{8}}$.

Since results are normalized on significant wave height H_s, in the approximation of a narrow-banded process ($H_s = 4\sigma_\eta$), results of Fedele's method hold when $\overline{\eta}_{ST} >> H_s/4$.

The method of Fedele differs from Piterbarg's theorem because, thanks to Euler Characteristics, it splits the average number of waves (3.2) into three contributions, namely (3.13), (3.14) and (3.15). This is aimed to take into account the probability that maxima could also occur on the boundaries of the space-time volume, i.e. on the [X,Y], [X,T], [Y,T] faces or on the X, Y, T lines. This allows the analysis to be performed even on small areas, i.e. areas with sides shorter than the mean wavelength. Moreover, a new coefficient for the correlation between space derivatives of $\eta(\mathbf{x}, t)$, i.e. α_{xy}, is introduced. Forristall's approximation holds on small areas too, but not on large ones.

3.4 Non-linear correction

To account for second-order non-linearities in the wave profile, we corrected expected maxima over an area $\overline{\xi}_{ST}$ and at a point $\overline{\xi}_T$, according to Tayfun quadratic equation (Tayfun, 1980) [1]:

$$\begin{aligned} \overline{\xi}_{ST,2} &= \overline{\xi}_{ST} + \frac{\mu}{2H_s}\overline{\xi}_{ST}^2 \\ \overline{\xi}_{T,2} &= \overline{\xi}_T + \frac{\mu}{2H_s}\overline{\xi}_T^2 \end{aligned} \tag{3.21}$$

In literature, when non-linear correction is applied to Piterbarg's theorem, i.e. to Piterbarg's theorem, the stochastic model is named Tayfun-Piterbarg model.

[1] Tayun equation has been originally derived for normalized crests (on standard deviation σ), hence in case of crests normalized on significant wave height H_s the second-order contribution has to be divided by H_s.

Here, μ is an integral measure of steepness (Fedele and Tayfun, 2009). It is related to the skewness coefficient λ, since $\mu = \lambda/3$. Nevertheless, this estimate of μ is statistically unstable, because it could be affected by the presence of trends or exceptionally high waves. A more stable estimate can be achieved by using the variance density spectrum $S(\sigma)$: for a narrow-banded sea state, μ is obtained as $\mu_m = \sigma_\eta \sigma_m^2/g$, being σ_η the standard deviation of η and $\sigma_m = m_1/m_0$ the mean frequency based on the first order moment m_1 of the variance density spectrum. Resorting to the bandwidth parameter $\nu = \sqrt{(m_0 m_2)/m_1^2 - 1}$ of Longuet-Higgins (1975), steepness calculation can be generalized to arbitrary bandwidth sea states:

$$\mu = \mu_m(1 - \nu + \nu^2) \tag{3.22}$$

3.5 Physical limiter to stochastic models: the wave breaking

According to wave mechanics, growth of a single wave is limited by the dissipative process known as wave breaking. Due to its strong non-linear character, wave breaking remains one of the least understood processes in wave mechanics. This is of two kinds:

- *depth-induced breaking*, occurring in coastal shallow waters when the wave looses its stability due to a wave height H too high with respect to the local water depth d. Thus, the breaking criterion is expressed through a breaker index γ_b

$$\frac{H_{max}}{d} = \gamma_b \tag{3.23}$$

  A typical range of γ_b for the individual wave height in an irregular wave field is $0.7 \div 0.8$ (Holthuijsen, 2007), though ratios of 0.5 as well as ratios of 1.5 have been observed, depending on the incident wave steepness and on the beach slope.

- *steepness-induced breaking (white-capping)*, occurring when the steepness H/L of an individual wave reaches a limiting value after which the wave looses its stability (L is wavelength). It occurs at any relative water depth, but since shoaling enhance wave steepness, white-capping increases its importance in coastal waters. It also verifies in presence of a strong opposing current, i.e. when current speed approaches one fourth of the wave phase speed. For a regular wave (i.e. periodic and fixed in shape), Miche (1944) obtained the following breaking criterion,

based on the fact that the particle velocity in the crest cannot overcome the phase speed of the wave:

$$\frac{H_{max}}{L} = 0.14 \tanh(kd) \tag{3.24}$$

Eq. (3.24) implies that $H_{max}/L = 0.14$, occurring in deep waters, is an upper bound. However, observations showed that also other parameters, e.g. degree of short-crestedness and wind speed, seem to control the phenomenon (Holthuijsen, 2007).

Hence, a wave is stable if:

$$H_{max} < \min(\gamma_b d, 0.14 \tanh(kd) L) \tag{3.25}$$

While the depth-induced breaking criterion (3.23) holds for an individual irregular wave, the steepness-induced one (3.24) was obtained for a individual regular wave. According to Tayfun (2008), Miche criterion cannot be used as a consistent indicator of wave breaking for irregular waves, but it represents an upper bound for the maximum height a large wave can reach. Indeed, according to the theory of Quasi-Determinism of Boccotti (2000), large waves behaves more like regular than irregular waves.

Quasi-determinism theory (Boccotti, 2000) states that if a large crest $C/\sigma_\eta >> 1$ (σ_η being standard deviation of $\eta(\mathbf{x}, t)$) occurs at a point $\mathbf{x}_0$, then most likely this is the crest of a 3D wave group at the apex of its development. In these conditions, the profile of the wave group has a deterministic shape. In the time domain, i.e. fixing $\mathbf{x} = \mathbf{x}_0$, it is

$$\overline{\eta}(\mathbf{x}_0, T) = C\psi(T) \tag{3.26}$$

where $\psi(T)$ is time autocovariance function [2] of $\eta(\mathbf{x}_0, t)$, normalized on the maximum in order to vary between 1 and -1. T is the time lag from the occurrence of the large crest t_0, herein set to $t_0 = 0$ without loss of generality. In accordance to the latter specifications, when $T = 0$, then $\overline{\eta}(\mathbf{x}_0, 0) = C$. Crest height C can be rewritten using Tayfun quadratic equation,

$$C = C_1 + \frac{\mu}{2\sigma_\eta} C_1^2 \tag{3.28}$$

[2] Time autocovariance function describes how much the surface elevation $\eta(t)$ and a T-shifted surface elevation $\eta(t+T)$ are correlated. In fact, for a zero-mean process as $\eta(t)$ is, autocovariance equals autocorrelation. It can be obtained from the time series, as $\psi(T) = \overline{\eta(t)\eta(t+T)}$, or alternatively via spectral estimate, according to the Wiener-Kintchine theorem:

$$\psi(T) = \int_0^\infty S(\sigma) \cos(\sigma T) d\sigma \tag{3.27}$$

C_1 being the linear component of the actual crest height C, obtained solving eq. (3.28) [3]. Hence, the deterministic profile of the wave group with large crest C can be corrected to account for second-order non-linearities:

$$\overline{\eta}(\mathbf{x}_0, T) = C_1\psi(T) + C_1^2\frac{\mu}{2}(\psi^2(T) - \hat{\psi}^2(T)) \tag{3.29}$$

where $\hat{\psi}(T)$ is the Hilbert transform [4] of $\psi(T)$.

To check if the expected maximum sea surface elevations estimated by the stochastic models of Piterbarg and Fedele belong to stable, i.e. non-breaking, waves the following approach could be followed:

1. consider the result of the model, i.e. $\overline{\xi}_{ST}$ (linear) or $\overline{\xi}_{ST,2}$ (non-linear). If $\overline{\xi}_{ST} >> H_s/4$ ($\overline{\xi}_{ST,2} >> H_s/4$), then the maximum expected sea surface height in space-time is likely to be the crest C of the central wave of a group at the apex of its development

$$C = \overline{\xi}_{ST} \quad \text{or} \quad C = \overline{\xi}_{ST,2} \tag{3.31}$$

Hence, according to Boccotti (2000) the profile of this wave is (3.26) (or (3.29) in case of second-order correction). The wavelength L of this wave can be inferred the dispersion relationship (2.2) by using the wave period estimated from the profile $\overline{\eta}(\mathbf{x}_0, T)$, after zero-crossing. Alternatively, the wave period can be assumed to be equal to the peak period T_p [5], since the the propagation speed of the waves in the group is nearly equal to that associated with T_p (Boccotti, 2000). The wave height H can be obtained following Quasi-determinism theory:

$$H = C(1 + |\psi(T*)|) \tag{3.32}$$

where T^* is the abscissa (time) of the first minimum of autocovariance function $\psi(T)$, herein taken in absolute value [6].

[3] Tayun equation has been originally derived for normalized crests (on standard deviation σ), hence in case of dimensional crests the second-order contribution has to be divided by σ.

[4] The Hilbert transform of a real-valued function $x(t)$, defined within $-\infty < x(t) < \infty$, is:

$$\hat{x}(t) = \frac{1}{\tau}\int_0^\infty \frac{x(\tau)}{t-\tau}d\tau \tag{3.30}$$

[5] If peak period is not available, the period T_C of the wave with crest C can be reasonably assumed to be $T_C = 1.3\overline{T}$ (Gōda, 2010), $\overline{T}$ being the mean wave period (see (2.7)). A similar result can be inferred assuming a JONSWAP spectrum according to (Boccotti, 2000). Indeed, $T_C = 0.97T_p$ and $T_p/\overline{T} = 1.41$ for a spectrum with high frequency tail proportional to σ^{-5} (σ is angular frequency). Hence, $T_C = 0.97 \cdot 1.41\overline{T} = 1.37\overline{T}$.

[6] $|\psi(T*)|$ is a narrow-bandedness parameter (Boccotti, 2000), being 1 for a narrow-banded process and 0 for a wide-banded process. Hence, if the process is linear and narrow-banded, then $H = 2C$ as expected.

2. the maximum wave height H_{max} of a stable wave is calculated according to the Miche criterion (3.24)

$$H_{max} = 0.14L \tanh(kd) \tag{3.33}$$

Here, L is the wavelength of the wave with crest C, previously estimated.

3. the maximum crest height $C_{max,1}$ of a stable linear wave is obtained from (3.32):

$$C_{max,1} = \frac{H_{max}}{1 + |\psi(T*)|} \tag{3.34}$$

The maximum crest height $C_{max,2}$ of a stable non-linear (second-order) wave is obtained from $C_{max,2}$ once again resorting to Tayfun quadratic equation (3.28).

4. finally, we end up with 3 breaking criteria: one for wave height H of the maximum wave in space-time [7], i.e. $H > H_{max}$, and two for the maximum crest in space-time, i.e. $C > C_{max,1}$ for linear crest and $C > C_{max,2}$ for non-linear (second-order) crest.

An alternative, more straightforward though equivalent, approach to evaluate the stability of waves predicted by stochastic models is to verify that the steepness ϵ of the wave with crest C (and wavenumber k_p, associated to peak period)

$$\epsilon = k_p C \tag{3.35}$$

does not exceed the Stokes limiting steepness ϵ_{max}, obtained from Miche-Stokes criterion (3.24):

- $\epsilon_{max} = 0.44$, for a narrow-banded linear process;
- $\epsilon_{max} = 0.89/(1 + |\psi(T^*)|)$, for a linear process with narrow-bandedness parameter $|\psi(T^*)|$.

A second-order-based criterion is herein ignored since its implementation requires the calculation of H_{max} through eq. (3.33).

[7] According to Stokes theory, second-order non-linearities do not affect wave height but only wave crest and wave trough.

Part III

Results

Chapter 4

Space-time extremes from stereo-photogrammetric data

4.1 Introduction

In this Chapter, we will report on the exploitation of field data to validate stochastic models for wave extreme prediction in the space-time domain. To our best knowledge, this is one of the first time such stochastic models are validated against field data. Indeed until now, their capability to predict wave extreme over space-time has been mostly proved resorting to laboratory experiments (Forristall, 2011) or numerical modeling (Forristall, 2005, 2007; Krogstad et al., 2004; Socquet-Juglard et al., 2005). Only recently, Fedele et al. (2011) compared stereo-photogrammetric measurements with theoretical prediction of Tayfun-Piterbarg's theorem. The aforementioned comparisons concern Piterbarg's theorem only. In fact, Fedele's method was validated for the first time by Fedele et al. (2012, 2013): using stereo-photogrammetric measurements they proved its capability to predict the expected ratio between the maximum over an area and the maximum at a given point during a sea state, i.e. $\overline{\eta}_{ST}/\overline{\eta}_{T}$.

In this context, we were aimed at testing the performance of both stochastic models in the prediction of the expected maximum sea surface elevation $\overline{\eta}_{ST}$ occurring during a sea state over an area. However, validation of such stochastic models is a challenging task. First of all, field data sets in space-time are difficult to be gathered for the same reasons that cause directional spectra to be rarely available (see Section 2.2). Then, the data sets must be sufficiently extended over both space and time, but particularly over space, to guarantee at the same time a numerous enough sample and stochastic independence of the elements included in the sample. Finally, the data sets

must be composed of elements consistent with the non-unique concept of a wave in space-time. In fact, as stated in Section 1.1.3, there is no univoque definition for a wave in space.

At present, only few instruments can record space-time evolution of waves: stereo-photogrammetric systems and radars. Though the latter can cover larger areas with high spatial resolutions, they cannot guarantee sufficient time resolutions. To validate Piterbarg's theorem and Fedele's method we took advantage of the 3D sea surface profile reconstructed by a novel stereo-photogrammetric technique, i.e. Wave Acquisition Stereo System (WASS, (Benetazzo, 2006)). This was used on one hand to extract the sea surface elevation maxima during a sea state at random points and over different size areas around the same points. On the other hand, it was used to calculate the directional spectrum of the sea state and to apply Tayfun-Piterbarg's and Fedele's models (corrected to the second order). Then, by comparing measured maxima with those predicted by stochastic models we evaluated their performance in predicting space-time maxima of sea states $\overline{\eta}_{ST}$.

WASS data were gathered during two different field campaigns. The first set of experiments was performed in March 2013 at the ISMAR-CNR oceanographic tower "Acqua Alta" (Figure 4.1), located in the northern Adriatic Sea 16 km off the Venice coast at 17 m water depth. The second field campaign was conducted in April 2013 in the southern Adriatic Sea from a ship, the ISMAR-CNR "R/V Urania". Description of this novel stereo-photogrammetric technique is detailed in (Benetazzo et al., 2014).

4.2 Field campaign at CNR-ISMAR oceanographic tower "Acqua Alta", northern Adriatic Sea

4.2.1 Data description

The first experiment was conducted on 15.03.2013 (11.41UTC) at ISMAR-CNR oceanographic tower "Acqua Alta" (Figure 4.1) in the northern Adriatic Sea, during a crossing-sea event: North-East wave (Bora) conditions were crossing South-East (Sirocco) waves. In fact, the wind was rotating from Bora to Sirocco. Mean wind speed was 5.20 m/s and significant wave height H_s was 0.58 m. Table 4.1 summarizes sea state conditions during the experiment, represented by the spectral parameters available from data recorded by permanent instrumentation installed on the sea bottom, i.e. an AWAC Acoustic Doppler Current Profiler (AWAC-ADCP).

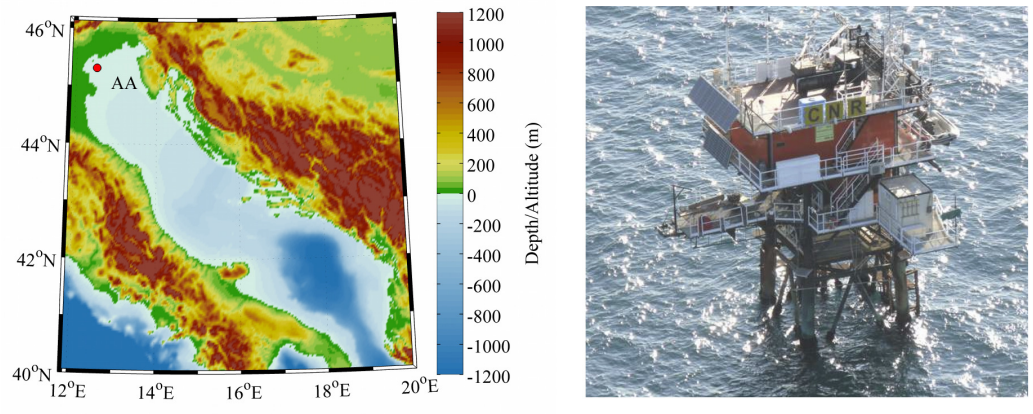

Figure 4.1: ISMAR-CNR oceanographic tower "Acqua Alta" (right), located in the northern Adriatic Sea (left) 16 km off the Venice coast at 17 m water depth (label AA in left panel).

Data	Unit	AWAC-ADCP
H_s	(m)	0.58
T_p	(s)	3.83
T_{02}	(s)	2.87
θ_p	(°N)	58.44
$\overline{\theta}$	(°N)	64.40

Table 4.1: Sea state conditions during experiment at oceanographic tower "Acqua Alta" (15.03.2013 11.41UTC) represented by spectral parameters from permanent instrumentation (AWAC-ADCP). H_s: spectral significant wave height; T_p: peak wave period; T_{02}: mean wave period; θ_p and $\overline{\theta}$: peak and mean wave direction, here intended as the directions from which waves are coming from, referred to the geographical North.

Data basically consist of 5850 stereo-photogrammetric image pairs recorded by two cameras installed on "Acqua Alta" tower 12.5 m above the mean sea level. The frame rate was 10 Hz, hence a sea state of nearly 10 minutes was remotely sensed (Figure 4.2). WASS system error on surface elevations was estimated to be 0.02 m. A detailed description of WASS deployment at "Acqua Alta" is reported in (Benetazzo et al., 2012).

4.2.2 Directional spectrum calculation

After the 3D profile was reconstructed, in order to calculate the directional spectrum $S(\sigma, \theta)$ 14 virtual probes were randomly chosen inside the area framed by WASS (Figure 4.2) and corresponding time series were extracted from the space-time data set. The relative positions of the probes were chosen in order to guarantee that the following criteria were satisfied (Gōda, 2010):

- no pair of probes should have the same vectorial distance;
- the vectorial distance should be distributed uniformly in a range as wide as possible;
- the minimum distance between a pair of probes should be smaller than half the wavelength of the shortest component included in spectral analysis.

The time series at the probes were smoothed to remove outliers and also filtered to remove high frequency noise. Smoothing was performed by using a weighted moving average. Since time series frequency spectra showed a noise floor from approximately 2 Hz (i.e. 12.57 rad/s) to the Nyquist frequency of 5 Hz (i.e. 31.42 rad/s) data were filtered by means of a low-band pass frequency filter, with cut-off frequency equal to 12.57 rad/s (Figure 4.3).

Following procedures described in Section 2.2.2, the directional spectrum $S(\sigma, \theta)$ was estimated by applying a stochastic method of analysis, precisely the Extended Maximum Entropy Method (EMEP), on an array of virtual wave probes. EMEP is implemented within the DIWASP toolbox for MATLAB (Johnson). The toolbox version available at the moment we performed analysis, i.e. version 1.3, showed some bugs [1]. Therefore, we adapted and

[1]The following version of DIWASP toolbox, i.e. version 1.4, has the cited bugs fixed and can be used to calculate directional spectrum with some warnings: (i) use cartesian convention for angles since nautical convention does not properly work again; (ii) cartesian 3D plots are not completely displayed, so it is preferable to use polar plots; (iii) the ambiguity in wave direction calculation is due to the possibility of performing cross-

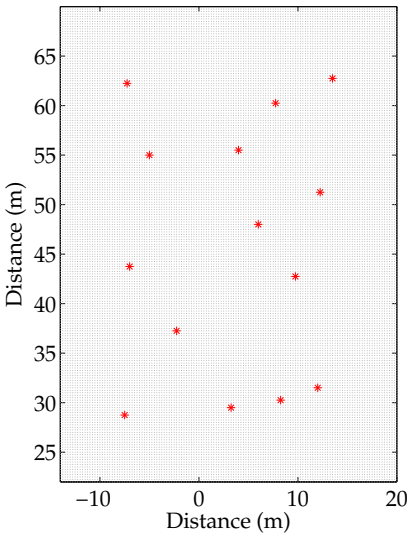

Figure 4.2: Area framed by WASS. Gray dots are points of stereo-photogrammetric analysis for profile reconstruction. Virtual probes for directional spectrum calculation are highlighted by red asterisks.

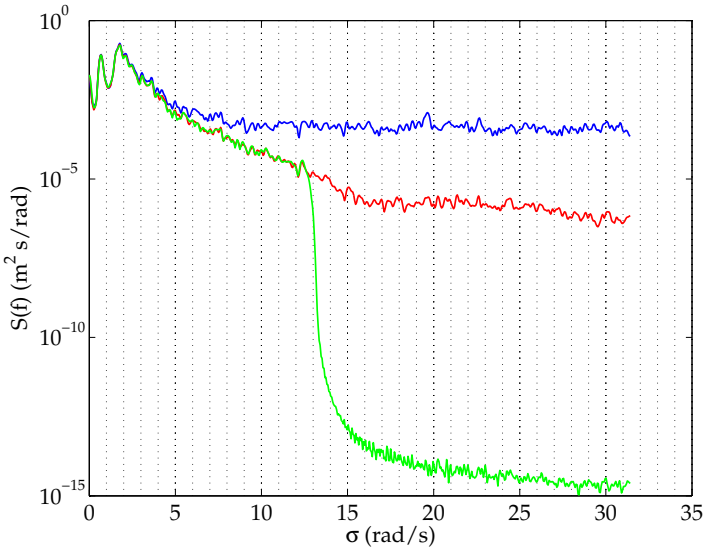

Figure 4.3: Time series frequency spectrum at one of the virtual probes of Figure 4.2 (blue): smoothed (red), smoothed and filtered (green).

corrected DIWASP version 1.3 to fix bugs concerning the estimate of spectral significant wave height H_s and ambiguity in wave direction calculation. After correction, we calculated the directional spectrum $S(\sigma, \theta)$, that is showed in Figure 4.4-a in cartesian (σ, θ) coordinates and in Figure 4.4-b in polar (σ, θ) coordinates. Directional and frequency resolutions are $\Delta\theta = 3°$ and $\Delta\sigma \sim 0.25$ rad/s, respectively. Some parameters of the directional spectrum, i.e. the same available from reference instrumentations in Table 4.1, are summarized in Table 4.2.

Data	Unit	Value
H_s	(m)	0.59 ± 0.02
T_p	(s)	3.66
T_{02}	(s)	3.02
θ_p	(°N)	58.00
$\overline{\theta}$	(°N)	85.00

Table 4.2: Parameters of the directional spectrum $S(\sigma, \theta)$ calculated using EMEP. H_s: spectral significant wave height; T_p: peak wave period; T_{02}: mean wave period; θ_p: peak wave direction; $\overline{\theta}$: mean wave direction. Directions are here intended as the direction from which waves are coming from.

A direct comparison of Table 4.1 and Table 4.2 revealed that spectral parameters of the directional spectrum calculated through EMEP are in agreement with the same parameters obtained by AWAC-ADCP and WASS: H_s differs for a 2% from ADCP observations; T_p, T_{02} and θ_p differ for 4%, 5% and 1%, respectively. $\overline{\theta}$ is less in agreement with AWAC-ADCP observations, differing for a 32%. This is probably due to an erroneous detection of a changing direction by AWAC-ADCP. Beside this, the omnidirectional frequency spectrum $S(\sigma) = \int_0^{2\pi} S(\sigma, \theta) d\theta$ in Figure 4.5 pointed out that the high frequency tail of the estimated spectrum is consistent with those generally observed on wave spectra, in particular by Forristall (1981) [2]. Indeed, it

spectral analysis with two different functions: in fact, built-in MATLAB function cpsd.m and DIWASP function diwasp_csd.m (according to the manual, to be used when built-in function is nota available) calculate opposite imaginary parts of spectra, hence results are 180° shifted; we recommend to use DIWASP function diwasp_csd.m to get correct results, otherwise directions are not consistent with the rest of the toolbox.

[2]Following Phillips (1958), the high frequency tail of $S(\sigma)$, i.e. $\sigma > \sigma_p$, decays following a power law of this kind: $S(\sigma) \sim \alpha g^2 \sigma^{-n}$. This range of the spectrum where the energy exchange between wind and sea is accounted for, is called saturation or equilibrium range. According to Phillips (1958), the power n was theoretically estimated to be equal to 5. However, observational studies (Toba, 1973; Forristall, 1981; Battjes et al., 1986) have shown different behaviors. For example, Forristall (1981) reported of a $n = 4$ power law

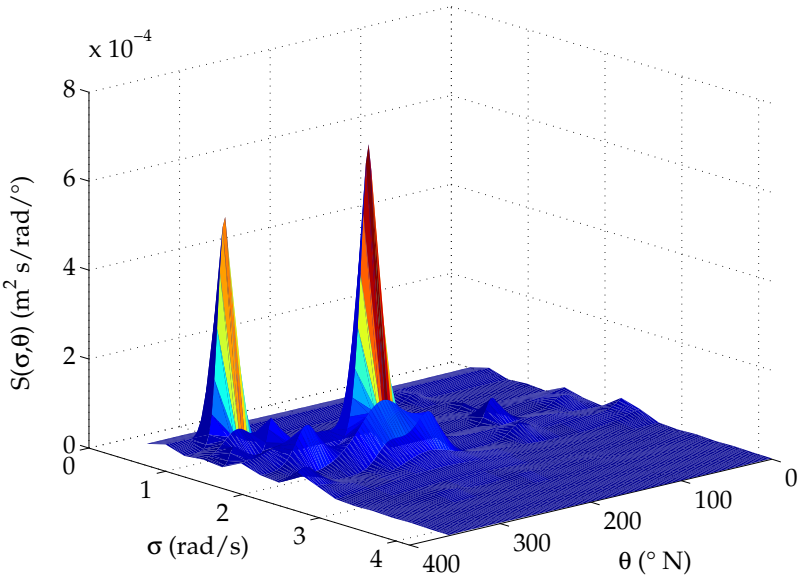

(a)

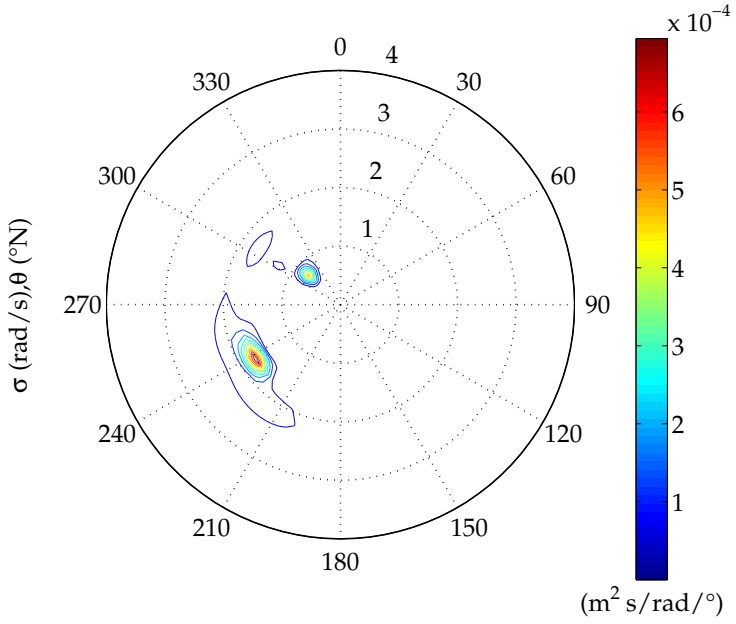

(b)

Figure 4.4: Directional spectrum $S(\sigma, \theta)$ calculated using EMEP. Directions here are propagation directions, therefore 180° shifted with respect to directions in Table 4.1 and Table 4.2. Resolutions are $\Delta\theta = 3°$ and $\Delta\sigma \sim 0.25$ rad/s). (a) Cartesian $\sigma - \theta$ coordinates. (b) Polar $\sigma - \theta$ coordinates.

initially decays with σ^{-4}, while it seems to decay with σ^{-5} for $\sigma > 3$ rad/s. Nevertheless, due to the limitations of EMEP and the fact that calculation is performed on a limited number of probes, we observed the presence of energy on directions that are not consistent with the wave field analyzed (Figure 4.4).

In such conditions, spectral analysis through EMEP detected a short-crestedness parameter $\gamma_s = 0.95$, hence short crested conditions, which is a situation consistent with a generating crossing-sea.

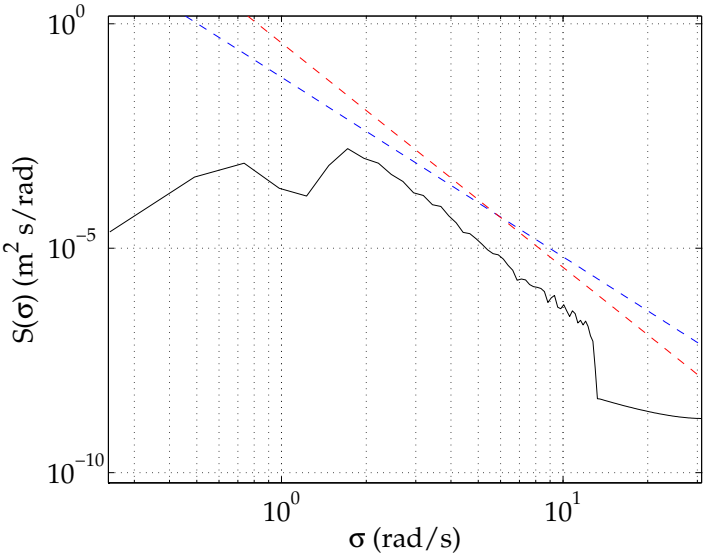

Figure 4.5: Omnidirectional frequency spectrum $S(\sigma)$. The power laws σ^{-4} and σ^{-5} are plotted as straight lines with -4 (blue) and -5 (red) slopes.

4.2.3 Stochastic models validation

To estimate the expected maxima from WASS measurements, the same 14 points used for EMEP analysis were chosen (Figure 4.6) and 26 square areas were built around each of them, whose sizes ranges from 0 to 156.25 m^2. The number of points and the size of the areas were constrained by the need of a sufficient number of space-time volumes from one side and by the small size of the framed area from the other side. In our opinion, what we got is a good compromise between these two constraints.

next to the peak, followed by a $n = 5$ power law. The higher frequency range of the spectrum has been less investigated because of the reduced signal-to-noise ratio.

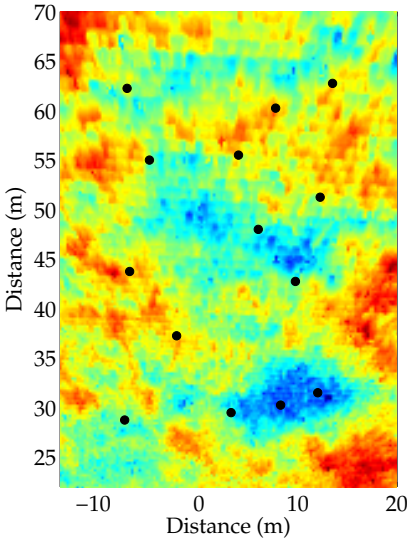

Figure 4.6: "Acqua Alta" tower experiment (15.03.2013 11.41UTC): rectangular area for space-time extremes analysis. Black circles are points of analysis.

For each area size, the expected maximum $\overline{\hat{\eta}}_{ST}$ was calculated averaging the maxima $\hat{\eta}_{ST}$ observed inside each area during the whole sea state duration, i.e. nearly 10 minutes [3]. Expected values of observations are provided with confidence interval $\pm\sigma_{\hat{\eta}_{ST}}$, which accounts also for the error of WASS system ($\sigma_{\hat{\eta}_{ST}}$ being the standard deviation of $\hat{\eta}_{ST}$). Then, space-time analysis was performed using Tayfun-Piterbarg's theorem and Fedele's method corrected to the second order to calculate the expected maxima $\overline{\eta}_{ST}$ over the areas of listed sizes and during approximately 10 minutes. Results are shown in Figure 4.7 for Tayfun-Piterbarg's theorem and in Figure 4.8 for Fedele's method.

Figure 4.7 and Figure 4.8 give another experimental proof of the fact that the maximum sea surface elevation over an area is larger than that occurring at a point. In fact looking at results for the largest area (i.e. 156.25 m^2), the normalized expected maximum sea surface elevation measured by WASS was $\overline{\hat{\xi}}_{ST} = \overline{\hat{\eta}}_{ST}/H_s = 1.27$. At the same time, the normalized expected maximum over a point, i.e. represented by 0 m^2 area, was $\overline{\hat{\xi}}_T = 0.90$. Hence, the ratio of the expected maxima over space-time and over time was $\overline{\hat{\xi}}_{ST}/\overline{\hat{\xi}}_T = 1.41$, at 156.25 m^2. The measurement uncertainties, indicated in Figures by the confidence interval, were quite large and reached their maximum at the smaller

[3] We recall that $\overline{x}$ means expectation of x and $\hat{x}$ indicates that x is observed.

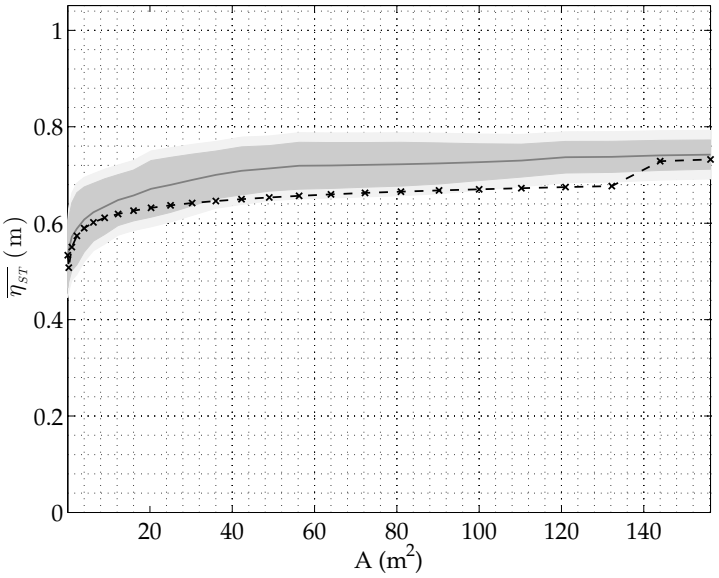

(a)

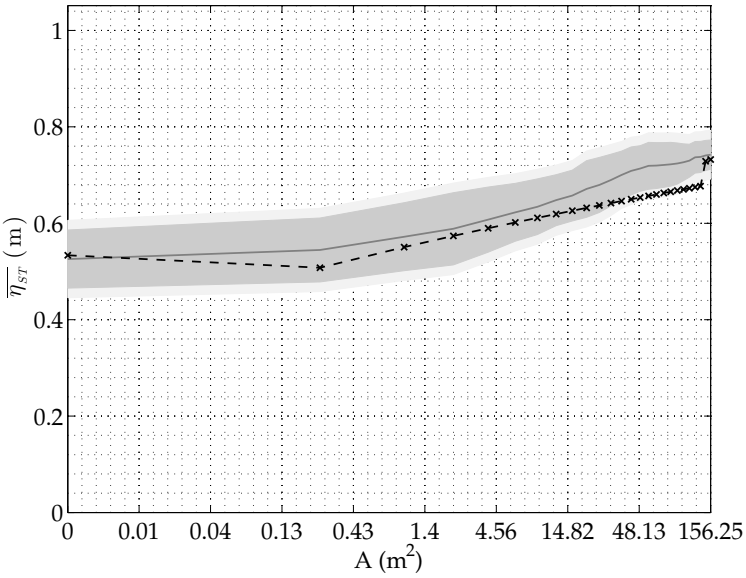

(b)

Figure 4.7: Tayfun-Piterbarg's theorem predictions (black asterisks) versus WASS observations (gray solid line) at "Acqua Alta" tower (15.03.2013 11.41UTC): expected maximum over space-time as a function of area size. Observations are provided with confidence interval $\pm\sigma_{\hat{\eta}_{ST}}$ (grey): the narrower band (darker gray) is without WASS error (i.e. 0.02 m). (a) Linear plot. (b) Log plot, to emphasize small areas.

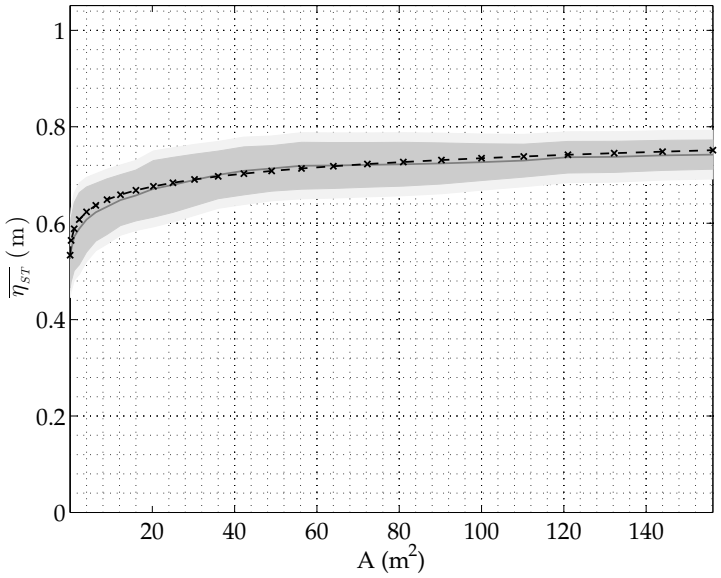

(a)

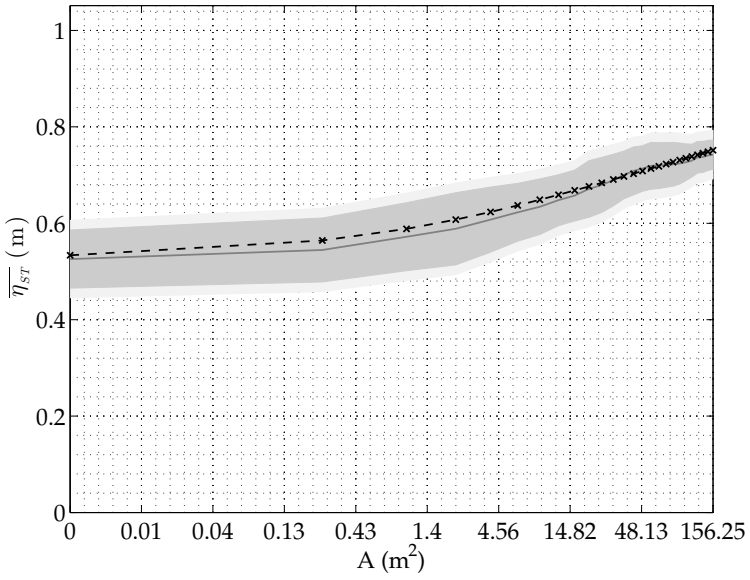

(b)

Figure 4.8: Fedele's method predictions (black asterisks) versus WASS observations (gray solid line) at "Acqua Alta" tower (15.03.2013 11.41UTC): expected maximum over space-time as a function of area size. Observations are provided with confidence interval $\pm\sigma_{\hat{\eta}_{ST}}$ (grey): the narrower band (darker gray) is without WASS error (i.e. 0.02 m). (a) Linear plot. (b) Log plot, to emphasize small areas.

areas and at the point observation (0 m^2). The large standard deviation at the point observation is an effect of short-crestedness of the sea state. In fact, in a long-crested sea spatial variability of the expected maximum $\overline{\hat{\eta}}_{ST}$ would have surely been much lower. Standard deviation decreased increasing area size. This means that the fluctuations around the expected value of the maxima measured over various equal size areas, here represented by the standard deviation, tend to decrease for larger areas. This can be due to a right convergence of maxima towards a single expected value but also to an effect of superposition of the areas that, while increasing, at some time could overlap and detect the same maxima. This latter effect could be avoided if larger framed areas were available. Unfortunately, at present it is not easy to meet the need of larger areas with high space-time resolutions.

Both stochastic models reproduced the trend of measured $\overline{\hat{\eta}}_{ST}(A)$. However, Tayfun-Piterbarg's theorem underpredicted the observed $\overline{\hat{\eta}}_{ST}$ for largest area sizes (Figure 4.7), at least while Forristall approximation is used. In fact, for area sizes greater than 40 m^2 and smaller than 140 m^2 Tayfun-Piterbarg's theorem predictions fell outside the confidence interval. On the contrary, Fedele's method was in agreement with observations, falling always within $\overline{\hat{\eta}}_{ST}(A) \pm \sigma_{\hat{\eta}_{ST}}$ (Figure 4.8). The motivation for Tayfun-Piterbarg's theorem underpredition is in the size of the space domain used. In fact, we were analyzing relatively small areas with respect to the average size of a 3D wave. The largest analyzed area, i.e. 156.25 m^2, has a 12.5 m side, while the wavelength $\overline{L}_x$ was 11 m. Hence, Tayfun-Piterbarg's theorem could not be applied in its original version for the smallest areas because, being asymptotic, it works only for large areas. For this reason, as stated in Section 3.2, we calculated the average number of waves in the domain through Forristall's approximation when area side was smaller than wavelength, i.e. below 140 m^2. As a matter of fact, Forristall's approximation seemed to be inaccurate for the bigger $\sqrt{A}/\overline{L}_x$ ratios [4]. Moreover, it seemed to be inconsistent with the point estimate for the smaller areas (Figure 4.7). Over 140 m^2 Tayfun-Piterbarg's theorem seemed to work fine. On the contrary, Fedele's method accounts for the possibility that maxima occur on the boundary of the domain, hence it works even for areas smaller than the characteristic size of a wave. Nevertheless, accuracy in prediction of maxima increased as area sizes increased (Figure 4.8).

[4]Forristall's expression for the number of waves in small areas condition was obtained experimentally but was not given together with a range of applicability. From results in (Forristall, 2005) it seems however that the agreement with simulations is good down to $\sqrt{A}/\overline{L}_x \sim 0.1$ and up to$\sqrt{A}/\overline{L}_x \sim 1$. Nevertheless, it must be pointed out that these results have been obtained by fitting theoretical predictions to simulations, since the irregularity parameter α was unknown.

Performances of stochastic models prediction with respect to WASS observations are summarized by statistics in Table 4.3. It is worthwhile to point out the high correlation coefficients (i.e. larger than 0.98) and the low RMSE (i.e. 0.02 m and 0.01 m) for both the stochastic models. Coefficient of determination and best fit line slope were considerably higher for Fedele's method. Moreover, a larger Bias (negative, meaning underestimation) was observed for Tayfun-Piterbarg's theorem, though rather small compared to the absolute value of observations.

	CC	RMSE (m)	p	Bias (m)	R^2
WASS/Tayfun-Piterbarg	0.96	0.02	0.79	-0.04	0.50
WASS/Fedele	1.00	0.01	0.93	0.01	0.98

Table 4.3: Statistics of prediction from stochastic models with respect to WASS observations at "Acqua Alta" tower. CC: correlation coefficient, RMSE: root mean square error, p: best fit line slope, Bias, R^2: coefficient of determination.

4.3 Field campaign from CNR-ISMAR oceanographic R/V "Urania", southern Adriatic Sea

4.3.1 Data description

The second experiment was conducted on 14.04.2013 08.12UTC. WASS system was deployed on board the ISMAR-CNR R/V Urania during an oceanographic cruise in the southern Adriatic Sea. Wind was blowing with an average wind speed of 7.1 m/s from 312.2°N. During the experiment the ship was drifting towards wind direction with average speed of 0.23 m/s. However, the space-time extremes analysis should not be affected by the slow drift of the ship, which can be estimated to be approximately the 6% of the wave celerity associated to the mean wave period. Moreover, since we are looking at maxima of time and space-time series rather than at a time sequence at a fixed point, maxima can be considered independent being separated one form each other by a certain time lag. 12 minutes long sequence was acquired by WASS cameras at 15 Hz while the ship was in 1000 m deep waters. Then, data were processed to retrieve the 3-D sea surface profile, accounting also for the rotations of the ship.

4.3.2 Directional spectrum calculation

Prior to spectral calculation, in order to remove high frequency noise on the data set, this was smoothed using a median filter in space using a 3x3 window. Then, the time series at each WASS point were filtered by means of low-pass frequency filter with 1 Hz cut-off frequency. Hence, wavenumber spectrum $S(k_x, k_y)$ was obtained by Fourier transforming the sea surface elevation field at each frame of the WASS dataset and averaging all the spectra so obtained. Then, resorting to (2.9), the directional spectrum $S(\sigma, \theta)$ was calculated (Fig. 4.9). Sea state spectral parameters from WASS are summarized in Table 4.4. They represent the only available data of the sea state, since no other instrument was deployed at the moment. To compare WASS measurements we benefitted of the SWAN numerical model results we set up on the Mediterranean Sea, forced by COSMO-I7 winds (see Chapter 7). For this sea state, short-crestedness parameter was estimated to be 0.51.

Data	Unit	Value
H_s	(m)	0.64 ± 0.02
T_p	(s)	3.22
T_{02}	(s)	2.34
θ_p	(°N)	335.90

Table 4.4: Parameters of the directional spectrum $S(\sigma, \theta)$. H_s: spectral significant wave height; T_p: peak wave period; T_{02}: mean wave period; θ_p: peak wave direction. Directions are here intended as the direction from which waves are coming from, in analogy with wind convention.

Differently from "Acqua Alta" experiment, spectral resolution for "R/V Urania" experiment depends upon the size of the framed area. Since it is quite small, the wavenumber spectrum $S(k_x, k_y)$ and the directional spectrum $S(\sigma, \theta)$ are roughly discretized over the spectral domain. This certainly introduce some inaccuracies in the space-time extremes prediction. In fact, besides the rough spectral discretization cited, low frequency components are not described within the spectrum but at the same time they contribute to the observed values of maxima. Nevertheless, at present this is the best resolution we can get. Hence, we accept it aware of the fact that space-time extremes obtained by stochastic analysis could underestimate to some extent the actual observed maxima.

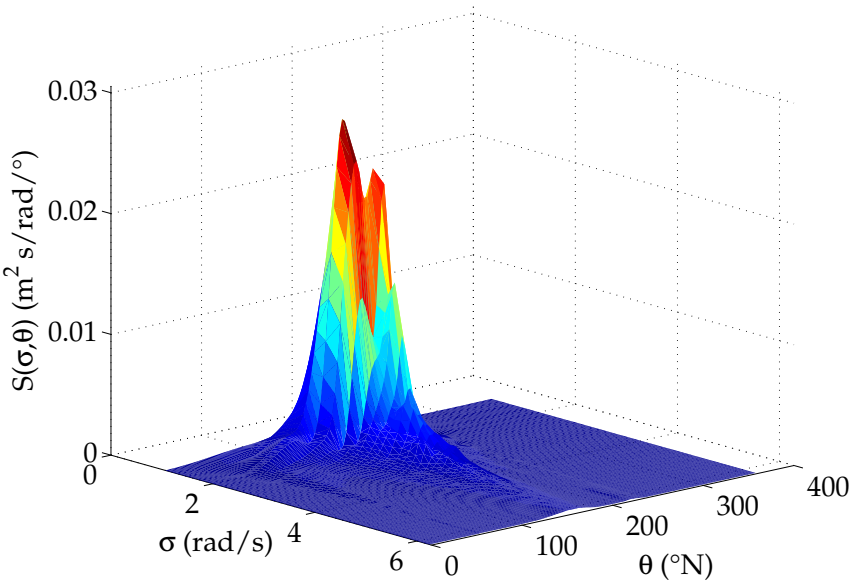

(a)

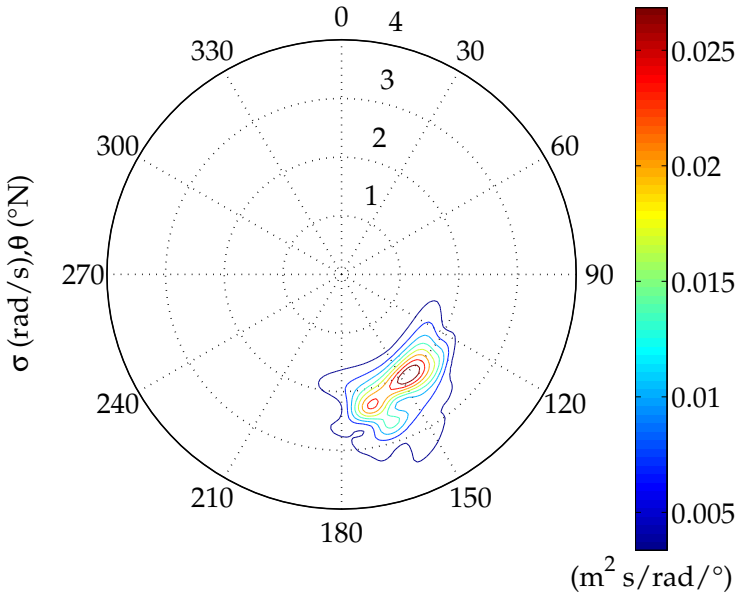

(b)

Figure 4.9: Spectra from R/V Urania experiment. (a) Directional spectrum $S(\sigma, \theta)$, cartesian $\sigma - \theta$ coordinates. (b) Directional spectrum $S(\sigma, \theta)$, polar $\sigma - \theta$ coordinates. Directions here are propagation directions, therefore 180° shifted with respect to directions in Table 4.4 and wind direction.

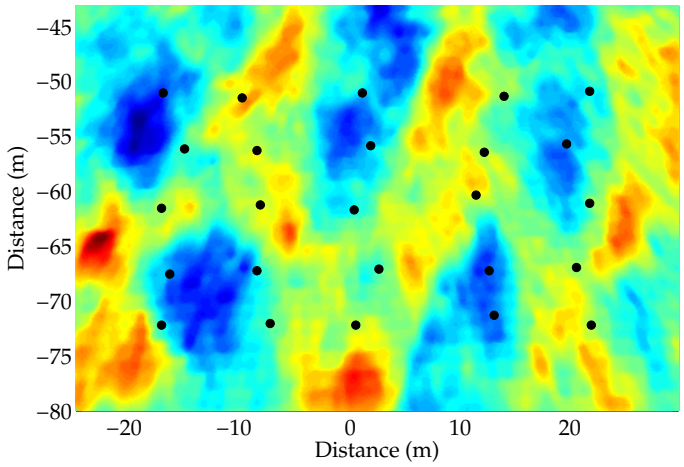

Figure 4.10: R/V "Urania" experiment (14.04.2013 08.12UTC): rectangular area for space-time extremes analysis. Black circles are points of analysis.

4.3.3 Stochastic models validation

Expected maxima from WASS measurements were estimated by choosing 25 points (Figure 4.10) over the framed sea portion and 26 square areas built around each point. Area size ranges from 0 to 156.25 m^2. As already stated for "Acqua Alta" experiment, the number of points and the size of the areas were constrained by the need of a sufficient number of space-time volumes from one side and by the small size of the framed area from the other side.

For each area size, the expected maximum $\overline{\hat{\eta}}_{ST}$ was calculated averaging the maxima $\hat{\eta}_{ST}$ observed inside each area during the whole sea state duration, i.e. nearly 12 minutes. Expected values of observations are provided with confidence interval $\pm\sigma_{\hat{\eta}_{ST}}$, which accounts also for the error of WASS system ($\sigma_{\hat{\eta}_{ST}}$ being the standard deviation of $\hat{\eta}_{ST}$). Then, space-time analysis was performed using Tayfun-Piterbarg's theorem and Fedele's method corrected to the second order to calculate the expected maxima $\overline{\eta}_{ST}$ over the areas of listed sizes and during approximately 12 minutes. Results are shown in Figure 4.11 for Tayfun-Piterbarg's theorem and in Figure 4.12 for Fedele's method.

The experimental evidence that the maximum over an area is larger than that at a single point was verified also in this experiment. Indeed, the normalized expected maximum sea surface elevation measured by WASS was

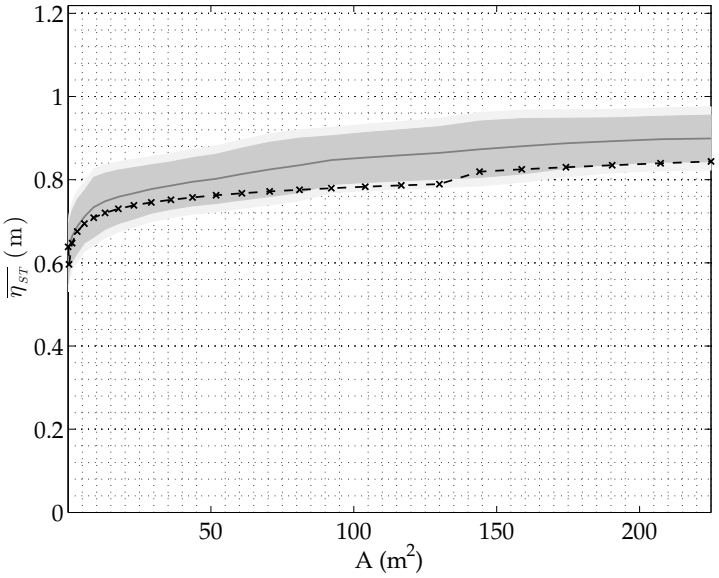

(a)

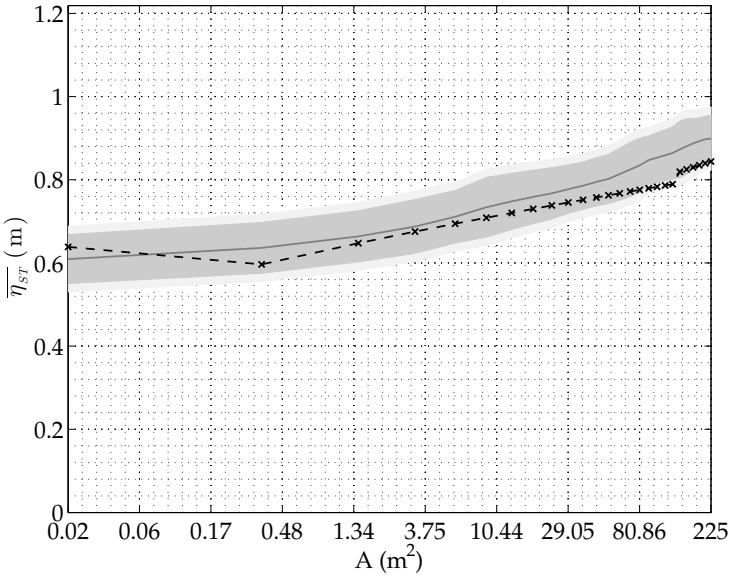

(b)

Figure 4.11: Tayfun-Piterbarg's theorem predictions (black asterisks) versus WASS observations (gray solid line) from R/V "Urania" (14.04.2013 08.12UTC): expected maximum over space-time as a function of area size. Observations are provided with confidence interval $\pm\sigma_{\hat{\eta}_{ST}}$ (grey): the narrower band (darker gray) is without WASS error (i.e. 0.02 m). (a) Linear plot. (b) Log plot, to emphasize small areas.

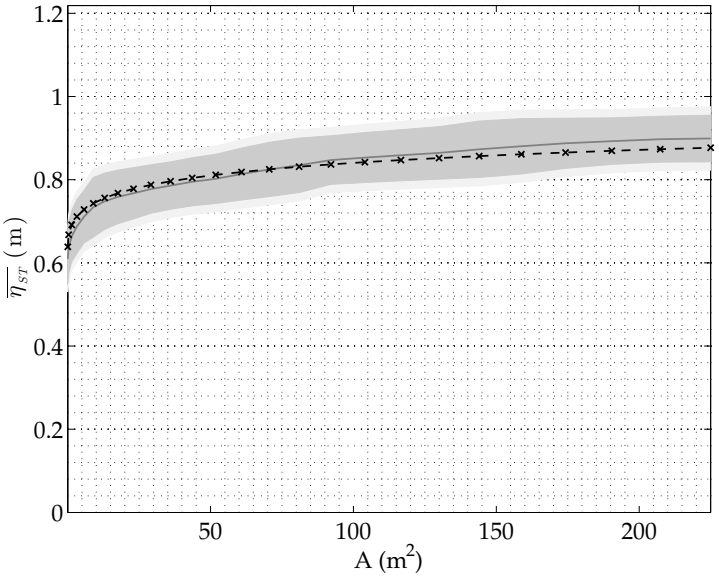

(a)

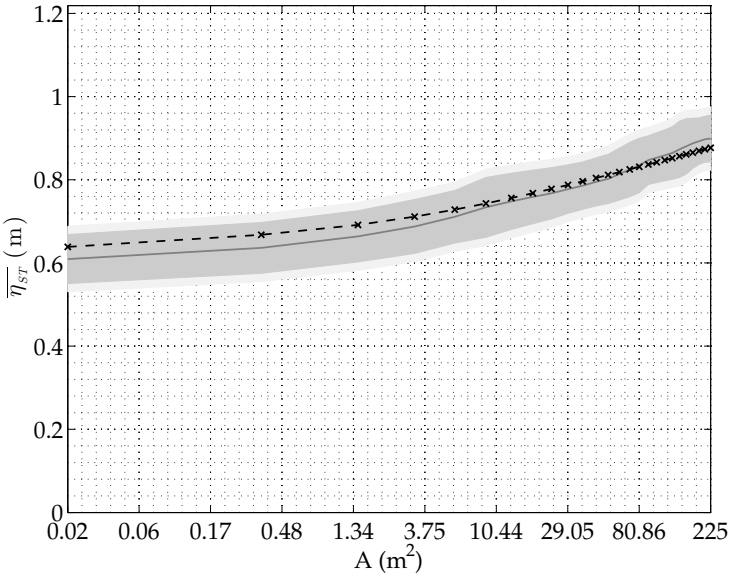

(b)

Figure 4.12: Fedele's method predictions (black asterisks) versus WASS observations (gray solid line) from R/V "Urania" (14.04.2013 08.12UTC): expected maximum over space-time as a function of area size. Observations are provided with confidence interval $\pm\sigma_{\hat{\eta}_{ST}}$ (grey): the narrower band (darker gray) is without WASS error (i.e. 0.02 m). (a) Linear plot. (b) Log plot, to emphasize small areas.

$\overline{\hat{\xi}}_{ST} = 1.42$ at the largest area (i.e. 156.25 m^2), while it was $\overline{\hat{\xi}}_T = 0.96$ at the smallest area. This leads to a ratio $\overline{\hat{\xi}}_{ST}/\overline{\hat{\xi}}_T = 1.48$. Both Tayfun-Piterbarg's theorem and Fedele's method correctly reproduced the growth of $\overline{\hat{\xi}}_{ST}$ with A. Nevertheless, Fedele's method was well performant over the whole range of tested areas, while Tayfun-Piterbarg's theorem worked fairly well at the smallest areas, where Forristall's approximation holds. At the largest areas, i.e. after $\overline{L}_x\overline{L}_y = 137.00$ m^2, original Tayfun-Piterbarg's theorem seemed to work better than Forristall's approximation, nevertheless prediction fell at the edge of confidence interval.

Performances of stochastic models prediction with respect to WASS observations are summarized by statistics in Table 4.5. As already observed in "Acqua Alta" experiment results, both the stochastic models exhibited high correlation coefficients (i.e. larger than 0.98) and low RMSE (i.e. 0.02 m). Coefficient of determination and best fit line slope were considerably higher for Fedele's method. Moreover, a larger Bias (negative, meaning underestimation) was observed for Tayfun-Piterbarg's theorem, though rather small compared to the absolute value of observations.

	CC	RMSE (m)	p	Bias (m)	R^2
WASS/Tayfun-Piterbarg	0.98	0.02	0.76	-0.04	0.67
WASS/Tayfun-Fedele	1.00	0.02	0.80	0.01	0.96

Table 4.5: Statistics of prediction from stochastic models with respect to WASS observations from R/V "Urania". CC: correlation coefficient, RMSE: root mean square error, p: best fit line slope, Bias, R^2: coefficient of determination.

4.4 Conclusions

In this Chapter, we compared stereo-photogrammetric observations (i.e. WASS) to stochastic models results to provide an observation-based validation to Tayfun-Piterbarg's theorem and Fedele's model for the first time to our best knowledge. Data were gathered during two different field campaigns: one from a fixed platform, one from a quasi-still ship. In the first experiment, at "Acqua Alta", we used a consolidated deployment of WASS. Hence, we got results with a satisfactory resolution and without warnings. Dealing with R/V "Urania" ship experiment, it is worth to say that this was the first WASS deployment on a moving platform. Besides this, the technique we had to use to calculate the spectrum led to a rough spectral resolution, which to some extent warned us on a potential underestimation of the expected maxima with respect to observations. During both the experiments, Tayfun-Piterbarg's theorem and Fedele's model exhibited the same trends. In fact, they correctly reproduced the growth of space-time extreme $\overline{\eta}_{ST}$ with area size. Nevertheless, Fedele's method was always within the observations confidence interval, remaining close to the observed expected value. On the contrary, Tayfun-Piterbarg's theorem was well performant at very small and very high (within the tested range) areas: that is, when Forristall's approximation and original theorem are in their best range of operation. In fact, at transition, predictions fell out of the confidence interval. However, the agreement of both models' predictions with "Acqua Alta" observations was better than with "Urania" observations, due to the already cited reasons.

To summarize, Fedele's method exhibited very good performance in predicting space-time extremes in the range of areas we tested. Tayfun-Piterbarg's theorem exhibited good performance at very small and large areas, but not on the whole tested range. As a final remark, we point out that the next step for validation is to perform it on larger areas.

Chapter 5

Space-time extremes from buoy data

5.1 Introduction

In the previous Chapter we validated the stochastic models for wave extremes prediction in space-time domain, i.e. Piterbarg's theorem and Fedele's method. Hence, hereinafter we will assume that they can be regarded as reliable theoretical tools to estimate the space-time extreme of a sea state, given significant wave height H_s, area A and duration D, i.e. $\overline{\eta}_{ST}/H_s = \overline{\xi}_{ST}(A, D)$.

In this Chapter, we will show how we modeled the dependence of $\overline{\xi}_{ST}$ upon the area size and inferred the probability distribution of $\overline{\xi}_{ST}(A)$ at a given geographical location, thanks to field data. We exploited the sea surface elevations and simultaneous horizontal displacements gathered during March 2012 from a directional buoy off the Catalan coast, in the north-west Mediterranean Sea (Figure 5.1). For each observed sea state, we obtained the directional spectra from buoy data in order to estimate the expected space-time maxima $\overline{\xi}_{ST}$ at the buoy location, according to Piterbarg's theorem and Fedele's method. To analyze the dependence of maxima upon area size (duration was fixed), we applied stochastic models to a variable area. The dependence could be expressed through a dimensionless quantity by introducing the parameter $S = A/\overline{L}^2$, being $\overline{L}$ the mean wavelength corresponding to mean wave period through linear dispersion relationship (2.2). Hence, $\overline{\xi}_{ST}(S)$ was analyzed as presented in the followings.

5.2 Data description

The input data herein used were recorded by a "Datawell MKIII" directional buoy deployed in front of Barcelona (Figure 5.1), at 41° 23.919' N,

2° 15.486' E, in 50 m deep waters. Data were provided by the XIOM network of the Catalan Government. The wave climate was widely described by Sánchez-Arcilla et al. (2008). In this nearshore portion of the Catalan Sea (north-west Mediterranean Sea) the predominant waves come from south and south-east, thanks to stronger winds and longer fetches.

Figure 5.1: Location of the buoy providing input data, off the Catalan coast at 50 m water depth.

Buoy measuring system stores the sea surface elevations $\eta(t)$ at a sampling rate of 1.28 Hz ($\Delta t = 0.7812$ s), simultaneously with the horizontal displacement components, along the $x(t)$ (i.e. east) and $y(t)$ (i.e. north) directions. Typically, the gathered raw data, i.e. $\eta(t)$, $x(t)$, $y(t)$, are routinely processed by the software of the buoy to provide synthetic spectral parameters, e.g. spectral significant wave height H_{m0}, mean wave period T_{02}, peak wave period T_p, peak wave direction θ_p, directional spreading Ds_p (red points in Figure 5.2, Table 5.1) and others (Datawell, 2009). In fact, directional spectrum is calculated but not usually provided as a result of the analysis. However, to apply stochastic models of Piterbarg and Fedele we need directional spectrum, hence we processed the time series of $\eta(t)$, $x(t)$ and $y(t)$ rather than using synthetic spectral parameters calculated by the buoy. The analysis was performed within the period of availability of the raw data, i.e. from 07.03.2012 00.23.00 to 31.03.2012 23.46.00. The time

series recorded by the buoy were 30 minutes long and continuous over approximately 25 days, hence a set of 1195 sea states was available. During the period of analysis, sea states with H_{m0} up to 2.62 m and T_{02} up to 6.78 s occurred (Table 5.1). The average mean wave direction was 122°, hence predominant waves came from South-East, as already stated.

	mean	std	min	max
H_{m0} (m)	0.66	0.50	0.12	2.62
T_p (s)	6.03	2.26	1.75	40.00
T_{02} (s)	4.22	1.02	2.25	6.78
θ_p (°)	122	41	43	341
Ds_p (°)	44	12	12	77

Table 5.1: Mean, standard deviation, minimum and maximum of the spectral parameters calculated by the software of the buoy during the period under analysis. Maximum T_p is certainly an outlier due to a measurement error.

Some statistical parameters of each time series were computed: mean, standard deviation, skewness and kurtosis (Table 5.2).

	mean	std	min	max
mean(η) (m)	$2{\cdot}10^{-6}$	$2{\cdot}10^{-4}$	$-9{\cdot}10^{-4}$	$8{\cdot}10^{-4}$
std(η) (m)	0.18	0.11	0.03	0.53
skewness(η)	0.04	0.05	-0.18	0.23
kurtosis(η)	3.08	0.18	2.65	5.22

Table 5.2: Mean, standard deviation, minimum and maximum of the basic statistical parameters of sea surface elevation η.

As any other measuring instrumentation, buoys have some bugs that could affect measurements. Indeed, it is well known that buoys tend to underestimate the very high waves because they go through the crests or, in short crested seas, they go around them (Allender et al., 1989). Hence, buoys tend to linearize waves. For this reason, Tucker and Pitt (2001) showed that buoys are not reliable instruments to study the nonlinear behavior of waves [1]. Unfortunately, this effect could not be avoided, but since we didn't

[1]We initially suspected that the data could suffer of this effect, because we obtained suspiciously low values of the wave steepness (Appendix A.2). Besides this, we observed that the sampling frequency value, i.e. 1.28 Hz, is a very low value, probably too low to sample the time evolving sea surface elevation with the needed resolution. A consequence

look at individual waves but rather at directional spectra, it was regarded as a minor importance effect. Nevertheless, other factors can still affect buoy measurements (Appendix A.1). To overcome these issues, 400 of the original 1195 sea states, i.e. 33%, were discarded after a quality control on the time series (Appendix A.1). The remaining 795 time series were analyzed and results of the analysis are reported in the followings.

5.3 Directional wave spectrum calculation

We obtained directional spectra of the 795 sea states following a procedure analogous to that adopted by the software of the buoy (Datawell, 2009), i.e. the truncated Fourier series decomposition. The method we implemented is called the Weighted Fourier Series Decomposition (WFS) (Benoit et al., 1997), see Chapter 2 (Part II). It is an easy-implementation and computational efficient method, though it is not one of the most accurate. Other stochastic methods, e.g. Extended Maximum Entropy Principle (EMEP) (Benoit et al., 1997) or Bayesian Direct Method (BDM) (Benoit et al., 1997), were also applied but without providing acceptable results, so we chose WFS. Besides, a more consistent comparison with the buoy software result could be done. In fact, to check the reliability of the directional spectra we obtained, we compared some spectral parameters with the outputs of the buoy processing software. In particular, we checked:

- spectral significant wave height $H_{m0} = 4\sqrt{m_{000}}$ (Figure 5.2-a);
- peak wave period $T_p = 2\pi/\sigma_p$ (Figure 5.2-b);
- peak wave direction θ_p (Figure 5.2-c);
- mean wave period $T_{02} = 2\pi\sqrt{\frac{m_{000}}{m_{002}}}$ (Figure 5.2-d);
- directional spreading $Ds_p = \frac{\pi}{180}\sqrt{2 - 2\sqrt{a_1(f_p)^2 + b_1(f_p)^2}}$ at the peak (Figure 5.2-e).

being m_{ijl} the ijl-th moment of the directional spectrum, according to (2.6). Table 5.3 summarizes the comparisons in terms of correlation coefficients (CC), root mean square errors (RMSE) and biases.

of this low value is that crest and troughs are sometimes beheaded and wave steepness is reduced.

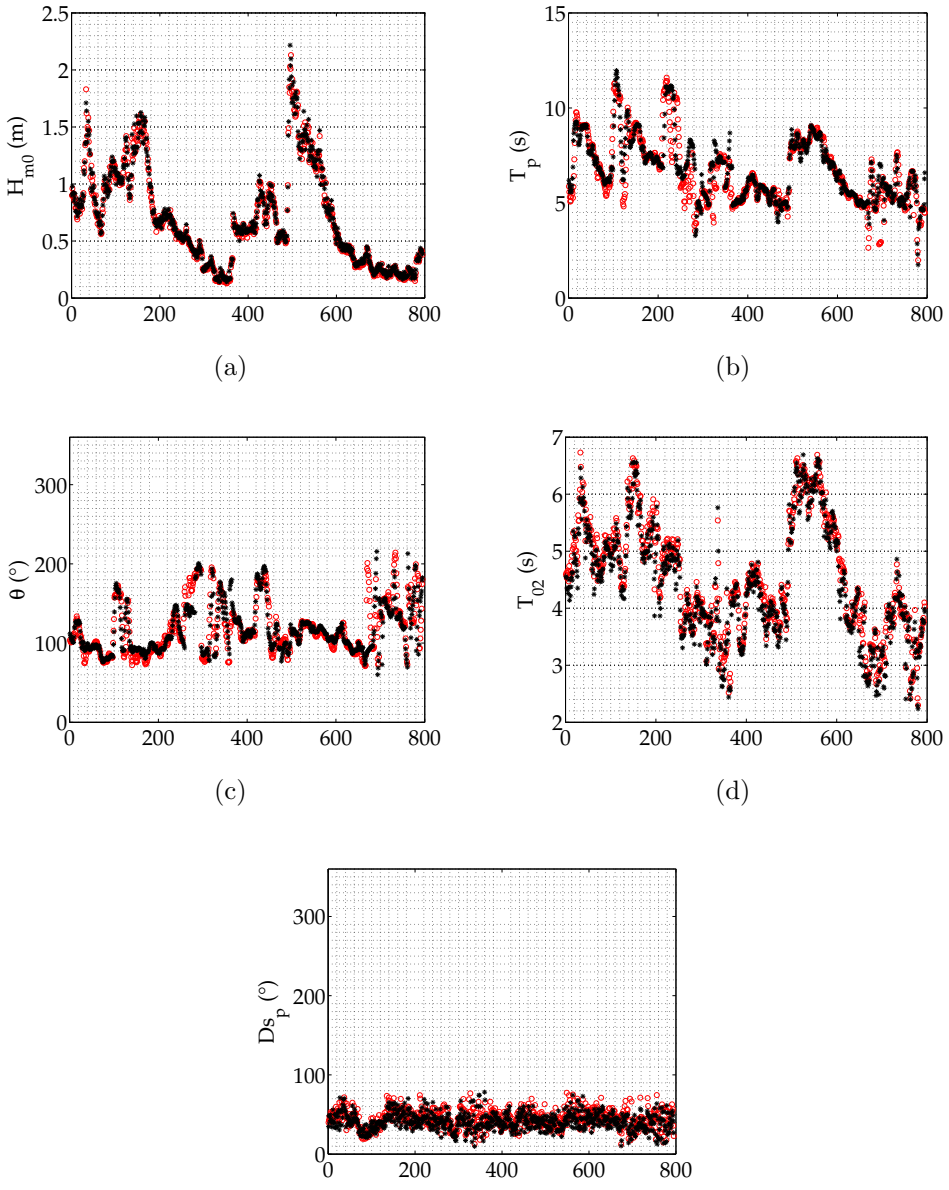

Figure 5.2: Wave parameters calculated from the directional spectrum $S(\sigma, \theta)$ obtained by performing WFS method on the 795 sea states that passed quality control (black). Comparison with wave parameters calculated from the buoy software (red). (a) Spectral significant wave height H_{m0}. (b) Peak wave period T_p. (c) Peak wave direction θ_p. (d) Mean wave period T_{02}. (e) Directional spreading at the peak Ds_p. x-labels are measured sea states, after quality control.

	CC	RMSE	Bias
H_{m0}	1.00	0.04 m	-0.01 m
T_p	0.87	0.88 s	-0.11 s
T_{02}	0.99	0.16 s	0.12 s
θ_p	0.81	19.2°	-0.89°
Ds_p	0.64	9.64°	3.11°

Table 5.3: Comparison between spectral parameters calculated from the directional spectrum obtained performing the WFS method with those provided by the buoy processing software. CC: correlation coefficient, RMSE: root mean square error.

Looking at Table 5.3, we can state that the directional spectra we calculated throughly resembled the spectra calculated by the buoy software. Indeed, except for the directional spreading Ds_p, the correlation coefficients CC were always above 0.8, reaching values close or equal to 1 for H_{m0} and T_{02}, which also showed the RMSE closest to 0. The calculation of θ_p and Ds_p could be affected by the choice of a different method for directional spreading function estimate.

5.4 Space-time extremes analysis

Piterbarg's theorem and Fedele's method analyses were performed on space-time domains of variable space size, in order to do a sensitivity analysis on the dimension of the area A. Duration of the sea state D=1800 s was fixed. We chose 50 squared areas with sizes $X = Y$ ranging from 1 to 50 m, hence areas $A = XY$ range from 1 to 2500 m^2. Increasing the area, the maximum expected elevation $\overline{\xi}_{ST} = \overline{\eta}_{ST}/H_s$ in the sea state grew, as illustrated in Figure 5.3 where a sea state with H_s =1.71 m and T_p =9.09 s has been chosen as an example. As already shown in Chapter 4, Fedele's method predictions were higher than Piterbarg's theorem predictions because the contribution of the domain boundaries has been accounted for in Fedele's method.

To generalize the analysis, we normalized the area A leading to the dimensioneless parameter S. Among various tentative normalizations we choose to define S as

$$S = \frac{A}{\overline{L}^2} \tag{5.1}$$

where $\overline{L}$ is the wavelength corresponding to the mean wave period T_{02} according to the linear dispersion relationship (2.2). We preferred this particular normalization with respect to others, e.g. dividing A by $\overline{L}_x\overline{L}_y$, because the

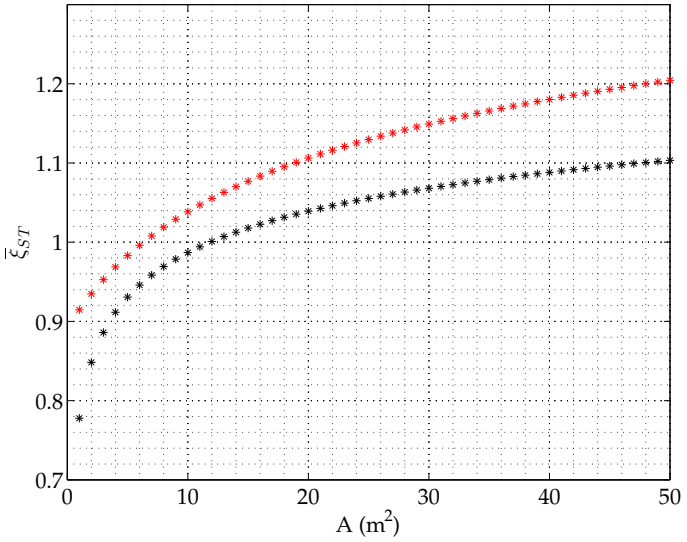

Figure 5.3: Space-time extremes dependence upon area size A for a given sea state (H_s =1.71 m, T_p =9.09 s), according to Piterbarg's theorem (black) and Fedele's method (red).

availability of $\overline{L}$ is greater than that of $\overline{L}_x$ and $\overline{L}_y$, since $\overline{L}$ can be obtained from the mean wave period T_{02} without the need of directional spectrum or other spatial information. S expresses on average the number of waves over the space domain considered, e.g. $S = 1$ means that there is on average one 20 m mean wavelength wave over an area of 20^2 m^2; $S = 2$ means that there are on average two 10 m mean wavelength over the same area.

In Figure 5.4-a, the maximum sea surface over an area according to Piterbarg's theorem are plotted as a function of the parameter S, i.e. $\overline{\xi}_{ST}(S)$. We observed that as S increased, $\overline{\xi}_{ST}$ increased too. We also noticed that approximately at $S = 1$ the data sets are highly discontinuous due to the different methods used to calculate $\overline{\xi}_{ST}$ at $S >1$ and $S <1$, i.e. Piterbarg's theorem and Piterbarg's theorem with Forristall's approximation, respectively. In Figure 5.4-b the maximum sea surface over an area according to Fedele's method are plotted as a function of the parameter S, i.e. $\overline{\xi}_{ST}(S)$. Similarly to Piterbarg's theorem results, $\overline{\xi}_{ST}$ increased with increasing S. This means that as the number of waves in space domain grew, higher sea surface heights were more likely to occur. This is reasonable in a short-crested sea. Due to the discontinuities encountered in the Piterbarg's theorem results (Figure 5.4-a), we chose to continue the analysis only taking into account Fedele's method results, which are continuous over S. We also choose to discard the left tails of the data sets shown in Figure 5.4-b by neglecting

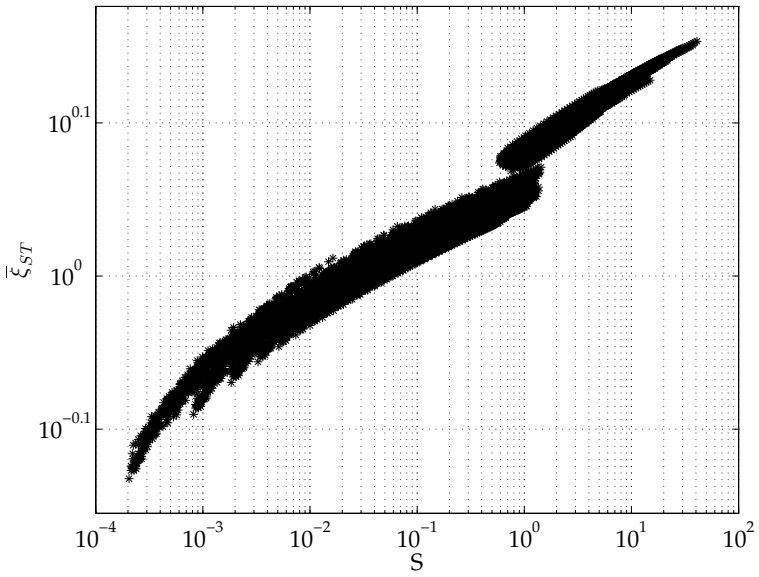

(a)

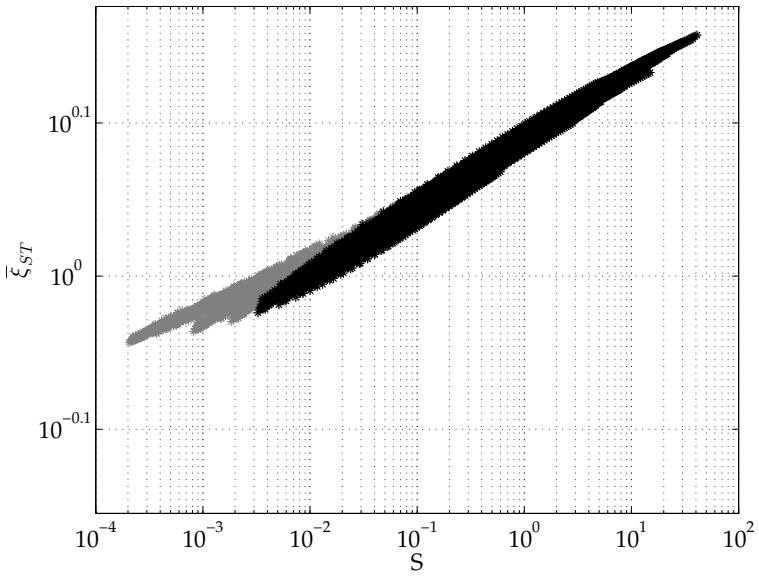

(b)

Figure 5.4: Space-time extremes dependence upon parameter S. (a) According to Piterbarg's theorem. (b) According to Fedele's method (data for $A \leq 3^2$ m^2 (grey) were discarded in the following analysis).

results for $A \leq 3^2$ m^2 (grey points in Figure 5.4). The resulting data set is the black one in Figure 5.4.

5.4.1 Modeling of $\overline{\xi}_{ST}(S)$

Looking at Figure 5.4-a, it can be observed that, despite a certain spreading, on average space-time expected maxima $\overline{\xi}_{ST}(S)$ behave linearly in a logarithmic plane. Thus, we can model expected maxima dependence upon S with a straight line:

$$\ln(\overline{\xi}_{ST}) = a \ln(S) + b \tag{5.2}$$

Consequently, in the original plane $\overline{\xi}_{ST}(S)$ can be modeled by an exponential function multiplied by a power law of S:

$$\overline{\xi}_{ST} = S^a \exp(b) \tag{5.3}$$

Coefficients a and b in (5.2) and (5.3) were determined through least square fitting of the data set in the logarithmic plane and are collected in Table 5.4. The goodness of the fit was checked using coefficient of determination R^2 and root mean square errors RMSE (Table 5.4). The first represents the correlation between the data and the fitted model, the second accounts for the errors in the regression. They both indicated a very good agreement between the data and the modeling functions. Besides, increasing the degree of the least square fitting seemed unnecessary. The linear regression modeling $\overline{\xi}_{ST}(S)$ is plotted in Figure 5.5.

a	b	R^2	RMSE
0.0447	0.2058	0.983	0.009

Table 5.4: Regression of space-time extremes as a function of parameter S ($A > 3^2$ m^2), according to Fedele's method. Coefficients of least square fitting of the data set, coefficients of determination R^2 and RMSE.

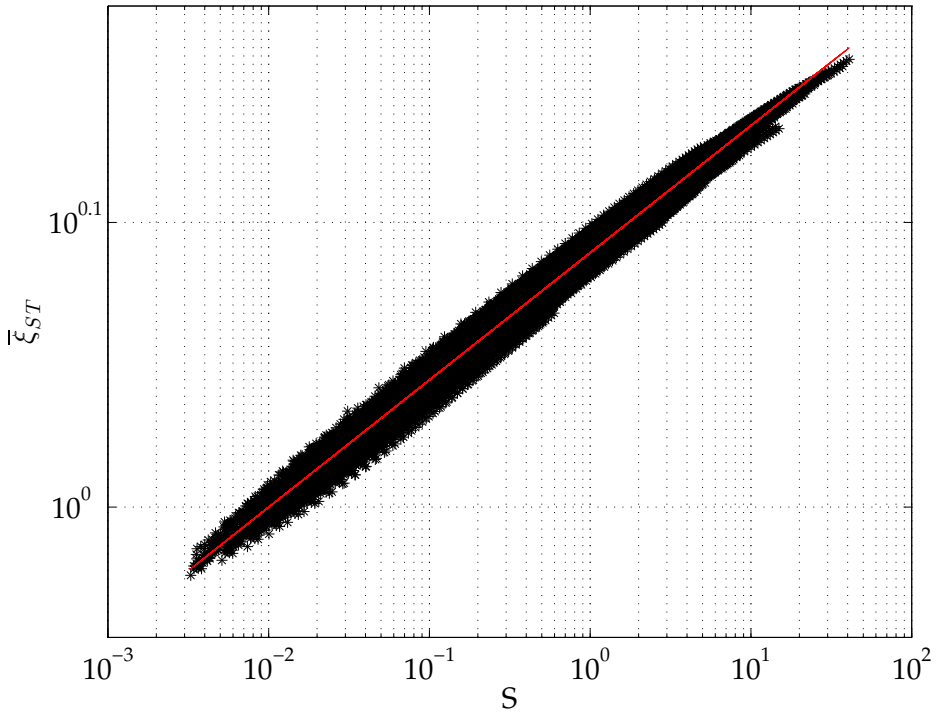

Figure 5.5: Linear regression of space-time extremes $\overline{\xi}_{ST}(S)$ (red line), according to Fedele's method ($A > 3^2$ m^2).

The function (5.3) together with coefficients in Table 5.4 can predict the expected maximum sea surface elevation over an area A at the buoy location, given H_s and T_{02}. Nevertheless, a certain variability still remains. It is due to the fact that (5.3) fit on average a data set which gather together maxima from different sea states. In fact, though normalized on H_s, different spectral features cause a spreading of the data about the average. Following a safety criterion, we individuated the upper bounds of the data set, i.e. the extremal $\overline{\xi}_{ST}(S)$ (black crosses in Figure 5.6). Looking at Figure 5.6, they can be modeled either by a linear or a quadratic function in the logarithmic plane:

$$\begin{aligned} \ln(\overline{\xi}_{ST}) &= a\ln(S) + b && \textit{linear} \\ \ln(\overline{\xi}_{ST}) &= a\ln(S)^2 + b\ln(A) + c && \textit{quadratic} \end{aligned} \tag{5.4}$$

In the original plane, the functions in (5.4) become:

$$\begin{aligned} \overline{\xi}_{ST} &= S^a \exp(b) && \textit{linear} \\ \overline{\xi}_{ST} &= (S^a)^{\ln S} S^b \exp(c) = S^{(a\ln S + b)} \exp(c) && \textit{quadratic} \end{aligned} \tag{5.5}$$

Coefficients a, b and c in (5.4) and (5.5) were obtained through least square fitting of the upper bound of the data set. They are collected in Table 5.5, together with coefficients of determinations R^2 and root mean square errors RMSE.

	a	b	c	R^2	RMSE
linear	0.0428	0.2201	/	0.996	0.007
quadratic	-0.0010	0.0407	0.2268	1.000	0.002

Table 5.5: Regressions of the upper bound of space-time extremes as a function of parameter S ($A > 3^2$ m^2), according to Fedele's method. Coefficients of least square fitting of the upper bounds of the data set, coefficients of determination R^2 and RMSE.

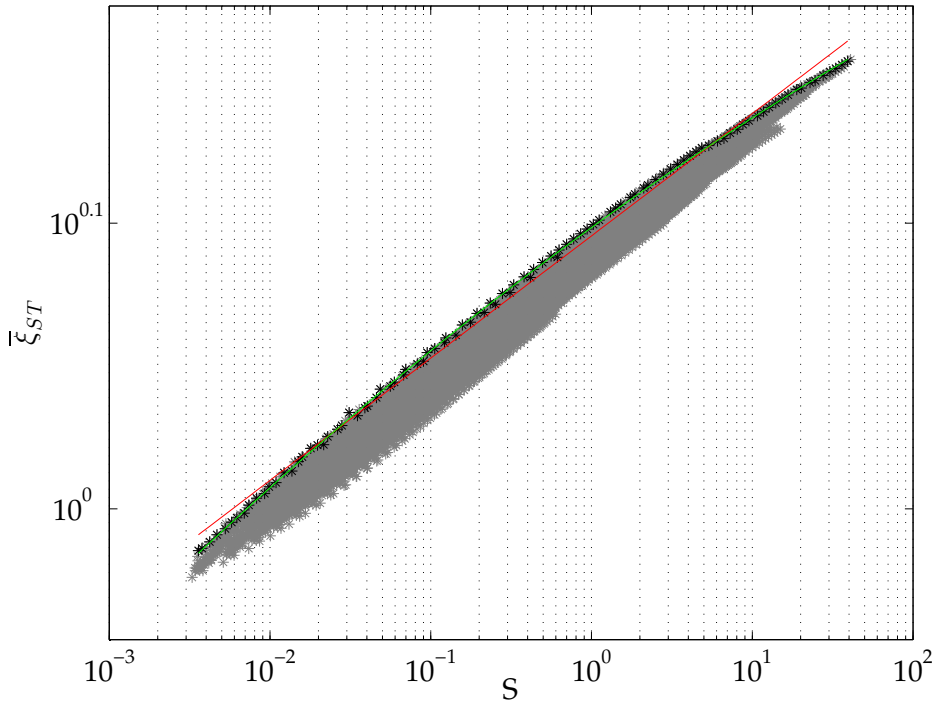

Figure 5.6: Linear and quadratic regressions of the upper bound of the space-time extremes $\overline{\xi}_{ST}(S)$ data set (red line), according to Fedele's method. $A > 3^2$ m^2. The upper bound is indicated by black asterisks.

5.4.2 Probability distributions of $\overline{\xi}_{ST}$

In this Section, $\overline{\xi}_{ST}$ is considered itself a random variable. In fact, we considered the set of the sea surface elevation maxima $\overline{\xi}_{ST}$, each one taken from a different sea state which is stationary in time and homogeneous in space. Hence, we can reasonably assume that $\overline{\xi}_{ST}$ are statistically independent. Moreover, they are identically distributed since they are expected values of the same parent distribution (3.19).

The data set we are using is too short over time (i.e. 25 days) to consider what we did in the following a long-term statistics. Nevertheless, over 25 days conditions are certainly non-stationary and the assumption of stationary process, which is the basis for short-term statistics, does not hold. Hence, the statistical analysis we will present are closer to long rather than to short-term statistics. Therefore, the methodology we will apply can be extended to wider data sets, i.e. longer over time, to actually perform a long-term statistics of $\overline{\xi}_{ST}$ at a given location.

We must start by saying that there is not a theoretical statistical model for the expected sea surface elevation maxima $\overline{\xi}_{ST}$ at present. Thus, we are aimed at find good representations of the probability distributions of $\overline{\xi}_{ST}$. In order to provide a statistical characterization of $\overline{\xi}_{ST}$ at a given location, we obtained experimental marginal pdf and EDF (Exceedence Distribution Function) of $\overline{\xi}_{ST}$ and we compared them to the theoretical probability distribution functions usually employed in long term statistics. Just to recall them, they are (Holthuijsen, 2007)

- Weibull distribution, employed to statistically represents the significant wave heights in the "initial-distribution" approach;
- Gumbel distribution, which represents the distribution of annual maximum significant wave heights, in the "annual-maximum" approach;
- Generalized Pareto distribution, that is used to model the maximum significant wave heights taken from storms, in the "peak-over-threshold" approach.

Weibull, Gumbel and Generalized Pareto EDFs are, respectively:

$$P_W(\overline{\xi}_{ST}) = \exp\left[-\left(\frac{\overline{\xi}_{ST}}{B}\right)^A\right] \tag{5.6}$$

$$P_G(\overline{\xi}_{ST}) = \exp\left(-\exp\left(-z\right)\right) \tag{5.7}$$

$$P_P(\overline{\xi}_{ST}) = (1 + Fy)^{1/F} \tag{5.8}$$

Here, A and B are the parameters of the Weibull distribution: A is the shape parameter and B is the scale parameter. $z = (\overline{\xi}_{ST} - D)/C$, where C and D are the scale and location parameters of Gumbel distribution, respectively. $y = (\overline{\xi}_{ST} - G)/E$, where E, F and G are the scale, shape and location parameters of Generalized Pareto distribution, respectively. Given a data set, parameters A to F can be inferred resorting to different techniques, e.g. the maximum likelihood method we used herein. Weibull, Gumbel and Generalized Pareto pdfs are, respectively:

$$p_W(\overline{\xi}_{ST}) = AB^{-A}\overline{\xi}_{ST}^{(A-1)} \exp\left[-\left(\frac{\overline{\xi}_{ST}}{B}\right)^A\right] \tag{5.9}$$

$$p_G(\overline{\xi}_{ST}) = \frac{1}{C}\exp\left(-(z + \exp(-z))\right) \tag{5.10}$$

$$p_P(\overline{\xi}_{ST}) = \frac{1}{E}(1 + Fy)^{-(1/F+1)} \tag{5.11}$$

If we consider $\overline{\xi}_{ST}$ representative of the sea state, just as significant wave height is, the listed theoretical distributions can be borrowed to check which one is the best to statistically model the experimental distribution of $\overline{\xi}_{ST}$ at a given location. To this end, we resorted to Q-Q (Quantile-Quantile) plots and probability plot correlation coefficients, i.e. the correlation coefficient between the paired sample quantiles. Perfect agreement between experimental and theoretical distributions is represented by a straight line (red in Figures). Figure 5.7, Figure 5.8 and Figure 5.9 show the Weibull, Gumbel and Generalized Pareto Q-Q plots of the Catalan buoy data set, respectively. Weibull distribution modeled correctly the experimental data set from $\overline{\xi}_{ST} \sim 1$ and above, while some differences were observed at the smallest $\overline{\xi}_{ST}$ values. Gumbel distribution behaves analogously but fit well the experimental data for values $\overline{\xi}_{ST} > 1$. On the contrary, Generalized Pareto distribution was not able to correctly describe the tails of the experimental distribution. The probability plot correlation coefficients are collected in Table 5.6. Even if they are very close to 1 for all the theoretical distribution tested, it is evident that the best one is Weibull distribution. We discarded Generalized Pareto and continued the analysis with Weibull and Gumbel distributions.

Weibull	Gumbel	Generalize Pareto
0.998	0.993	0.981

Table 5.6: Probability plot correlation coefficients for the theoretical distribution functions used to model the experimental $\overline{\xi}_{ST}$.

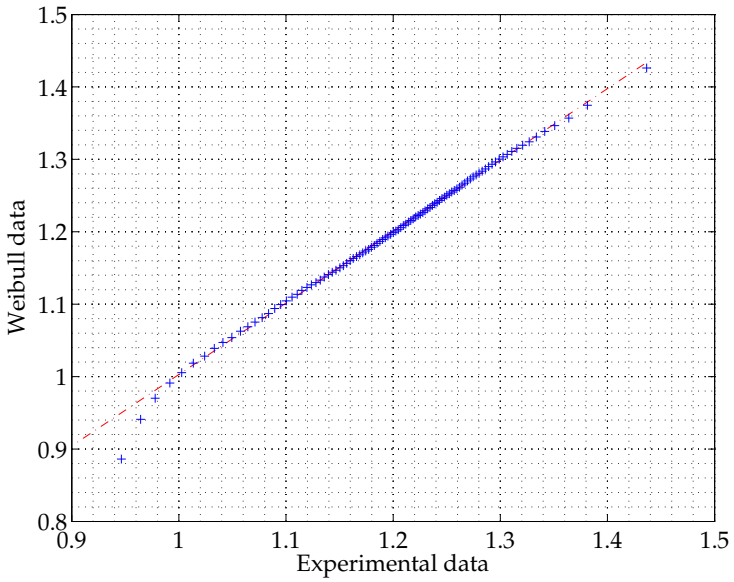

Figure 5.7: Q-Q plot of experimental and Weibull distributions of $\overline{\xi}_{ST}$. Reference line (red) represents perfect agreement with Weibull distribution.

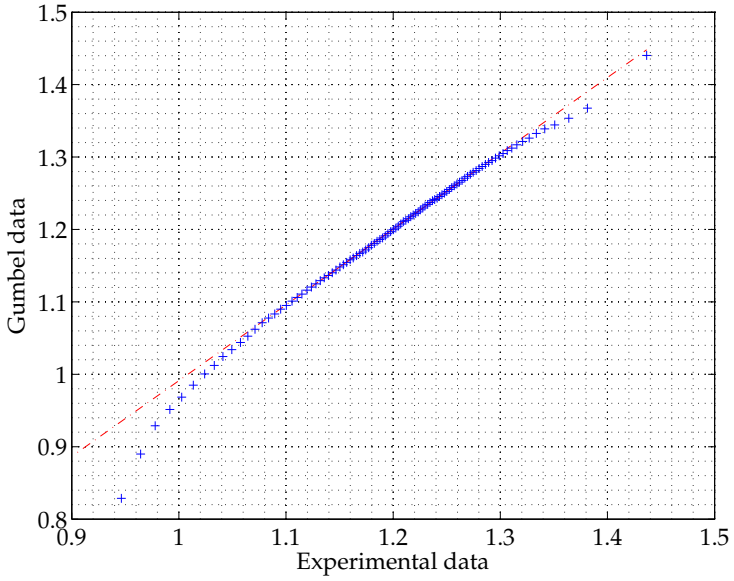

Figure 5.8: Q-Q plot of experimental and Gumbel distributions of $\overline{\xi}_{ST}$. Reference line (red) represents perfect agreement with Gumbel distribution.

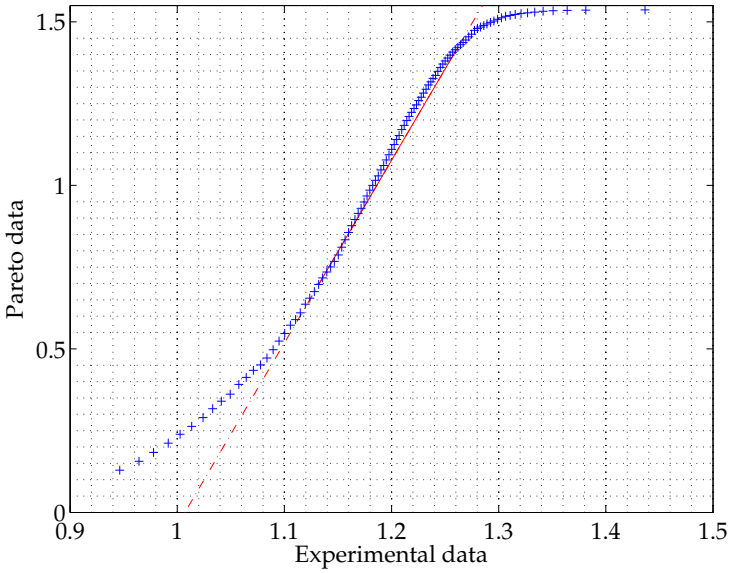

Figure 5.9: Q-Q plot of experimental and Generalized Pareto distributions of $\overline{\xi}_{ST}$. Reference line (red) represents perfect agreement with Pareto distribution.

In Figure 5.10 the experimental marginal EDF of $\overline{\xi}_{ST}$ is compared with Weibull and Gumbel EDFs, i.e. (5.6) and (5.7) respectively. Similarly, in Figure 5.11 the experimental marginal pdf of $\overline{\xi}_{ST}$ was compared to Weibull and Gumbel pdfs. The agreements are good, especially for the right hand side part of the data set, i.e. $\overline{\xi}_{ST} > 1$.

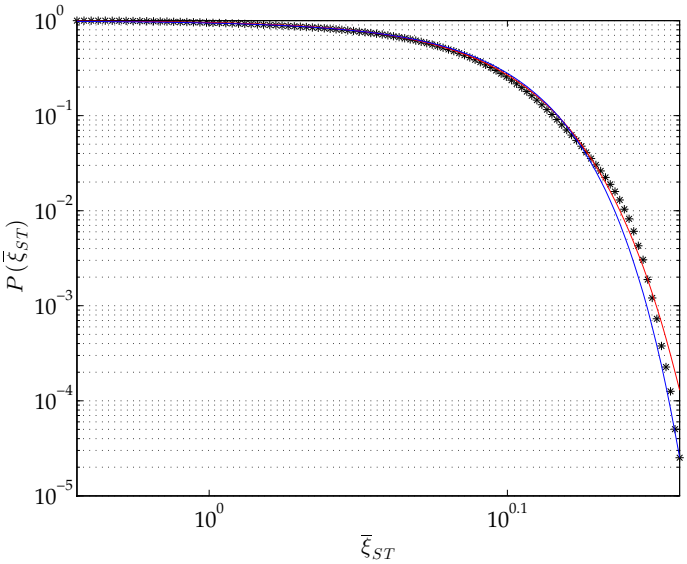

Figure 5.10: Experimental marginal EDF of $\overline{\xi}_{ST}$ (black asterisks), Weibull EDF ($A = 1.24$ and $B = 14.42$, red solid line) and Gumbel EDF ($C = 1.24$ and $D = 0.08$, blue solid line).

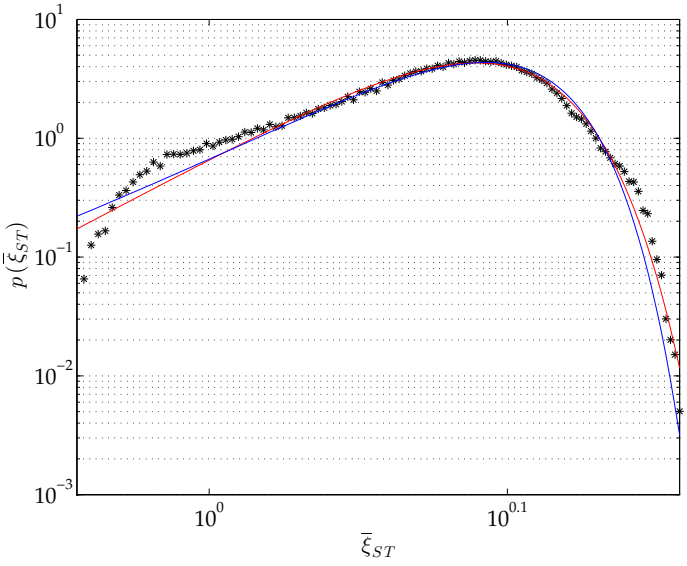

Figure 5.11: Experimental marginal pdf of $\overline{\xi}_{ST}$ (black asterisks), Weibull pdf ($A = 1.24$ and $B = 14.42$, red solid line) and Gumbel pdf ($C = 1.24$ and $D = 0.08$, blue solid line).

From the results shown, we could argue that the expected sea surface elevations $\overline{\xi}_{ST}$ provided by Fedele's method are well represented by Weibull and Gumbel distributions. The definition of a theoretical distribution function

modeling the experimental data set turns out to be useful for extrapolation in order to obtain exceedence probabilities of unobserved values.

The experimental joint probability distribution function (pdf) of $\overline{\xi}_{ST}$ and S was also obtained (Figure 5.12). From the joint pdf we could infer the most probable $(\overline{\xi}_{ST}, S)$ pair, which in the Catalan buoy case corresponded to (1.09,0.01). Moreover, from Figure 5.12 we can state that the most of the maxima occurred for $S < 1$ and corresponding values are $\overline{\xi}_{ST} < 1.23$.

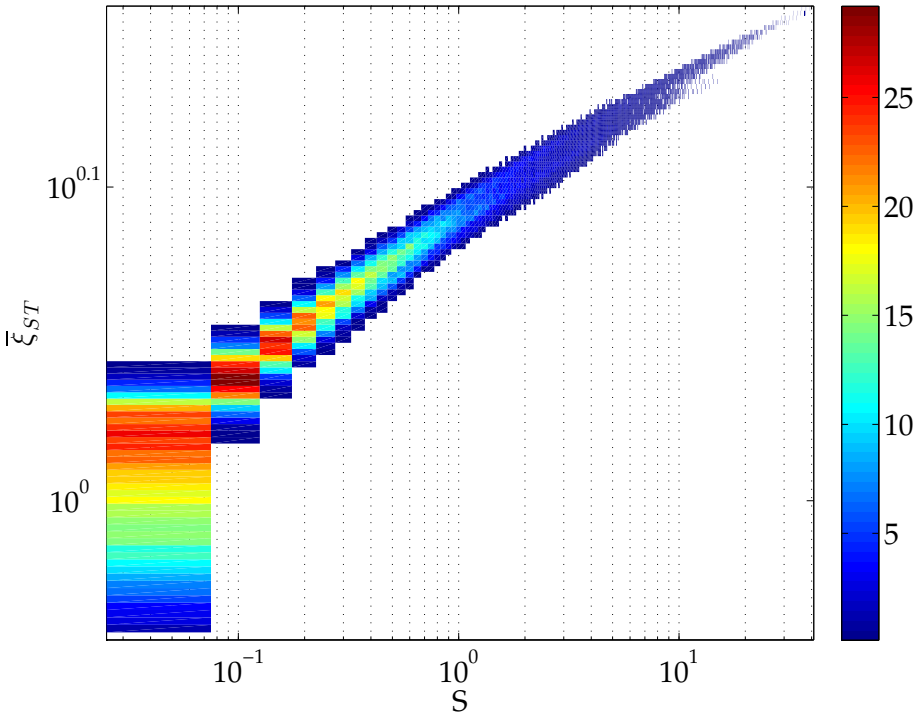

Figure 5.12: Experimental joint pdf of $\overline{\xi}_{ST}$ and S.

5.5 Conclusions

In this Chapter, we used data gathered from a directional buoy to model the behavior of space-time extremes $\overline{\xi}_{ST}$ with space domain size, which was represented by means of the dimensionless parameter $S = A/\overline{L}^2$ ($\overline{L}$ being the mean wavelength associated to mean wave period according to linear dispersion relationship). We found that $\overline{\xi}_{ST}(S)$ can be modeled with enough accuracy by a function composed of a power law multiplied by an exponential law. The coefficients we got through linear regression are location dependent,

nevertheless the functional behavior is general and the same analysis can be repeated elsewhere leading to expression that allow to model and also to predict the space-time extremes $\overline{\xi}_{ST}$ at given location, if significant wave height H_s and mean wave period $\overline{T}$ are provided. To meet a safety criterion and reduce the spreading of the data about the function obtained, the upper bound of the $\overline{\xi}_{ST}(S)$ data set was also modeled.

Besides this, we inferred some probabilistic features of $\overline{\xi}_{ST}$, considered itself a random variable. We analyzed the experimental marginal pdf and EDF of $\overline{\xi}_{ST}$ and the joint pdf of $\overline{\xi}_{ST}$ and S. We found that $\overline{\xi}_{ST}$ at a given location is well represented by a Weibull or Gumbel law. This could be useful to perform extrapolations oriented to long-term prediction of the space-time extremes.

Chapter 6

Analytical results

6.1 Introduction

In this Chapter, we explored the possibility of performing a wave extreme analysis in the space-time domain starting from analytical spectral shapes. This could meet the scarce availability of directional wave spectra that limit the possibility of estimating maximum sea surface elevation over an area. For the proposed aim, we considered two commonly used and easy to be manipulated directional wave spectra, i.e. Pierson-Moskowitz (2.25) or JONSWAP (2.29) frequency spectra combined with a $\cos^2$ directional spreading function (2.33). Under some specific assumptions the analytical integration of the directional spectra $S(\sigma, \theta)$ is possible. Hence, we should be able to get closed forms of spectral moments (2.6) and spectral parameters (2.7), and thus perform space-time extremes analysis according to Piterbarg's theorem and Fedele's method. Besides, results obtained were used to discuss the dependence of the sea surface elevation maxima, i.e. $\overline{\xi}_{ST}$ and $\overline{\xi}_{T}$, and of their ratio upon wind speed ($U = U_{10}$), fetch length (F) and size of the area of analysis ($A = XY$).

The assumptions we added to the general hypotheses stated in Chapter 2 are:

- deep waters wave propagation, i.e. $d/L > 0.5$ (being d water depth and L wavelength), for every spectral component;
- short-crested wind sea state, i.e. shortcrestedness $\gamma_s >> 0$ or, equivalently, wave crests only slightly longer than wavelengths ($\overline{L}_y \gtrsim \overline{L}_x$);
- fully developed wind sea state represented by Pierson-Moskowitz spectral shape (2.25), or partially developed and fetch-limited wind sea

states represented by JONSWAP spectrum (2.29);

- sea state duration equals to 100 mean wave periods; indeed, 100 waves has been indicated as the minimum of the number of waves in a real sea-state, according to the definitions of Boccotti (2000) and Holthuijsen (2007).

We just recall that for sake of simplicity we chose a frame of reference such that wave propagation is oriented along x axis, hence $\theta_p = 0$, $\overline{L}_y$ is wave crest and $\overline{L}_x$ is wavelength. This can be achieved after a rotation of the directional spectrum. This does not affect at all the results of space-time analysis. However, a procedure to obtain the spectral parameters in an arbitrary frame of reference, e.g. North oriented, was obtained and it is reported in the followings.

6.2 Spectral parameters computation

Under the listed assumptions, we obtained analytic expressions for the spectral parameters of $S(\sigma, \theta)$ required to perform extreme analysis in the space-time domain, i.e. average wave period $\overline{T}$, mean wave and crest length $\overline{L}_x$ and $\overline{L}_y$, irregularity parameters α_{xy}, α_{xt}, α_{yt}, according to (2.7). They all depend on the moments of the directional wave spectrum m_{ijl}, i.e. (2.6). Assuming deep waters propagation, frequency to wavenumber dependence can be made explicit from linear dispersion relationship

$$\sigma^2 = gk \tag{6.1}$$

leading to the possibility of explicitly express wavenumber components in terms of frequency σ, as follows:

$$\begin{aligned} k_x &= \frac{\sigma^2}{g}\cos(\theta) \\ k_y &= \frac{\sigma^2}{g}\sin(\theta) \end{aligned} \tag{6.2}$$

According to (6.2), (2.6) can be rewritten in deep water as:

$$m_{ijl} = \int_0^{2\pi}\int_0^{\infty} \frac{\sigma^{2(i+j)+l}}{g^{i+j}} \cos^i(\theta)\sin^j(\theta) S(\sigma,\theta) d\sigma d\theta \tag{6.3}$$

Using directional spectrum decomposition (2.32), (6.3) becomes

$$m_{ijl} = \int_0^{2\pi}\int_0^{\infty} \frac{\sigma^{2(i+j)+l}}{g^{i+j}} \cos^i(\theta)\sin^j(\theta) S(\sigma) D(\theta) d\sigma d\theta \tag{6.4}$$

Since the chosen directional distribution function depends on direction θ only, we can rearrange (6.4) in order to separate the integrals

$$m_{ijl} = \int_0^{2\pi} \cos^i(\theta) \sin^j(\theta) D(\theta) d\theta \int_0^{\infty} \frac{\sigma^{2(i+j)+l}}{g^{i+j}} S(\sigma) d\sigma \tag{6.5}$$

It has been demonstrated that if the tail of the frequency spectrum is proportional to σ^{-5}, as in the Pierson-Moskowitz and JONSWAP spectra, the 4th moment in frequency is not finite (Ochi, 2005). Thus, if

$$2(i+j)+l = 4$$

the corresponding m_{ijl} moments are not finite and we cannot calculate spectral parameters depending on them. The solution we adopted is to limit the upper bound of integration in the frequency domain to a reasonable value, σ_∞. Obviously, this forces the spectral parameter, and so results of space-time extreme analysis, to depend on the choice of the cut-off frequency σ_∞. For this reason we decided to link σ_∞ to the physics of surface gravity waves, assuming it represents the higher frequency an harmonic wave could experience in the ordinary gravity waves range. σ_∞ is then the gravity-capillary limit, i.e. $\sigma_\infty = 60$ rad/s (Holthuijsen, 2007). We investigated the effects of the choice of this value on the space-time extremes, through a sensitivity analysis (Section 6.4). Among the moments in (2.7), the limitation of integrals up to σ_∞ has to be applied to m_{200}, m_{020} and m_{110}.

6.2.1 Pierson-Moskowitz and $\cos^2$ function

Assuming the Pierson-Moskowitz spectral shape (2.26) with $\cos^2$ function (2.33), under the fully developed sea hypothesis, (6.4) and (6.5) can be rewritten as:

$$m_{ijl} = \int_0^{2\pi} \int_0^{\infty} \frac{2}{\pi} A g^{2-(i+j)} \frac{\sigma^{2(i+j)+l}}{\sigma^5} \cos^{i+2}(\theta) \sin^j(\theta) e^{-P(\sigma/\sigma_m)^{-4}} d\sigma d\theta \tag{6.6}$$

$$m_{ijl} = \frac{2}{\pi} A g^{2-(i+j)} \int_0^{2\pi} \cos^{i+2}(\theta) \sin^j(\theta) d\theta \int_0^{\infty} \frac{\sigma^{2(i+j)+l}}{\sigma^5} e^{-P(\sigma/\sigma_m)^{-4}} d\sigma \tag{6.7}$$

Using computer algebra system Maxima (2011), analytic calculation of the integrals was performed and the resulting expression for the moments of

the Pierson-Moskowitz spectrum with $\cos^2$ directional distribution are:

$$\begin{aligned}
m_{000} &= \frac{Ag^2}{4\sigma_m^4 P} \\
m_{002} &= \frac{Ag^2\sqrt{\pi}}{4\sigma_m^2\sqrt{P}} = \sqrt{\pi P} m_{000}\sigma_m^2 \\
m_{020} &= \frac{A\Gamma(0,s)}{16} = \frac{P\Gamma(0,s)}{4g^2} m_{000}\sigma_m^4 \\
m_{200} &= \frac{3A\Gamma(0,s)}{16} = \frac{3P\Gamma(0,s)}{4g^2} m_{000}\sigma_m^4 \\
m_{101} &= \frac{2Ag\Gamma(1/4)}{3\pi\sigma_m P^{1/4}} = \frac{8P^{3/4}\Gamma(1/4)}{3\pi g} m_{000}\sigma_m^3 \\
m_{110} &= 0 \\
m_{011} &= 0
\end{aligned} \tag{6.8}$$

with $s = \frac{\sigma_m^4 P}{1.296 \cdot 10^7}$. In the previous formulae, $\Gamma(a)$ and $\Gamma(a,z)$ are the Gamma and upper incomplete Gamma functions, respectively (Abramowitz and Stegun, 1972):

$$\Gamma(a) = \int_0^\infty t^{a-1} e^{-t} dt \tag{6.9}$$

$$\Gamma(a,z) = \int_z^\infty t^{a-1} e^{-t} dt \tag{6.10}$$

While $\Gamma(a)$ was easily obtained from Maxima or MATLAB (2012) built-in functions, $\Gamma(a,z)$ was calculated (see Appendix B.1) by using its upper limiting function $E_1(z)$ (Abramowitz and Stegun, 1972)

$$E_1(z) = -\gamma - \ln(z) - \sum_1^\infty (-1)^k \frac{z^k}{k(k!)} \tag{6.11}$$

where $\gamma \sim 0.5772$ is Euler-Mascheroni constant. In fact, when $a = 0$ (Abramowitz and Stegun, 1972)

$$\Gamma(0,z) = \lim_{a\to 0}\Gamma(a) - \frac{1}{a} - \left(\gamma(a,z) - \frac{1}{a}\right) = E_1(z) \tag{6.12}$$

being $\gamma(a,z)$ the lower incomplete Gamma function. Note that since s depends upon σ_m, $\Gamma(0,s)$ is itself function of σ_m.

Spectral parameters were finally obtained substituting eqs. (6.8) into eqs. (2.7)

$$
\begin{aligned}
\overline{T} &= \frac{4.46}{\sigma_m} \\
\overline{L}_x &= \frac{63.6}{\sigma_m^2\sqrt{\Gamma(0,s)}} \\
\overline{L}_y &= \frac{110.0}{\sigma_m^2\sqrt{\Gamma(0,s)}} \\
\alpha_{xy} &= 0 \\
\alpha_{xt} &= \frac{2.68}{\sqrt{\Gamma(0,s)}} \\
\alpha_{yt} &= 0
\end{aligned}
\tag{6.13}
$$

Explicit dependence of spectral parameters (6.13) upon wind speed U (Figure 6.1) can be pointed out through $\sigma_m = 0.87(g/U)$ (Ochi, 2005), as shown in Appendix (B.2). The same has been done for significant wave height H_s, again in Appendix (B.2).

Ochi (2005) obtained the analytic expressions of zero-th moment and mean zero-crossing period for a spectral formulation with σ^{-5} tail, $S(\sigma) = \frac{C}{\sigma^5}e^{-D/\sigma^4}$

$$
m_{000} = C/(4D) \qquad \overline{T} = 4.72D^{-1/4}
$$

If Pierson-Moskowitz spectrum is considered, i.e. (2.26), then $C = Ag^2$, $D = P\sigma_m^4$ and first eqs. of (6.8) and (6.13) are exactly recovered.

The ratio $m_{200}/m_{020} = 3$ is constant, i.e. independent from σ_m. Consequently, the ratio $\overline{L}_x/\overline{L}_y = 0.58$ is also constant. Hence, crests are only a little longer than waves, consistently with the chosen directional spreading function ($\cos^2$), representative of short-crested conditions ($\gamma_s = 0.76$).

Consistently with Baxevani and Rychlik (2006), the irregularity parameters are null, except for the one expressing correlation between surface derivatives along direction of propagation (x) and time (t), i.e. α_{xt}. From (2.7), α_{xy} and α_{yt} equal zero since m_{110} and m_{011} are zero. In fact, when the symmetric $\cos^2$ function is multiplied by a sine function, whose integral is zero in $[-\pi/2,\pi/2]$, the global integral is again zero. Meaning of $\alpha_{xt} \neq 0$ is that, due to a organized motion along x direction, a reduced number of exceedances of a certain threshold has to be expected inside the space-time domain and on its [X,T] boundary.

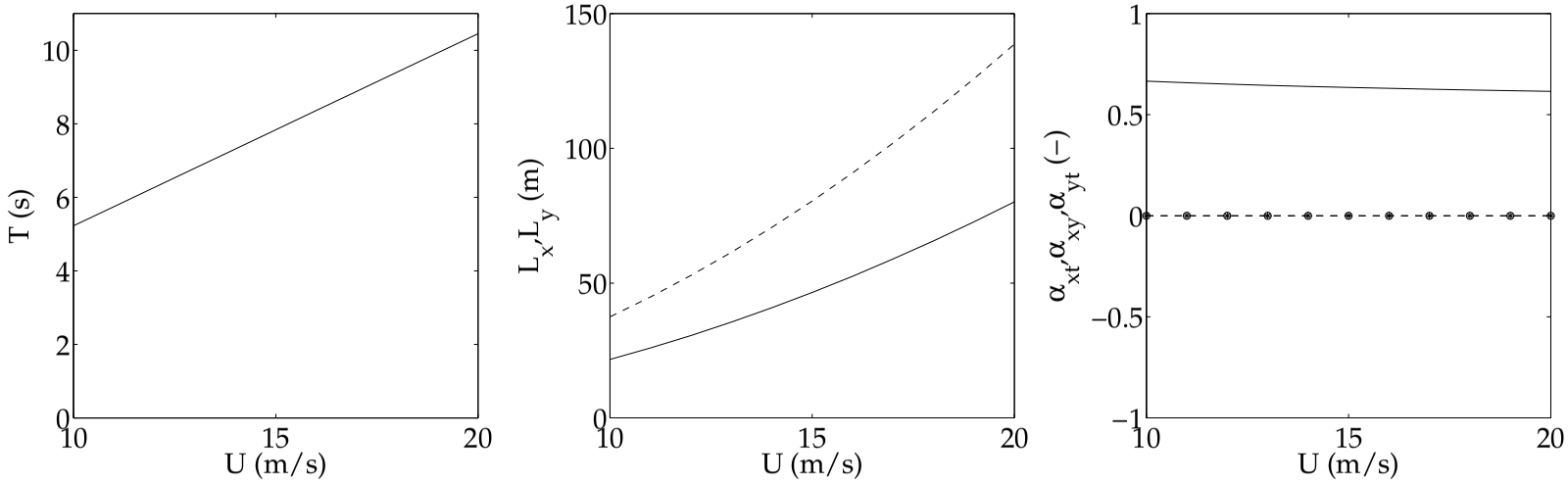

Figure 6.1: Spectral parameters of the Pierson-Moskowitz spectrum with $\cos^2$ function depending on the wind speed U. Left panel: average wave period $\overline{T}$. Central panel: average wavelength $\overline{L}_x$ (solid) and wave crest $\overline{L}_y$ (dashed). Right panel: irregularity parameters α_{xt} (solid), α_{xy} (dashed-asterisks) and α_{yt} (dashed-circles).

6.2.2 JONSWAP and $\cos^2$ function

JONSWAP frequency spectrum (2.29) cannot be integrated analytically (Holthuijsen, 2007). Thus, moments of the spectrum had to be calculated under some assumptions and approximations. Yamaguchi (1984) obtained good approximations for zero-th, first and second order moments of (2.29). Nevertheless, we needed moments up to the fourth order, so we adapted the procedure due to Gran (1992) to get approximate form of integrals. Following the work of Gran, moments of JONSWAP spectrum can be obtained in approximate form if the spectrum is considered as a peak-enhanced wave spectrum consisting of two independent wave components:

- a broad-banded random wave component ζ_{PM}, conforming with a Pierson-Moskowitz spectrum with modal frequency σ_m and responsible for the low and high frequency tails of the spectrum;
- a narrow-banded random wave component ζ_{NB} with density closely centered about the peak, i.e. at modal frequency σ_m.

Indeed, according to Gran, the area of the additional peak in the JONSWAP spectrum corresponds approximately to the variance of an additional narrow-banded peak-wave about σ_m. The variance of the narrow-banded wave ζ_{PM} relative to the broad-banded wave was thus described by the η parameter (not to be confused with sea surface elevation, never used explicitly within this Section)

$$\eta = \frac{m_{000,NB}}{m_{000,PM}} \tag{6.14}$$

Assuming parameter $\beta = 0.08$ in (2.29), i.e. the average value between $\beta_a = 0.07$ and $\beta_b = 0.09$, Gran (1992) estimated η for the JONSWAP spectrum to be approximately

$$\eta \sim \frac{\gamma - 1}{6} \tag{6.15}$$

thus, proportional to the peak-enhancement factor γ and such that:

- if $\gamma = 1$, i.e. the Pierson-Moskowitz spectrum is recovered, $\eta = 0$. In fact, no additional variance is added to the broad-banded wave;
- if $\gamma = 7$, i.e. the maximum value it can assume, then $\eta = 1$ and the variance is equally distributed between the broad and the narrow-banded components.

Under the chosen assumptions, we can extend the work of Gran to yield the m_{ijl} moments of a directional wave spectrum consisting of the JONSWAP

frequency spectrum and $\cos^2$ directional distribution function

$$m_{ijl} = m_{ijl,PM} + m_{ijl,NB} \tag{6.16}$$

where $m_{ijl,PM}$ are the moments of the Pierson-Moskowitz spectrum and $\cos^2$ function, i.e. eqs. (6.8), while $m_{ijl,NB}$ are the moments of the additional peak. Thanks to narrow-bandedness, the latters can be written as:

$$m_{ijl,NB} = \frac{\sigma_m^{2(i+j)+l}}{g^{(i+j)}} m_{000,NB} \int_0^{2\pi} \cos^i(\theta) \sin^j(\theta) D(\theta) d\theta \tag{6.17}$$

Then, according to (6.14):

$$m_{ijl,NB} = \eta \frac{\sigma_m^{2(i+j)+l}}{g^{(i+j)}} m_{000,PM} \int_0^{2\pi} \cos^i(\theta) \sin^j(\theta) D(\theta) d\theta \tag{6.18}$$

Using computer algebra system Maxima (2011), analytic calculation of the integrals was performed leading to needed moments $m_{ijl,NB}$

$$\begin{aligned}
m_{000,NB} &= \eta \frac{A_J g^2}{4P\sigma_m^4} \\
m_{002,NB} &= \eta \frac{A_J g^2}{4P\sigma_m^2} \\
m_{020,NB} &= \eta \frac{A_J}{16P} \\
m_{200,NB} &= \eta \frac{3A_J}{16P} \\
m_{101,NB} &= \eta \frac{2A_J g}{3\pi P\sigma} \\
m_{110,NB} &= 0 \\
m_{011,NB} &= 0
\end{aligned} \tag{6.19}$$

being A_J the JONSWAP spectrum scaling parameter.

Hence, following (6.16), the approximate moments of the directional spectrum consisting of JONSWAP frequency spectral shape with $\cos^2$ function

are:

$$
\begin{aligned}
m_{000,J} &= (\eta+1)\frac{A_J g^2}{4P\sigma_m^4} = (\eta+1)m_{000,PM} \\
m_{002,J} &= (\eta+\sqrt{\pi P})\frac{A_J g^2}{4P\sigma_m^2} = (\eta+\sqrt{\pi P})m_{000,PM}\sigma_m^2 \\
m_{020,J} &= (\eta+P\Gamma(0,s))\frac{A_J}{16P} = \left(\frac{\eta+P\Gamma(0,s)}{4g^2}\right)m_{000,PM}\sigma_m^4 \\
m_{200,J} &= (\eta+P\Gamma(0,s))\frac{3A_J}{16P} = 3\left(\frac{\eta+P\Gamma(0,s)}{4g^2}\right)m_{000,PM}\sigma_m^4 \\
m_{101,J} &= (\eta+P^{5/4}\Gamma(1/4))\frac{2gA_J}{3\pi P\sigma_m} = \frac{8}{3\pi g}(\eta+P^{3/4}\Gamma(1/4))m_{000,PM}\sigma_m^3 \\
m_{110,J} &= 0 \\
m_{011,J} &= 0
\end{aligned}
\tag{6.20}
$$

where $m_{000,PM} = A_J g^2/(4P\sigma_m^4)$ is the variance of the broad-banded component with Pierson-Moskowitz spectral shape scaled by the JONSWAP scaling parameter A_J. Here, $s = \frac{\sigma_m^4 P}{1.296\cdot 10^7}$ and $\Gamma(0,s)$ is the upper incomplete Gamma function.

Finally, spectral parameters were obtained according to (2.7), (6.15) and (6.20)

$$
\begin{aligned}
\overline{T} &= \frac{6.28}{\sigma_m}\sqrt{\frac{\eta+1}{\eta+1.98}} = \frac{6.28}{\sigma_m}\sqrt{\frac{\gamma+5.0}{\gamma+10.88}} \\
\overline{L}_x &= \frac{71.2}{\sigma_m^2}\sqrt{\frac{\eta+1}{\eta+1.25\Gamma(0,s)}} = \frac{71.2}{\sigma_m^2}\sqrt{\frac{\gamma+5.0}{\gamma+7.5\Gamma(0,s)-1}} \\
\overline{L}_y &= \frac{123.0}{\sigma_m^2}\sqrt{\frac{\eta+1}{\eta+1.25\Gamma(0,s)}} = \frac{123.0}{\sigma_m^2}\sqrt{\frac{\gamma+5.0}{\gamma+7.5\Gamma(0,s)-1}} \\
\alpha_{xy} &= 0 \\
\alpha_{xt} &= \frac{0.981}{\sqrt{\eta+1.25\Gamma(0,s)}}\frac{\eta+4.28}{\sqrt{\eta+1.98}} = \frac{0.981(\gamma+24.68)}{\sqrt{\gamma+10.88}\sqrt{\gamma+7.5\Gamma(0,s)-1}} \\
\alpha_{yt} &= 0
\end{aligned}
\tag{6.21}
$$

where dependence on modal frequency σ_m and peak-enhancement factor γ was made explicit. The dependence of spectral parameters (6.21) upon wind speed U and fetch length F (Figure 6.2) is provided by expression for γ and

σ_m in (2.31). An alternative formulation to (6.21) based on U and F is presented in Appendix (B.2).

For $\eta = 0$ or $\gamma = 1$, corresponding to Pierson-Moskowitz spectrum, parameters (6.13) are recovered. As already obtained for Pierson-Moskowitz spectrum and $\cos^2$ function, the ratio $m_{200}/m_{020} = 3$ is independent from σ_m and leads to $\overline{L}_x/\overline{L}_y = 0.58$ ($\gamma_s = 0.76$). Irregularity parameters α_{xt}, α_{xy} and α_{yt} behave in the same way described earlier for Pierson-Moskowitz spectrum and $\cos^2$ function, revealing that they are affected only by directional characteristics of the sea state.

6.3 Comparison with numerical results

Though we did not employed any numerical technique to calculate moments and spectral parameters of JONSWAP spectrum with $\cos^2$ function, the procedure of Gran (1992), which we herein extended, takes advantage of some approximations. Among all, the principal ones are:

- the peak-enhanced JONSWAP spectrum is approximated by a scaled Pierson-Moskowitz spectral shape plus a narrow-banded spectrum about the modal frequency;

- the relationship between η and γ for JONSWAP spectrum is the approximate result of a numerical technique, i.e. the method of the steepest descent.

In order to evaluate the reliability of the results we obtained for the JONSWAP spectrum with $\cos^2$ function, we compared moments and spectral parameters obtained analytically through eqs. (6.20) and (6.21) respectively, with the corresponding quantities obtained by numerical integration of a chosen JONSWAP and $\cos^2$ function directional spectrum (Figure 6.3). Prior to this, we performed the same comparison for the Pierson-Moskowitz and $\cos^2$ function directional spectrum, to verify reliability of numerical integration procedure.

Spectral domain was discretized by using:

- an exponential frequency axis with 32 bins in the interval [0.05,1.00] Hz and a resolution $\Delta\sigma/\sigma = 0.1$;

- a uniform directional axis with 315 bins in the interval [-π/2, π/2] rad and resolution $\Delta\theta = 0.01$ rad.

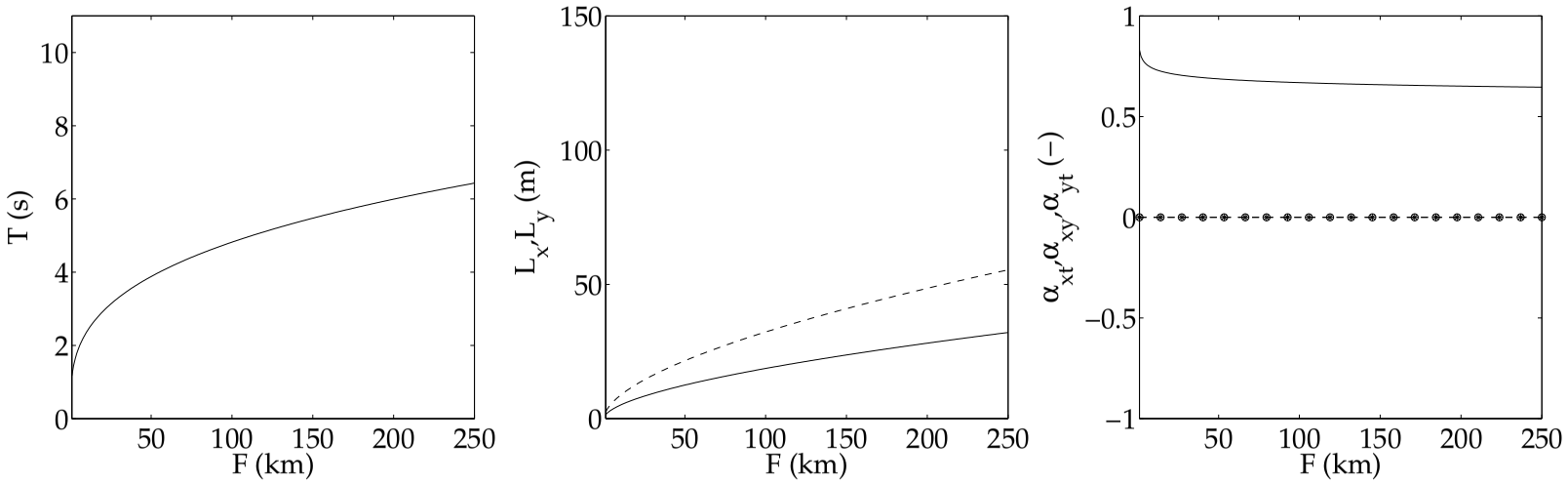

Figure 6.2: Spectral parameters of the JONSWAP spectrum with $\cos^2$ function depending on the fetch length F. Wind speed $U = 15$ m/s and F values are chosen in order to keep $\overline{F}$ between 0 and 10^4, according to Lewis and Allos (1990). Left panel: average wave period $\overline{T}$. Central panel: average wavelength $\overline{L}_x$ (solid) and wave crest $\overline{L}_y$ (dashed). Right panel: irregularity parameters α_{xt} (solid), α_{xy} (dashed-asterisks) and α_{yt} (dashed-circles).

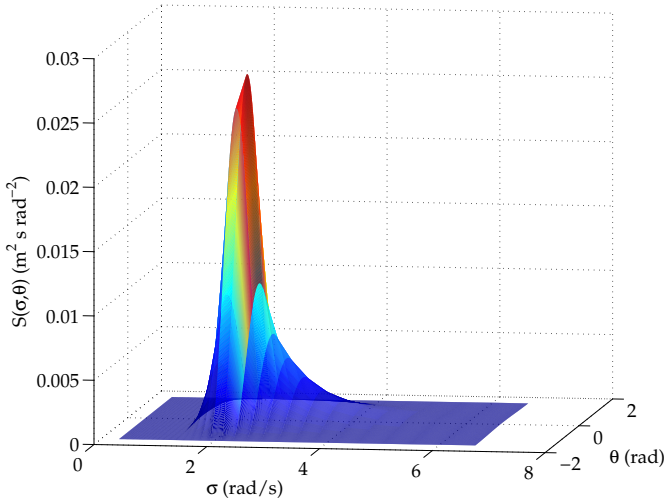

Figure 6.3: Directional wave spectrum used for numerical integration of a JONSWAP spectrum and $\cos^2$ function.

Numerical integration was performed using trapezoidal rule up to the maximum cut-off frequency, i.e. 1.00 Hz. Over this value, a diagnostic frequency tail, proportional to σ^{-5}, was added and analytic integration was performed. For 4th order m_{ijl} moments, analytic integration was bounded above by $\sigma_\infty = 60$ rad/s, i.e. the capillary-gravity limit.

6.3.1 Pierson-Moskowitz and $\cos^2$ function

The values of the directional spectrum with (2.26) and (2.33) were calculated at the discrete bins above indicated. We assumed a modal frequency $\sigma_m = 0.75$ rad/s, corresponding to $H_s = 2.81$ m. Hence, m_{ijl} moments (6.6) and spectral parameters (2.7) were numerically calculated and then compared to that obtained from (6.8) and (6.13), respectively.

Table 6.1 and Table 6.2 show an excellent agreement for both the spectral moments and spectral parameters, with differences of an order smaller than 10^{-5} for spectral moments and smaller than 10^{-3} for spectral parameters that can be ascribed to numerics. Thus, we verified the reliability of the numerical calculation technique. We then used it for the evaluation of the analytical results for JONSWAP spectrum under the specified assumptions and approximations.

Technique	m_{000} (m^2)	m_{002} (m^2 rad^2 s^{-2})	m_{020} (rad^2)
NUMERICAL	0.4927	0.5493	0.0085
ANALYTICAL	0.4927	0.5492	0.0085
Technique	m_{200} (rad^2)	m_{101} (m rad^2 s^{-1})	m_{110} (rad^2)
NUMERICAL	0.0254	0.0771	-10^{-14}
ANALYTICAL	0.0254	0.0771	0
Technique	m_{011} (m rad^2 s^{-1})		
NUMERICAL	-10^{-11}		
ANALYTICAL	0		

Table 6.1: Spectral moments of a Pierson-Moskowitz spectrum with $\cos^2$ function. Comparison between numerical and analytical techniques results.

Technique	$\overline{T}$ (s)	$\overline{L}_x$ (m)	$\overline{L}_y$ (m)	α_{xt} (-)	α_{xy} (-)	α_{yt} (-)
NUMERICAL	5.95	27.67	47.93	0.65	-10^{-12}	-10^{-8}
ANALYTICAL	5.95	27.67	47.93	0.65	0	0

Table 6.2: Spectral parameters of a Pierson-Moskowitz spectrum with $\cos^2$ function. Comparison between numerical and analytical techniques results.

6.3.2 JONSWAP and $\cos^2$ function

We first calculated the values of the directional spectrum with (2.29) and (2.33) at the specified discrete bins. We assumed $\sigma_m = 0.75$ rad/s, the average value for the peak-enhancement factor $\gamma = 3.3$ and the average value for β, i.e. $\beta = 0.08$, as done by Gran (1992). For simplicity, we assumed $A_J = A$. Considered sea state had a significant wave height $H_s = 3.47$ m, obtained by numerical integration of the spectrum.

Table 6.3 and Table 6.4 show that analytically obtained spectral moments and parameters are consistent with that calculated by numerical integration of the spectrum. Nevertheless, some differences due to the cited approximations in the Gran procedure emerged. The most considerable is the 9% difference on m_{000}, which leads to a 5% difference on the significant wave height estimate. We observed that greater differences are associated with smaller orders of the spectral moments in frequency, e.g. the fourth order moments m_{200}, m_{020} and m_{110} present the smaller differences, less than 1%. For what concerns spectral parameters, excellent estimates resulted for the irregularity parameters. Maximum differences, i.e. 4%, were observed for $\overline{L}_x$

and $\overline{L}_y$, while for the other parameters the agreement was better. Changing peak-enhancement factor γ affected only slightly the differences between analytical and numerical results. Differences dropped as γ decreased down to $\gamma = 1$, while they didn't show significant increases as γ was raised up to $\gamma = 7$.

Technique	m_{000} (m^2)	m_{002} (m^2 rad^2 s^{-2})	m_{020} (rad^2)
NUMERICAL	0.7509	0.6954	0.0087
ANALYTICAL	0.6816	0.6555	0.0086
Technique	m_{200} (rad^2)	m_{101} (m rad^2 s^{-1})	m_{110} (rad^2)
NUMERICAL	0.0259	0.0867	-10^{-14}
ANALYTICAL	0.0261	0.0840	0
Technique	m_{011} (m rad^2 s^{-1})		
NUMERICAL	-10^{-11}		
ANALYTICAL	0		

Table 6.3: Spectral moments of a JONSWAP spectrum with $\cos^2$ function. Comparison between numerical and analytical techniques results.

Technique	$\overline{T}$ (s)	$\overline{L}_x$ (m)	$\overline{L}_y$ (m)	α_{xt} (-)	α_{xy} (-)	α_{yt} (-)
NUMERICAL	6.53	33.73	58.41	0.64	-10^{-12}	-10^{-8}
ANALYTICAL	6.41	32.25	55.86	0.64	0	0

Table 6.4: Spectral parameters of a JONSWAP spectrum with $\cos^2$ function. Comparison between numerical and analytical techniques results.

We can conclude that:

- for a Pierson-Moskowitz spectrum with $\cos^2$ directional distribution, the proposed analytical formulae of spectral parameters represent a valuable alternative to the lack of directional spectra (from measurements, numerical modeling, etc). They are exact in the range of the surface-gravity waves frequency range and they can be used without the need of numerical tools or softwares. They depend only on the modal frequency σ_m, hence on wind speed U or significant wave height H_s, and not for example on the discretization of the spectral domain (frequency and directional resolution, cut-off frequencies among all);
- for a JONSWAP spectrum with $\cos^2$ directional distribution, the proposed formulae are affected by the approximations used in the deriva-

tion procedure. This cause discrepancies within 5% from results of numerical integration, herein assumed as a benchmark. Hence, proposed formulae are not exact but they however represents a valuable alternative in absence of directional spectra, since they don't need numerical tools or softwares to be used. Moreover, they make the dependence upon wind speed U and fetch length F explicit.

6.4 Cut-off frequency: sensitivity analysis

As already specified in Section 6.2, the choice of the cut-off frequency σ_∞ affects the results of wave space-time extreme analysis. Therefore, we performed a sensitivity analysis to investigate the effects of the choice of $\sigma_\infty = 60$ rad/s on spectral parameters (2.7) and on the expected maximum sea surface elevation $\overline{\xi}_{ST}$ (or, equivalently, on the ratio with $\overline{\xi}_{ST}/\overline{\xi}_T$).

We considered Pierson-Moskowitz and cosine square function directional spectra, assuming wind speeds $U = [10, 20]$ m/s. We fixed a square area $A = 10^4$ m^2 and a duration $D = 100\overline{T}$. Spectral parameters were obtained by analytic integration of (6.7) according to the procedure in Section 6.2.1, but σ_∞ was forced to vary of $\pm 10\%$ and $\pm 50\%$. Then, space-time extreme analysis was performed following Fedele's method (Section 3.3). We compared spectral parameters (Figure 6.4 and Table 6.5) and the expected maximum sea surface elevation obtained from different cut-off frequencies analyses (Table 6.5). Then, we calculated percentage differences with respect to $\sigma_\infty = 60$ rad/s analysis results (Table 6.5), for $U = 20$ m/s, i.e. the condition associated to maximum variations of investigated parameters (Figure 6.4).

We observed that percentage differences were equal for all the non-null spectral parameters interested by the cut-off frequency variations, i.e. those dependent upon 4th order moments ($\overline{L}_x$, $\overline{L}_y$, α_{xt}). We also observed that these differences were within 10% with respect to the chosen $\sigma_\infty = 60$ rad/s analysis even when the cut-off frequency was increased of 50%. The expected maximum sea surface elevation was less sensitive to cut-off frequency variations. In fact, differences with respect to the chosen $\sigma_\infty = 60$ rad/s analysis are always within the 1.1%. For smaller areas, the differences on $\overline{\xi}_{ST}$ drop below 1.0%.

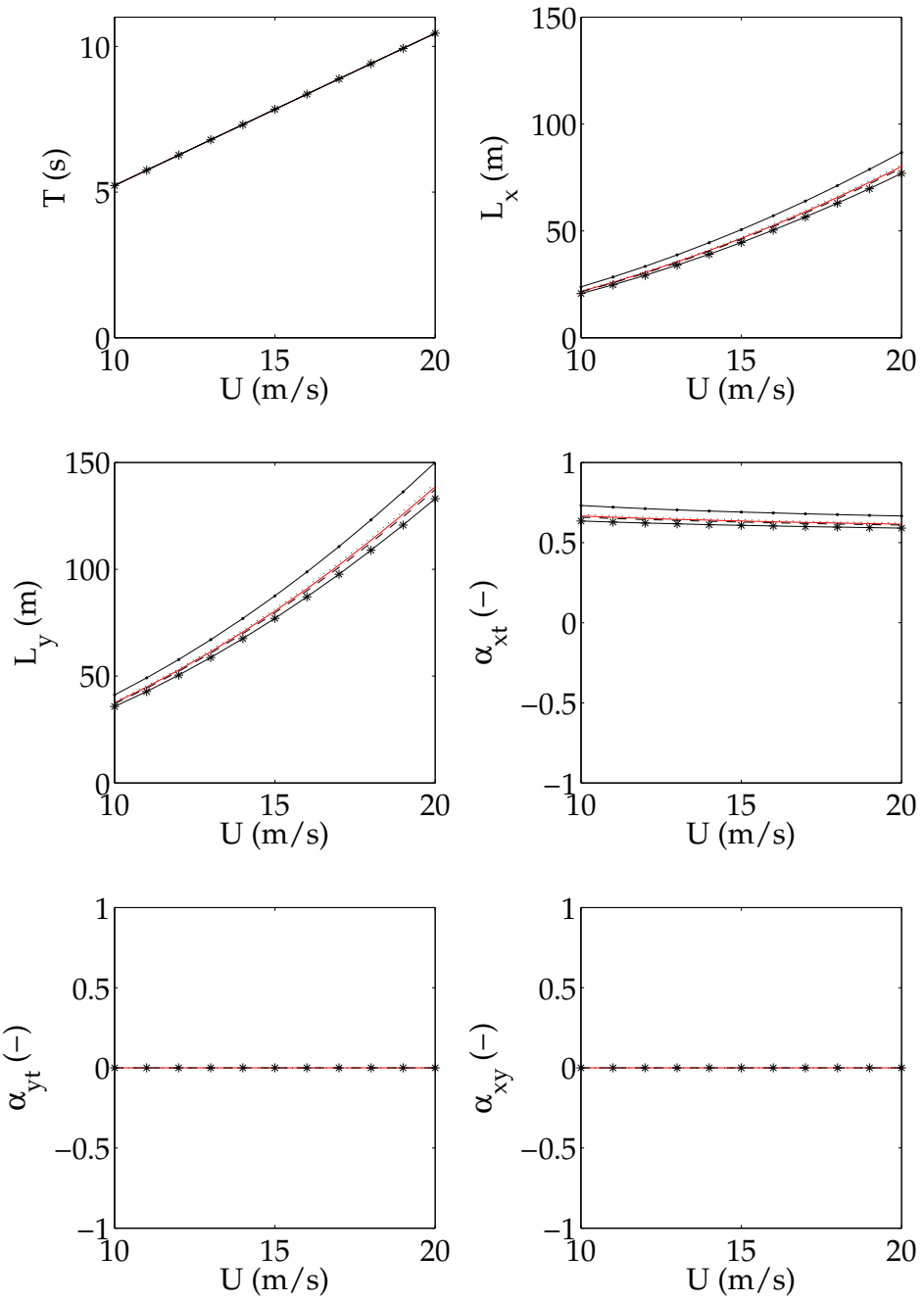

Figure 6.4: Sensitivity analysis on cut-off frequency σ_∞. Spectral parameters as a function of wind speed U: $\sigma_\infty = 60$ rad/s (red solid line), +10% variation (dashed black line), −10% variation (dotted black line), +50% variation (solid-asterisks black line), −50% variation (solid-dotted line). Pierson-Moskowitz and cosine square function directional spectra; $A = 10^4$ m^2, $D = 100\overline{T}$; Fedele's method.

σ_∞ (rad/s)	$\overline{T}$ (s)	$\overline{L}_x$ (m)	$\overline{L}_y$ (m)	α_{xt} (-)	α_{xy} (-)	α_{yt} (-)	$\overline{\xi}_{ST}$ (-)
60	10.45	80.16	138.74	0.62	0	0	1.11
66 (+10%)	10.45	79.37	137.27	0.61	0	0	1.11
54 (−10%)	10.45	81.06	140.21	0.62	0	0	1.11
90 (+50%)	10.45	79.94	133.07	0.59	0	0	1.12
30 (−50%)	10.45	86.74	150.03	0.67	0	0	1.10
σ_∞ (rad/s)	$\Delta\overline{T}$ (%)	$\Delta\overline{L}_x$ (%)	$\Delta\overline{L}_y$ (%)	$\Delta\alpha_{xt}$ (%)	$\Delta\alpha_{xy}$ (%)	$\Delta\alpha_{yt}$ (%)	$\Delta\overline{\xi}_{ST}$ (%)
66 (+10%)	0.0	-1.0	-1.0	-1.0	0.0	0.0	+0.1
54 (−10%)	0.0	+1.1	+1.1	+1.1	0.0	0.0	-0.1
90 (+50%)	0.0	-4.0	-4.0	-4.0	0.0	0.0	+0.5
30 (−50%)	0.0	+8.2	+8.2	+8.2	0.0	0.0	-1.1

Table 6.5: Sensitivity analysis on cut-off frequency σ_∞. Spectral parameters and expected maximum sea surface elevation for $U = 20$ m/s. Pierson-Moskowitz and cosine square function directional spectra; $A = 10^4$ m^2, $D = 100\overline{T}$; Fedele's method.

6.5 Spectral parameters in the original frame of reference

The assumption of wave propagation along the x positive direction, i.e. $\theta_p = 0$, was used to simplify the final formulae of spectral parameters. The letters lost dependence upon the actual wave propagation direction θ_p. Although neither the spectral shape nor the space-time extreme analysis are affected by a rotation of the frame of reference, some of the spectral parameters depend upon the chosen frame of reference. These are spectral parameters obtained from moments having non-null exponents for wavenumber components k_x,k_y, i.e. $\overline{L}_x$, $\overline{L}_y$, α_{xt}, α_{xy}, α_{yt}. Hence, it could be useful to correct these spectral parameters formulae in the rotated frame of reference to get the ones in the original frame of reference.

6.5.1 Wavelength and wave crest

To correct wavelength $\overline{L}_x$ and wave crest $\overline{L}_y$, first consider that although k_x,k_y depend upon the frame of reference, the wavenumber vector magnitude k is instead the same. Hence, once the latter has been obtained it is sufficient to project it onto the axes $(\hat{x}, \hat{y})$ of the original frame of reference to get $(k_{\hat{x}},k_{\hat{y}})$

$$k_{\hat{x}} = k\cos\hat{\theta} \qquad k_{\hat{y}} = k\sin\hat{\theta} \tag{6.22}$$

$\hat{\theta}$ being the direction of wave propagation in the original frame of reference:

$$\hat{\theta} = \arctan\left(\frac{k_{\hat{y}}}{k_{\hat{x}}}\right) \tag{6.23}$$

Then, wavelength $\overline{L}_{\hat{x}}$ and wave crest $\overline{L}_{\hat{y}}$ are obtained as:

$$\overline{L}_{\hat{x}} = \frac{2\pi}{k_{\hat{x}}} \qquad \overline{L}_{\hat{y}} = \frac{2\pi}{k_{\hat{y}}} \tag{6.24}$$

Since we are using second order moments to calculate wavenumber components k_x,k_y, the directions of wavenumber vector in the rotated or in the original frame of reference are different from the direction of propagation θ_p. To summarize

$$\hat{\theta} \neq \theta \neq \theta_p \tag{6.25}$$

Hence, referring to rotated frame of reference, we will never obtain $k_y = 0$, unless the sea state is long-crested. In fact, we recall that short-crestedness

parameter is defined as

$$\gamma_s = \sqrt{\frac{m_{020}}{k_{200}}} = \frac{k_y}{k_x} \tag{6.26}$$

where $\gamma_s = 0$ corresponds to long-crested conditions, while $\gamma_s = 1$ represents short-crested conditions.

To obtain $\hat{\theta}$, we built a directional spectrum (Pierson-Moskowitz and $\cos^2$ function) and we changed direction of wave propagation θ_p between $-\pi/2$ and $\pi/2$, i.e. in the domain of definition of the directional spreading function. Then, we calculated the directions of propagation in the following ways:

- $\hat{\theta}$, directly from numerical integration of the spectrum;
- θ, from analytical formulae of wavelength and wave crest in the rotated frame of reference.

The ratios $r_\theta = \hat{\theta}/\theta$ we obtained at different θ_p can be modeled as:

$$r_\theta = 1.5 + \frac{\cos\left(2(\theta_p + \pi/2)\right)}{2} \tag{6.27}$$

Hence, we can express $\hat{\theta}$ as a function of θ_p:

$$\begin{aligned} \hat{\theta}(\theta_p) &= \theta r_\theta \\ &= \theta \left(1.5 + \frac{\cos\left(2(\theta_p + \pi/2)\right)}{2}\right) \end{aligned} \tag{6.28}$$

and we were finally able to correct the analytical formulae for $\overline{L}_x$ and $\overline{L}_y$ to get them in the original frame of reference with an error smaller than 1%.

6.5.2 Irregularity parameters

To correct the irregularity parameters α_{xt}, α_{xy}, α_{yt} we could not proceed as for the wavelength and wave crest since magnitudes of the specular velocity vectors are not the same in different frame of references. So, we directly modeled the ratio of the quantities in the two frames of reference for different wave propagation directions. Since α_{xy} and α_{yt} are null in the rotated reference frame, we proceeded as following:

- we calculated $r_{xt} = \alpha_{\hat{x}t}/\alpha_{xt}$ at different θ_p and modeled it by using a 8-th degree polynomial fitting function, depending on θ_p only; $\alpha_{\hat{x}t}$ was obtained by numerical integration of the spectrum. By this way we corrected α_{xt};

- we calculated the ratios $r_t = \alpha_{\hat{x}t}/\alpha_{\hat{y}t}$ and $r_x = \alpha_{\hat{x}t}/\alpha_{\hat{x}\hat{y}}$ between $\alpha_{\hat{x}t}$, $\alpha_{\hat{y}t}$, and $\alpha_{\hat{x}\hat{y}}$ respectively, at different θ_p. Then, we modeled the ratios using hyperbolic cotangent functions thus correcting α_{xy} and α_{yt}.

However, probably due to the approximations in the modeling of the ratios, the errors committed with this correction were too large to consider this procedure reliable, at least for α_{xy} and α_{yt}. Thus, we consider the correction of the spectral parameters acceptable only for wavelength and wave crest.

6.6 Results

The analysis of wave extremes in the space-time domain can now be performed, taking advantage of eqs. (6.13) or (6.21). This means that if one assumes either a Pierson-Moskowitz (PM) or a JONSWAP (JON) spectral shape and a $\cos^2$ directional distribution, one can analytically estimate the spectral parameters characterizing the sea state, under some specified assumptions and approximations. Then, the maximum sea surface elevation expected over an area $\overline{\xi}_{ST}$ can be computed by applying one of the described stochastic methods, i.e. Piterbarg's theorem or Fedele's method.

In this Chapter, we obtained and discussed the dependence upon area size A, wind speed U and fetch length F of the maximum expected sea surface elevation over an area $\overline{\eta}_{ST}$ (or normalized $\overline{\xi}_{ST}$). Wind speeds considered were in the range for which Pierson-Moskowitz spectral shape was deduced (Pierson and Moskowitz, 1964; Ochi, 2005), i.e. $U = [10, 20]$ m/s. For the Pierson-Moskowitz case, they corresponded to $H_s = [2.15, 8.56]$ m (Figure 6.5, left panel). Fetch lengths F, which only enter JONSWAP spectrum that is fetch limited, were in the range $F = [10, 260]$ km. For simplicity of discussion, fetch was let vary when the wind speed $U = 15$ m/s was constant. Corresponding significant wave heights were $H_s = [0.69, 3.65]$ m (Figure 6.5, right panel). The choice of area size, in particular of the minimum one, was led by the fact that we wanted to compare results from different stochastic methods. Since Piterbarg's theorem fails when the area side is shorter than a wavelength, as it will be shown later on, we could not go down much less than the minimum average wavelength, i.e. 22 m for the Pierson-Moskowitz case and 5 m for the JONSWAP case. Nevertheless, we wanted to discuss Forristall's approximation as well as Fedele's method, working even down to less than 1 m^2. We then chose a 100 m^2 minimum area for the Pierson-Moskowitz case and a 10 m^2 for the JONSWAP case. Duration D was chosen such that an average number of 100 waves was contained within time domain: $D = 100\overline{T}$

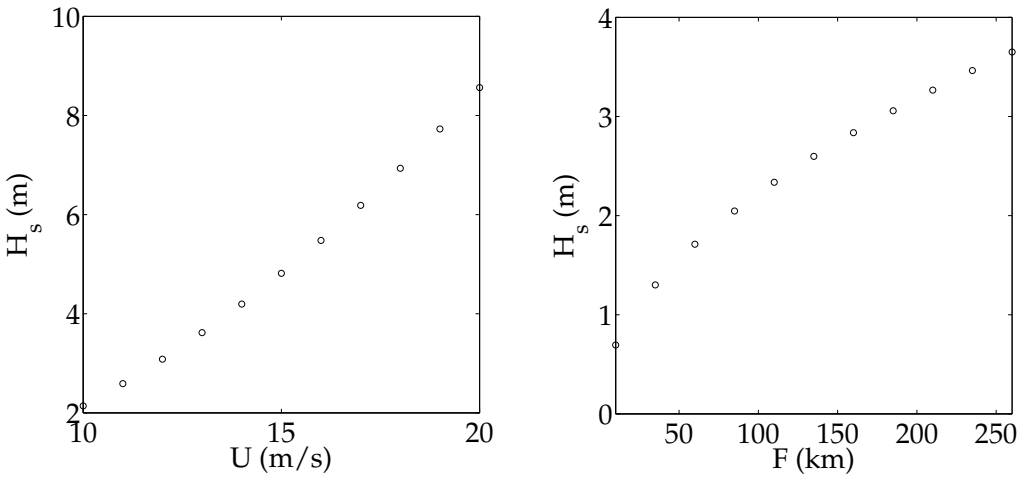

Figure 6.5: Significant wave heights of the analyzed sea states. Left panel: Pierson-Moskowitz and $\cos^2$ function. Right panel: JONSWAP and $\cos^2$ function, with fixed wind speed U=15 m/s.

for every sea state. This allowed a parametric analysis on the wind speed U, fetch length F and space domain size A only.

Note that within this Chapter, we separated Piterbarg's theorem and Forristall approximation, meaning that Piterbarg's theorem results are not modified to account for Forristall's approximation. Moreover, at this step of analysis, we focused only on the linear prediction from stochastic models, i.e. without accounting for second order correction.

6.6.1 Pierson-Moskowitz and $\cos^2$ function

Piterbarg's theorem

Following Figures show results of wave extreme analysis in the space-time domain, performed with the stochastic method of Piterbarg. Expected maximum sea surface elevation over an area $\overline{\xi}_{ST}$ and at a fixed point inside that area $\overline{\xi}_T$ were calculated according to (3.7), using (3.4) and $h_N = \sqrt{2 \log N}$, respectively. The ratio r of the expected maximum sea surface elevation over an area to that at a point was obtained as $r = \overline{\xi}_{ST}/\overline{\xi}_T$.

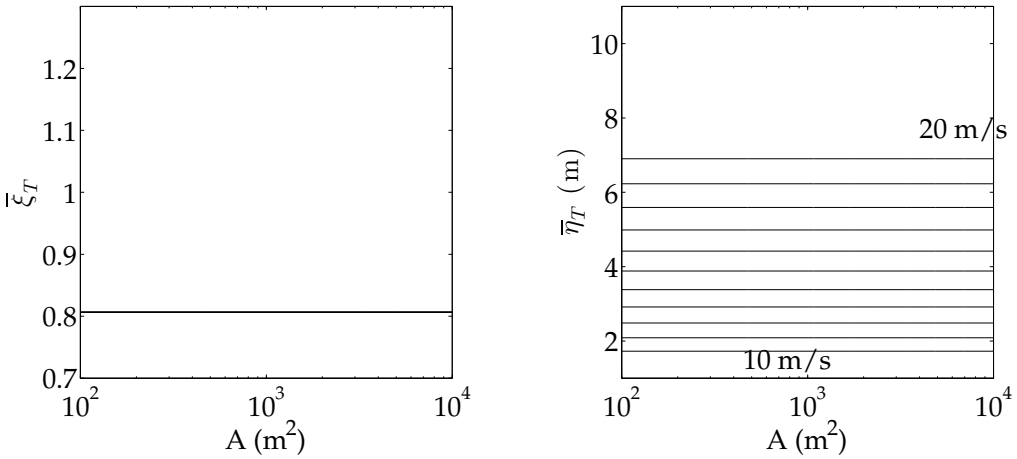

(a) (b)

Figure 6.6: *PM-Piterbarg's theorem.* Expected maximum sea surface elevation at a point as a function of area size and wind speed; semilogarithmic plot, spacing between lines: 1 m/s. (a) Normalized on the significant wave height. (b) Non-normalized.

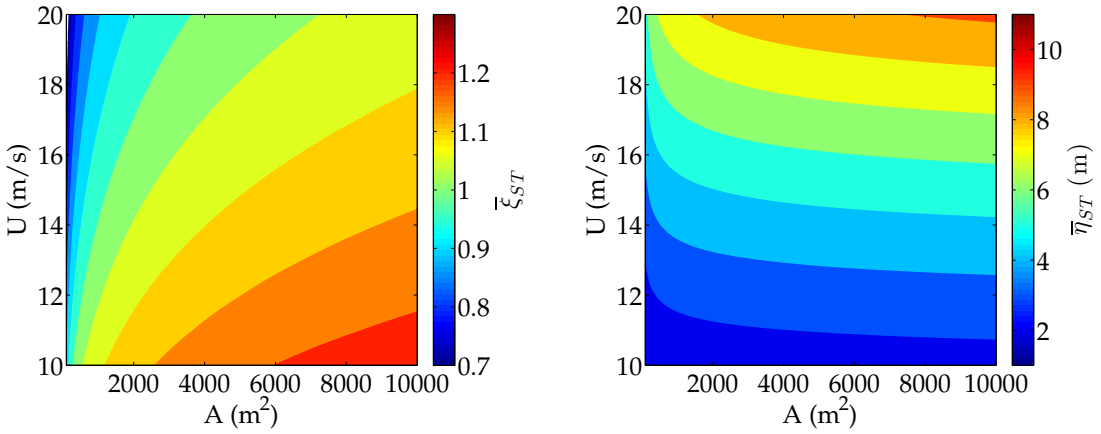

(a) (b)

Figure 6.7: *PM-Piterbarg's theorem.* Expected maximum sea surface elevation over an area as a function of area size and wind speed; contour plot, spacing between contours: 0.05. (a) Normalized on the significant wave height. (b) Non-normalized.

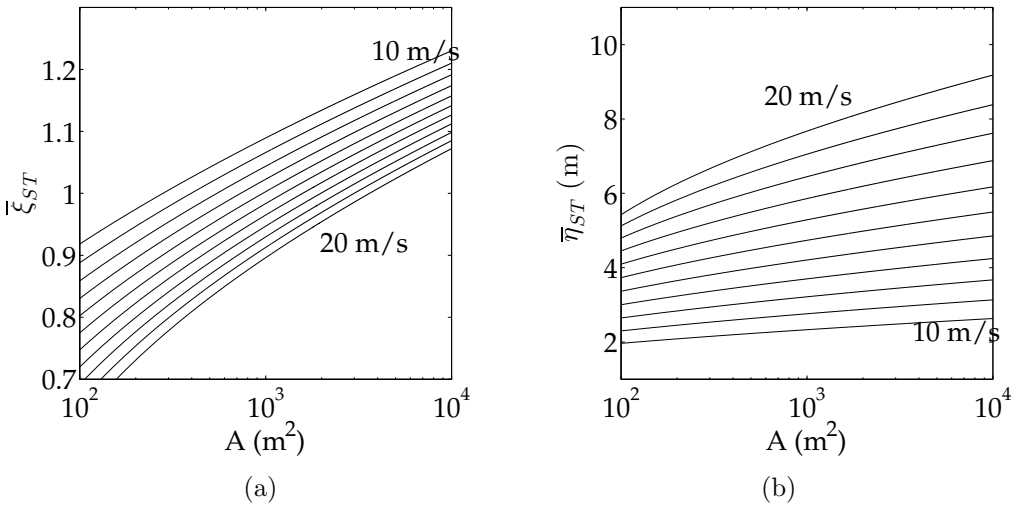

(a) (b)

Figure 6.8: *PM-Piterbarg's theorem.* Expected maximum sea surface elevation over an area as a function of area size and wind speed; semilogarithmic plot, spacing between lines: 1 m/s.(a) Normalized on the significant wave height. (b) Non-normalized.

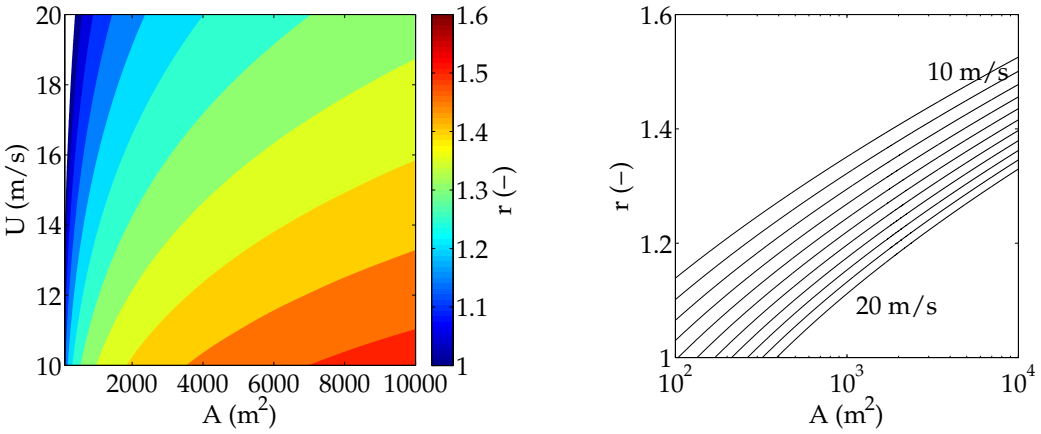

(a) (b)

Figure 6.9: *PM-Piterbarg's theorem.* Ratio of the expected maximum sea surface elevation over an area to the expected maximum at a point as a function of area size and wind speed. (a) Contour plot, spacing between contours: 0.05. (b) Semilogarithmic plot, spacing between lines: 1 m/s.

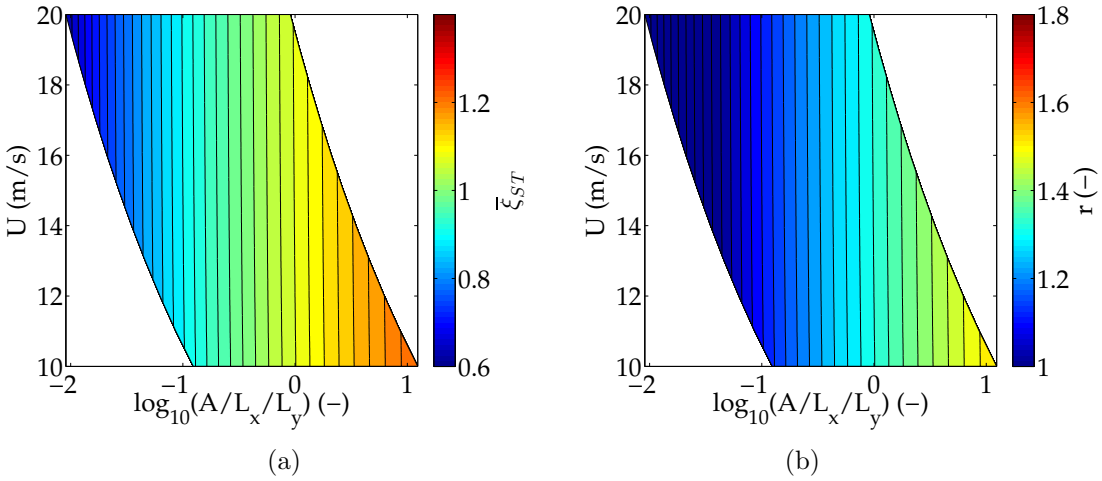

(a) (b)

Figure 6.10: *PM-Piterbarg's theorem.* Contribution of organization: A is normalized on $\overline{L}_x\overline{L}_y$ to highlight dependence upon space-time irregularity parameters α_{xt}, α_{yt}, α_{xy}. (a) Expected maximum sea surface elevation over an area, normalized on H_s. (b) Ratio of the expected maximum sea surface elevation over an area to the expected maximum at a point.

Figures show that:

- expected maximum sea surface elevation at a point $\overline{\eta}_T$ grows as wind speed increases (Figure 6.6, right panel), but obviously it does not change as area size increases (Figure 6.6). Moreover, the normalized elevation $\overline{\xi}_T$ at a point does not vary with wind speed (Figure 6.6, left panel). In the context of a linear wave model, from left panel of Figure 6.6, expected maximum wave height $\overline{H}_{max}$ at a point can be evaluated as

  $$\overline{H}_{max} = 2\overline{\eta}_T = 2 \cdot 0.81 H_s = 1.62 H_s$$

  The ratio $\overline{H}_{max}/H_s$ obtained is lower than the usual 1.8÷2.0 (Dysthe et al., 2008). The reason is that the number of waves imposed, i.e. 100, is lower than that associated to the usual ratio, i.e. 500÷1000. In both the cases the parent statistics is the Rayleigh distribution and it is sufficient to impose a number of 500 waves in time domain to recover $\overline{H}_{max}/H_s \sim 1.8$.

- expected maximum sea surface over an area $\overline{\eta}_{ST}$ grows as both wind speed and area size increase (right panels of Figure 6.7 and Figure 6.8). Normalized one, i.e. $\overline{\xi}_{ST}$, instead drops as wind speed increases and grows as area size increases (left panels of Figure 6.7 and Figure 6.8).

Indeed, referring to the left panel of Figure 6.7, taking a fixed area size and increasing wind speed the expected maximum sea surface $\overline{\xi}_{ST}$ drops since longer wavelengths yields to a smaller number of waves inside the space-time domain. If then wind speed is fixed, as the area widens $\overline{\xi}_{ST}$ grows since a bigger number of constant wavelength waves is contained inside the space-time domain.
The expected maximum wave height $\overline{H}_{max}$ can be evaluated in the context of a linear wave model

$$10 \text{ m/s: } \overline{H}_{max} = 2\overline{\eta}_{ST} = 2 \cdot 1.22 H_s = 2.44 H_s$$
$$20 \text{ m/s: } \overline{H}_{max} = 2\overline{\eta}_{ST} = 2 \cdot 1.06 H_s = 2.12 H_s$$

with values at $A = 10^4$ m^2. Even with a relatively low number of waves in the time domain, the ratios $\overline{H}_{max}/H_s$ exceed the usual $1.8 \div 2.0$ ratio (Dysthe et al., 2008).

- the ratio r of the maximum expected sea surface over an area to the maximum at a point drops as wind speed increases and grows as area increases (Figure 6.9). This is a natural consequence of $\overline{\xi}_T$ being constant over wind speed and area size and of the described dependence of $\overline{\xi}_{ST}$. In fact, left and right panel of (Figure 6.9) are strongly consistent with left panel of Figure 6.7 and left panel of Figure 6.8, respectively.

- variations of $\overline{\xi}_{ST}$ and r are mainly due to changes of $\overline{T}$, $\overline{L}_x$ and $\overline{L}_x$. In fact, contribution of organization of the wave field, through space-time irregularity parameters, is less effective (Figure 6.10). This is reasonable, since variations of wind speed U affect frequency spectrum, while directional distribution, which was showed to be responsible for effects on irregularity parameters, didn't change.

Forristall's approximation for small areas

Piterbarg's analysis was also performed according to Forristall's approximation for small areas (3.10). Following Figures contain expected maximum sea surface elevations (3.7) over an area and at a fixed point, calculated according to Forristall (black lines) while $X < \overline{L}_x$ and according to Piterbarg while $X \geq \overline{L}_x$.

Figures show that for areas smaller than a wavelength, both the expected maximum over an area $\overline{\xi}_{ST}$ (Figure 6.12) and the ratio r (Figure 6.13) increased with respect to Piterbarg's theorem results. This is due to the asymptotic character of Piterbarg's theorem, which works for large number of waves, i.e. for large areas. Moreover, Forristall's approximation assumes the maximum could occur on the area side.

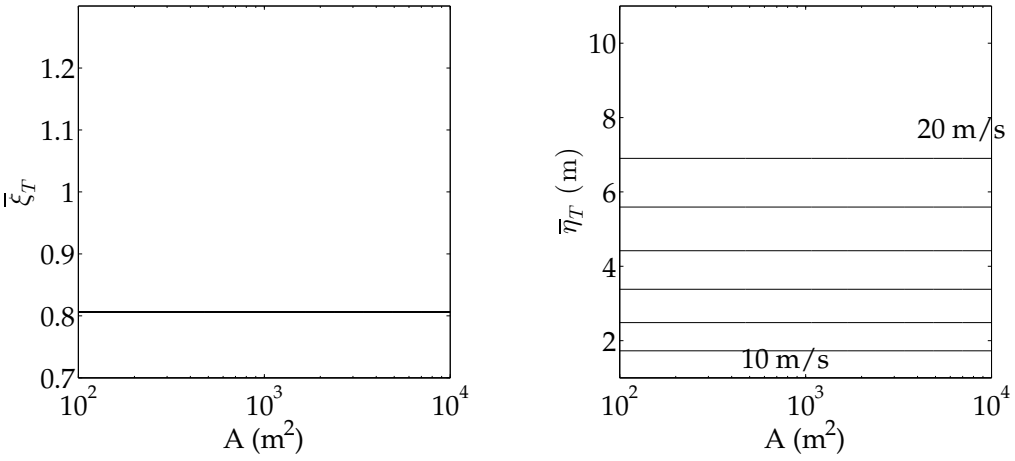

Figure 6.11: *PM-Forristall's approximation.* Expected maximum sea surface elevation at a point as a function of area size and wind speed; semilogarithmic plot, spacing between lines: 2 m/s. (a) Normalized on the significant wave height. (b) Non-normalized.

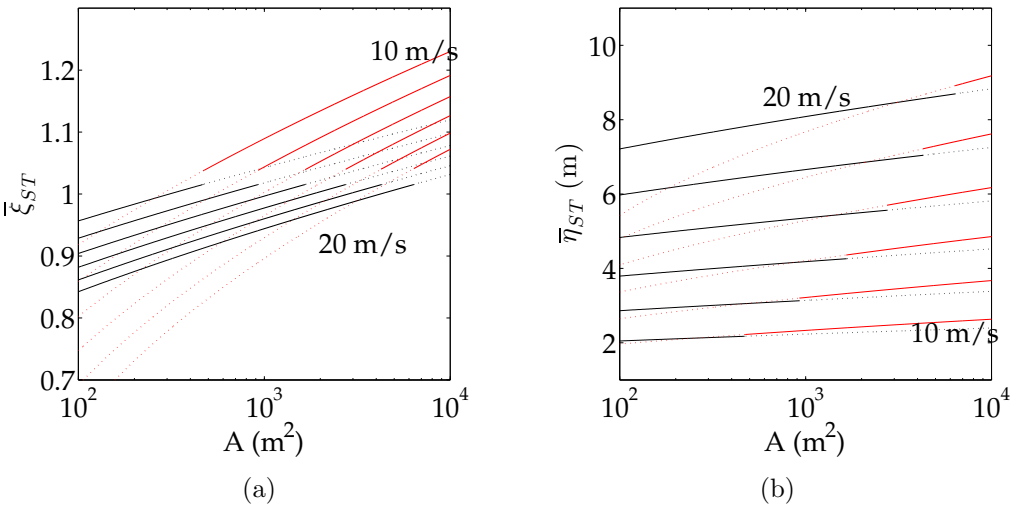

Figure 6.12: *PM-Forristall's approximation.* Expected maximum sea surface elevation over an area as a function of area size and wind speed; semilogarithmic plot, spacing between lines: 2 m/s. Forristall's approximation (black) is used while $X < \overline{L}_x$; over, Piterbarg's theorem (red) is applied. (a) Normalized on the significant wave height. (b) Non-normalized.

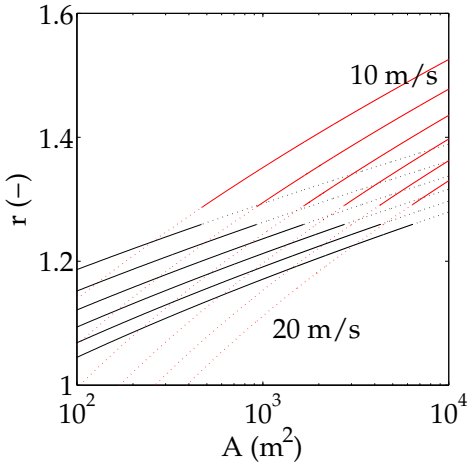

Figure 6.13: *PM-Forristall's approximation.* Ratio of the expected maximum sea surface elevation over an area to the expected maximum at a point as a function of area size and wind speed, semilogarithmic plot, spacing between lines: 2 m/s. Forristall's approximation (black) is used while $X < \overline{L}_x$; over, Piterbarg's theorem (red) is applied.

Fedele's method

Following Figures show results of wave extreme analysis in the space-time domain, performed with the stochastic method of Fedele. Expected maximum sea surface elevation over an area $\overline{\xi}_{ST}$ and at a fixed point inside that area $\overline{\xi}_T$ are calculated according to (3.18) and (3.20) respectively. The ratio r of the expected maximum sea surface elevation over an area to that at a point was obtained as $\overline{\xi}_{ST}/\overline{\xi}_T$.

Figures show that:

- expected maximum sea surface at a point $\overline{\eta}_T$ grows as wind speed increases (Figure 6.14, right panel), but obviously it does not change as area size increases (Figure 6.14). Moreover, the normalized maximum sea surface elevation at a point $\overline{\xi}_T$ does not vary with wind speed (Figure 6.14, left panel). In the context of a linear wave model, from the left panel of Figure 6.14, expected maximum wave height $\overline{H}_{max}$ at a point can be evaluated as

$$\overline{H}_{max} = 2\overline{\eta}_T = 2 \cdot 0.81 H_s = 1.62 H_s$$

  The ratio $\overline{H}_{max}/H_s$ obtained is lower than the usual 1.8÷2.0 (Dysthe et al., 2008). The reason is that the number of waves imposed, i.e. 100, was lower than that associated to the usual ratio, i.e. 500÷1000. In both the cases the parent statistics is the Rayleigh distribution and it

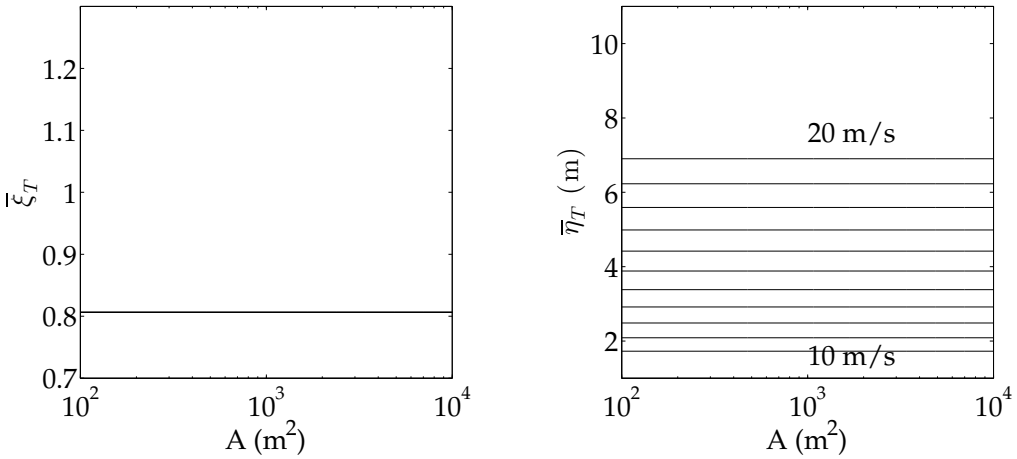

Figure 6.14: *PM-Fedele's method.* Expected maximum sea surface elevation at a point as a function of area size and wind speed; semilogarithmic plot, spacing between lines: 1 m/s. (a) Normalized on the significant wave height. (b) Non-normalized.

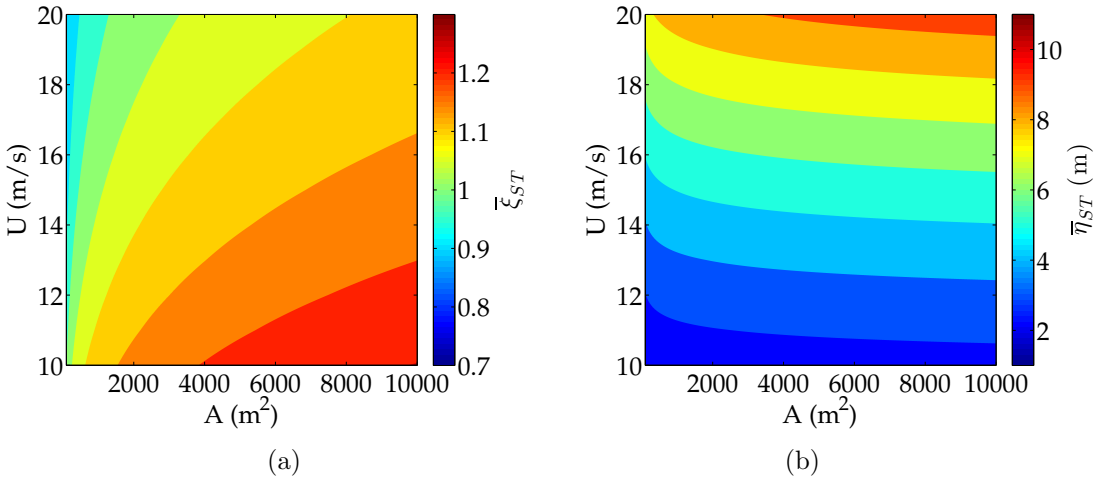

Figure 6.15: *PM-Fedele's method.* Expected maximum sea surface elevation over an area as a function of area size and wind speed; contour plot, spacing between contours: 0.05. (a) Normalized on the significant wave height. (b) Non-normalized.

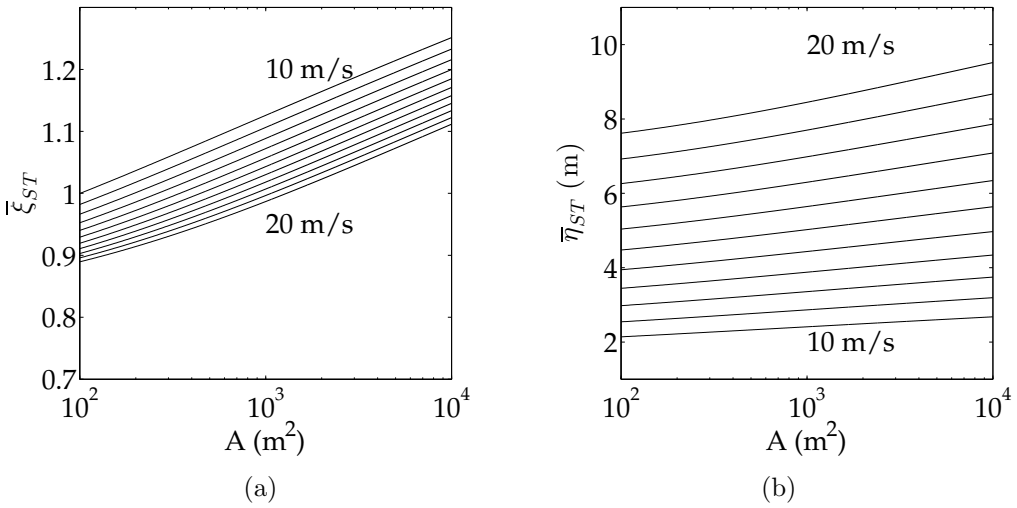

(a) (b)

Figure 6.16: *PM-Fedele's method.* Expected maximum sea surface elevation over an area as a function of area size and wind speed; semilogarithmic plot, spacing between lines: 1 m/s. (a) Normalized on the significant wave height. (b) Non-normalized.

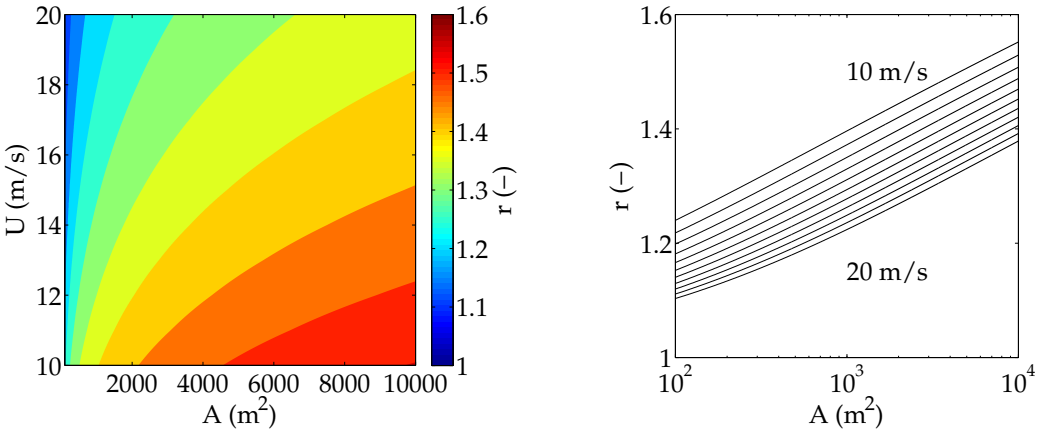

(a) (b)

Figure 6.17: *PM-Fedele's method.* Ratio of the expected maximum sea surface elevation over an area to the expected maximum at a point as a function of area size and wind speed. (a) Contour plot, spacing between contours: 0.05. (b) Semilogarithmic plot, spacing between lines: 1 m/s.

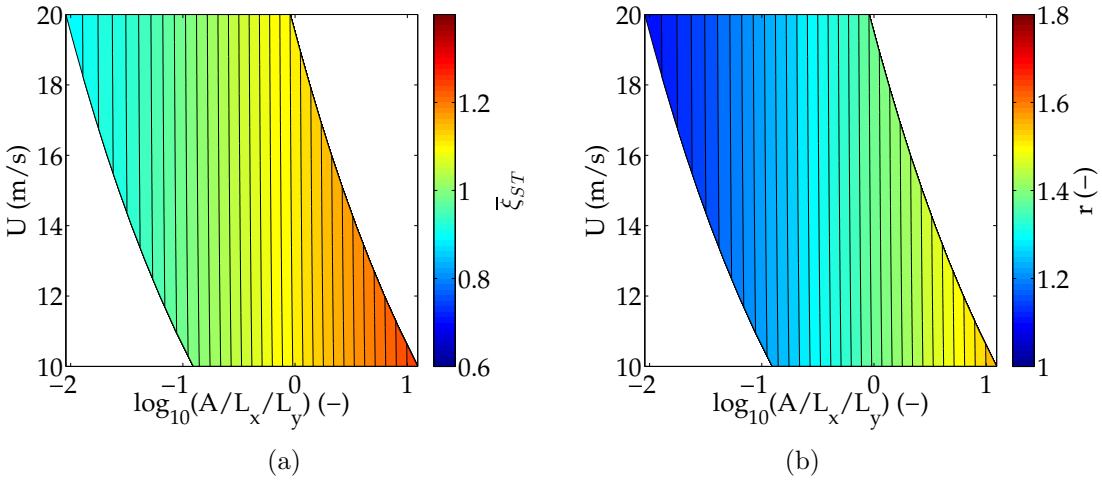

Figure 6.18: *PM-Fedele's method.* Contribution of organization: A is normalized on $\overline{L}_x\overline{L}_y$ to highlight dependence upon space-time irregularity parameters α_{xt}, α_{yt}, α_{xy}. (a) Expected maximum sea surface elevation over an area, normalized on H_s. (b) Ratio of the expected maximum sea surface elevation over an area to the expected maximum at a point.

is sufficient to impose a number of 500 waves in time domain to recover $\overline{H}_{max}/H_s \sim 1.8$. Note that the same result was obtained performing Piterbarg's analysis, as expected.

- expected maximum sea surface over an area $\overline{\eta}_{ST}$ grows as both wind speed and area size increase (right panels of Figure 6.15 and Figure 6.16). If normalized, i.e. $\overline{\xi}_{ST}$, it drops as wind speed increases and grows as area size increases (left panels of Figure 6.15 and Figure 6.16). In the context of a linear wave model, expected maximum wave height $\overline{H}_{max}$ can be evaluated as

$$10 \text{ m/s: } \overline{H}_{max} = 2\overline{\eta}_{ST} = 2 \cdot 1.25 H_s = 2.50 H_s$$
$$20 \text{ m/s: } \overline{H}_{max} = 2\overline{\eta}_{ST} = 2 \cdot 1.11 H_s = 2.22 H_s$$

  with values at $A = 10^4$ m^2. Even with a relatively low number of waves in the time domain, the ratios $\overline{H}_{max}/H_s$ exceed the usual 1.8÷2.0 ratio (Dysthe et al., 2008). We observed that expected maximum wave heights herein obtained are slightly higher than those predicted by Piterbarg's theorem. This is due to the contribution of the space-time domain boundaries.

- the ratio r of the maximum expected sea surface over an area to the

maximum at a point drops as wind speed increases and grows as area increases (Figure 6.17).

- variations of $\overline{\xi}_{ST}$ and r are mainly due to changes of $\overline{T}$, $\overline{L}_x$ and $\overline{L}_x$. In fact, contribution of organization of the wave field, through space-time irregularity parameters, is less effective (Figure 6.18). This is reasonable, since variations of wind speed U affect frequency spectrum, while directional distribution didn't change.

If we compare results from Piterbarg's and Fedele's method we observe that:

- predicted expected maxima at a fixed point $\overline{\xi}_T$ are equal among the two methods; this is obvious since both methods estimate time maxima from the same distribution, i.e. Rayleigh for wave crests, taking the same number of waves, i.e. $N = D/\overline{T}$;

- Fedele's method globally predicts higher expected maximum surface elevations $\overline{\xi}_{ST}$ and higher ratios r than Piterbarg's theorem; the reason is the correction in Fedele's method to account for the boundaries of the space-time domain;

- major differences between the two methods results occur at small areas. In fact, Piterbarg's theorem states the "asymptotic" distribution of maxima of a Gaussian random field, meaning it works fine for large number of waves N, or equivalently, for large areas A. As a matter of fact, Piterbarg's theorem does not work for areas whose side is smaller than the average wavelength. On the contrary, splitting the number of waves calculation over space-time domain and its boundaries, Fedele's method allows performing the analysis even if the area side is smaller than a wavelength. Figure 6.19 shows the ratio of the expected maximum sea surface elevations over an area calculated by Piterbarg's and Fedele's method, respectively. As the number of waves increases, i.e. area widens or wind speed decreases, differences tend to cancel and the ratio tends to 1.

Figure 6.20 compare results of the different performed methods for a $U = 10$ m/s wind speed. For both $\overline{\xi}_{ST}$ and r, we observe that differences between Fedele's and Piterbarg's theorems decrease at large areas, while differences between Fedele's method and Forristall's approximation decreases at small areas. This confirms the wider range of application of Fedele's method. Finally, we observed that Fedele's method predicts higher sea surface elevations and ratios for all the analyzed areas. This is due to the boundary

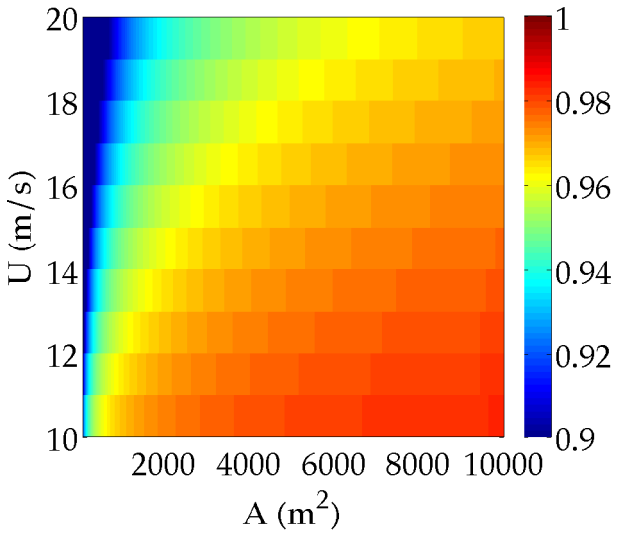

Figure 6.19: Expected maximum sea surface elevation over an area as a function of area size and wind speed. Ratio of the maximum calculated by Piterbarg's theorem ($\overline{\xi}_{ST,K}$) to that calculated by Fedele's method($\overline{\xi}_{ST,F}$).

correction, included to account for possible occurrencies of maxima over the boundaries of the space-time domain.

6.6.2 JONSWAP and cos^2 function

Piterbarg's theorem

Following Figures show results of wave extreme analysis in the space-time domain, performed with the stochastic method of Piterbarg. Expected maximum sea surface elevation over an area $\overline{\xi}_{ST}$ and at a fixed point inside that area $\overline{\xi}_T$ were calculated according to (3.7), using (3.4) and $h_N = \sqrt{2\log N}$, respectively. The ratio r of the expected maximum sea surface elevation over an area to that at a point was obtained as $r = \overline{\xi}_{ST}/\overline{\xi}_T$.

Figures show that:

- expected maximum sea surface at a point $\overline{\eta}_T$ grows as fetch length increases (Figure 6.21, right panel), but obviously it does not change as area size increases (Figure 6.21). Moreover, the normalized maximum sea surface elevation at a point $\overline{\xi}_T$ does not vary with fetch length (Figure 6.21, left panel). In the context of a linear wave model, from left panel of Figure 6.21, expected maximum wave height $\overline{H}_{max}$ at a point can be evaluated

$$\overline{H}_{max} = 2\overline{\eta}_T = 2 \cdot 0.81 H_s = 1.62 H_s$$

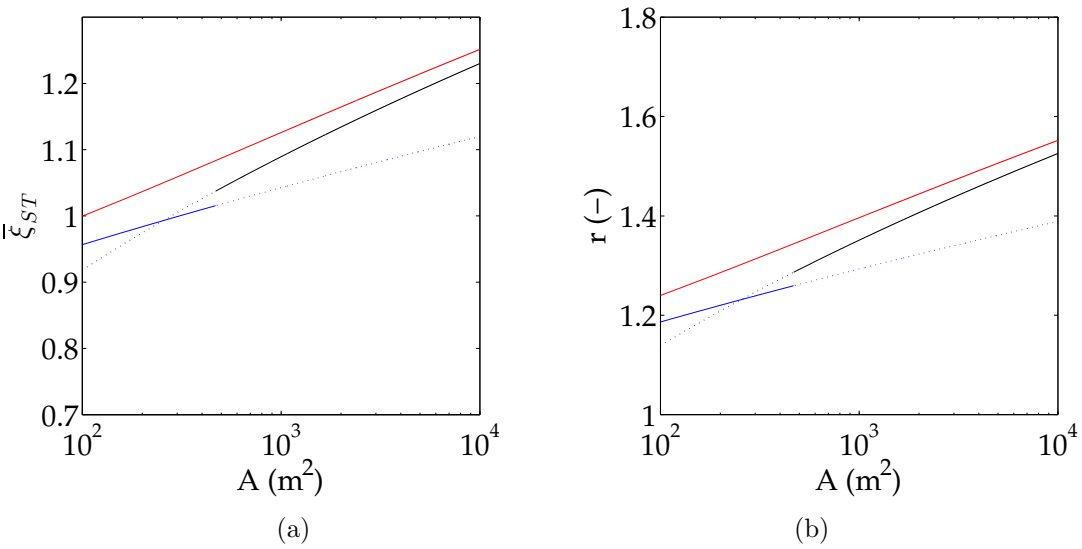

(a) (b)

Figure 6.20: Comparison among methods, assuming wind speed $U = 10$ m/s: Piterbarg (black), Forristall (blue), Fedele (red). Change between dotted and solid lines occurs where $X = \overline{L}_x$. (a) Expected maximum sea surface elevation over an area, normalized on H_s. (b) Ratio of the expected maximum sea surface elevation over an area to the expected maximum at a point.

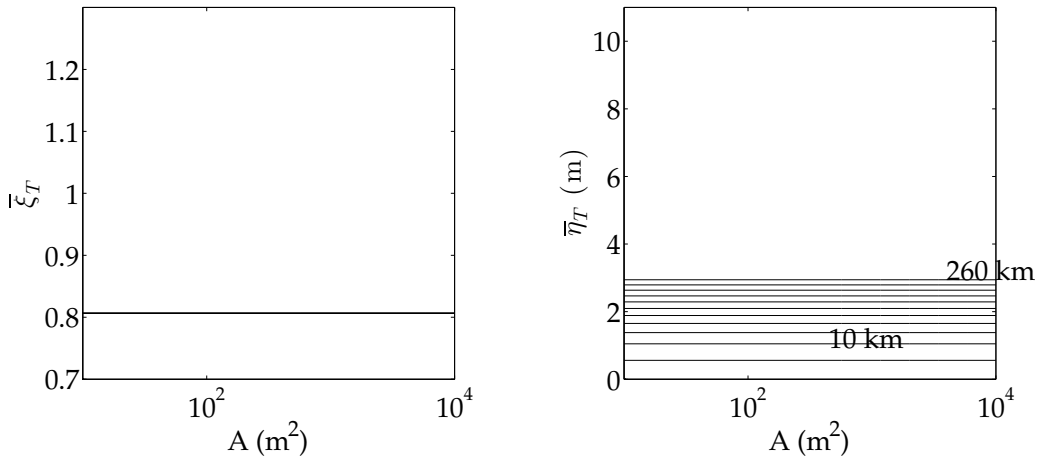

(a) (b)

Figure 6.21: *JON-Piterbarg's theorem.* Expected maximum sea surface elevation at a point as a function of area size and fetch length (wind speed $U = 15$ m/s); semilogarithmic plot, spacing between lines: 25 km. (a) Normalized on the significant wave height. (b) Non-normalized.

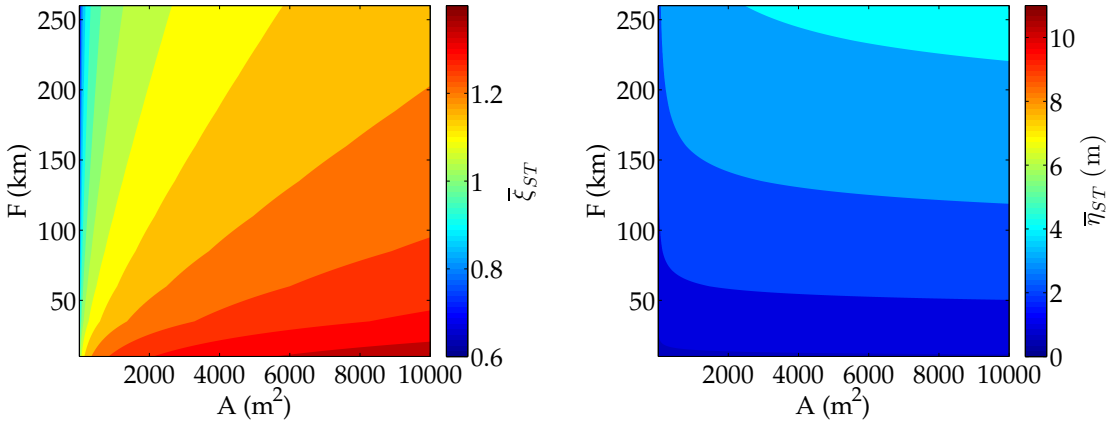

(a) (b)

Figure 6.22: *JON-Piterbarg's theorem.* Expected maximum sea surface elevation over an area as a function of area size and fetch length (wind speed $U = 15$ m/s); contour plot, spacing between contours: 0.05. (a) Normalized on the significant wave height. (b) Non-normalized.

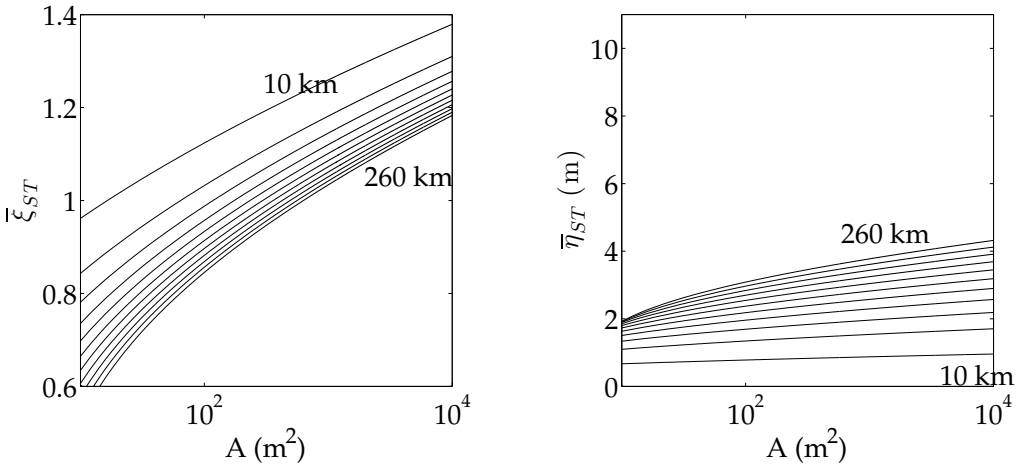

(a) (b)

Figure 6.23: *JON-Piterbarg's theorem.* Expected maximum sea surface elevation over an area as a function of area size and fetch length (wind speed $U = 15$ m/s); semilogarithmic plot, spacing between lines: 25 km. (a) Normalized on the significant wave height. (b) Non-normalized.

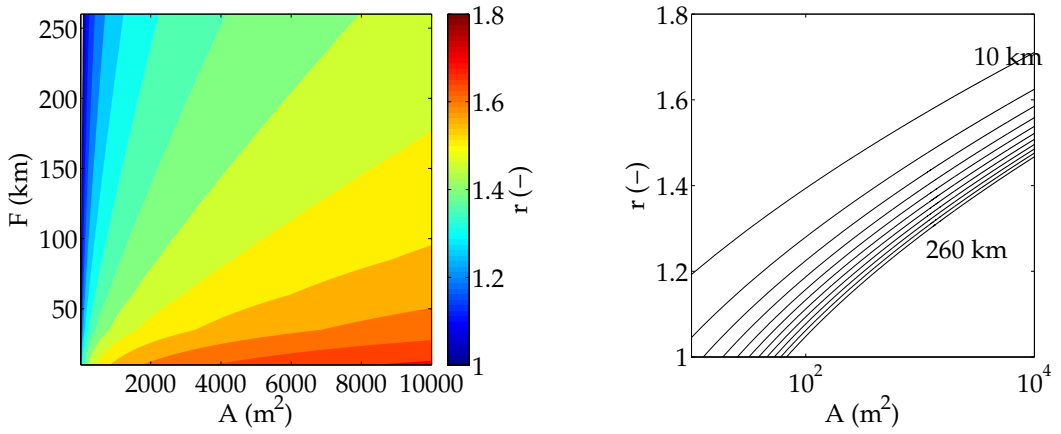

(a) (b)

Figure 6.24: *JON-Piterbarg's theorem.* Ratio of the expected maximum sea surface elevation over an area to the expected maximum at a point as a function of area size and fetch length (wind speed $U = 15$ m/s). (a) Contour plot, spacing between contours: 0.05. (b) Semilogarithmic plot, spacing between lines: 25 km.

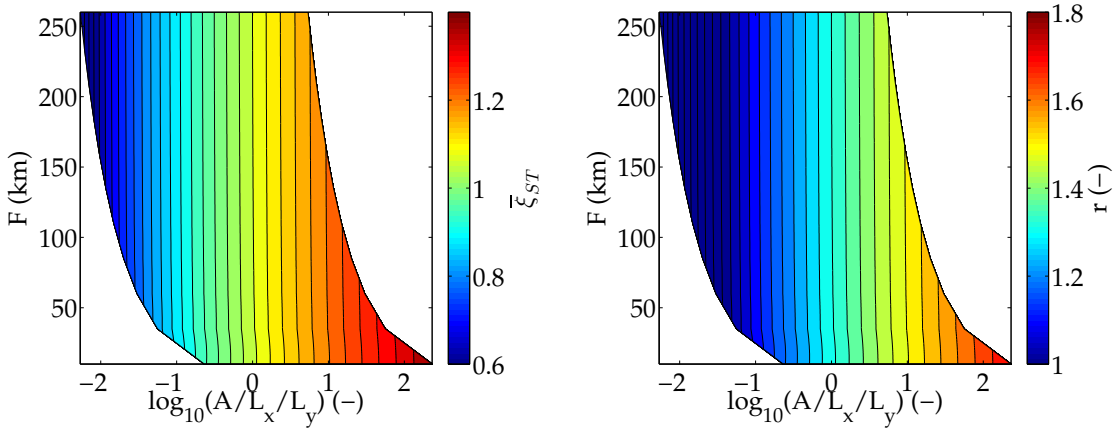

(a) (b)

Figure 6.25: *JON-Piterbarg's theorem.* Contribution of organization: A is normalized on $\overline{L}_x\overline{L}_y$ to highlight dependence upon space-time irregularity parameters α_{xt}, α_{yt}, α_{xy}. (a) Expected maximum sea surface elevation over an area, normalized on H_s. (b) Ratio of the expected maximum sea surface elevation over an area to the expected maximum at a point.

The ratio $\overline{H}_{max}/H_s$ obtained is lower than the usual 1.8÷2.0 (Dysthe et al., 2008). The reason is that the number of waves imposed, i.e. 100, was lower than that associated to the usual ratio, i.e. 500÷1000. In both the cases the parent statistics is the Rayleigh distribution and it is sufficient to impose a number of 500 waves in time domain to recover $\overline{H}_{max}/H_s \sim 1.8$.

- expected maximum sea surface over an area $\overline{\eta}_{ST}$ grows as both fetch length and area size increase (right panels of Figure 6.22 and Figure 6.23). Normalized one, i.e. $\overline{\xi}_{ST}$, instead drops as fetch length increases and grows as area size increases (left panels of Figure 6.22 and Figure 6.23). Indeed, referring to the left panel of Figure 6.7, taking a fixed area size and increasing fetch length the expected maximum sea surface $\overline{\xi}_{ST}$ drops since longer wavelengths yields to a smaller number of waves inside the space-time domain. If then fetch length is fixed, as the area widens $\overline{\xi}_{ST}$ grows since a bigger number of constant wavelength waves is contained inside the space-time domain.
  The expected maximum wave height $\overline{H}_{max}$ can be evaluated in the context of a linear wave model

$$\begin{aligned} 10 \text{ km: } \overline{H}_{max} &= 2\overline{\eta}_{ST} = 2 \cdot 1.38 H_s = 2.76 H_s \\ 260 \text{ km: } \overline{H}_{max} &= 2\overline{\eta}_{ST} = 2 \cdot 1.18 H_s = 2.36 H_s \end{aligned}$$

  with values at $A = 10^4$ m^2. Even with a relatively low number of waves in the time domain, the ratios $\overline{H}_{max}/H_s$ exceed the usual 1.8÷2.0 ratio (Dysthe et al., 2008).

- the ratio r of the maximum expected sea surface over an area to the maximum at a point drops as fetch length increases and grows as area increases (Figure 6.24). This is a natural consequence of $\overline{\xi}_T$ being constant over fetch length and area size and of the described dependence of $\overline{\xi}_{ST}$. In fact, left and right panel of (Figure 6.24) are strongly consistent with left panel of Figure 6.22 and left panel of Figure 6.23, respectively.

- variations of $\overline{\xi}_{ST}$ and r are mainly due to changes of $\overline{T}$, $\overline{L}_x$ and $\overline{L}_x$. In fact, contribution of organization of the wave field, through space-time irregularity parameters, is less effective (Figure 6.25). This is reasonable, since variations of fetch length F affect frequency spectrum, while directional distribution doesn't change.

Compared to Pierson-Moskowitz based directional spectra, results of Piterbarg's analysis are higher in terms of both expected maximum over an area

$\overline{\xi}_{ST}$ and ratio r. This is consistent with the sea state represented, i.e. a developing sea with shorter wavelengths and shorter wave crests with respect to a fully developed sea state. Thus, there is a greater number of waves inside the space-time domain.

Forristall's approximation for small areas

Piterbarg's analysis was also performed according to Forristall's approximation for small areas (3.10). Following Figures contain expected maximum sea surface elevations (3.7) over an area $\overline{\xi}_{ST}$ and at a fixed point $\overline{\xi}_T$, calculated according to Forristall (black lines) while $X < \overline{L}_x$ and according to Piterbarg while $X \geq \overline{L}_x$.

Figures show that for areas smaller than a wavelength, both the expected maximum over an area $\overline{\xi}_{ST}$ (Figure 6.27) and the ratio r (Figure 6.28) increase with respect to Piterbarg's theorem results. This is due to the asymptotic character of Piterbarg's theorem, which works for large number of waves, i.e. for large areas. Moreover, Forristall's approximation assumes the maximum occurs on the area side.

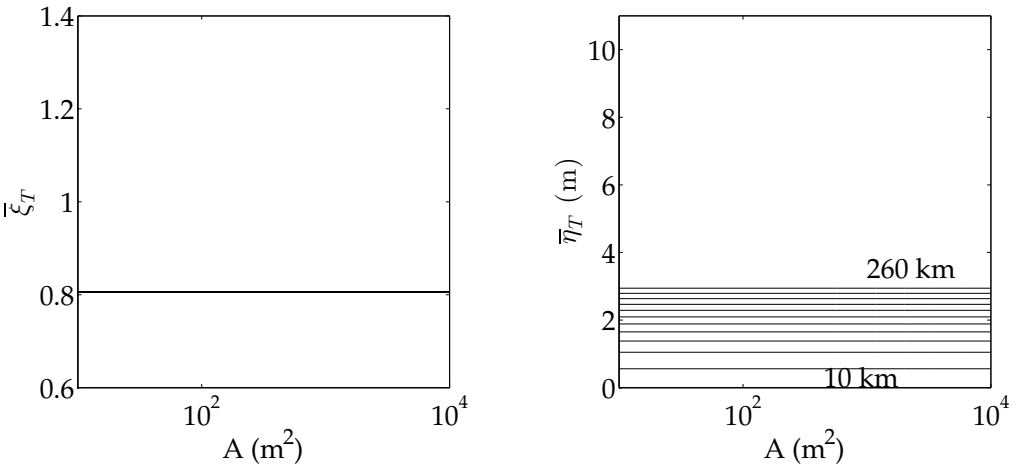

Figure 6.26: *JON-Forristall's approximation.* Expected maximum sea surface elevation at a point as a function of area size and wind speed; semilogarithmic plot, spacing between lines: 25 km. (a) Normalized on the significant wave height. (b) Non-normalized.

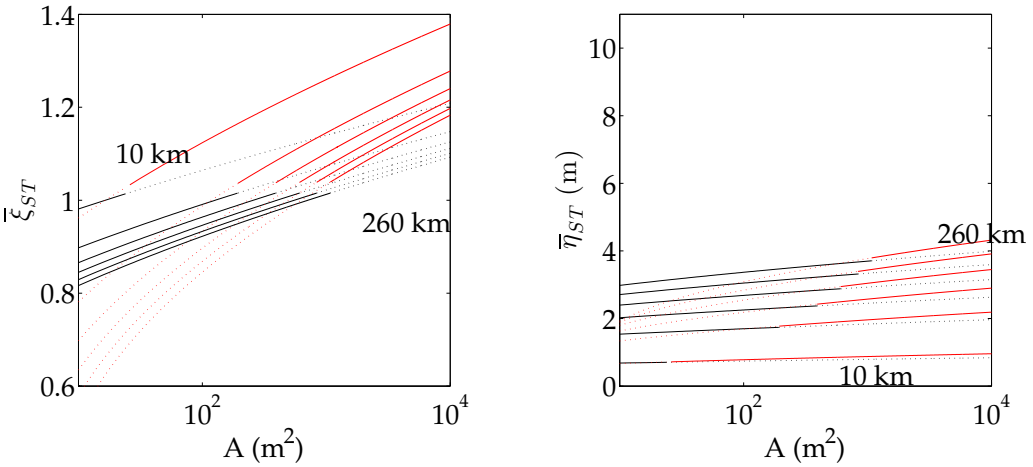

Figure 6.27: *JON-Forristall's approximation.* Expected maximum sea surface elevation over an area as a function of area size and wind speed; semilogarithmic plot, spacing between lines: 25 km. Forristall's approximation (black) is used while $X < \overline{L}_x$; over, Piterbarg's theorem (red) is applied. (a) Normalized on the significant wave height. (b) Non-normalized.

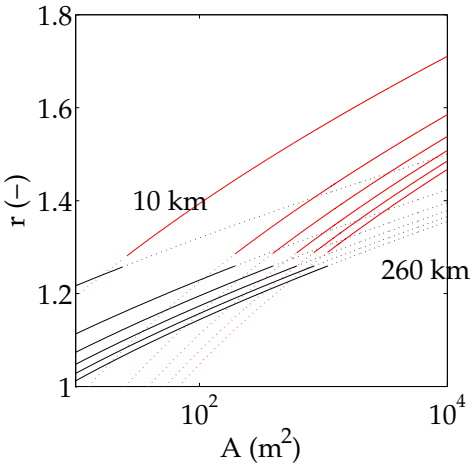

Figure 6.28: *JON-Forristall's approximation.* Ratio of the expected maximum sea surface elevation over an area to the expected maximum at a point as a function of area size and wind speed, semilogarithmic plot, spacing between lines: 25 km. Forristall's approximation (black) is used while $X < \overline{L}_x$; over, Piterbarg's theorem (red) is applied.

Fedele's method

Following Figures show results of wave extreme analysis in the space-time domain, performed with the stochastic method of Fedele. Expected maximum sea surface elevation over an area $\overline{\xi}_{ST}$ and at a fixed point inside that area $\overline{\xi}_T$ were calculated according to (3.18) and (3.20) respectively. The ratio r of the expected maximum sea surface elevation over an area to that at a point was obtained as $r = \overline{\xi}_{ST}/\overline{\xi}_T$.

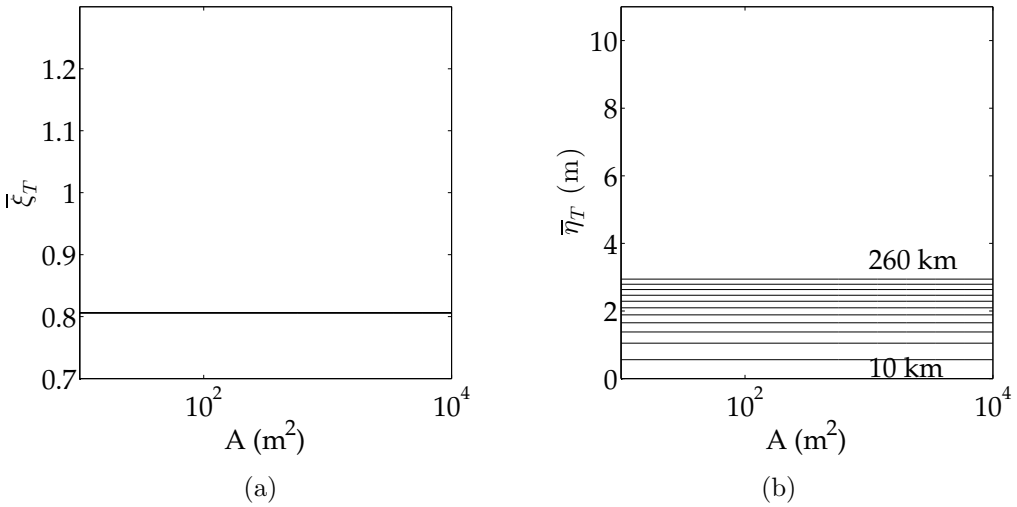

Figure 6.29: *JON-Fedele's method.* Expected maximum sea surface elevation at a point as a function of area size and fetch length (wind speed $U = 15$ m/s); semilogarithmic plot, spacing between lines: 25 km. (a) Normalized on the significant wave height. (b) Non-normalized.

Figures show that:

- expected maximum sea surface at a point $\overline{\eta}_T$ grows as fetch length increases (Figure 6.29, right panel), but obviously it does not change as area size increases (Figure 6.29). Moreover, the normalized maximum sea surface elevation at a point $\overline{\xi}_T$ does not vary with fetch length (Figure 6.29, left panel). In the context of a linear wave model, from the left panel of Figure 6.29, expected maximum wave height $\overline{H}_{max}$ at a point can be evaluated as

$$\overline{H}_{max} = 2\overline{\eta}_T = 2 \cdot 0.81 H_s = 1.62 H_s$$

The ratio $\overline{H}_{max}/H_s$ obtained is lower than the usual 1.8÷2.0 (Dysthe et al., 2008). The reason is that the number of waves imposed, i.e. 100,

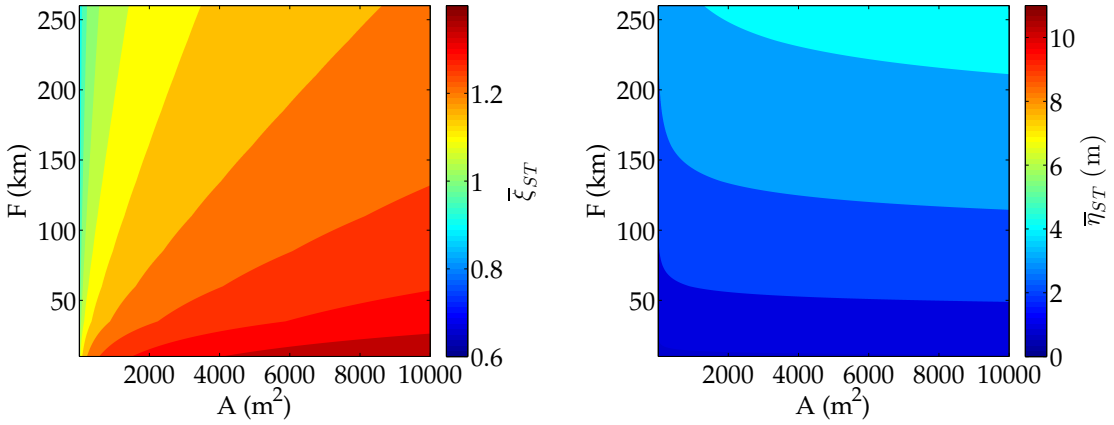

(a) (b)

Figure 6.30: *JON-Fedele's method.* Expected maximum sea surface elevation over an area as a function of area size and fetch length (wind speed $U = 15$ m/s); contour plot, spacing between contours: 0.05. (a) Normalized on the significant wave height. (b) Non-normalized.

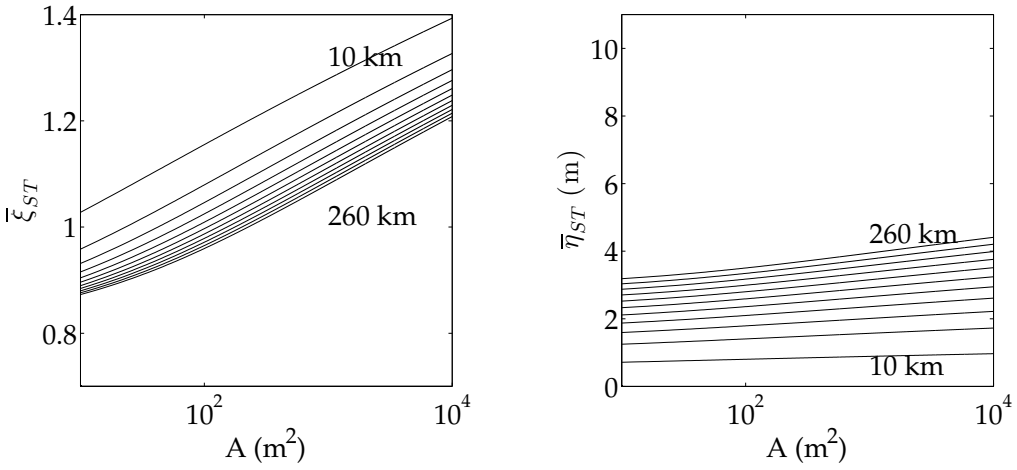

(a) (b)

Figure 6.31: *JON-Fedele's method.* Expected maximum sea surface elevation over an area as a function of area size and fetch length (wind speed $U = 15$ m/s); semilogarithmic plot, spacing between lines: 25 km. (a) Normalized on the significant wave height. (b) Non-normalized.

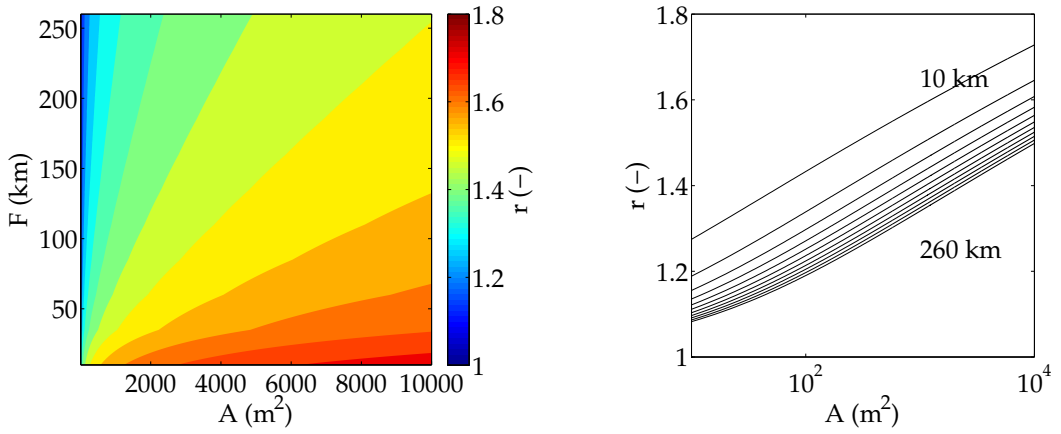

Figure 6.32: *JON-Fedele's method.* Ratio of the expected maximum sea surface elevation over an area to the expected maximum at a point as a function of area size and fetch length (wind speed $U = 15$ m/s). (a) Contour plot, spacing between contours: 0.05. (b) Semilogarithmic plot, spacing between lines: 25 km.

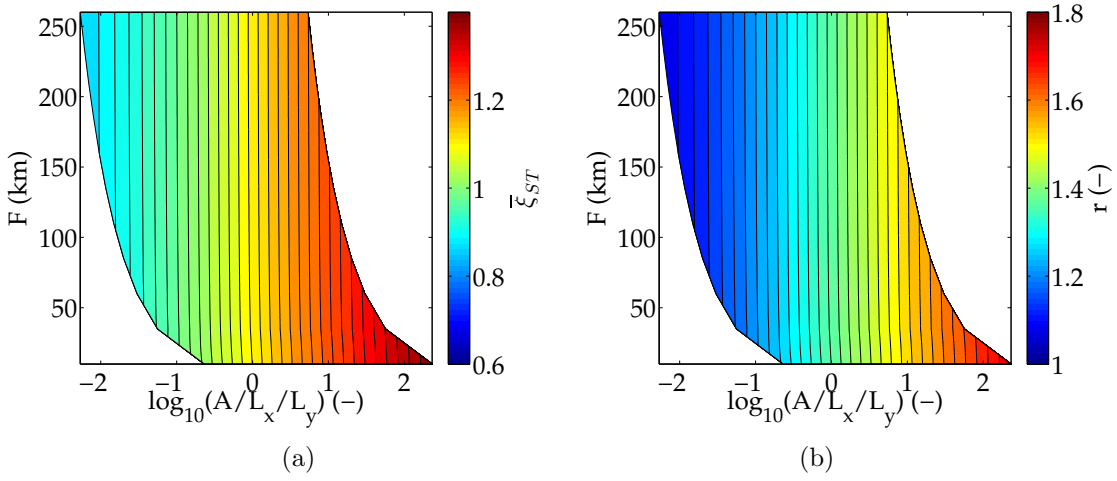

Figure 6.33: *JON-Fedele's method.* Contribution of organization: A is normalized on $\overline{L}_x\overline{L}_y$ to highlight dependence upon space-time irregularity parameters α_{xt}, α_{yt}, α_{xy}. (a) Expected maximum sea surface elevation over an area, normalized on H_s. (b) Ratio of the expected maximum sea surface elevation over an area to the expected maximum at a point.

was lower than that associated to the usual ratio, i.e. 500÷1000. In both the cases the parent statistics is the Rayleigh distribution and it is sufficient to impose a number of 500 waves in time domain to recover $\overline{H}_{max}/H_s \sim 1.8$. Note that the same result was obtained performing Piterbarg's analysis, as expected.

- expected maximum sea surface over an area $\overline{\eta}_{ST}$ grows as both fetch length and area size increase (right panels of Figure 6.30 and Figure 6.31). If normalized, i.e. $\overline{\xi}_{ST}$, it drops as fetch length increases and grows as area size increases (left panels of Figure 6.30 and Figure 6.31). In the context of a linear wave model, expected maximum wave height $\overline{H}_{max}$ can be evaluated as

$$\begin{aligned} 10 \text{ km: } \overline{H}_{max} &= 2\overline{\eta}_{ST} = 2 \cdot 1.39 H_s = 2.78 H_s \\ 260 \text{ km: } \overline{H}_{max} &= 2\overline{\eta}_{ST} = 2 \cdot 1.21 H_s = 2.42 H_s \end{aligned}$$

  with values at $A = 10^4$ m^2. Even with a relatively low number of waves in the time domain, the ratios $\overline{H}_{max}/H_s$ exceed the usual 1.8÷2.0 ratio (Dysthe et al., 2008). We observe that expected maximum wave heights herein obtained are slightly higher than those predicted by Piterbarg's theorem. This is due to the contribution of the space-time domain boundaries.

- the ratio of the maximum expected sea surface over an area to the maximum at a point drops as fetch length increases and grows as area increases (Figure 6.32).

- variations of $\overline{\xi}_{ST}$ and r are mainly due to changes of $\overline{T}$, $\overline{L}_x$ and $\overline{L}_x$. In fact, contribution of organization of the wave field, through space-time irregularity parameters, is less effective (Figure 6.33). This is reasonable, since variations of fetch length F affect frequency spectrum, while directional distribution doesn't change.

If we compare results from Piterbarg's and Fedele's method we observe that:

- predicted expected maxima at a fixed point $\overline{\xi}_T$ are equal among the two methods; this is obvious since both methods estimate time maxima from the same distribution, i.e. Rayleigh for wave crests, taking the same number of waves, i.e. $N = D/\overline{T}$;

- Fedele's method globally predicts higher expected maximum surface elevations $\overline{\xi}_{ST}$ and higher ratios r than Piterbarg's theorem; the reason

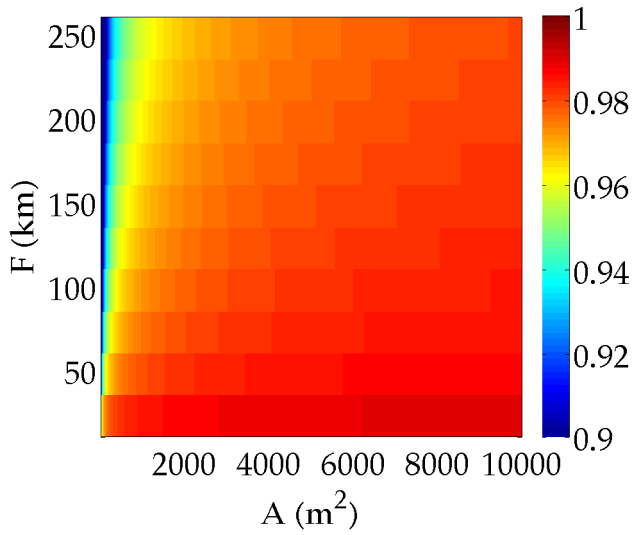

Figure 6.34: Expected maximum sea surface elevation over an area as a function of area size and fetch length . Ratio of the maximum calculated by Piterbarg's theorem ($\overline{\xi}_{ST,K}$) to that calculated by Fedele's method($\overline{\xi}_{ST,F}$).

is the correction in Fedele's method to account for the boundaries of the space-time domain;

- major differences between the two methods results occur at small areas. In fact, Piterbarg's theorem states the "asymptotic" distribution of maxima of a Gaussian random field, meaning it works fine for large number of waves N, or equivalently, for large areas. As a matter of fact, Piterbarg's theorem does not work for areas whose side is smaller than the average wavelength. On the contrary, splitting the number of waves calculation over space-time domain and its boundaries, Fedele's method allows performing the analysis even if the area side is smaller than a wavelength. Figure 6.34 shows the ratio of the expected maximum sea surface elevations over an area calculated by Piterbarg's and Fedele's method, respectively. As the number of waves increases, i.e. area widens or fetch length decreases, differences tend to cancel and the ratio tends to 1.

Figure 6.35 compare results of the different performed analyses for a $U = 15$ m/s wind speed and $F = 260$ km fetch length. For both $\overline{\xi}_{ST}$ and r, we observe that differences between Fedele's and Piterbarg's theorems decrease at large areas, while differences between Fedele's method and Forristall's approximation decreases at small areas. This confirms again the wider range of application of Fedele's method. Finally, we observed that Fedele's method

predicts higher sea surface elevations and ratios for all the analyzed areas. This is due to the boundary correction, included to account for possible occurrences of maxima over the boundaries of the space-time domain.

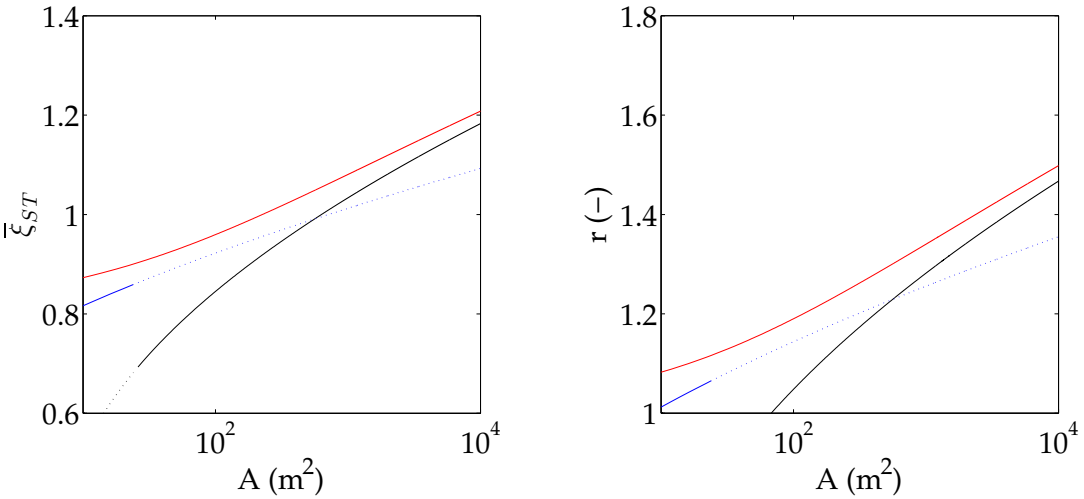

Figure 6.35: Comparison among methods, assuming wind speed $U = 15$ m/s and fetch length $F = 260$ km: Piterbarg (black), Forristall (blue), Fedele (red). Change between dotted and solid lines occurs where $X = \overline{L}_x$. (a) Expected maximum sea surface elevation over an area, normalized on H_s. (b) Ratio of the expected maximum sea surface elevation over an area to the expected maximum at a point.

6.7 Conclusions

In this Chapter, we explored the possibility of applying analytical methods to space-time extreme analysis. We analytically integrated the directional spectra to obtain closed formulae of spectral moments and spectral parameters. We could benefit of parametric spectral formulations, i.e. Pierson-Moskowitz and JONSWAP, combined with $\cos^2$ directional distribution function. Thanks to this, we could relate spectral moments and spectral parameters to physical quantities governing mechanics of wave growth, e.g. wind speed U and fetch length F. For Pierson-Moskowitz, integration could be performed straightforwardly, while for JONSWAP (which is not analytically integrable) an approximation was introduced. We had to limit integration for moments m_{020}, m_{200} and m_{110} to an upper bound, since the integral does not exist otherwise for spectra having frequency tail proprtional to σ^{-5}.

Qualitatively, results confirmed what we expected. Indeed, $\overline{\xi}_{ST}$ increased with space domain size S. Moreover, $\overline{\xi}_{ST}$ decreased with increasing U and F: in fact, being $\overline{\eta}_{ST}$ normalized on significant wave height H_s, the latter also increased together with space-time characteristic size of waves, i.e. $\overline{T}$, $\overline{L}_x$, $\overline{L}_y$, causing smaller numbers of waves in the domain and hence smaller $\overline{\xi}_{ST}$. We also observed that even for relatively small areas, maximum wave height estimates exceeded the time domain estimates and the conventional $H_{max} = 2H_s$. Besides this, results allowed us to quantify the entity of the maximum space-time sea surface elevations that could occur. Finally, it is worthwhile to point out that we provided a possible solution to scarcity of directional spectra by means of closed formulae of spectral parameters that depend only upon wind speed U, for Pierson-Moskowtiz case, or wind speed U and fetch length F for JONSWAP case.

Chapter 7

Numerical results

7.1 Introduction

In this Chapter, we present the results we obtained after applying a numerical approach to the problem of estimating maxima in the space-time domain. As already stated, the aims were to provide a solution to scarcity of directional spectra on the one hand and to discuss the dependence of space-time extremes $\overline{\xi}_{ST}$ upon physical parameters, i.e. ambient current speed magnitude V and bottom slope λ, on the other. The basic idea of this approach is to benefit of the directional spectra that are used by spectral numerical models. Saving spectra over all the computational domain (x, y, t) is an unfeasible task for realistic geophysical simulations. Hence, spectra are usually saved as outputs at few user-specified locations. Nevertheless, we intended to gather all the spectra the models calculate. Thus, we modified the numerical wave model SWAN (Simulating WAves Nearshore model, version 40.85 (The SWAN Team, 2011)) by providing new routines that calculate spectral parameters (2.7) as output variables. We called this new version SWAN-ST (Space-Time).

Then, using SWAN-ST we investigated two test cases. The first one was aimed at analyzing the effects of wave-current interactions and shoaling on space-time extremes of sea states. We set-up a rectangular grid and forced the model on a boundary by means of Pierson-Moskowitz spectrum. The second test case was focussed on testing the potentialities of using SWAN-ST for geophysical applications. To this end, we run a Mediterranean Sea hindcast over 3 years. We also run the first months of 2013 with the aim of hindcasting both the events we observed through WASS in the northern and southern Adriatic Sea. Doing so, we could compare results of space-time analysis with observations and validate the use of numerical models spectra

to perform space-time analysis.

7.2 A SWAN model version to estimate space-time extremes of sea states: SWAN-ST

As stated, we developed a modified version of SWAN version 40.85, called SWAN Space-Time (SWAN-ST). Doing so, we provide SWAN new routines to obtain the parameters (2.7) of the directional spectrum. After that, stochastic models can be easily implemented off-line in post-processing, with the advantage of saving a lot of memory, since the user is prevented to save directional spectra all over the computational domain (x, y, t).

Assume the following spectral domain discretization in SWAN: directions are represented by P bins $\theta_1 \leq \theta_r \leq \theta_R$, separated by a constant step $\Delta\theta$. Frequencies instead are geometrically distributed as $\sigma_{q+1} = 1.1\sigma_q$ between minimum and maximum cut-off frequencies, i.e $\sigma_1 \leq \sigma_q \leq \sigma_Q$, respectively. To calculate moments of the spectrum, a diagnostic tail proportional to σ^{-m} is added beyond σ_Q (m=4,5 but m=5 is often preferred to resemble observed spectral tails (Forristall, 1981)).

Within SWAN-ST, spectral parameters (2.7) are obtained at each node of the computational domain (x, y, t) by calculation of the spectral moments through integration of the directional spectrum $S(\sigma, \theta) = \sigma N(\sigma, \theta)$. In the prognostic range of frequencies $\sigma_1 \leq \sigma \leq \sigma_Q$, integration is performed numerically by means of the technique routinely used within SWAN (The SWAN Team, 2011), which can be straightforwardly applied to calculate every moment m_{ijl}:

$$m_{ijl,P} \simeq \mu \sum_{r=1}^{R} \sum_{q=1}^{Q} k_q^{2(i+j)} \cos\theta_r{}^i \sin\theta_r{}^l \sigma_q^{(2+l)} N(\sigma_q, \theta_r) \Delta\theta \tag{7.1}$$

where $\mu = \ln(\sigma_{i+1}/\sigma_i)$. Integration over the diagnostic tail $\sigma_Q \leq \sigma \leq \infty$ is performed analytically according to the technique implemented in SWAN (The SWAN Team, 2011):

$$m_{ijl,D} \simeq \tau \left(k_Q^{2(i+j)} \cos\theta_R{}^i \sin\theta_R{}^l \sigma_Q^{(2+l)} N(\sigma_Q, \theta_R) \Delta\theta \right) \tag{7.2}$$

where $\tau = 1/(\chi(1 + \chi(\upsilon - 1)))$, $\chi = r - l - 2(i + j) - 1$ and $\upsilon = \sqrt{\sigma_{i+1}/\sigma_i}$. Though, since we chose m=5, (7.2) cannot be performed to calculate the moments m_{ijl} realizing $2(i + j) + l = 4$ (i.e. m_{200}, m_{020} and m_{110}), because χ cancels. Hence, similarly to what we did in the analytical approach, in

deep waters we limit the integration over σ to the gravity-capillary limit, i.e. $\sigma_c = 60$ rad/s, coming to:

$$m_{ijl,Dc} \simeq \kappa \left(k_Q^{2(i+j)} \cos\theta_R{}^i \sin\theta_R{}^l \sigma_Q^{(2+l)} N(\sigma_Q, \theta_R) \Delta\theta \right) \tag{7.3}$$

where $\kappa = (\ln(\sigma_c) - \ln(\upsilon\sigma_Q))$ Accordingly, moments of the directional spectrum (2.6) are obtained as

$$\begin{aligned} m_{ijl} &\simeq m_{ijl,P} + m_{ijl,D} \text{ when } 2(i+j)+l \neq 4 \\ m_{ijl} &\simeq m_{ijl,P} + m_{ijl,Dc} \text{ when } 2(i+j)+l = 4 \end{aligned} \tag{7.4}$$

Spectral parameters follow straightforwardly from (2.7).

FORTRAN 90 subroutines we developed from scratch and those we modified for SWAN-ST are entirely reported in Appendix C.1.

7.3 Test case: wave-current interaction and shoaling effects on space-time extremes

7.3.1 Model set-up

The effects of wave-current interactions on space-time extremes could be investigated thanks to SWAN-ST. We set-up a 500 km-long deep-waters 1-D model with $\Delta x = 500$ m spatial resolution. On the $x = 0$ boundary, the model was forced by Pierson-Moskowitz distributed energy with a $\cos^2$ directional distribution function to represent short-crested sea states. Peak direction (counterclockwise from x axis) was 0°, hence energy propagated mainly along positive x direction. Spectral space was discretized using 180 directions in the range [-90°,90°] and 39 frequencies geometrically distributed within [0.05,2.00] Hz. Five different sea severities were tested, ranging from 0.5 m to 8.0 m. To highlight the effects of wave-current interactions and shoaling, simulations were performed in stationary mode without source terms, i.e. no generation, wave-wave interaction, dissipation. The spectral parameters obtained as outputs of SWAN-ST were used to implement Fedele's model (in its linear version, i.e. without second order corrections) and discuss the dependence of $\overline{\eta}_{ST}$ and $\overline{\xi}_{ST}$ upon V_x. Space-time sizes of domain of analysis were chosen in order to avoid scale effects, hence they were proportional to the characteristics sizes of the sea state: $T = 100\overline{T}$ and $S = \overline{L}_x\overline{L}_y$, $\overline{L}_x$ and $\overline{L}_y$ being the wavelength and wave crests in absence of current ($V_x = 0$ m/s) or in deep waters flat bottom ($\lambda = 0$), respectively.

7.3.2 Model validation

Prior to run the model in its space-time configuration, we checked its capabilities in reproducing the desired phenomena: wave-current interactions and shoaling. To this end we, ran an extremely narrow banded spectrum along both frequency and direction to simulate a regular wave train.

Wave-current interaction

To validate wave-current interactions, we tested 4 configurations combining 2 boundary conditions with 2 current speeds: a narrow-banded spectrum forced the model at the left boundary, while a current speed (+1 m/s or -1 m/s) was imposed in the range [250,500] km. Results for the 4 tested configurations (details in Table 7.1) are depicted in Figure 7.1, Figure 7.2, Figure 7.3 and Figure 7.4, showing current speed V_x, significant wave height H_s, spectral parameters ($\overline{T}$, $\overline{L}_x$, $\overline{L}_y$, α_{xt}, α_{xy}, α_{yt}) and space-time extremes ($\overline{\xi}_{ST}$, $\overline{\eta}_{ST}$).

Variations of significant wave height from still waters (V_x=0 m/s) to the moving field (with V_x) were compared with theoretical predictions from (2.45). SWAN-ST outputs, summarized in Table 7.1, are in good agreement with theoretical predictions. We also verified qualitatively a shortening of the mean wavelength $\overline{L}_x$ with opposing current and a lengthening with following current (Figure 7.1, Figure 7.2, Figure 7.3 and Figure 7.4). What we observed is consistent with the theory of wave-current interactions, hence we considered the model validated.

V_x (m/s)	H_s (m)			H_0 (m)			T_0 (s)
IN	IN	OUT_{NUM}	OUT_{TH}	IN	OUT_{NUM}	OUT_{TH}	IN
1.00	2.00	1.87	1.70	1.41	1.32	1.20	7.0
-1.00	2.00	2.69	2.49	1.41	1.90	1.76	7.0
1.00	4.00	3.82	3.56	2.82	2.70	2.52	10.0
-1.00	4.00	4.87	4.62	2.82	3.44	3.27	10.0

Table 7.1: Validation of wave-current interaction on SWAN-ST. Inputs and outputs (numerical (NUM), i.e. SWAN-ST, and theoretical (TH), i.e. according to (2.45). Relation between spectral significant wave height H_s and regular wave height H_0 is $H_s = \sqrt{2}H_0$.

Shoaling

To validate shoaling, we tested the variations of significant wave height occurring after a sloping bottom with slope λ=1/500, from -150.0 m to -1.0 m.

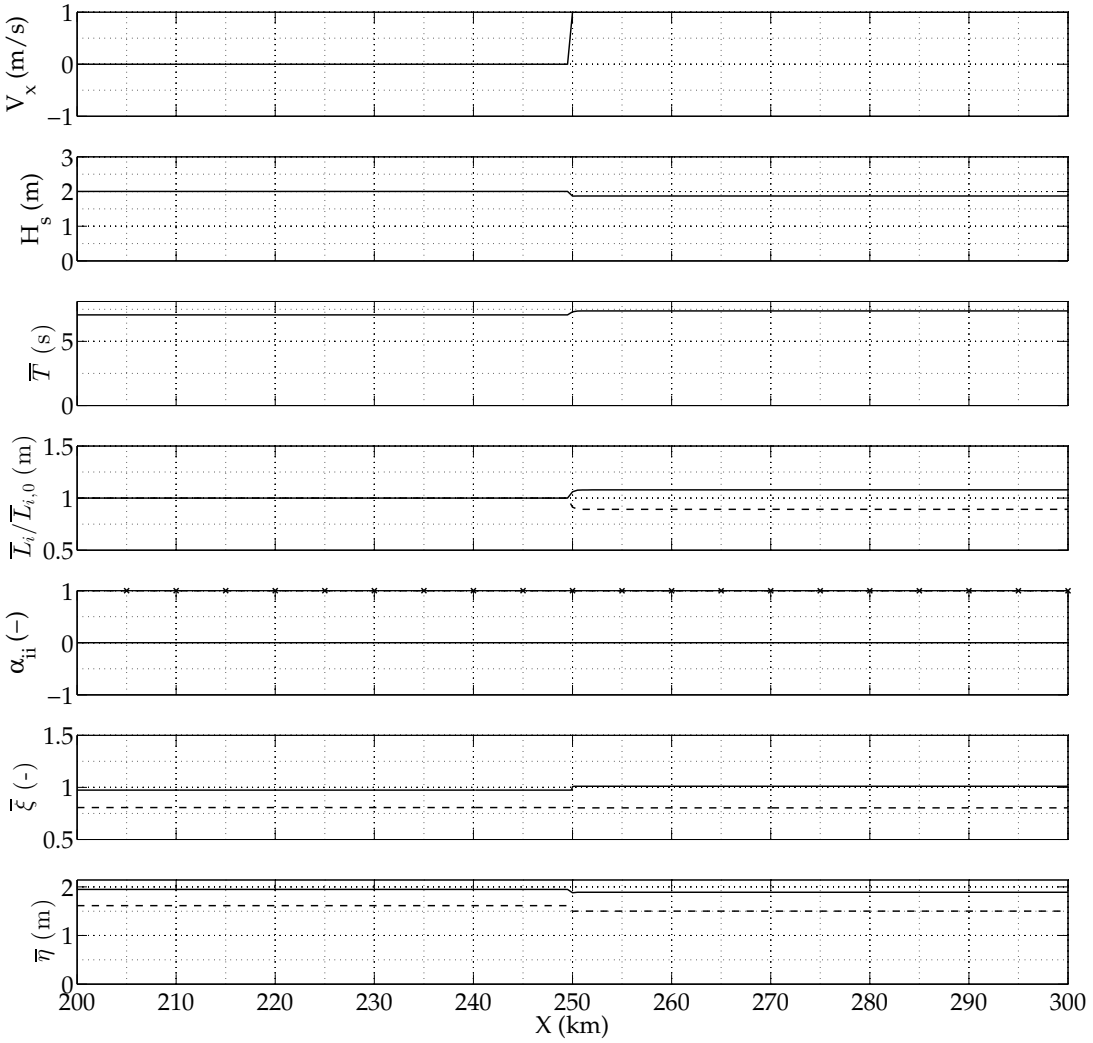

Figure 7.1: Validation of wave-current interaction on SWAN-ST: Pierson-Moskowitz spectrum with H_s=2.0 m, $V_x = 1.0$ m/s. $\overline{L}_i$ panel: wavelength (solid) and wave crest (dashed); α_{ii} panel: α_{xt} (dashed-crossed), α_{yt} (dotted) and α_{xy} (solid); $\overline{\xi}$ panel: $\overline{\xi}_{ST}$ (solid) and $\overline{\xi}_T$ (dashed); $\overline{\eta}$ panel: $\overline{\eta}_{ST}$ (solid) and $\overline{\eta}_T$ (dashed).

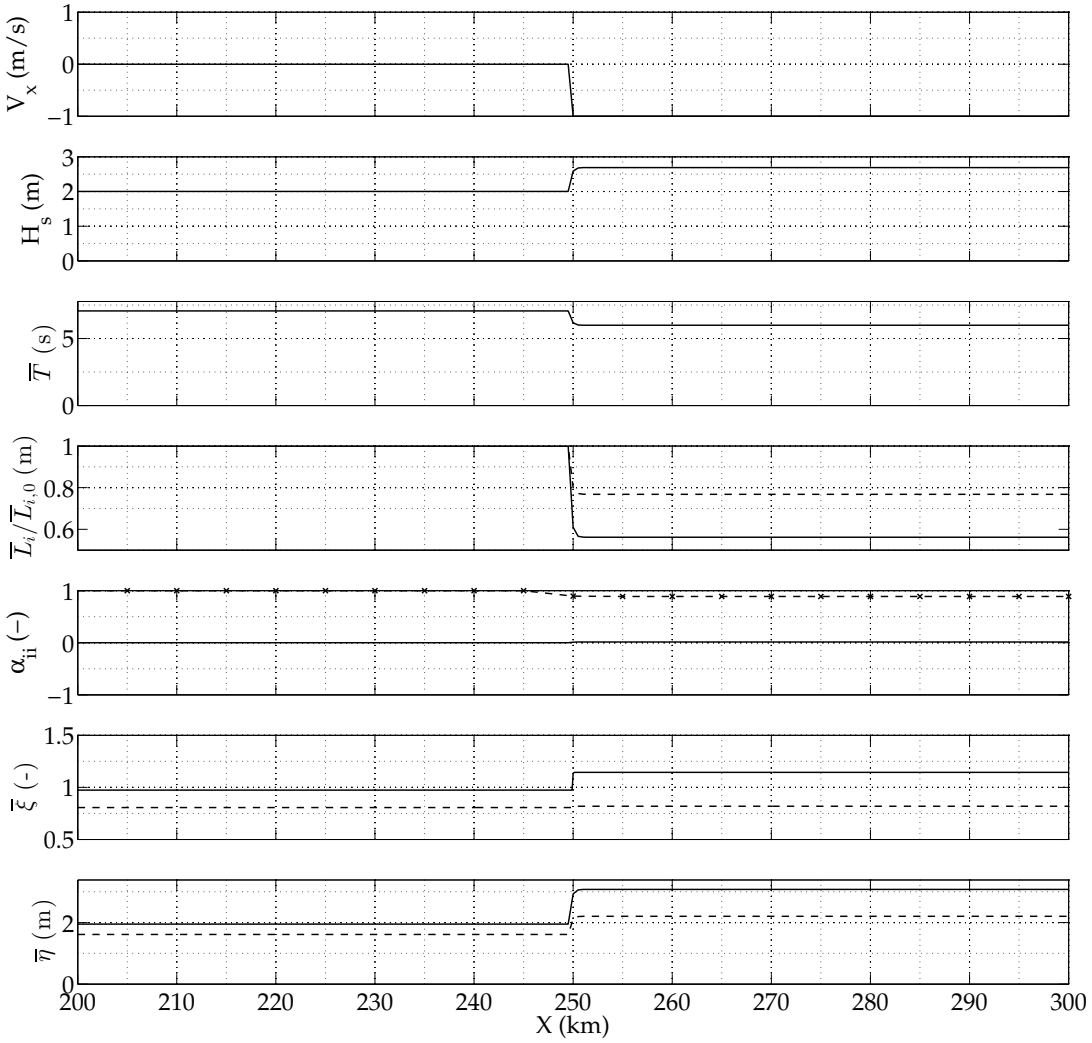

Figure 7.2: Validation of wave-current interaction on SWAN-ST: Pierson-Moskowitz spectrum with H_s=2.0 m, $V_x = -1.0$ m/s. $\overline{L}_i$ panel: wavelength (solid) and wave crest (dashed); α_{ii} panel: α_{xt} (dashed-crossed), α_{yt} (dotted) and α_{xy} (solid); $\overline{\xi}$ panel: $\overline{\xi}_{ST}$ (solid) and $\overline{\xi}_T$ (dashed); $\overline{\eta}$ panel: $\overline{\eta}_{ST}$ (solid) and $\overline{\eta}_T$ (dashed).

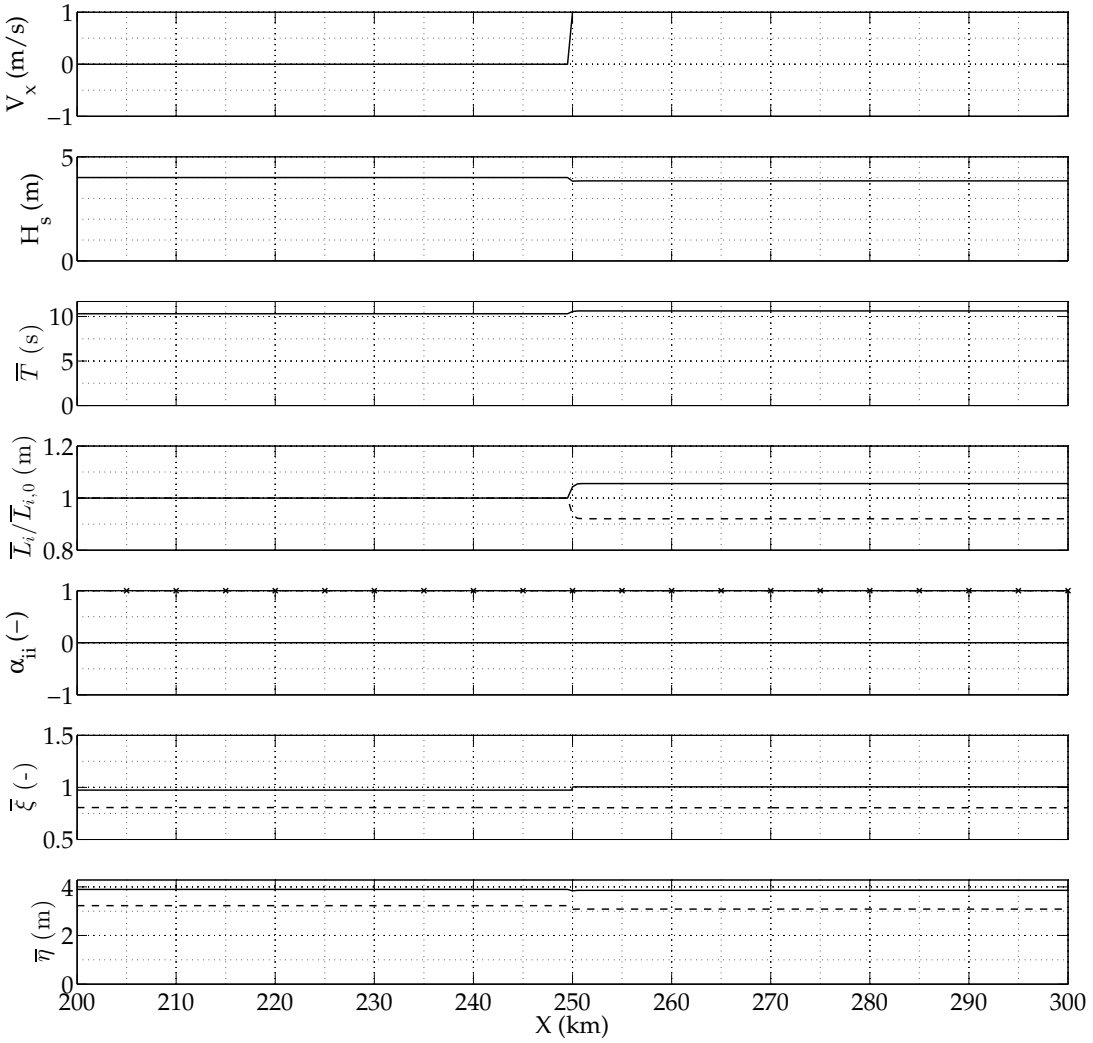

Figure 7.3: Validation of wave-current interaction on SWAN-ST: Pierson-Moskowitz spectrum with H_s=4.0 m, $V_x = 1.0$ m/s. $\overline{L}_i$ panel: wavelength (solid) and wave crest (dashed); α_{ii} panel: α_{xt} (dashed-crossed), α_{yt} (dotted) and α_{xy} (solid); $\overline{\xi}$ panel: $\overline{\xi}_{ST}$ (solid) and $\overline{\xi}_T$ (dashed); $\overline{\eta}$ panel: $\overline{\eta}_{ST}$ (solid) and $\overline{\eta}_T$ (dashed).

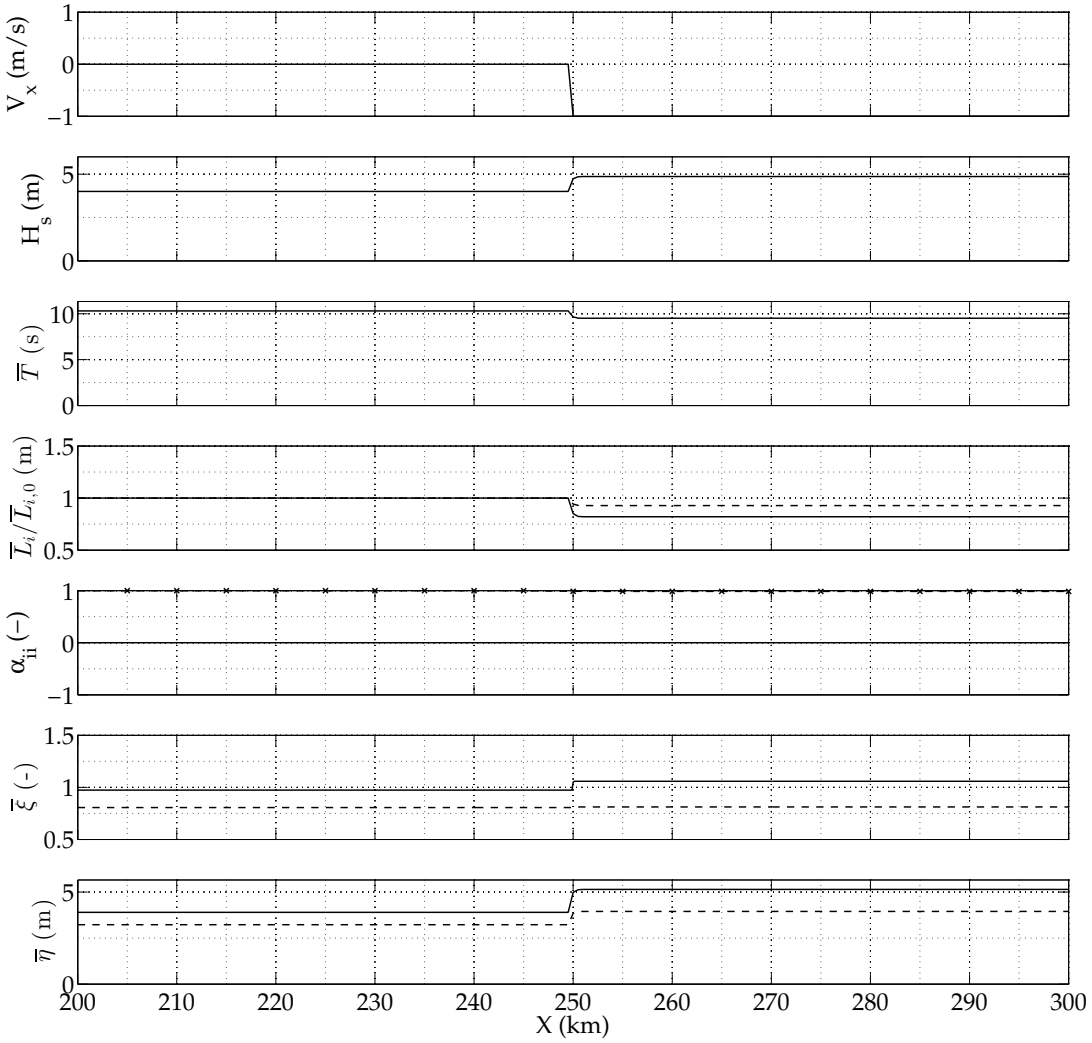

Figure 7.4: Validation of wave-current interaction on SWAN-ST: Pierson-Moskowitz spectrum with H_s=4.0 m, $V_x = -1.0$ m/s. $\overline{L}_i$ panel: wavelength (solid) and wave crest (dashed); α_{ii} panel: α_{xt} (dashed-crossed), α_{yt} (dotted) and α_{xy} (solid); $\overline{\xi}$ panel: $\overline{\xi}_{ST}$ (solid) and $\overline{\xi}_T$ (dashed); $\overline{\eta}$ panel: $\overline{\eta}_{ST}$ (solid) and $\overline{\eta}_T$ (dashed).

Then, we compared results with theoretical prediction from (2.40). Results are depicted in Figure 7.5 and summarized in Table 7.2: agreement between numerical and theoretical outputs is excellent. Besides this, in Figure 7.5 we observed a shortening of wavelength $\overline{L}_x$ and a slight decrease of wave height H_s followed by an increase of it, consistently with shoaling theory (Holthuijsen, 2007).

λ (m/s)	H_s (m)			H_0 (m)			T_0 (s)
IN	IN	OUT_{NUM}	OUT_{TH}	IN	OUT_{NUM}	OUT_{TH}	IN
1/500	2.00	2.71	2.70	1.41	1.92	1.91	7.0

Table 7.2: Validation of shoaling on SWAN-ST. Inputs and outputs (numerical (NUM), i.e. SWAN-ST, and theoretical (TH), i.e. according to (2.45). Relation between spectral significant wave height H_s and regular wave height H_0 is $H_s = \sqrt{2}H_0$.

7.3.3 Results: wave-current interaction

For wave-current interaction tests, the following sea severities (i.e. H_s) were accounted for: 0.50, 1.00, 2.00, 4.00, 8.00 m. Different current fields were imposed in the range [250,500] km, changing V_x component of the velocity vector V=(V_x,0) within [-1,+1] m/s, which is a reasonable range for sea current speeds. Tested speeds were: -1.00, -0.50, -0.40, -0.35, -0.30, -0.25, -0.20, -0.10, +0.25, +0.50, +1.00 m/s. Here, negative speed means opposing current, while positive means following. Detailed results for each velocity V_x are shown for H_s = 1.00 m only (from Figure 7.6 to Figure 7.16). In the followings (from Figure 7.17 to Figure 7.31), results accounting for every velocity we tested are summarized by 3 Figures for each considered sea severity: the first one deals with spectral parameters and space-time extremes at different V_x, the second and the third one depict directional spectrum modifications due to current speed. Spectral modifications are represented by bandwidth parameter ν and directional spreading δ.

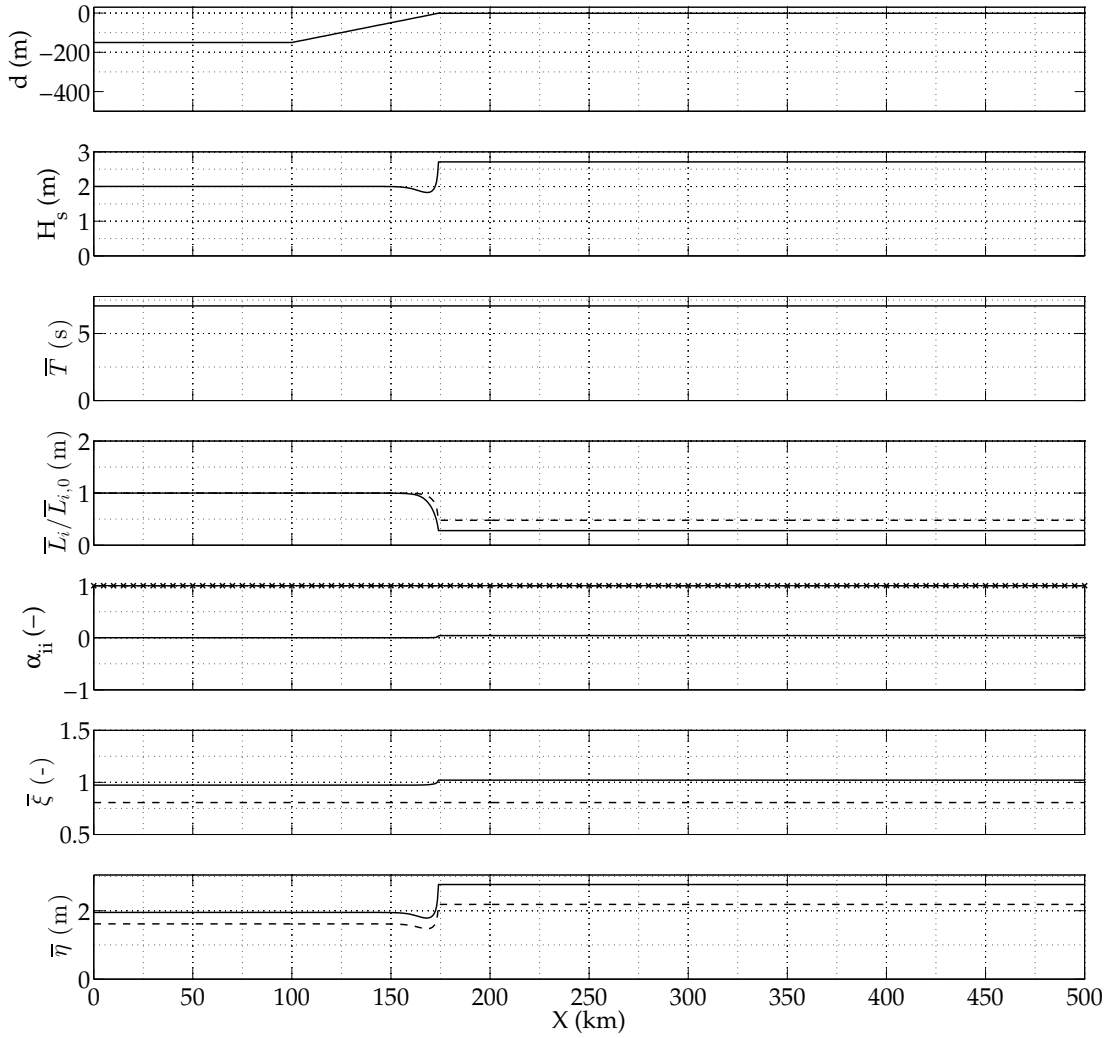

Figure 7.5: Validation of shoaling on SWAN-ST: Pierson-Moskowitz spectrum with H_s=2.0 m, λ=1/500. $\overline{L}_i$ panel: wavelength (solid) and wave crest (dashed); α_{ii} panel: α_{xt} (dashed-crossed), α_{yt} (dotted) and α_{xy} (solid); $\overline{\xi}$ panel: $\overline{\xi}_{ST}$ (solid) and $\overline{\xi}_T$ (dashed); $\overline{\eta}$ panel: $\overline{\eta}_{ST}$ (solid) and $\overline{\eta}_T$ (dashed).

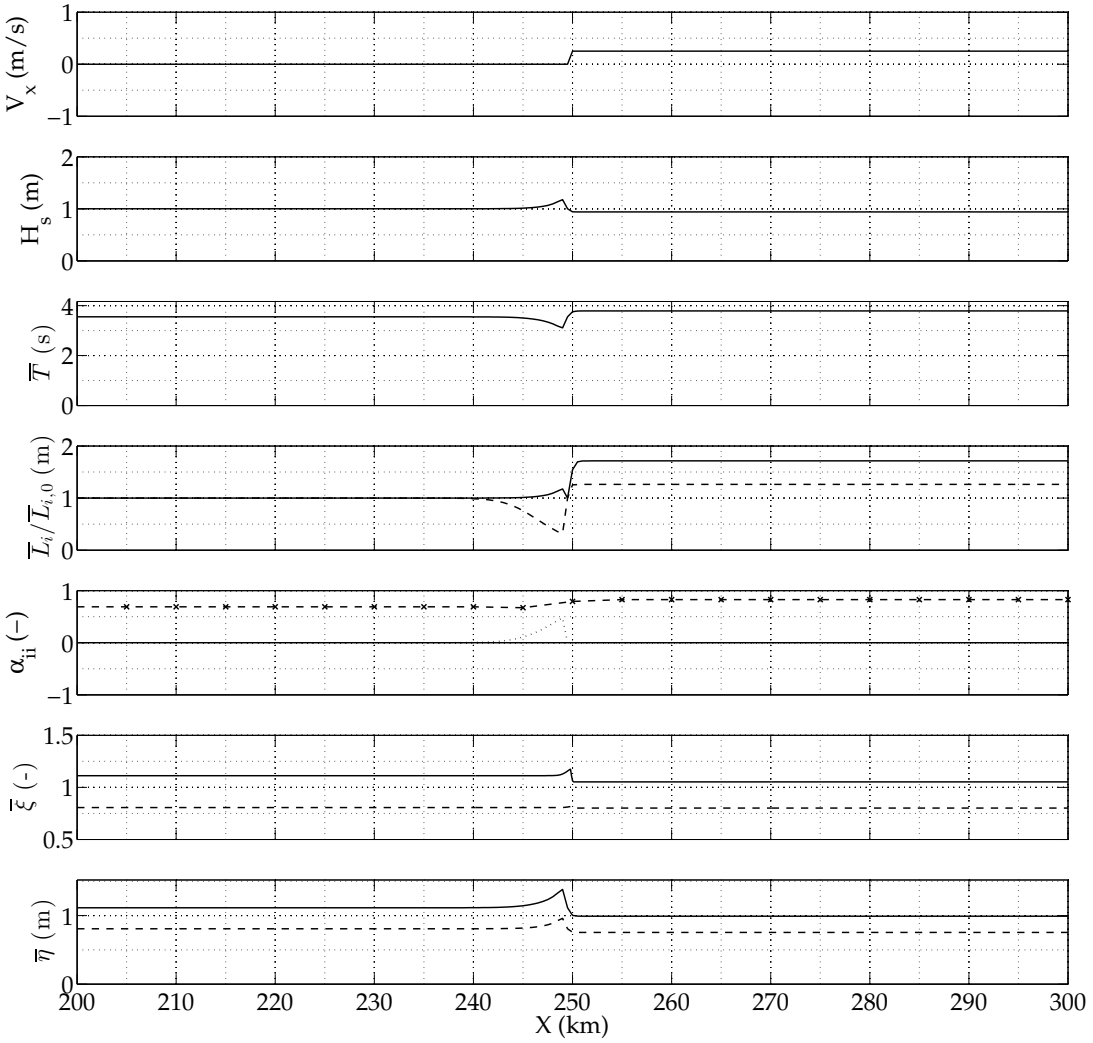

Figure 7.6: Wave-current interactions effect on space-time extremes: Pierson-Moskowitz spectrum with H_s=1.0 m, $V_x = 0.25$ m/s. $\overline{L}_i$ panel: wavelength (solid) and wave crest (dashed); α_{ii} panel: α_{xt} (dashed-crossed), α_{yt} (dotted) and α_{xy} (solid); $\overline{\xi}$ panel: $\overline{\xi}_{ST}$ (solid) and $\overline{\xi}_T$ (dashed); $\overline{\eta}$ panel: $\overline{\eta}_{ST}$ (solid) and $\overline{\eta}_T$ (dashed).

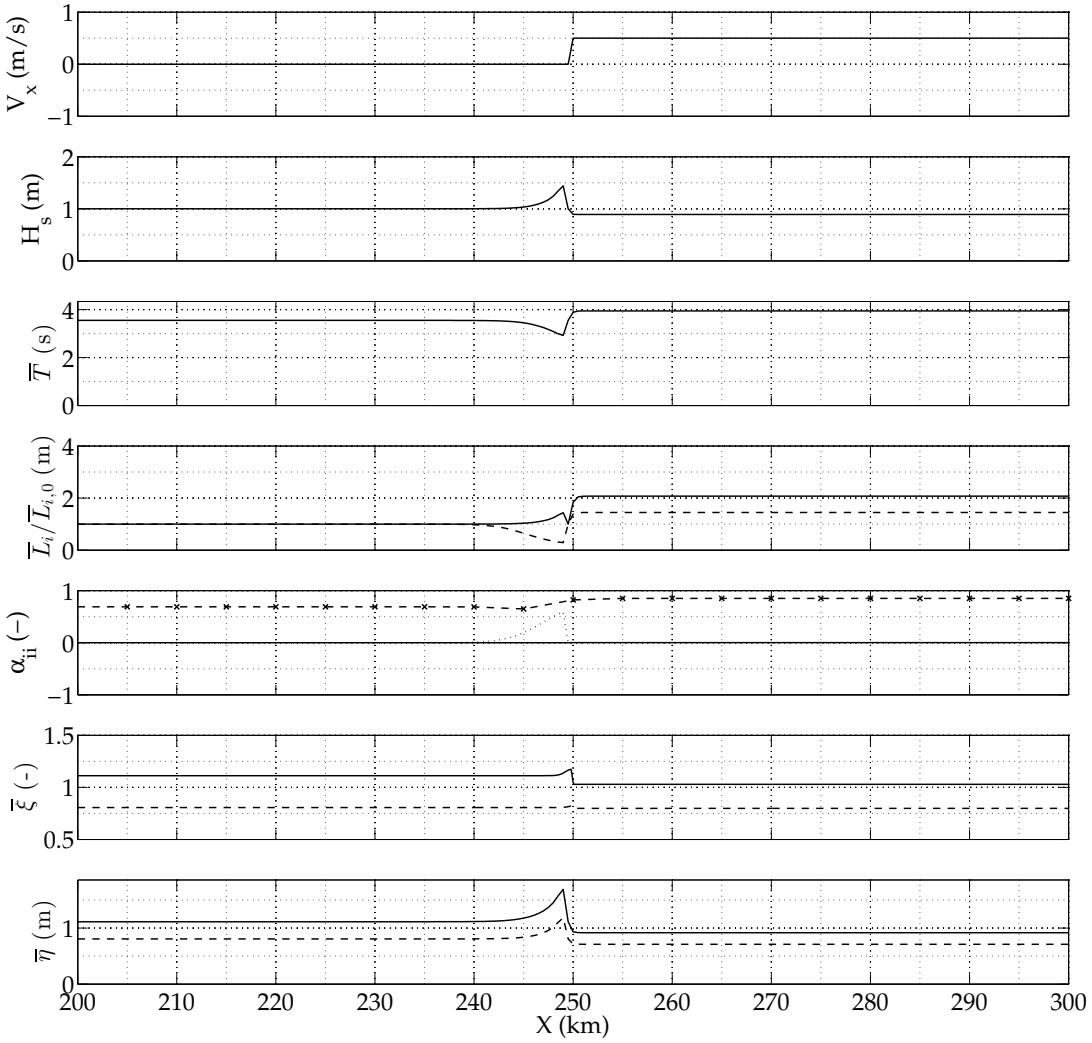

Figure 7.7: Wave-current interactions effect on space-time extremes: Pierson-Moskowitz spectrum with H_s=1.0 m, V_x = 0.50 m/s. $\overline{L}_i$ panel: wavelength (solid) and wave crest (dashed); α_{ii} panel: α_{xt} (dashed-crossed), α_{yt} (dotted) and α_{xy} (solid); $\overline{\xi}$ panel: $\overline{\xi}_{ST}$ (solid) and $\overline{\xi}_T$ (dashed); $\overline{\eta}$ panel: $\overline{\eta}_{ST}$ (solid) and $\overline{\eta}_T$ (dashed).

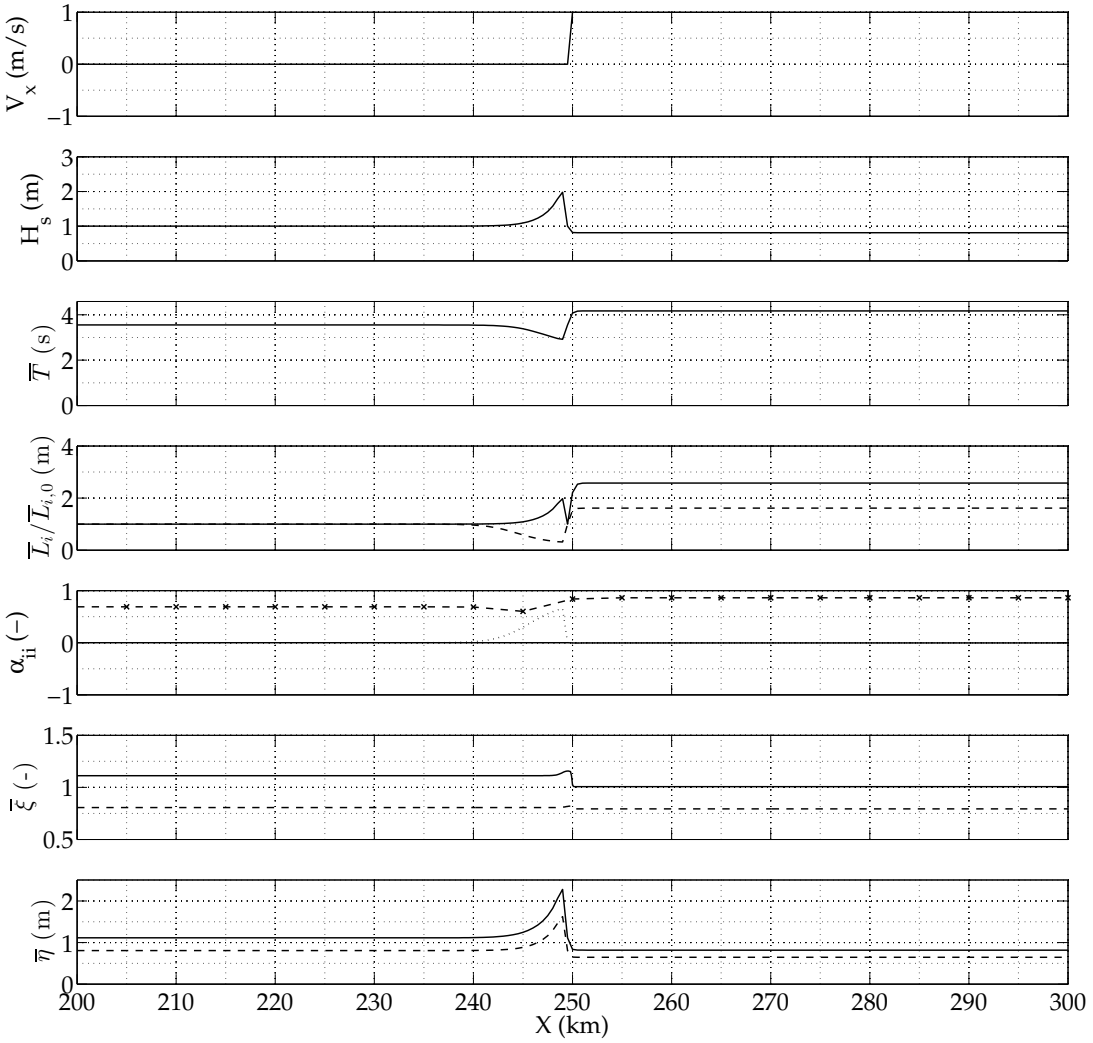

Figure 7.8: Wave-current interactions effect on space-time extremes: Pierson-Moskowitz spectrum with H_s=1.0 m, V_x = 1.00 m/s. $\overline{L}_i$ panel: wavelength (solid) and wave crest (dashed); α_{ii} panel: α_{xt} (dashed-crossed), α_{yt} (dotted) and α_{xy} (solid); $\overline{\xi}$ panel: $\overline{\xi}_{ST}$ (solid) and $\overline{\xi}_T$ (dashed); $\overline{\eta}$ panel: $\overline{\eta}_{ST}$ (solid) and $\overline{\eta}_T$ (dashed).

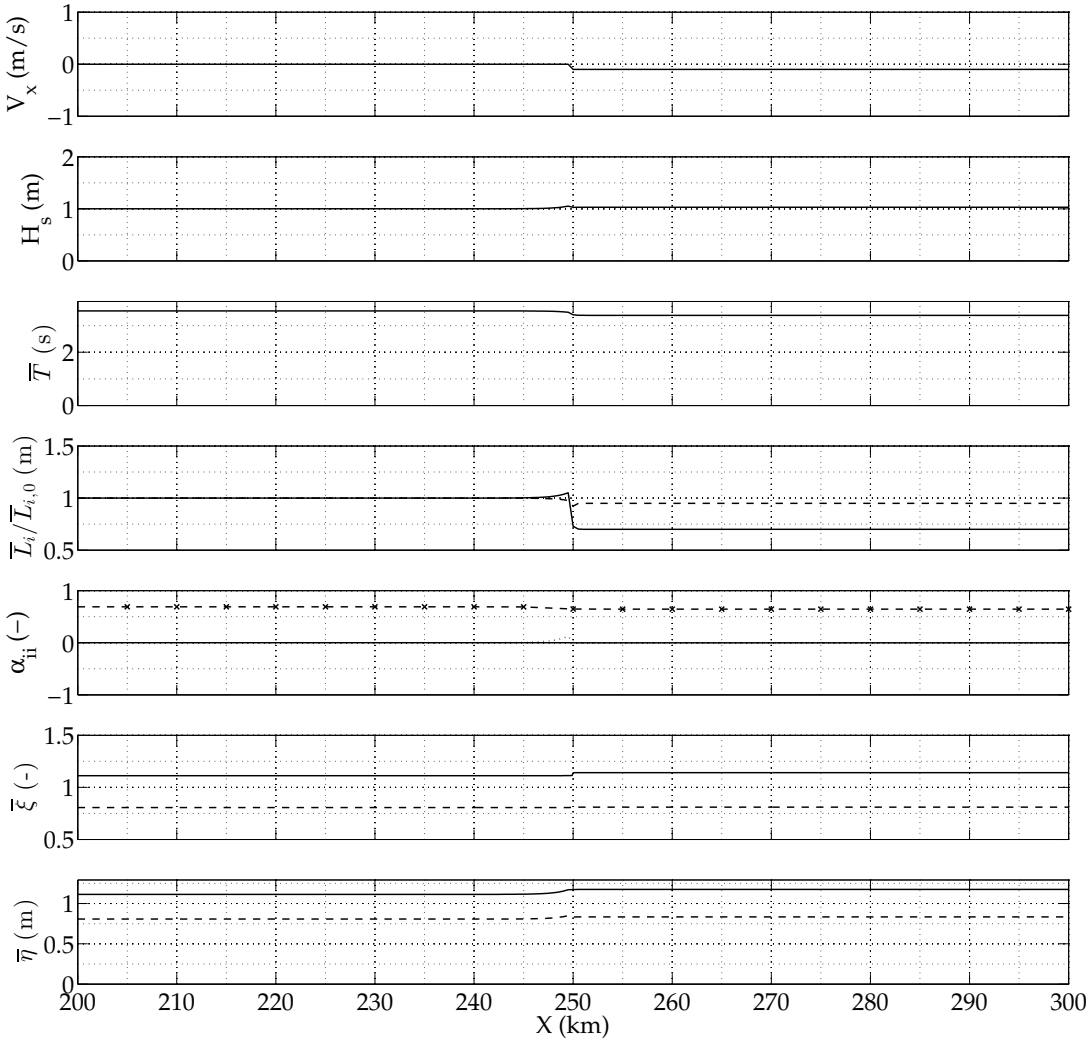

Figure 7.9: Wave-current interactions effect on space-time extremes: Pierson-Moskowitz spectrum with H_s=1.0 m, $V_x = -0.10$ m/s. $\overline{L}_i$ panel: wavelength (solid) and wave crest (dashed); α_{ii} panel: α_{xt} (dashed-crossed), α_{yt} (dotted) and α_{xy} (solid); $\overline{\xi}$ panel: $\overline{\xi}_{ST}$ (solid) and $\overline{\xi}_T$ (dashed); $\overline{\eta}$ panel: $\overline{\eta}_{ST}$ (solid) and $\overline{\eta}_T$ (dashed).

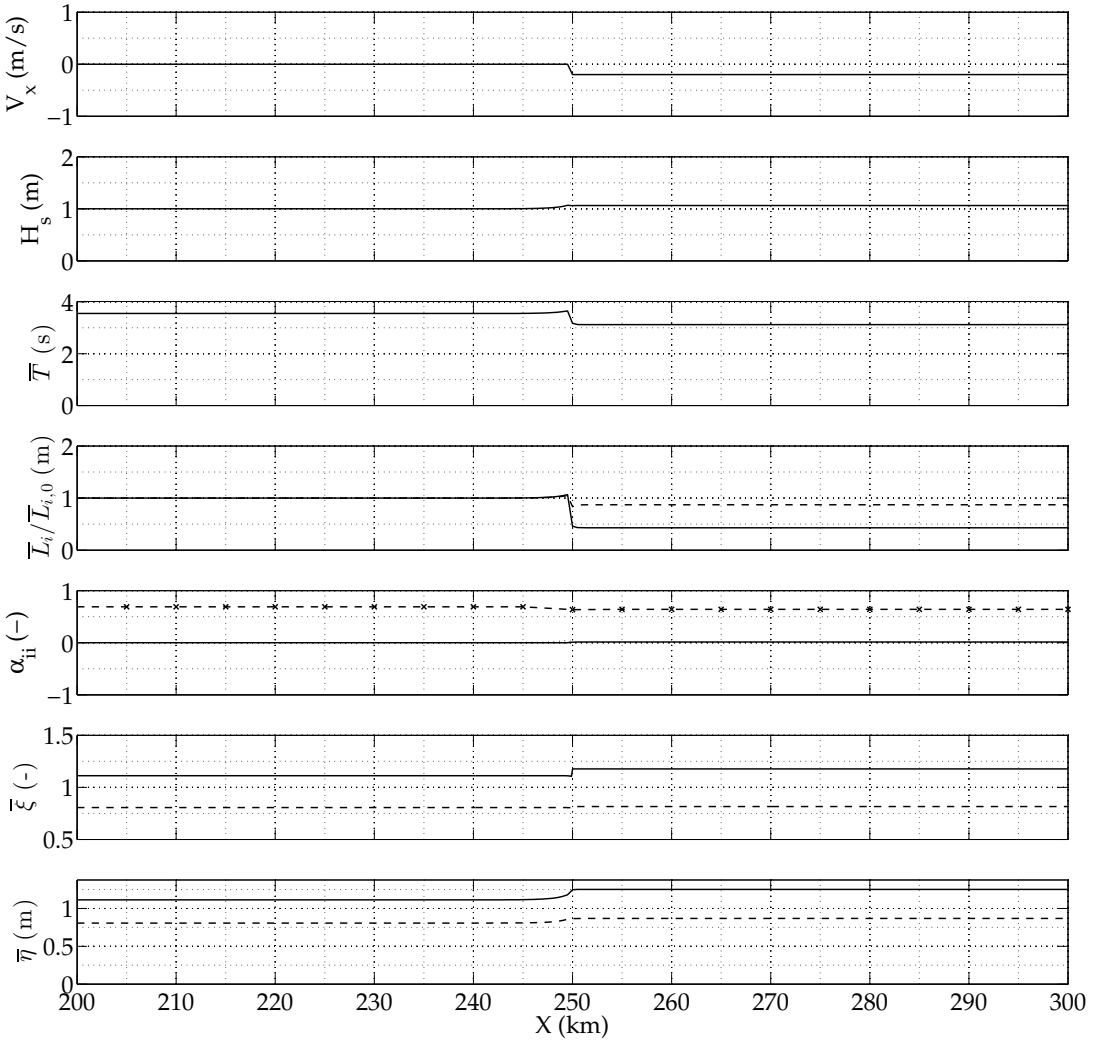

Figure 7.10: Wave-current interactions effect on space-time extremes: Pierson-Moskowitz spectrum with H_s=1.0 m, $V_x = -0.20$ m/s. $\overline{L}_i$ panel: wavelength (solid) and wave crest (dashed); α_{ii} panel: α_{xt} (dashed-crossed), α_{yt} (dotted) and α_{xy} (solid); $\overline{\xi}$ panel: $\overline{\xi}_{ST}$ (solid) and $\overline{\xi}_T$ (dashed); $\overline{\eta}$ panel: $\overline{\eta}_{ST}$ (solid) and $\overline{\eta}_T$ (dashed).

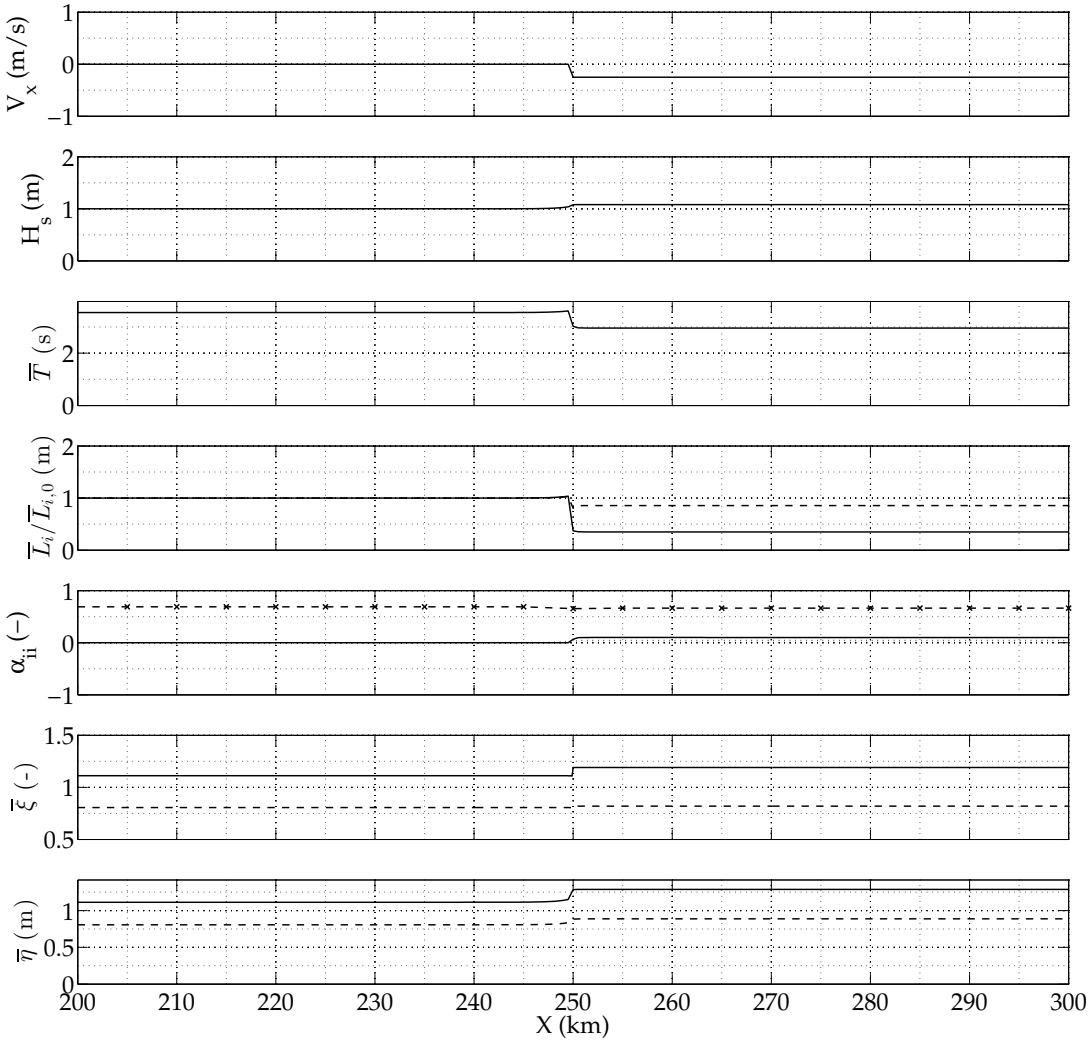

Figure 7.11: Wave-current interactions effect on space-time extremes: Pierson-Moskowitz spectrum with H_s=1.0 m, $V_x = -0.25$ m/s. $\overline{L}_i$ panel: wavelength (solid) and wave crest (dashed); α_{ii} panel: α_{xt} (dashed-crossed), α_{yt} (dotted) and α_{xy} (solid); $\overline{\xi}$ panel: $\overline{\xi}_{ST}$ (solid) and $\overline{\xi}_T$ (dashed); $\overline{\eta}$ panel: $\overline{\eta}_{ST}$ (solid) and $\overline{\eta}_T$ (dashed).

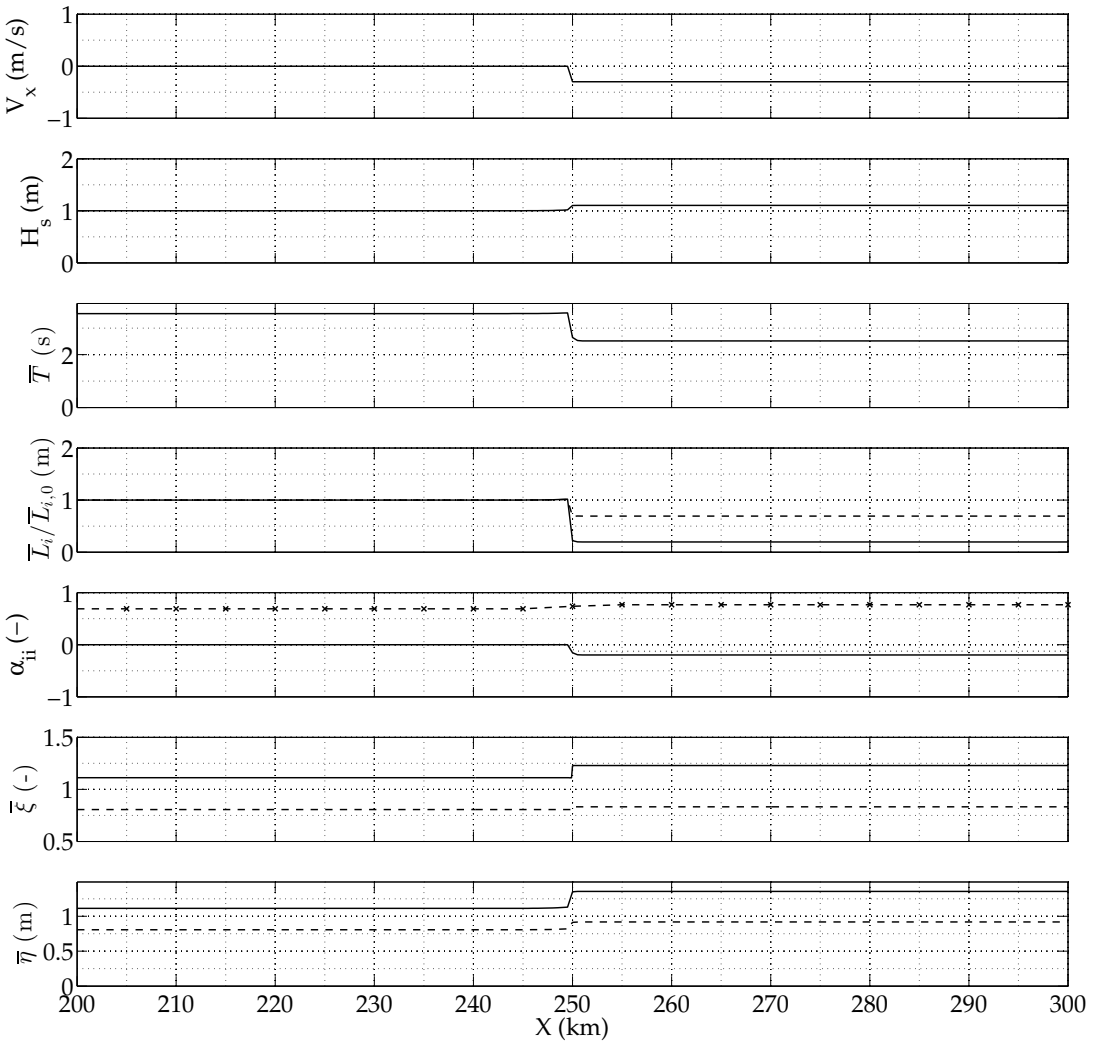

Figure 7.12: Wave-current interactions effect on space-time extremes: Pierson-Moskowitz spectrum with H_s=1.0 m, $V_x = -0.30$ m/s. $\overline{L}_i$ panel: wavelength (solid) and wave crest (dashed); α_{ii} panel: α_{xt} (dashed-crossed), α_{yt} (dotted) and α_{xy} (solid); $\overline{\xi}$ panel: $\overline{\xi}_{ST}$ (solid) and $\overline{\xi}_T$ (dashed); $\overline{\eta}$ panel: $\overline{\eta}_{ST}$ (solid) and $\overline{\eta}_T$ (dashed).

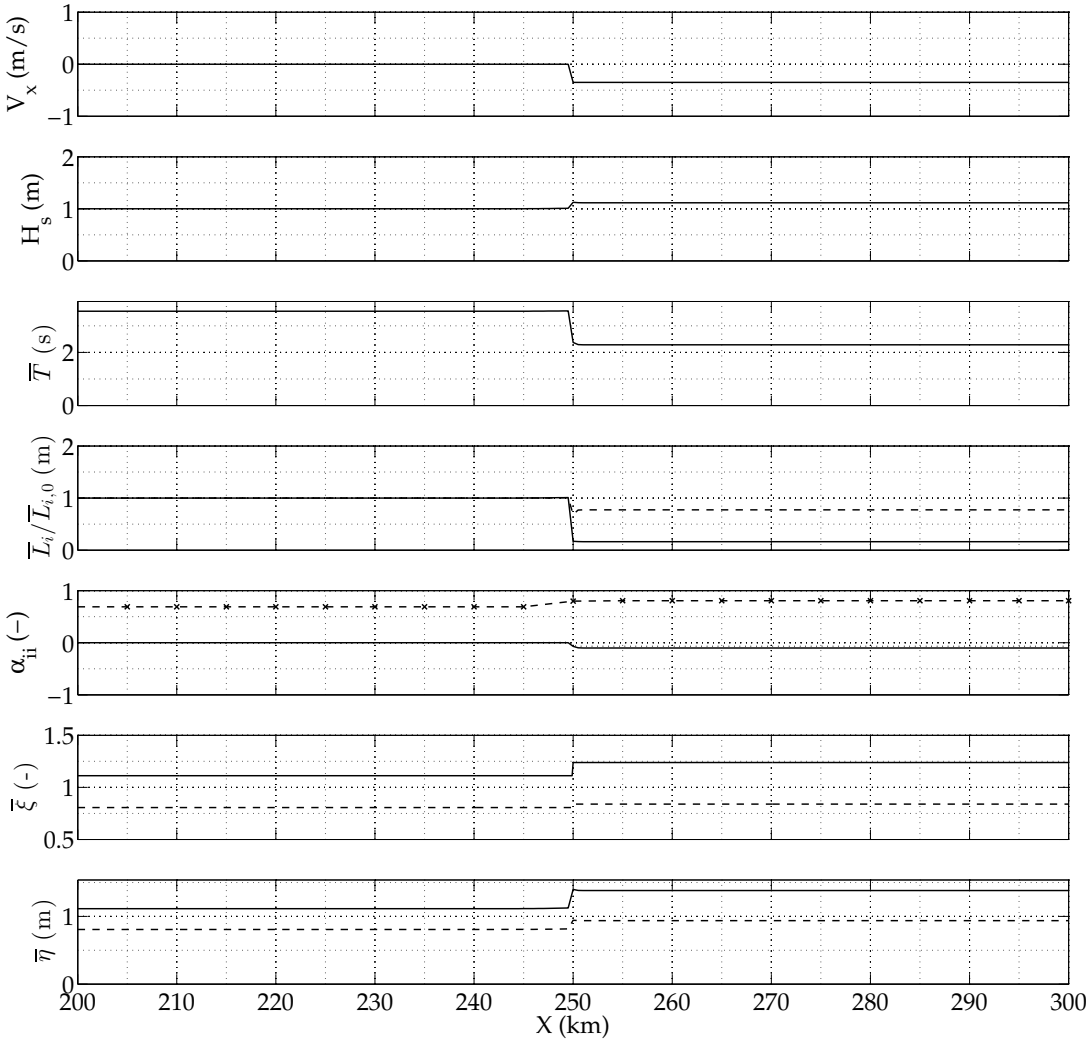

Figure 7.13: Wave-current interactions effect on space-time extremes: Pierson-Moskowitz spectrum with H_s=1.0 m, $V_x = -0.35$ m/s. $\overline{L}_i$ panel: wavelength (solid) and wave crest (dashed); α_{ii} panel: α_{xt} (dashed-crossed), α_{yt} (dotted) and α_{xy} (solid); $\overline{\xi}$ panel: $\overline{\xi}_{ST}$ (solid) and $\overline{\xi}_T$ (dashed); $\overline{\eta}$ panel: $\overline{\eta}_{ST}$ (solid) and $\overline{\eta}_T$ (dashed).

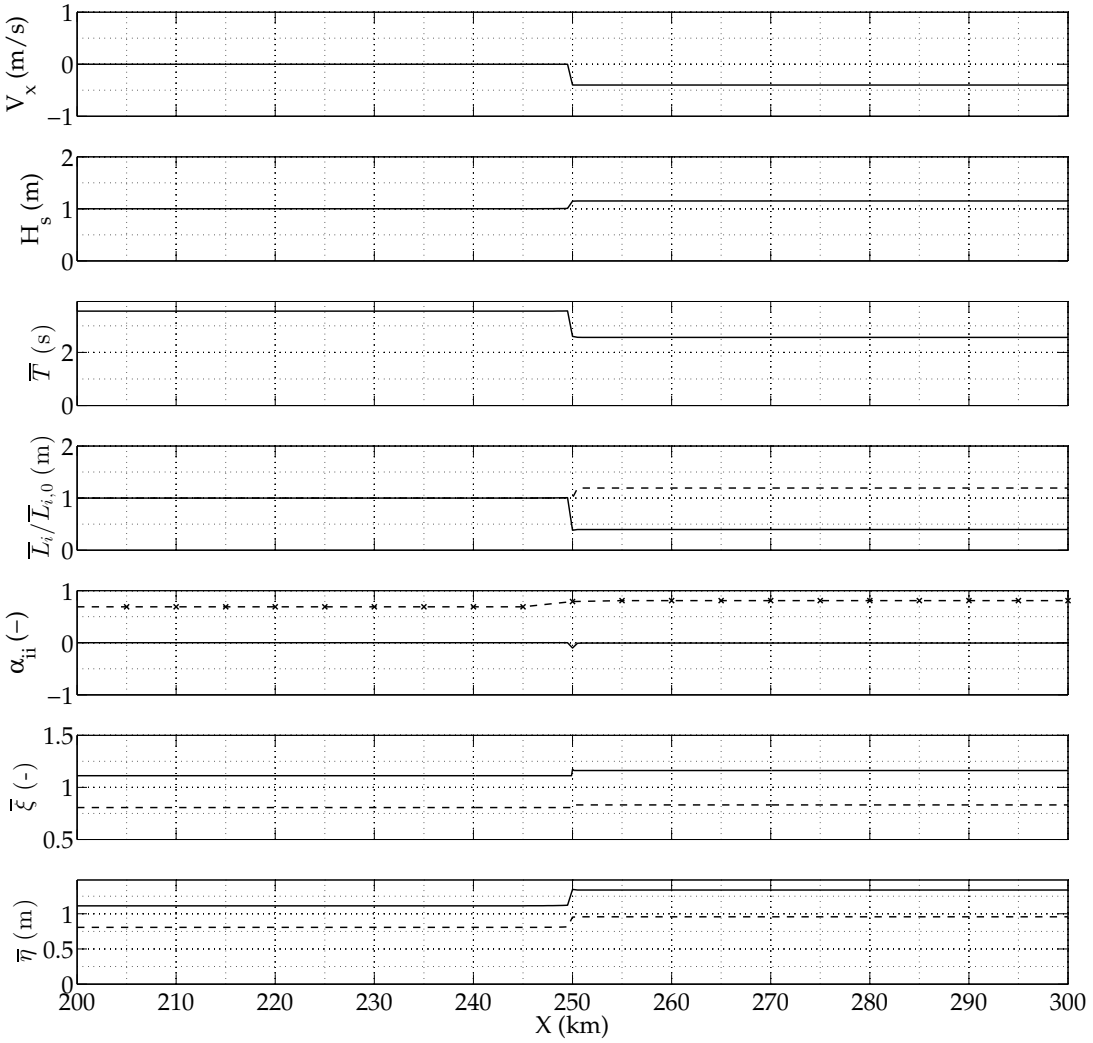

Figure 7.14: Wave-current interactions effect on space-time extremes: Pierson-Moskowitz spectrum with H_s=1.0 m, $V_x = -0.40$ m/s. $\overline{L}_i$ panel: wavelength (solid) and wave crest (dashed); α_{ii} panel: α_{xt} (dashed-crossed), α_{yt} (dotted) and α_{xy} (solid); $\overline{\xi}$ panel: $\overline{\xi}_{ST}$ (solid) and $\overline{\xi}_T$ (dashed); $\overline{\eta}$ panel: $\overline{\eta}_{ST}$ (solid) and $\overline{\eta}_T$ (dashed).

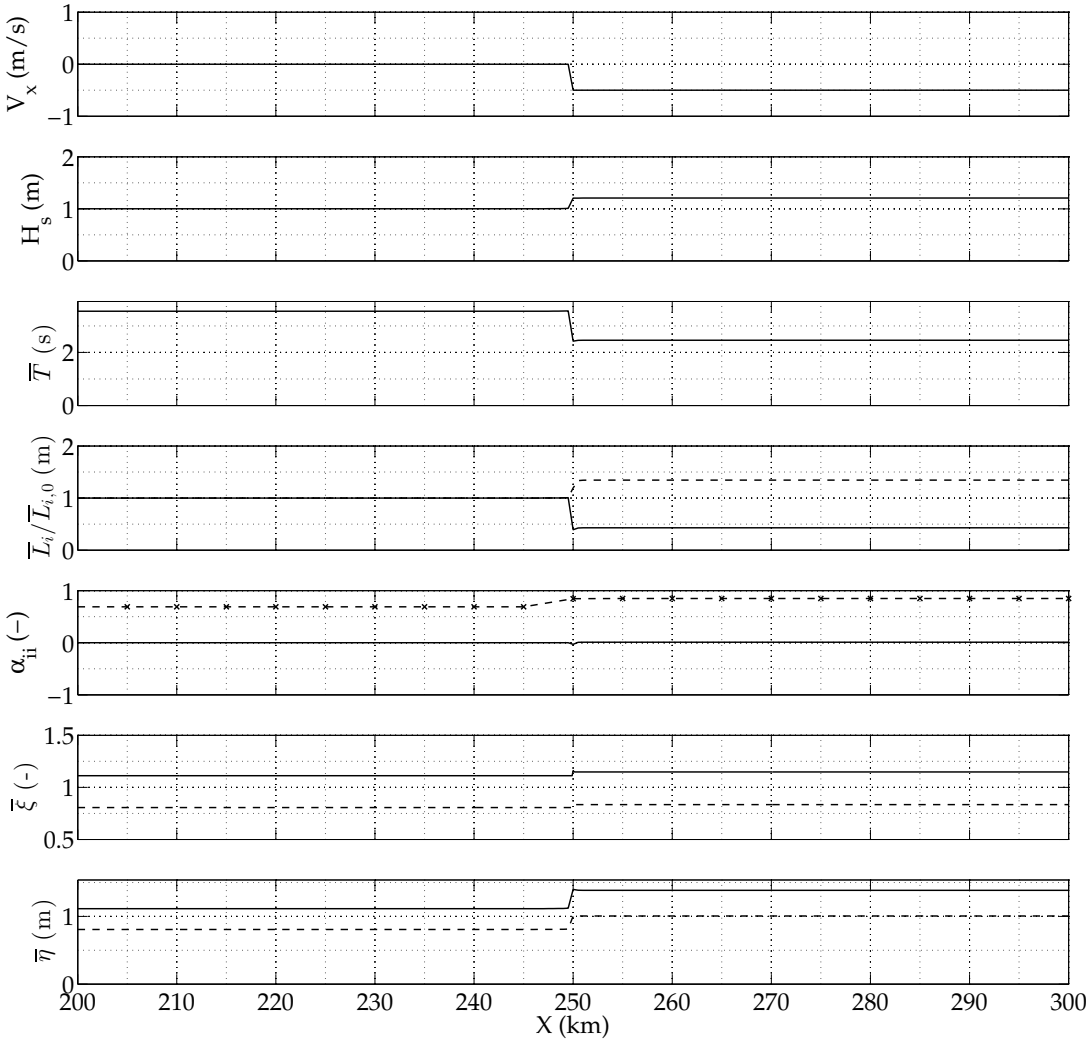

Figure 7.15: Wave-current interactions effect on space-time extremes: Pierson-Moskowitz spectrum with H_s=1.0 m, $V_x = -0.50$ m/s. $\overline{L}_i$ panel: wavelength (solid) and wave crest (dashed); α_{ii} panel: α_{xt} (dashed-crossed), α_{yt} (dotted) and α_{xy} (solid); $\overline{\xi}$ panel: $\overline{\xi}_{ST}$ (solid) and $\overline{\xi}_T$ (dashed); $\overline{\eta}$ panel: $\overline{\eta}_{ST}$ (solid) and $\overline{\eta}_T$ (dashed).

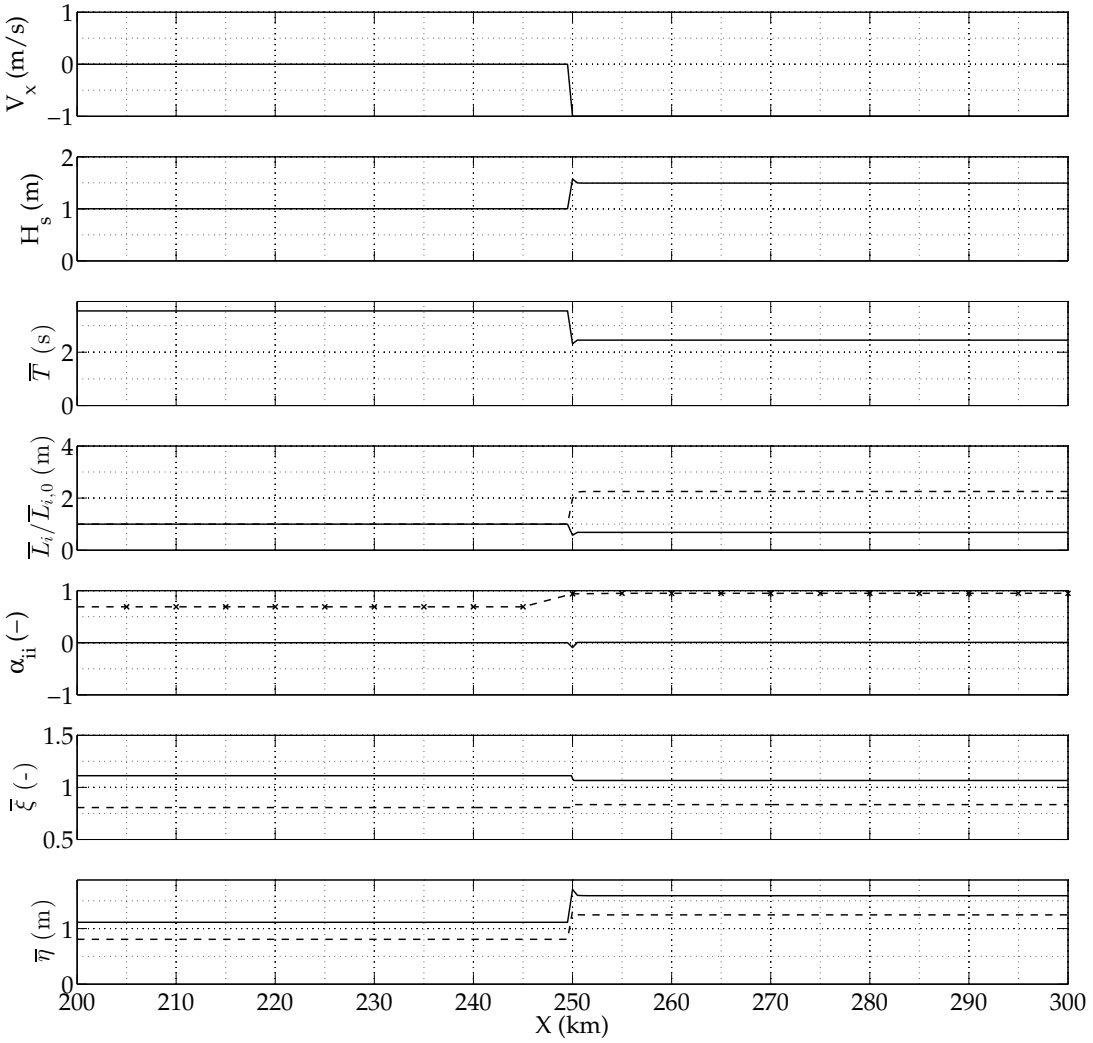

Figure 7.16: Wave-current interactions effect on space-time extremes: Pierson-Moskowitz spectrum with H_s=1.0 m, $V_x = -1.00$ m/s. $\overline{L}_i$ panel: wavelength (solid) and wave crest (dashed); α_{ii} panel: α_{xt} (dashed-crossed), α_{yt} (dotted) and α_{xy} (solid); $\overline{\xi}$ panel: $\overline{\xi}_{ST}$ (solid) and $\overline{\xi}_T$ (dashed); $\overline{\eta}$ panel: $\overline{\eta}_{ST}$ (solid) and $\overline{\eta}_T$ (dashed).

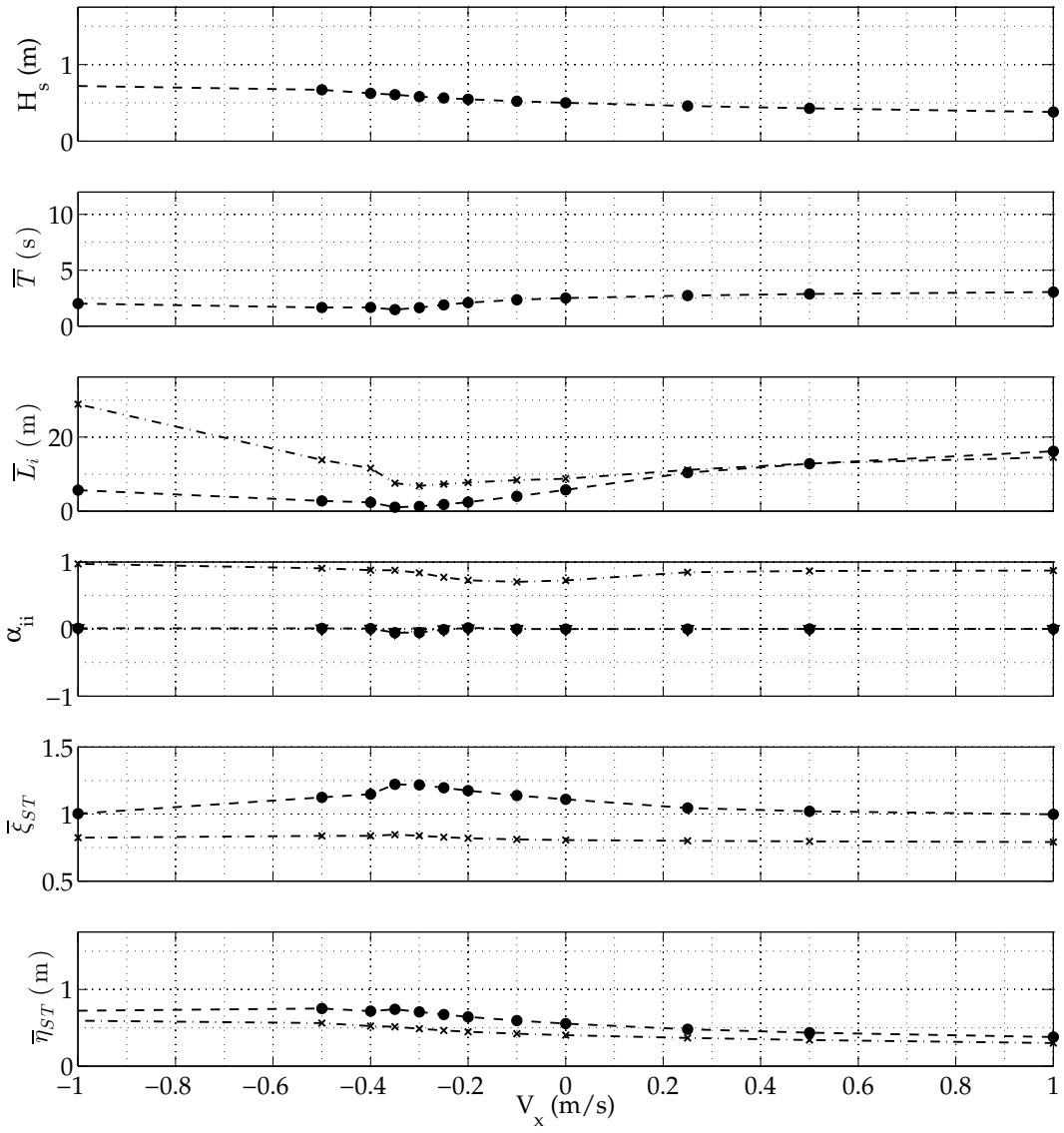

Figure 7.17: Wave-current interactions effect on space-time extremes: Pierson-Moskowitz spectrum with H_s=0.5 m. $\overline{L}_i$ panel: wavelength (dashed-dotted) and wave crest (dashed-crossed); α_{ii} panel: α_{xt} (dashed-crossed), α_{yt} (dashed-triangled) and α_{xy} (dashed-dotted); $\overline{\xi}$ panel: $\overline{\xi}_{ST}$ (solid) and $\overline{\xi}_T$ (dashed); $\overline{\eta}$ panel: $\overline{\eta}_{ST}$ (solid) and $\overline{\eta}_T$ (dashed).

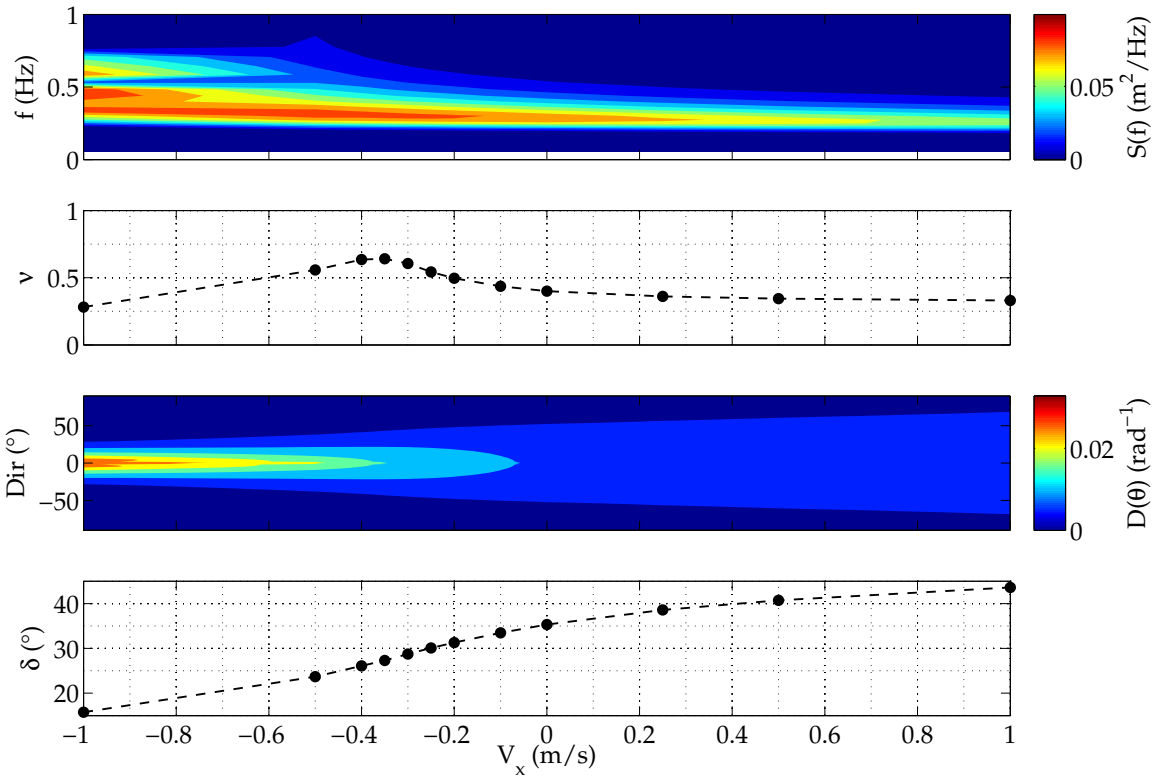

Figure 7.18: Wave-current interactions effect on directional spectra and spectral shape parameters: Pierson-Moskowitz spectrum with H_s=0.5 m.

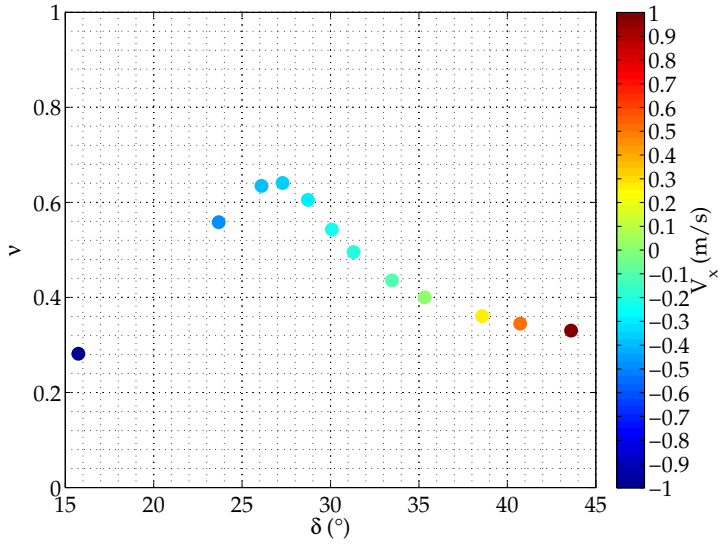

Figure 7.19: Wave-current interactions effect on spectral shape parameters: Pierson-Moskowitz spectrum with H_s=0.5 m.

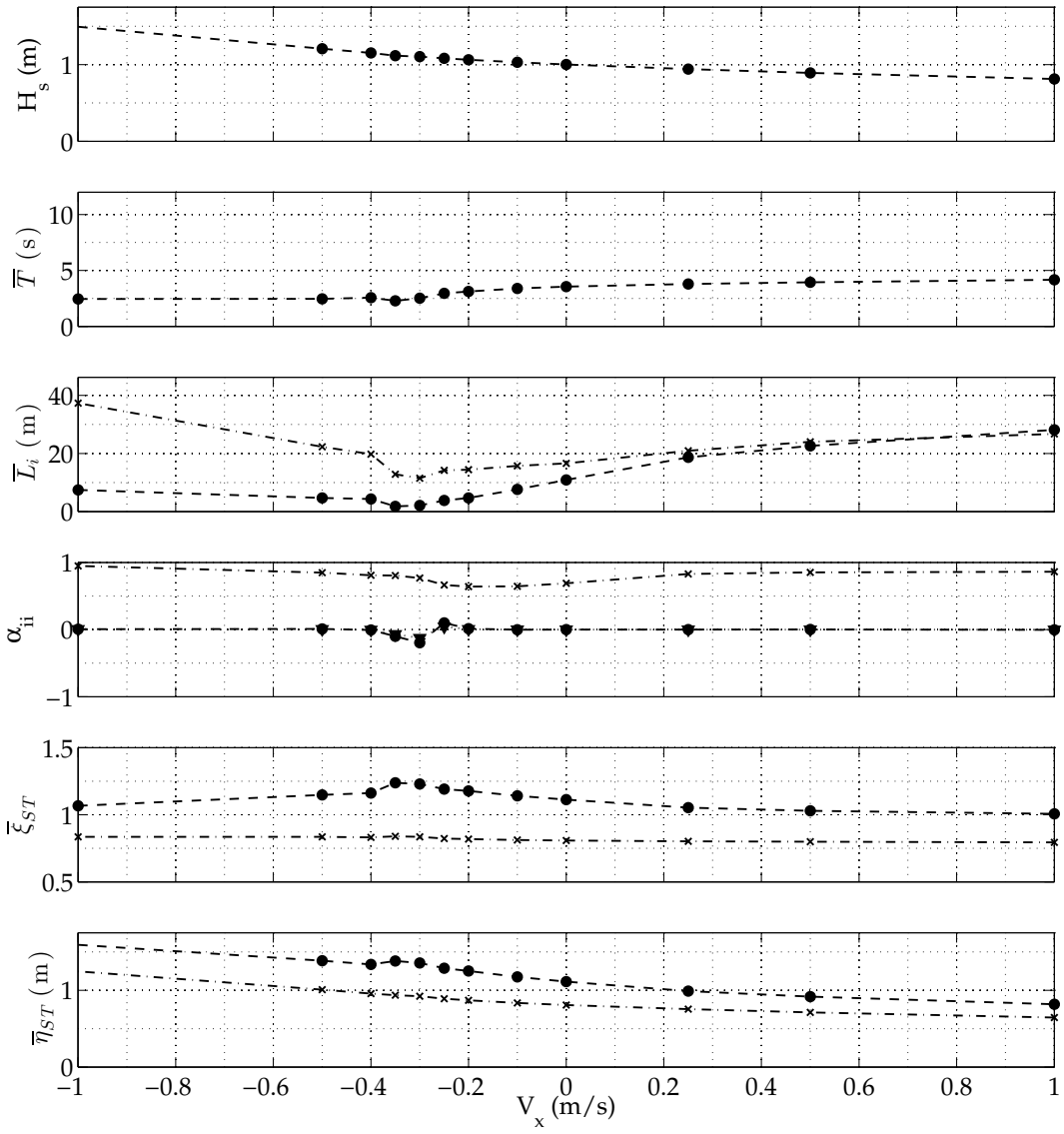

Figure 7.20: Wave-current interactions effect on space-time extremes: Pierson-Moskowitz spectrum with H_s=1.0 m. $\overline{L}_i$ panel: wavelength (dashed-dotted) and wave crest (dashed-crossed); α_{ii} panel: α_{xt} (dashed-crossed), α_{yt} (dashed-triangled) and α_{xy} (dashed-dotted); $\overline{\xi}$ panel: $\overline{\xi}_{ST}$ (solid) and $\overline{\xi}_T$ (dashed); $\overline{\eta}$ panel: $\overline{\eta}_{ST}$ (solid) and $\overline{\eta}_T$ (dashed).

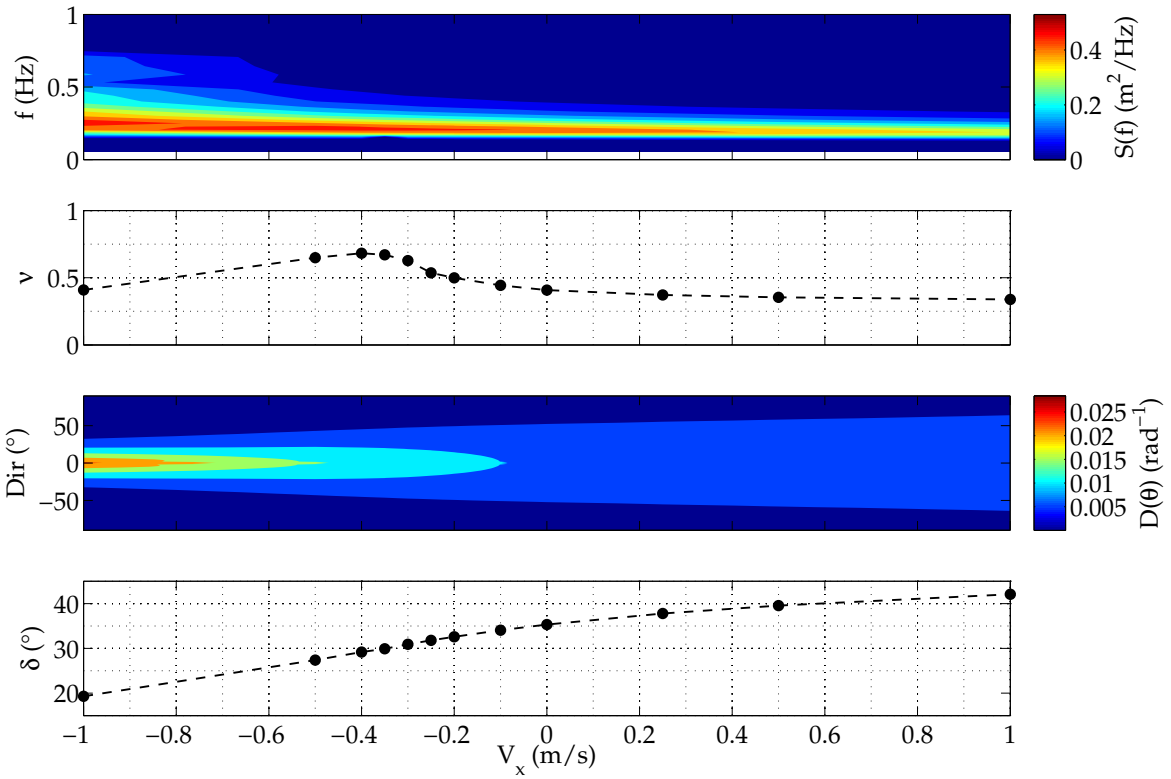

Figure 7.21: Wave-current interactions effect on directional spectra and spectral shape parameters: Pierson-Moskowitz spectrum with H_s=1.0 m.

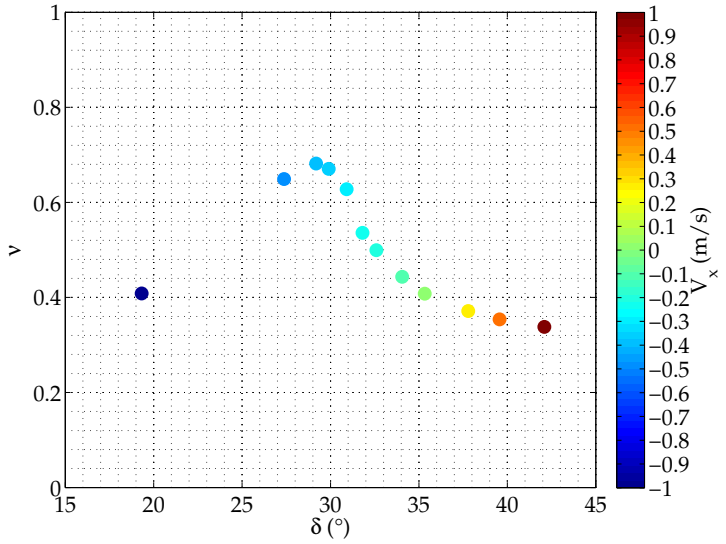

Figure 7.22: Wave-current interactions effect on spectral shape parameters: Pierson-Moskowitz spectrum with H_s=1.0 m.

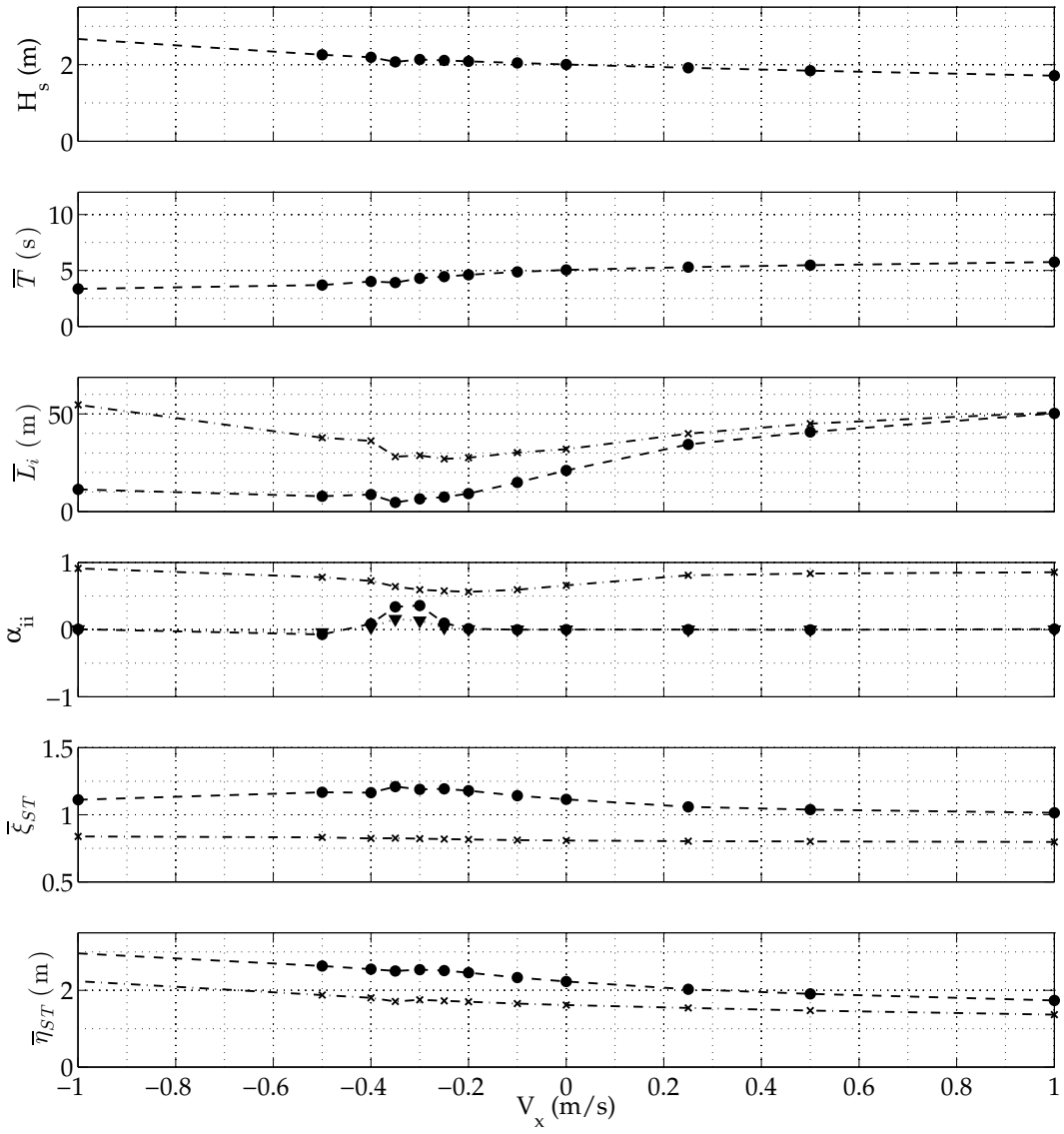

Figure 7.23: Wave-current interactions effect on space-time extremes: Pierson-Moskowitz spectrum with H_s=2.0 m. $\overline{L}_i$ panel: wavelength (dashed-dotted) and wave crest (dashed-crossed); α_{ii} panel: α_{xt} (dashed-crossed), α_{yt} (dashed-triangled) and α_{xy} (dashed-dotted); $\overline{\xi}$ panel: $\overline{\xi}_{ST}$ (solid) and $\overline{\xi}_T$ (dashed); $\overline{\eta}$ panel: $\overline{\eta}_{ST}$ (solid) and $\overline{\eta}_T$ (dashed).

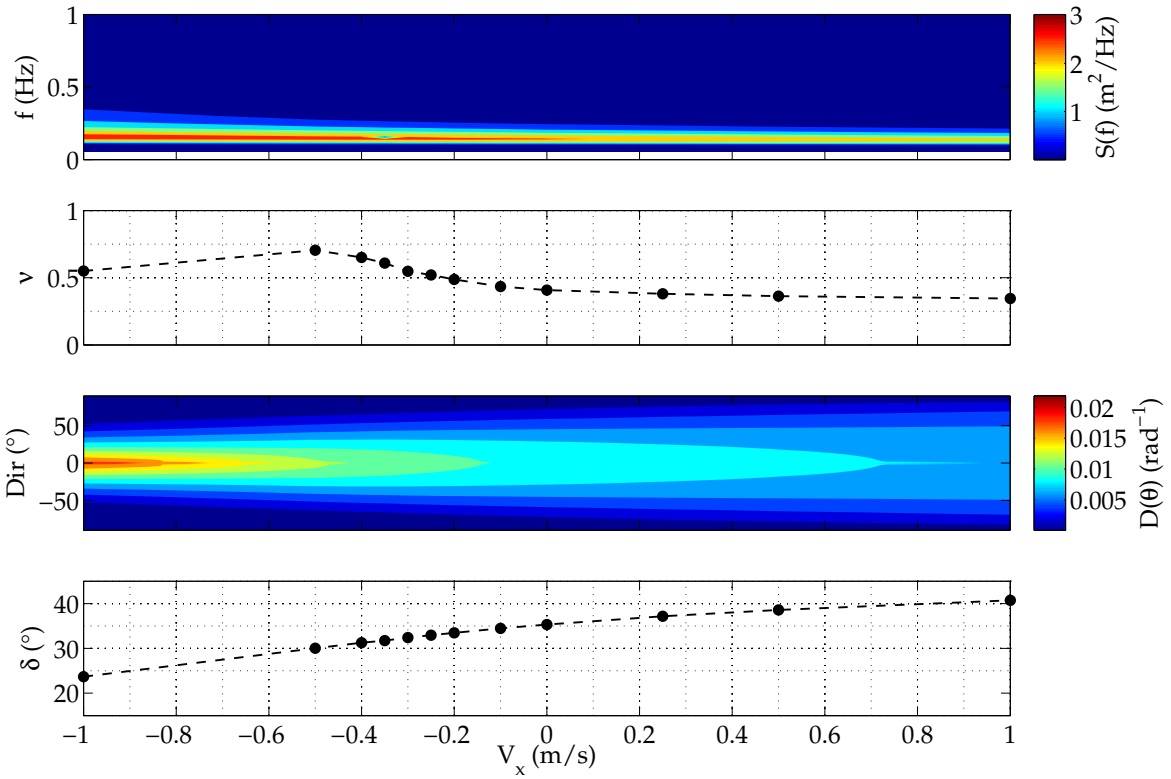

Figure 7.24: Wave-current interactions effect on directional spectra and spectral shape parameters: Pierson-Moskowitz spectrum with H_s=2.0 m.

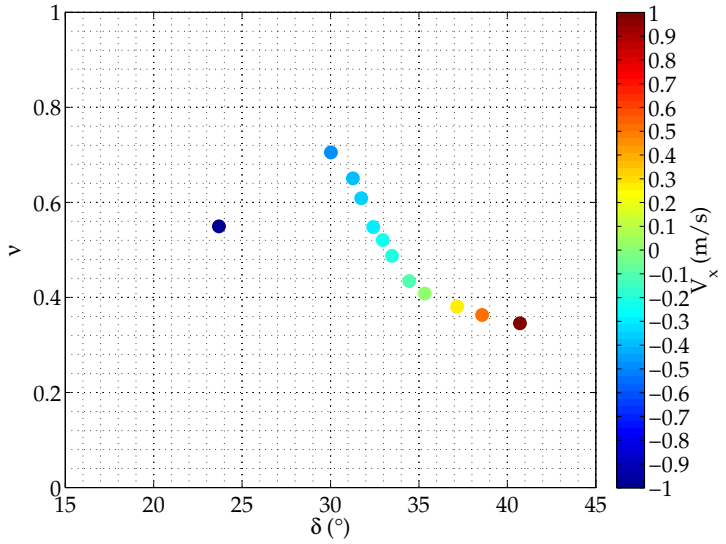

Figure 7.25: Wave-current interactions effect on spectral shape parameters: Pierson-Moskowitz spectrum with H_s=2.0 m.

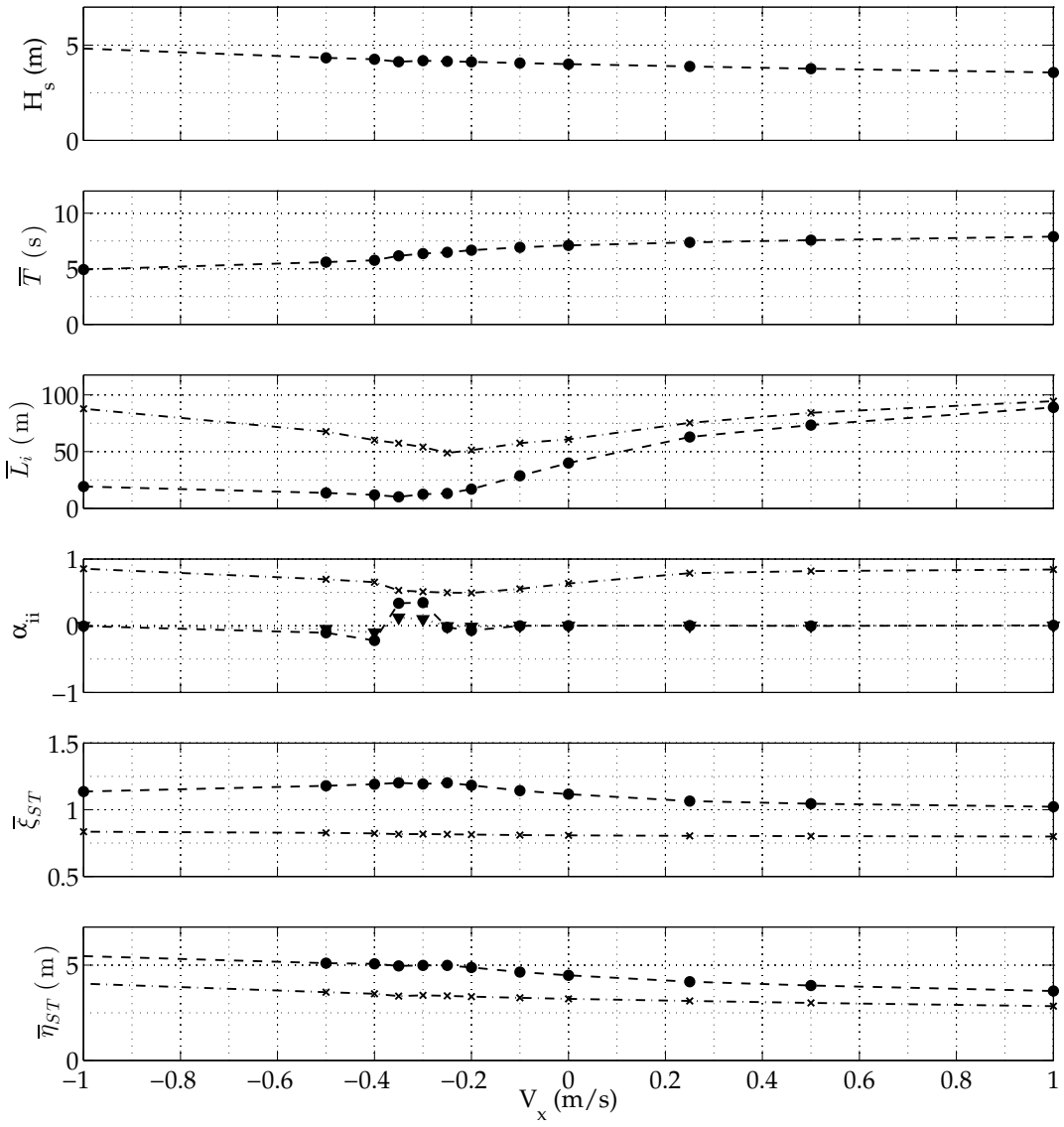

Figure 7.26: Wave-current interactions effect on space-time extremes: Pierson-Moskowitz spectrum with H_s=4.0 m. $\overline{L}_i$ panel: wavelength (dashed-dotted) and wave crest (dashed-crossed); α_{ii} panel: α_{xt} (dashed-crossed), α_{yt} (dashed-triangled) and α_{xy} (dashed-dotted); $\overline{\xi}$ panel: $\overline{\xi}_{ST}$ (solid) and $\overline{\xi}_T$ (dashed); $\overline{\eta}$ panel: $\overline{\eta}_{ST}$ (solid) and $\overline{\eta}_T$ (dashed).

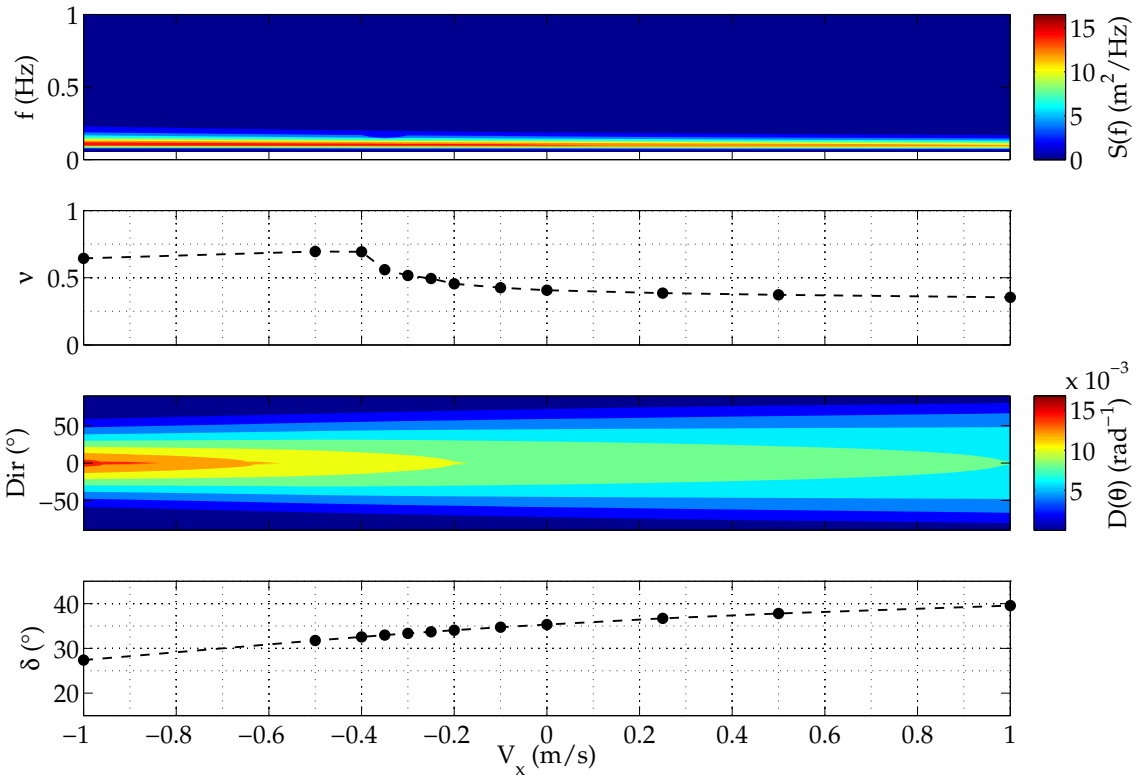

Figure 7.27: Wave-current interactions effect on directional spectra and spectral shape parameters: Pierson-Moskowitz spectrum with H_s=4.0 m.

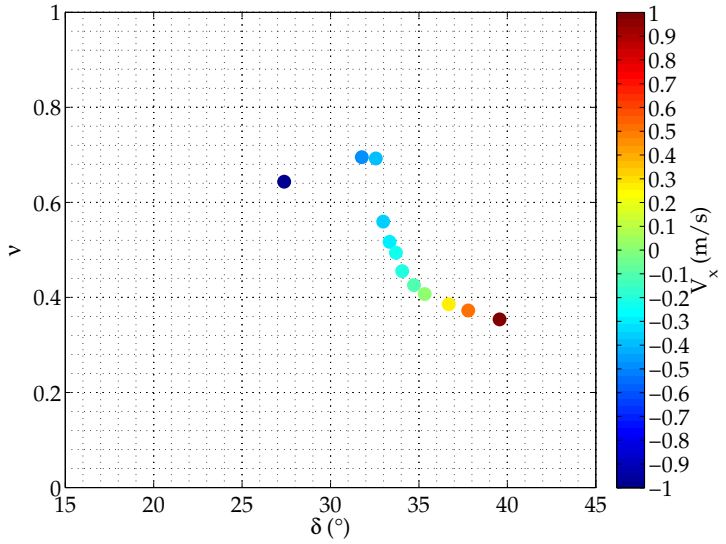

Figure 7.28: Wave-current interactions effect on spectral shape parameters: Pierson-Moskowitz spectrum with H_s=4.0 m.

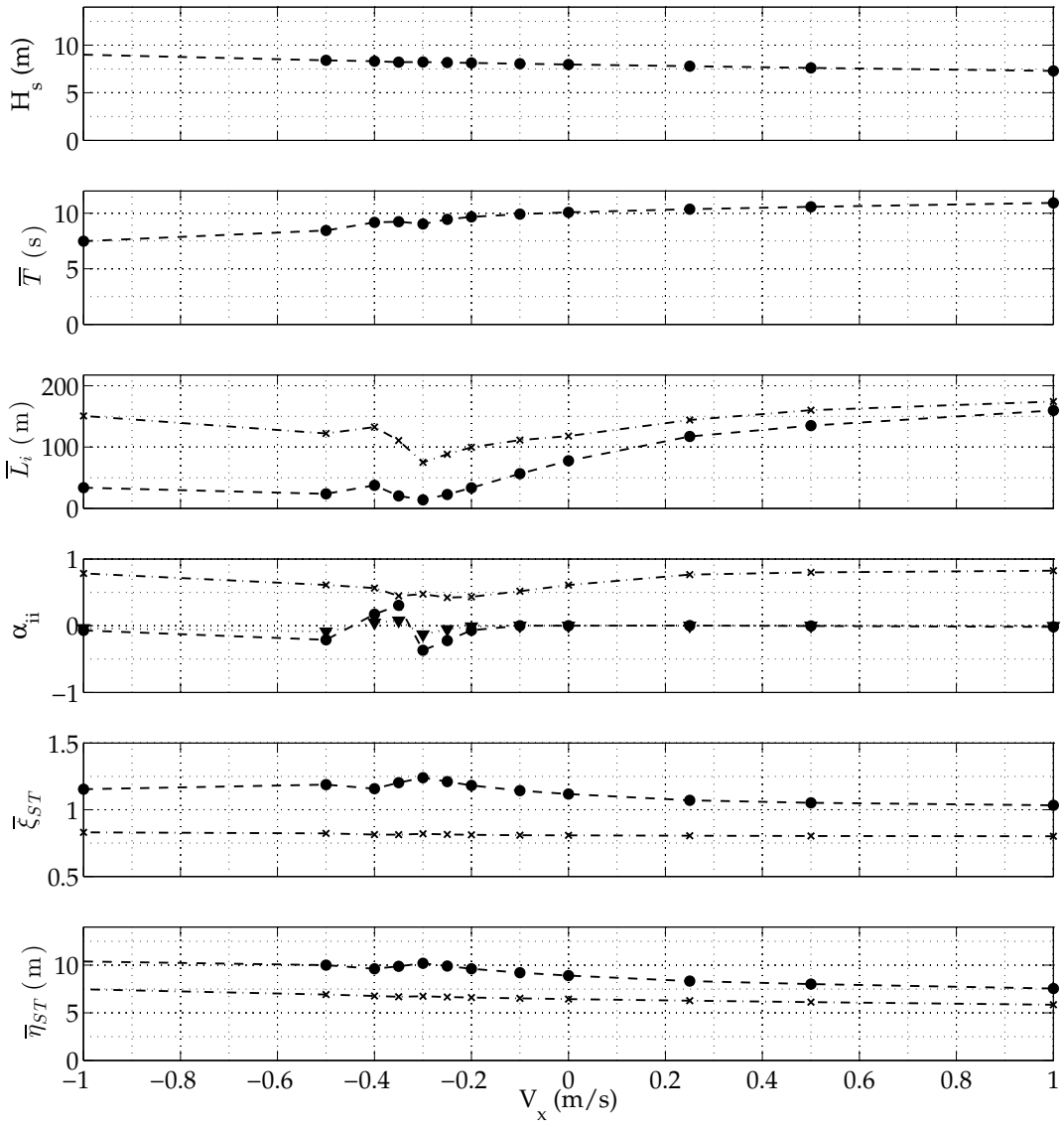

Figure 7.29: Wave-current interactions effect on space-time extremes: Pierson-Moskowitz spectrum with H_s=8.0 m. $\overline{L}_i$ panel: wavelength (dashed-dotted) and wave crest (dashed-crossed); α_{ii} panel: α_{xt} (dashed-crossed), α_{yt} (dashed-triangled) and α_{xy} (dashed-dotted); $\overline{\xi}$ panel: $\overline{\xi}_{ST}$ (solid) and $\overline{\xi}_T$ (dashed); $\overline{\eta}$ panel: $\overline{\eta}_{ST}$ (solid) and $\overline{\eta}_T$ (dashed).

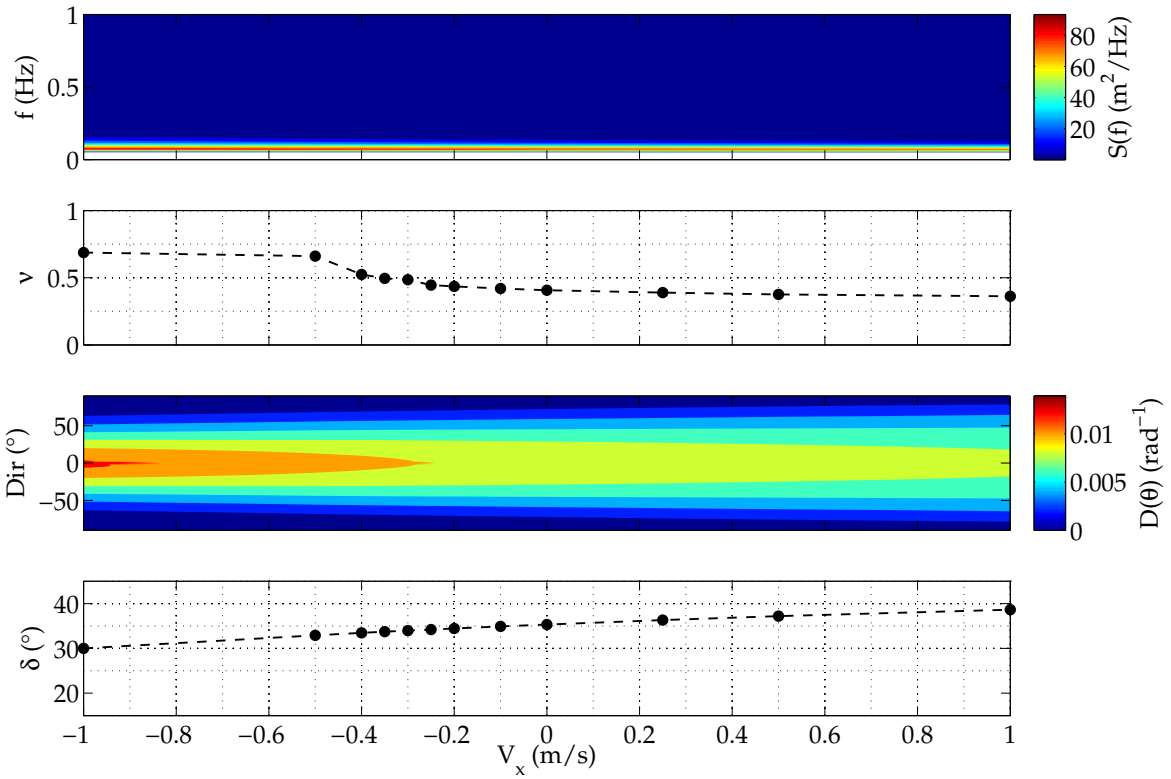

Figure 7.30: Wave-current interactions effect on directional spectra and spectral shape parameters: Pierson-Moskowitz spectrum with H_s=8.0 m.

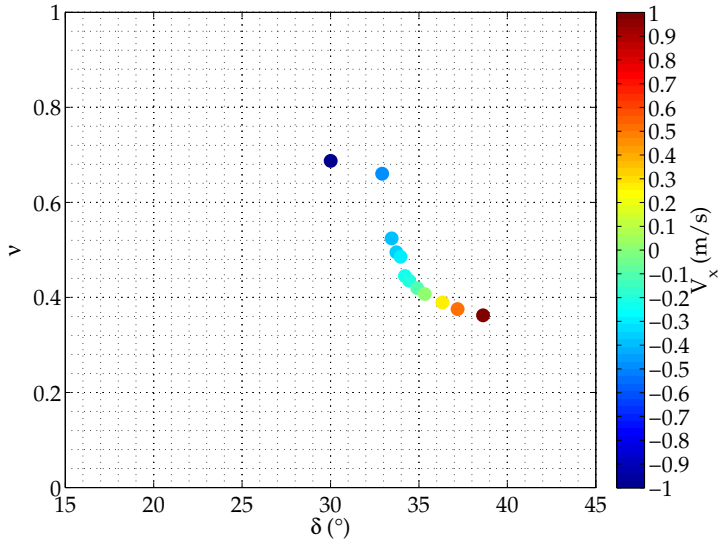

Figure 7.31: Wave-current interactions effect on spectral shape parameters: Pierson-Moskowitz spectrum with H_s=8.0 m.

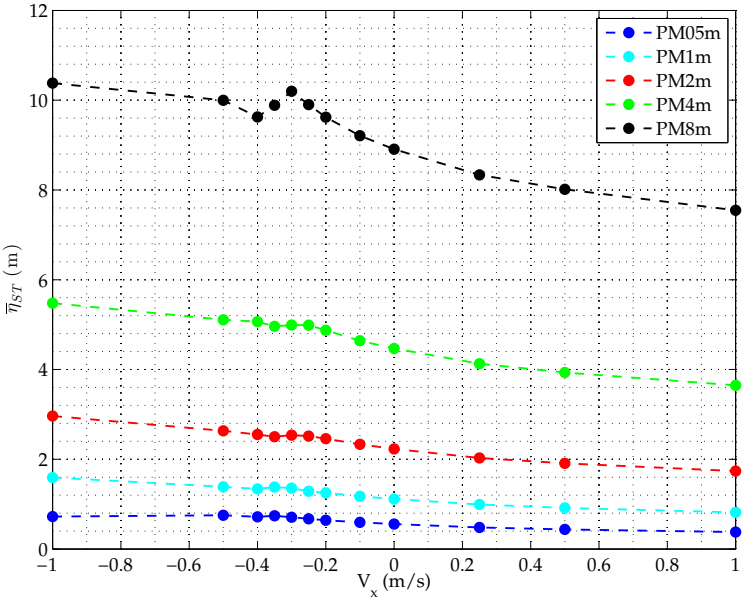

Figure 7.32: Wave-current interactions effect on space-time extremes $\overline{\eta}_{ST}$.

Finally, results for all the sea severities and velocities we tested are summarized in Figures from Figure 7.32 to Figure 7.34. Figure 7.32 shows that $\overline{\eta}_{ST}$ grew higher in presence of opposing (i.e. negative) currents. All the sea severities tested exhibited the same behavior, that is however enhanced for the highest H_s. On the contrary, a following (i.e. positive) current reduced $\overline{\eta}_{ST}$. What described is consistent with the mechanics of wave-current interactions (e.g., see Holthuijsen (2007)). It is worthwhile to notice that all the experimental curves of Figure. 7.32 have a singularity at approximately -0.3 m/s. To interpret this fact, we normalized space-time extremes on sea severity H_s, looking at $\overline{\xi}_{ST}$, which is depicted in Figure 7.33. Indeed, we observed more clearly singularities between -0.25 and -0.35 m/s. Here, $\overline{\xi}_{ST}$ exhibited an absolute maximum and after this it sharply decayed. This behavior in presence of opposing currents was almost certainly due to the blocking effect at the highest frequencies of the spectrum. In fact, the highest frequency waves modeled, i.e. 2 Hz, have blocking speed at -0.2 m/s, meaning that for negative values larger than this the tail of the spectrum began to experience loss of energy due to the impossibility of the highest frequencies of propagating against current. However, further investigations are planned to better interpret results in proximity of blocking speed.

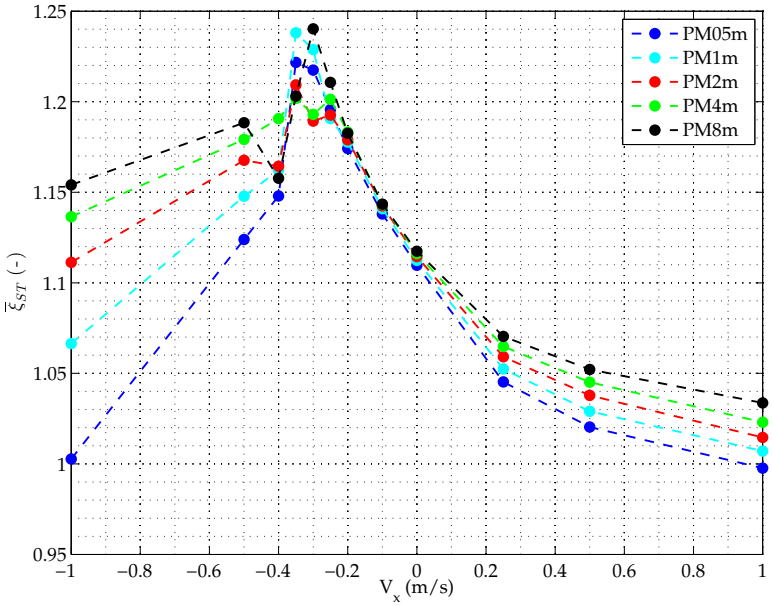

Figure 7.33: Wave-current interactions effect on space-time extremes $\overline{\xi}_{ST}$.

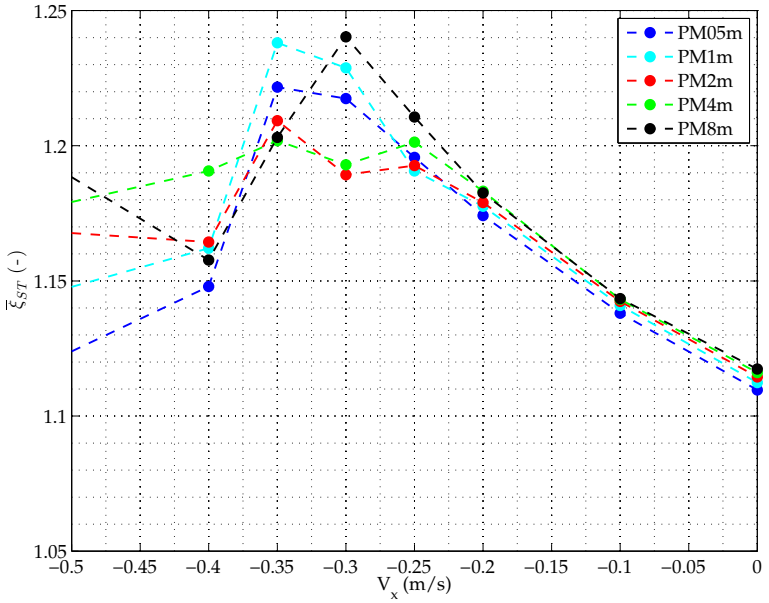

Figure 7.34: Wave-current interactions effect on space-time extremes $\overline{\xi}_{ST}$. Zoom on the discontinuity zone.

7.3.4 Results: shoaling

For shoaling effect tests, a single sea severity was tested, i.e. H_s =2.00 m (Pierson-Moskowitz spectrum). Three different bottom slopes were imposed: $\lambda = 1/1000$, $\lambda = 1/500$ and $\lambda = 1/100$. Depth difference, from -150.0 m to -1.0 m was the same of the three tests. We had no source terms in wave action density conservation equation, but for 1/500 test we tried to activate depth-induced breaking and bottom friction alternatively and simultaneously. Detailed results are shown in Figures, from Figure 7.35 to Figure 7.36. Here, we observed that the effect induced on space-time extremes $\overline{\eta}_{ST}$ by a sloping bottom, whichever it is, is consistent with the behavior of wave height H_s. Indeed, after an initial decrease, $\overline{\eta}_{ST}$ increased. However, $\overline{\eta}_{ST}$ increase never came with a $\overline{\xi}_{ST}$ increase. Besides this, the increase was always localized very close to the coast (here represented by -1.0 m depth), where depth-induced breaking was likely to occur. In fact, when the depth-induced breaking was activated (Figure 7.37), we did not observed any increase in $\overline{\eta}_{ST}$. Bottom friction caused the same effect but due to slightly different reasons. In fact, while $\overline{\eta}_{ST}$ did not increase, $\overline{\xi}_{ST}$ increased because wave crest $\overline{\mathrm{L}}_y$ significantly dropped and so the number of waves significantly increased. When both processes were activated, they combined but bottom friction effect seemed to prevail.

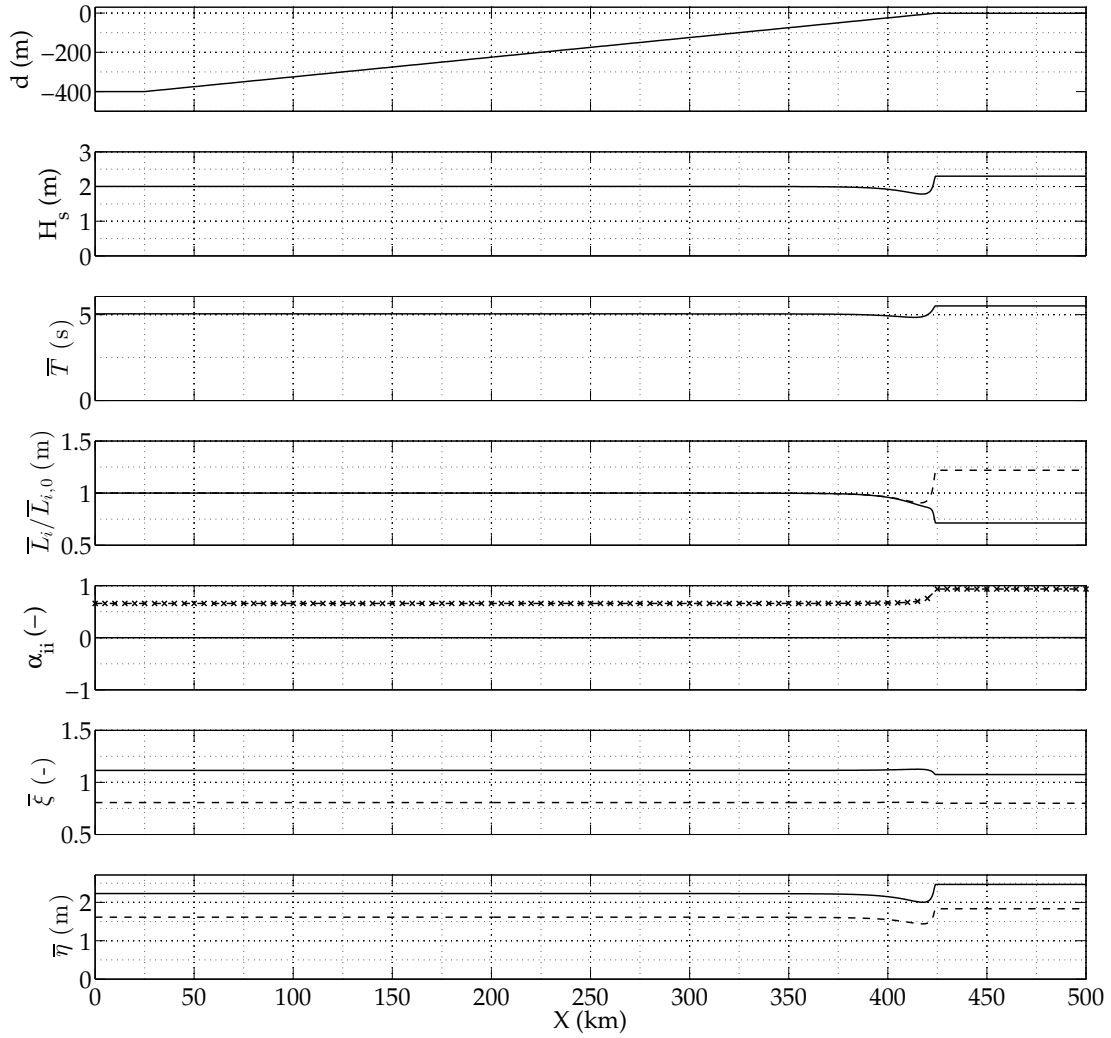

Figure 7.35: Shoaling effect on space-time extremes: Pierson-Moskowitz spectrum with H_s=2.0 m, $\lambda = 1/1000$. $\overline{L}_i$ panel: wavelength (solid) and wave crest (dashed); α_{ii} panel: α_{xt} (dashed), α_{yt} (dashed-dotted) and α_{xy} (solid); $\overline{\xi}$ panel: $\overline{\xi}_{ST}$ (solid) and $\overline{\xi}_T$ (dashed); $\overline{\eta}$ panel: $\overline{\eta}_{ST}$ (solid) and $\overline{\eta}_T$ (dashed).

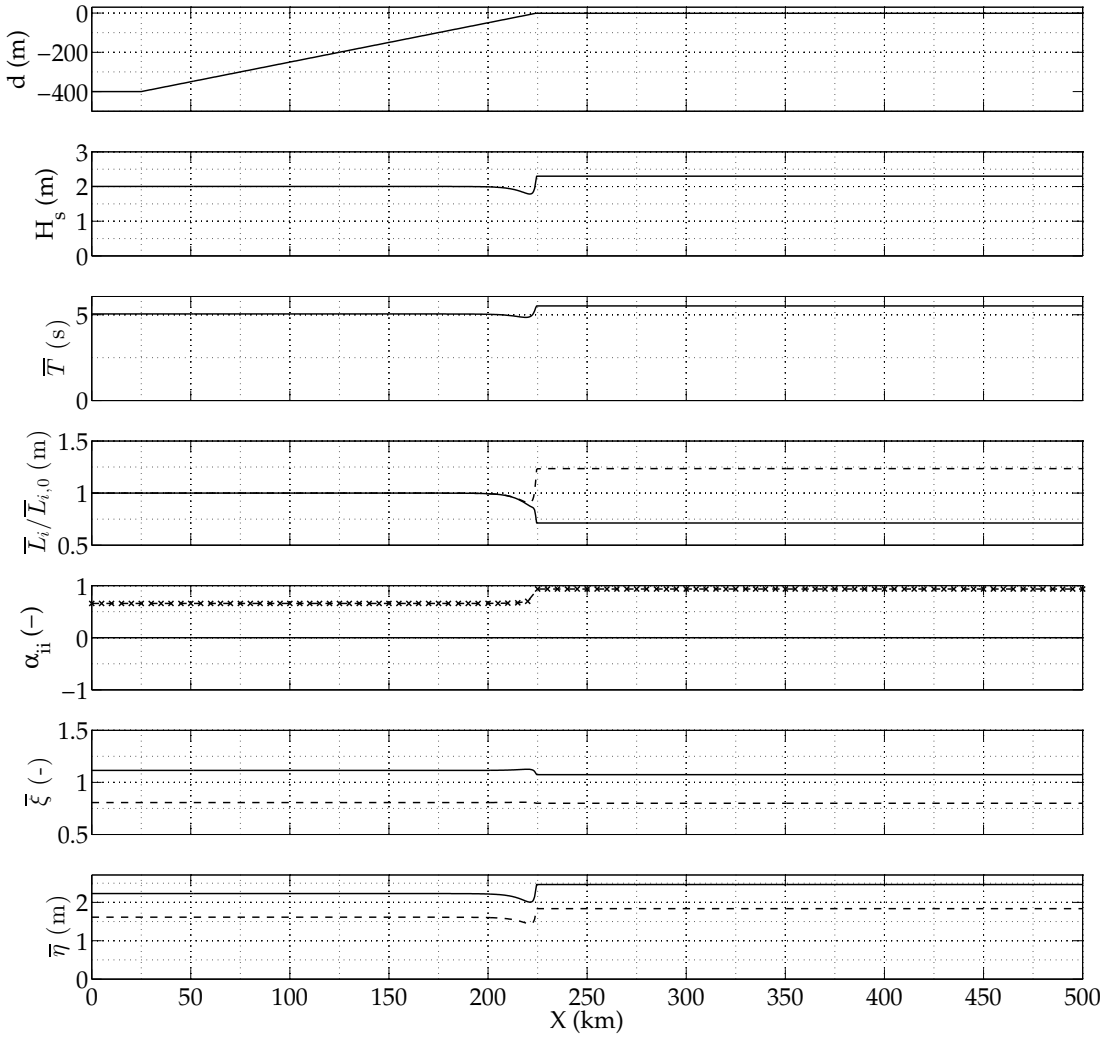

Figure 7.36: Shoaling effect on space-time extremes: Pierson-Moskowitz spectrum with H_s=2.0 m, $\lambda = 1/500$. $\overline{L}_i$ panel: wavelength (solid) and wave crest (dashed); α_{ii} panel: α_{xt} (dashed), α_{yt} (dashed-dotted) and α_{xy} (solid); $\overline{\xi}$ panel: $\overline{\xi}_{ST}$ (solid) and $\overline{\xi}_T$ (dashed); $\overline{\eta}$ panel: $\overline{\eta}_{ST}$ (solid) and $\overline{\eta}_T$ (dashed).

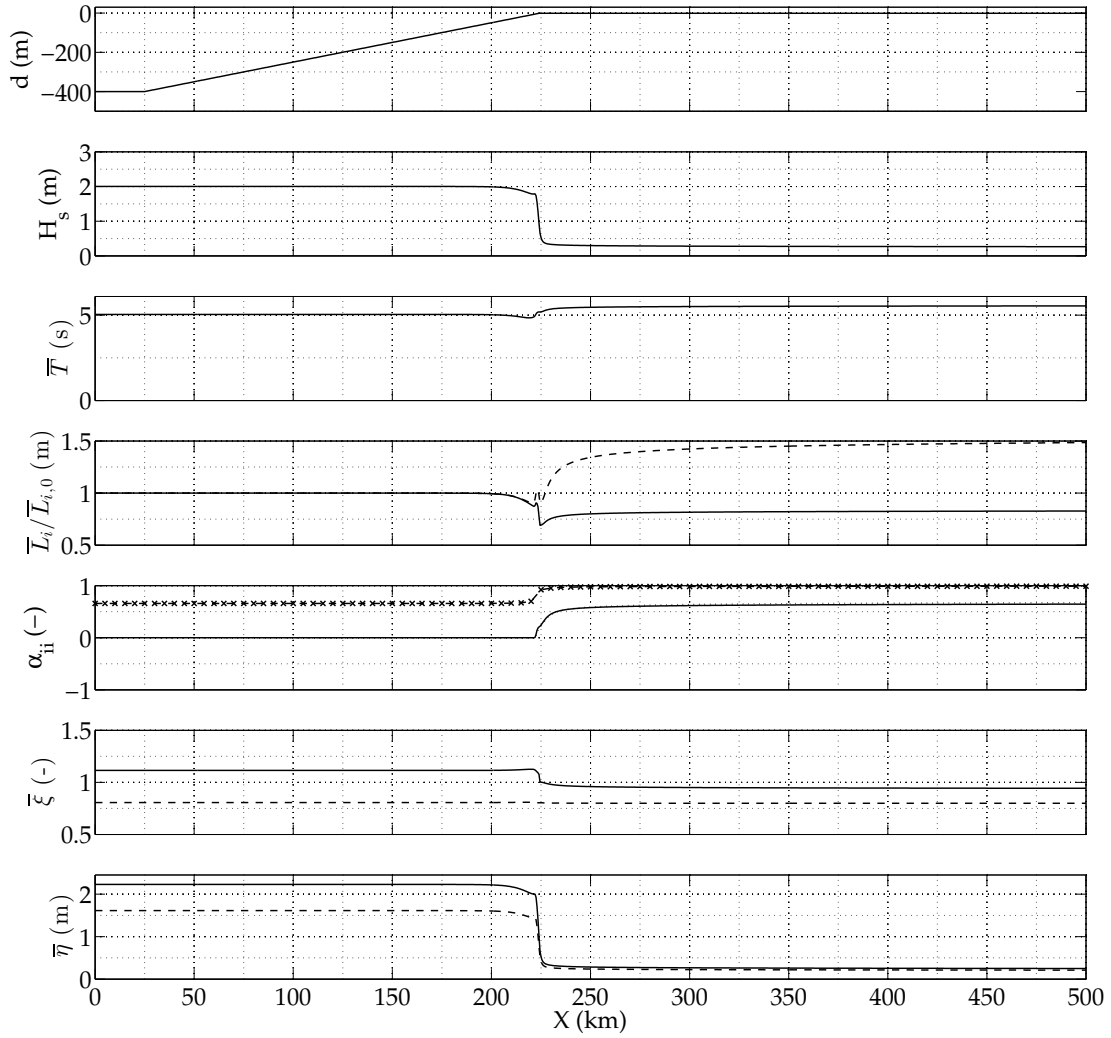

Figure 7.37: Shoaling effect on space-time extremes: Pierson-Moskowitz spectrum with H_s=2.0 m, $\lambda = 1/500$, depth-induced breaking activated. $\overline{L}_i$ panel: wavelength (solid) and wave crest (dashed); α_{ii} panel: α_{xt} (dashed), α_{yt} (dashed-dotted) and α_{xy} (solid); $\overline{\xi}$ panel: $\overline{\xi}_{ST}$ (solid) and $\overline{\xi}_T$ (dashed); $\overline{\eta}$ panel: $\overline{\eta}_{ST}$ (solid) and $\overline{\eta}_T$ (dashed).

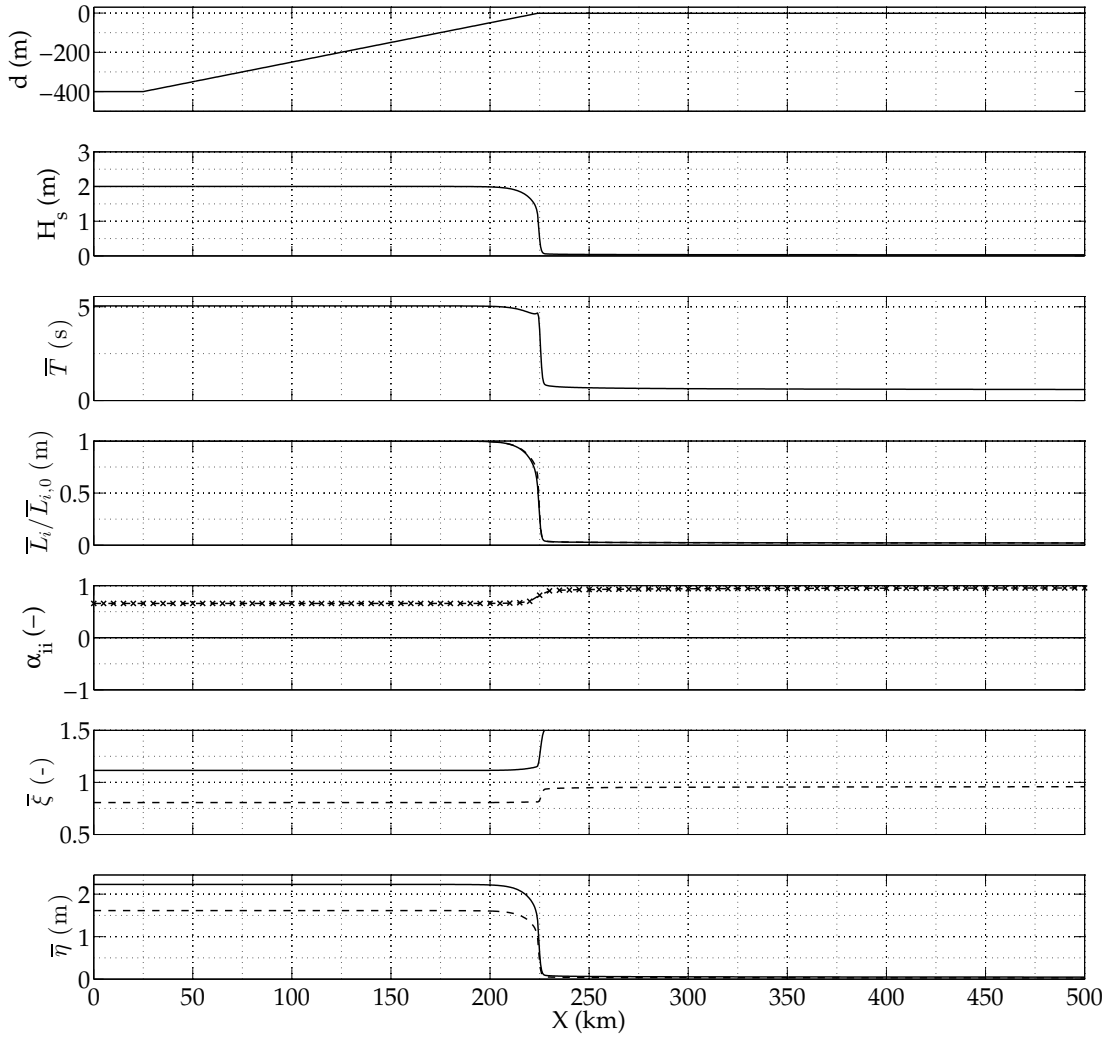

Figure 7.38: Shoaling effect on space-time extremes: Pierson-Moskowitz spectrum with H_s=2.0 m, $\lambda = 1/500$, bottom friction activated. $\overline{L}_i$ panel: wavelength (solid) and wave crest (dashed); α_{ii} panel: α_{xt} (dashed), α_{yt} (dashed-dotted) and α_{xy} (solid); $\overline{\xi}$ panel: $\overline{\xi}_{ST}$ (solid) and $\overline{\xi}_T$ (dashed); $\overline{\eta}$ panel: $\overline{\eta}_{ST}$ (solid) and $\overline{\eta}_T$ (dashed).

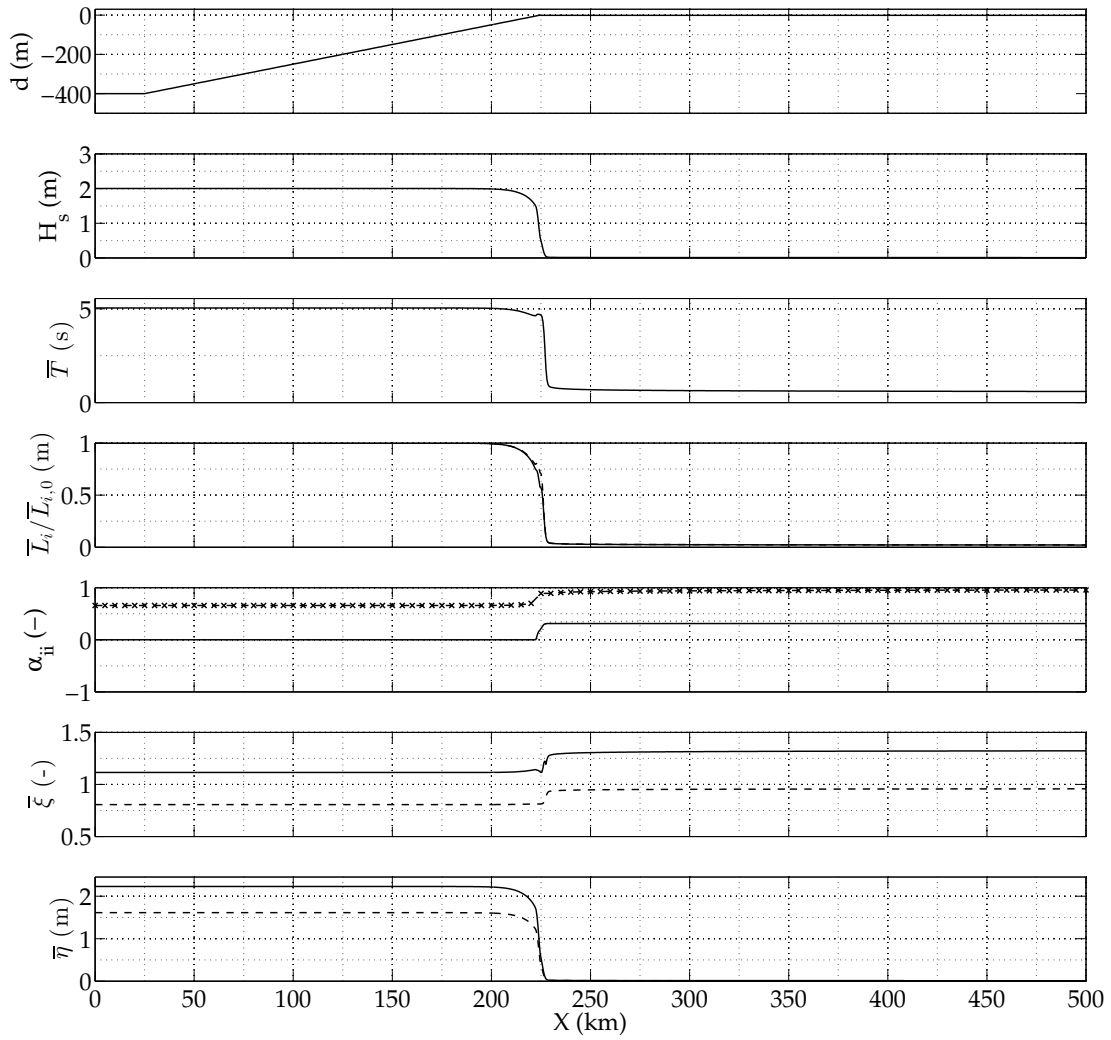

Figure 7.39: Shoaling effect on space-time extremes: Pierson-Moskowitz spectrum with H_s=2.0 m, $\lambda = 1/500$, depth-induced breaking and bottom friction activated. $\overline{L}_i$ panel: wavelength (solid) and wave crest (dashed); α_{ii} panel: α_{xt} (dashed), α_{yt} (dashed-dotted) and α_{xy} (solid); $\overline{\xi}$ panel: $\overline{\xi}_{ST}$ (solid) and $\overline{\xi}_T$ (dashed); $\overline{\eta}$ panel: $\overline{\eta}_{ST}$ (solid) and $\overline{\eta}_T$ (dashed).

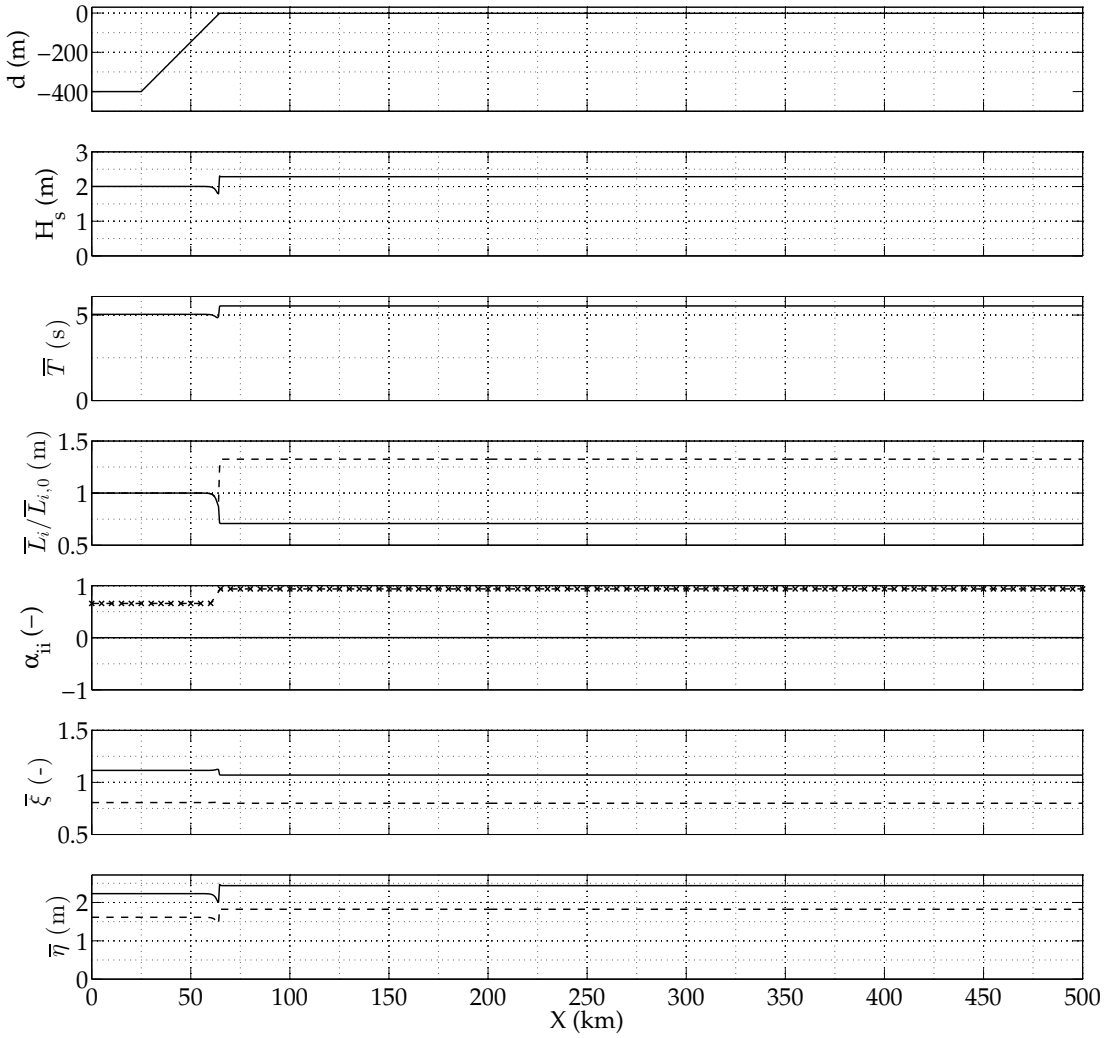

Figure 7.40: Shoaling effect on space-time extremes: Pierson-Moskowitz spectrum with H_s=2.0 m, $\lambda = 1/100$. $\overline{L}_i$ panel: wavelength (solid) and wave crest (dashed); α_{ii} panel: α_{xt} (dashed), α_{yt} (dashed-dotted) and α_{xy} (solid); $\overline{\xi}$ panel: $\overline{\xi}_{ST}$ (solid) and $\overline{\xi}_T$ (dashed); $\overline{\eta}$ panel: $\overline{\eta}_{ST}$ (solid) and $\overline{\eta}_T$ (dashed).

7.4 Test case: Mediterranean Sea states

In order to test the capability of SWAN-ST in predicting space-time extremes on complex realistic conditions we set up a Mediterranean Sea model. We benefitted of high-resolution wind fields to hindcast 3 years (2008-2010) of Mediterranean sea states. Fedele's model (in its linear version, i.e. without second-order corrections) was then applied thanks to spectral parameters computed by SWAN-ST at each computational grid node and time step. We chose it with respect to Piterbarg's theorem because we focused on the model that provided the more accurate predictions, according to results of Chapter 4. At this step, we performed the space-time extremes analysis by considering fixed space and time domains. This kind of analysis could be employed for example for operational forecasts aimed at defining safe routes for navigation.

7.4.1 Model set-up

The Mediterranean Sea model had a grid resolution of approximately 6x6 km^2 and a temporal resolution of 1200 s. To set-up the domain, depicted in Fig. 7.41, ETOPO-1 (http://www.ngdc.noaa.gov/mgg/global/) and GSHHS-H (http://www.ngdc.noaa.gov/mgg/shorelines/gshhs.html) databases were used. The model was forced by COSMO-I7 (Steppeler et al., 2003) high resolution hourly wind fields (10 m above sea level). For this reason, Mediterranean Sea region was cropped to the entail COSMO-I7 modeled area (Fig. 7.41). Spectral space was discretized using 36 direction (within [0°,360°]) and 39 frequencies (within [0.05,2.00] Hz). The model was run in third generation mode, using a saturation-based whitecapping formulation with wind input from Yan (1987). Wave-wave interaction was modeled through DIA (8 fully explicit computations). Friction was modeled according to Madsen formulation (Madsen et al., 1988) and depth-induced breaking was assumed with default parameters. Numerical scheme employed was Backward Space-Backward Time (BSBT). Outputs were provided by SWAN-ST every hour and with computational grid resolution of 6 km.

7.4.2 Space-time extreme analysis of sea states

We implemented the model of Fedele on the spectral parameters calculated by SWAN-ST (mean wave period $\overline{T}$, mean wavelength components $\overline{L}_x$ and $\overline{L}_y$, space-space and space-time correlation parameters α_{xt}, α_{yt}, α_{xy}). Time domain D was fixed to 1 hour. Space domain $A = XY$ was chosen in order to reproduce the area covered by a container ship, e.g. MAERSK Eleonora. Hence, it was fixed to 24000 m^2. We limited Fedele's model es-

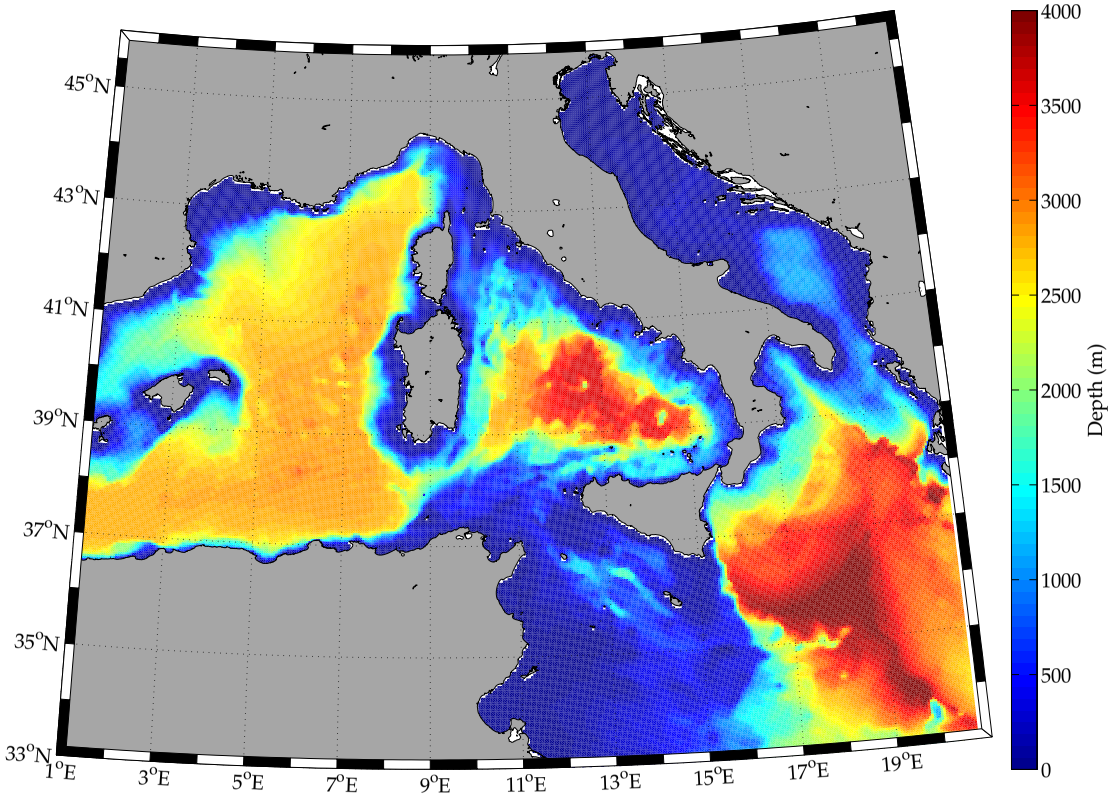

Figure 7.41: Mediterranean Sea computational domain for SWAN-ST simulations.

timates by using the breaking criterion (3.35). Hence, maximum allowed steepness was $\epsilon = 0.44$, according to Stokes breaking limit. At this step, extremes were calculated without applying non-linear correction, i.e. under a linear wave model assumption.

7.4.3 Validation

Prior to analyze results, we compared space-time extremes obtained from spectra at "Acqua Alta" tower and R/V "Urania" locations during experiments we used to validate Piterbarg's and Fedele's stochastic models (see Chapter 4). To this aim, SWAN-ST simulations of the first 6 months of 2013 were carried out with the same described model set-up. In this validation step, we accounted also for Piterbarg's theorem predictions, though Mediterranean Sea results were obtained only from Fedele's method application.

"Acqua Alta" tower experiment

In Figure 7.42, spectra computed by SWAN-ST and by EMEP technique from WASS data are compared. We observed an underestimation of wave variance by SWAN-ST, which can be ascribed to an underestimation of the input wind by COSMO-I7 model. Therefore, results of Piterbarg's (Figure 7.43-a) and Fedele's model (Figure 7.43-a) computed from SWAN-ST spectra underestimated the observations in terms of $\overline{\eta}_{ST}$. But if the space-time extremes are normalized on significant wave height (i.e. $\overline{\xi}_{ST}$), results resembled EMEP results with an excellent accuracy (Figure 7.43-b and Figure 7.44-b). In order to calculate $\overline{\eta}_{ST}$, we scaled SWAN-ST spectrum (Figure 7.42-a) with respect to EMEP spectrum (Figure 7.42-b) to recover the same significant wave height. To this end, we multiplied SWAN-ST spectrum by the zero-th moments ratio. Stochastic models results in terms of $\overline{\eta}_{ST}$ resembled very well the EMEP predictions, in particular for Fedele's model (Figure 7.45). This means that, apart from a total variance underestimation, spectra computed by SWAN-ST can be used to predict spec-time extremes with an accuracy comparable to that obtained from WASS measurements (Table 4.3).

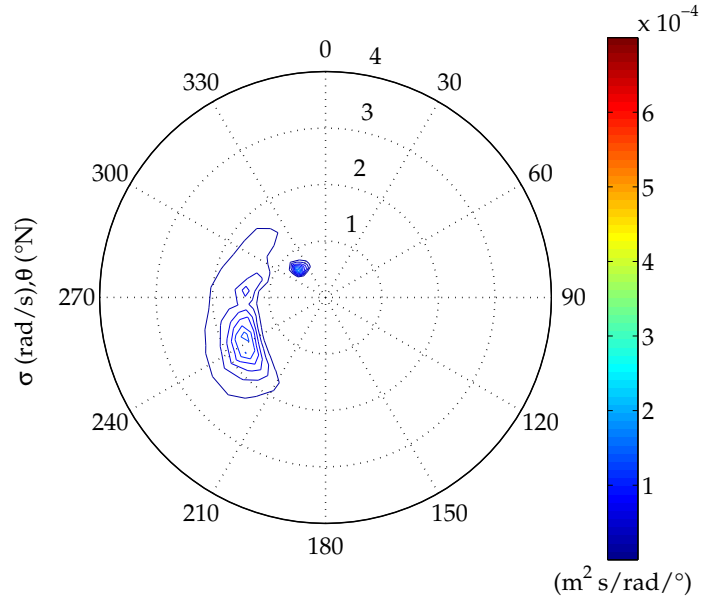

(a)

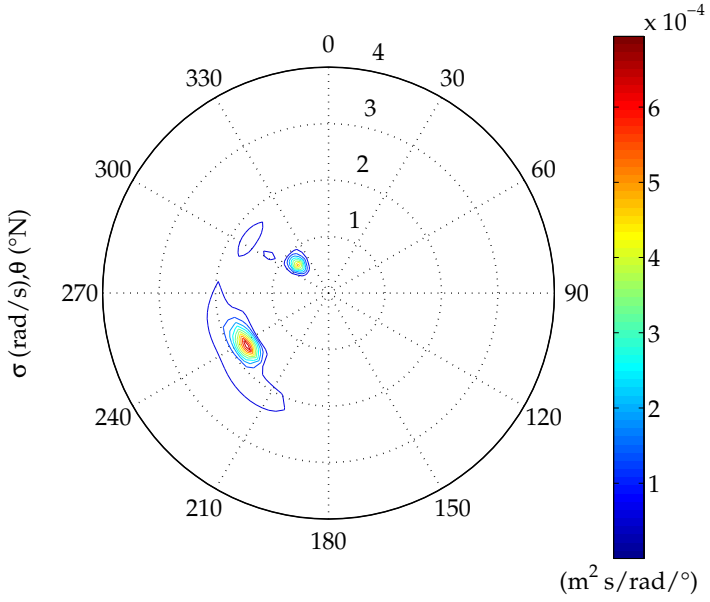

(b)

Figure 7.42: Directional spectrum $S(\sigma, \theta)$ at "Acqua Alta" tower, polar (σ, θ) coordinates. (a) $S(\sigma, \theta)$ from SWAN-ST runs. (b) $S(\sigma, \theta)$ from WASS measurements (EMEP). Directions are propagation directions.

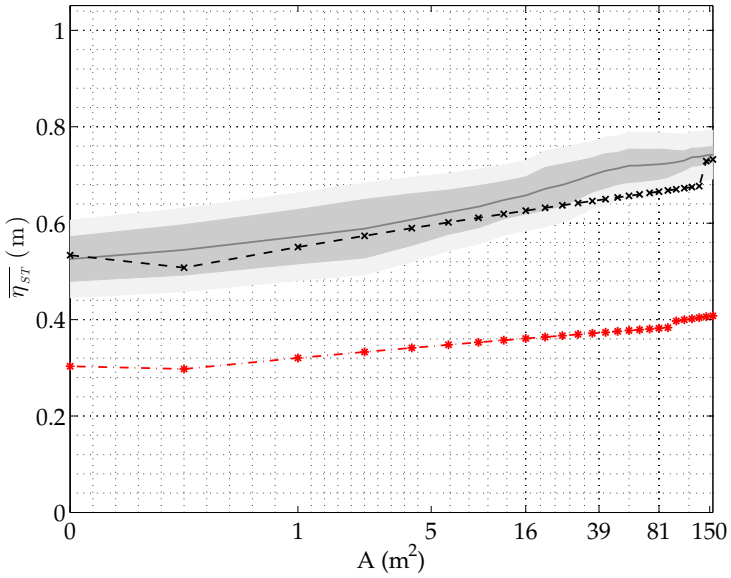

(a)

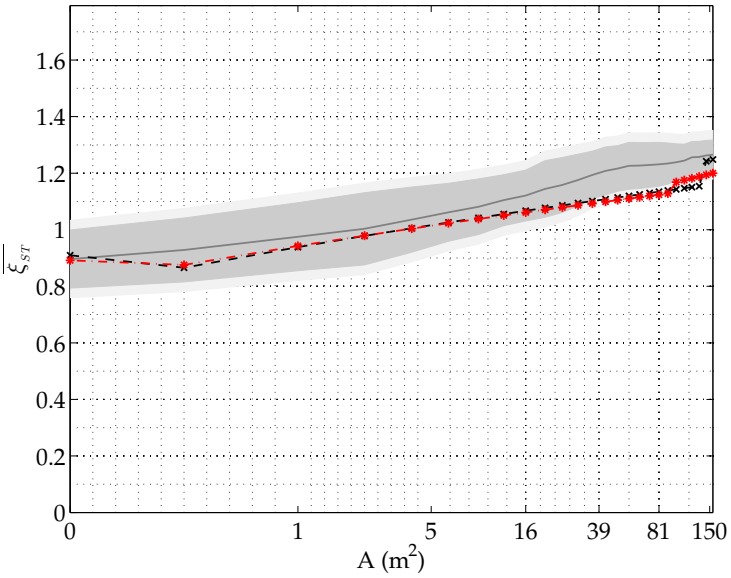

(b)

Figure 7.43: Piterbarg's model prediction (red crosses: SWAN-ST runs; black asterisks: EMEP) versus WASS observations (gray solid line): expected maximum over space-time as a function of area size. Observations are provided together with error bands (grey): the wider band (brighter gray) includes WASS error. (a) Non-normalized extremes $\overline{\eta}_{ST}$. (b) Normalized extremes $\overline{\xi}_{ST}$.

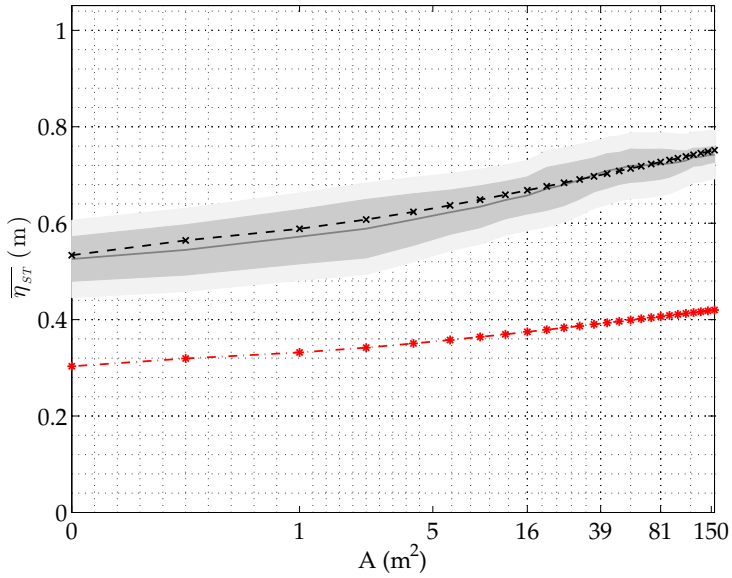

(a)

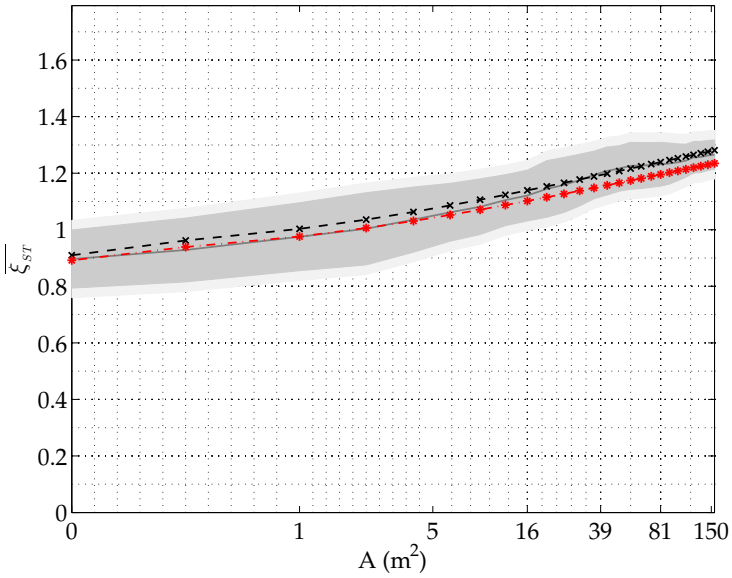

(b)

Figure 7.44: Fedele's model prediction (red crosses: SWAN-ST runs; black asterisks: EMEP) versus WASS observations (gray solid line): expected maximum over space-time as a function of area size. Observations are provided together with error bands (grey): the wider band (brighter gray) includes WASS error. (a) Non-normalized extremes $\overline{\eta}_{ST}$. (b) Normalized extremes $\overline{\xi}_{ST}$.

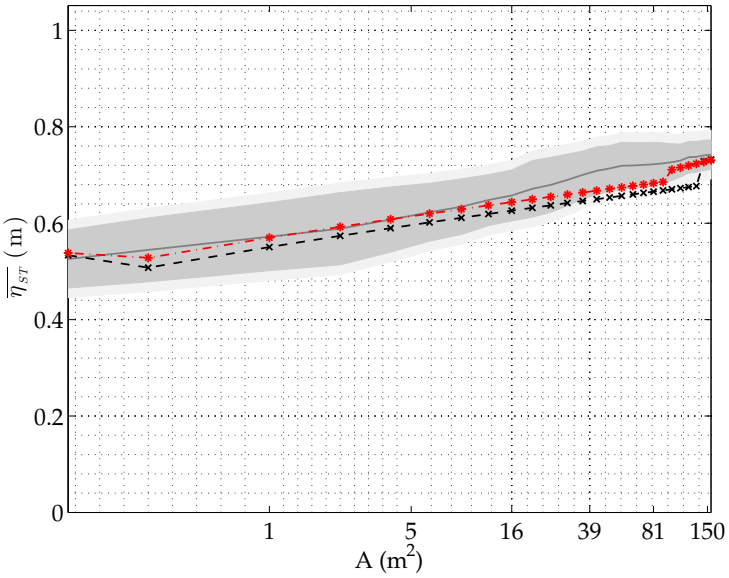

(a)

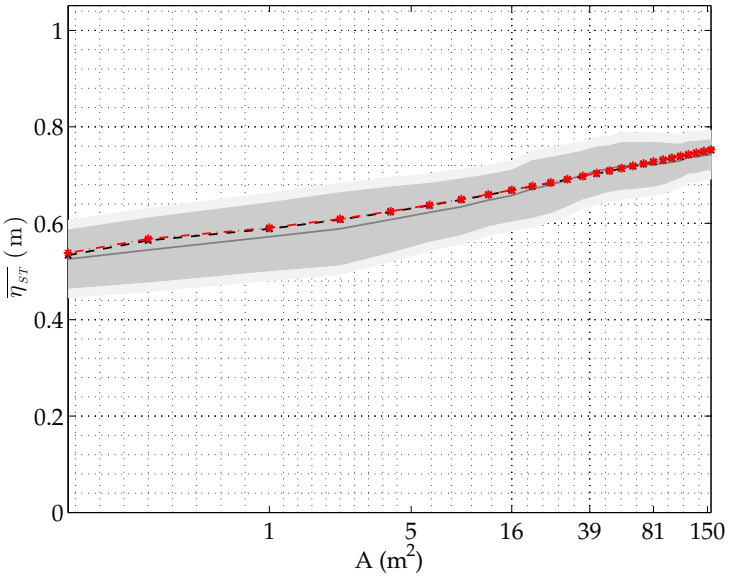

(b)

Figure 7.45: Stochastic models prediction (red crosses: SWAN-ST runs; black asterisks: EMEP) versus WASS observations (gray solid line): expected maximum over space-time as a function of area size. Observations are provided together with error bands (grey): the wider band (brighter gray) includes WASS error. SWAN-ST spectrum scaled by the ratio of zero-th moments r_{m0}. (a) Piterbarg's model. (b) Fedele's model.

R/V "Urania" experiment

In Figure 7.46, spectra computed by SWAN-ST and by EMEP technique from WASS data are compared. As for "Acqua Alta" experiment, we observed an underestimation of wave variance by SWAN-ST, which can be again ascribed to an underestimation of the input wind by COSMO-I7 model. Moreover, we noticed the presence of additional energy at a direction specular with respect to the peak. Therefore, results of Piterbarg's (Figure 7.47-a) and Fedele's model (Figure 7.47-a) computed from SWAN-ST spectra underestimated the observations in terms of $\overline{\eta}_{ST}$. If the space-time extremes are normalized on significant wave height (i.e. $\overline{\xi}_{ST}$), results poorly resembled EMEP results (Figure 7.47-b and Figure 7.48-b). In fact, they both overestimated reference lines, probably due to the additional energy observed in SWAN-ST spectra. In order to calculate $\overline{\eta}_{ST}$, we scaled SWAN-ST spectrum (Figure 7.46-a) with respect to EMEP spectrum (Figure 7.46-b) to recover the same significant wave height. To this end, we multiplied SWAN-ST spectrum by the zero-th moments ratio. Stochastic models results in terms of $\overline{\eta}_{ST}$ overestimated the EMEP predictions, in particular for Fedele's model (Figure 7.49). These results force us to do additional investigations to strengthen the reliability of SWAN-ST results. Nevertheless, we recall that R/V "Urania" experiment were gathered and analyzed with some warnings (see Chapter 4), hence we plan to perform additional experiments.

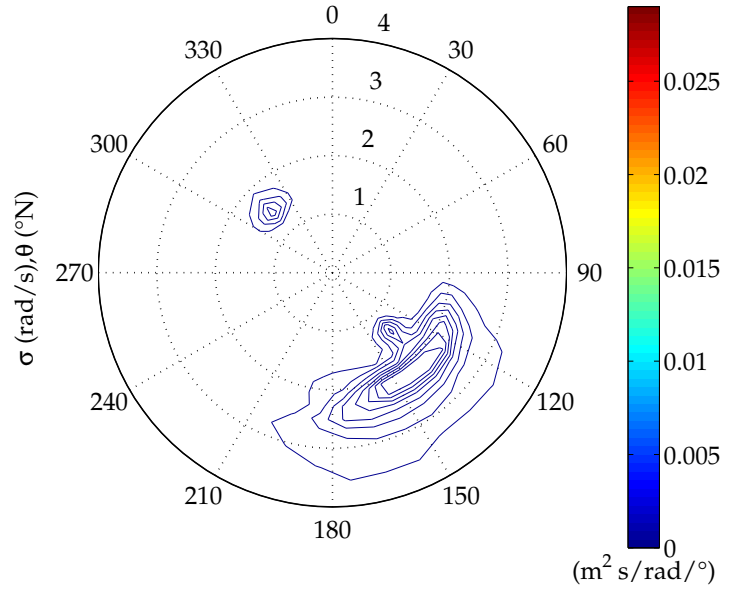

(a)

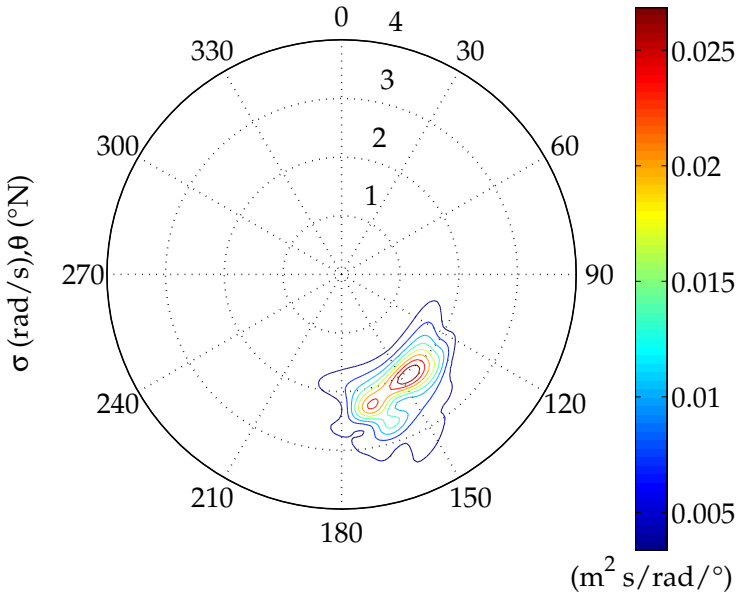

(b)

Figure 7.46: Directional spectrum $S(\sigma,\theta)$ at R/V"Urania" position, polar (σ,θ) coordinates. (a) $S(\sigma,\theta)$ from SWAN-ST runs. (b) $S(\sigma,\theta)$ from WASS measurements (EMEP). Directions are propagation directions.

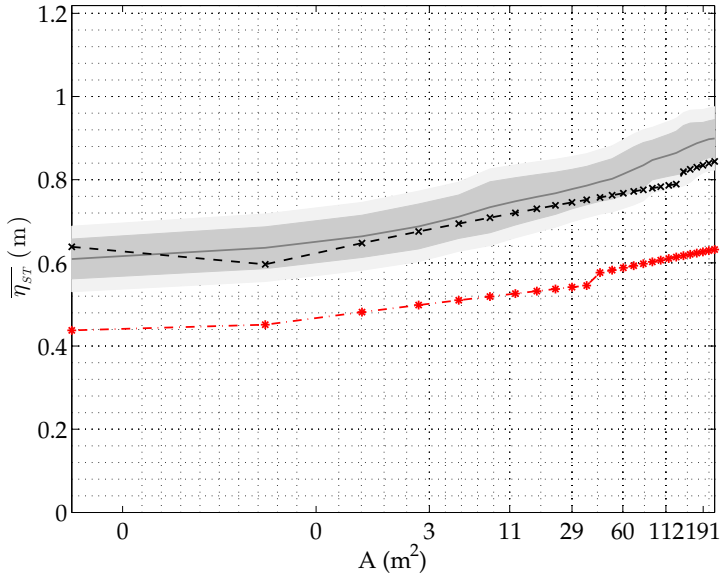

(a)

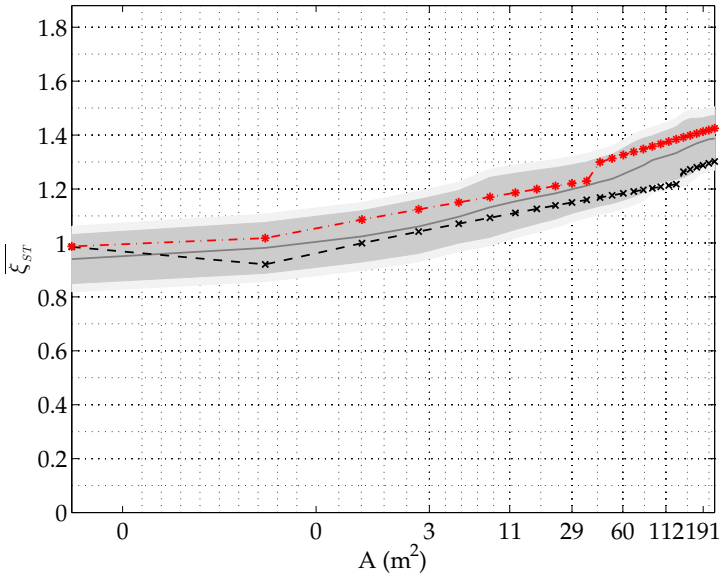

(b)

Figure 7.47: Piterbarg's model prediction (red crosses: SWAN-ST runs; black asterisks: EMEP) versus WASS observations (gray solid line): expected maximum over space-time as a function of area size. Observations are provided together with error bands (grey): the wider band (brighter gray) includes WASS error. (a) Non-normalized extremes $\overline{\eta}_{ST}$. (b) Normalized extremes $\overline{\xi}_{ST}$.

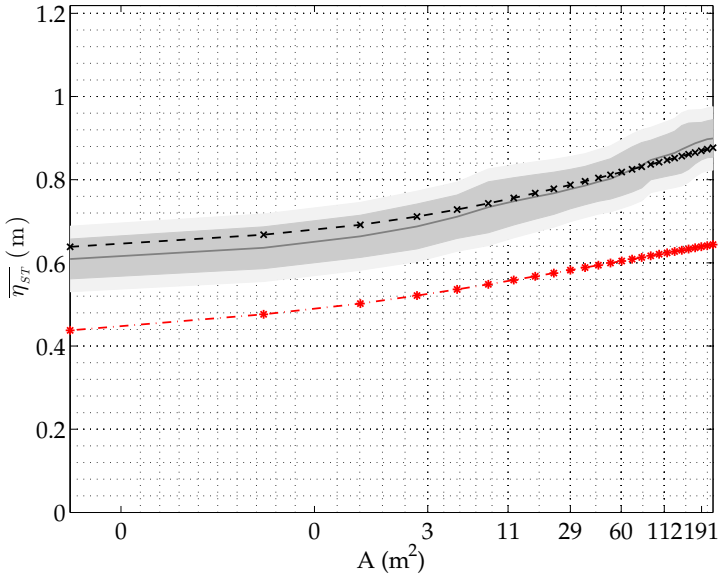

(a)

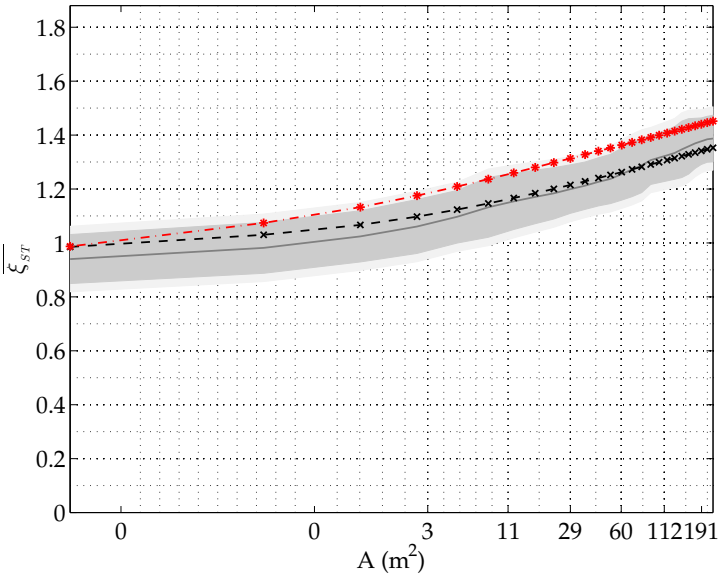

(b)

Figure 7.48: Fedele's model prediction (red crosses: SWAN-ST runs; black asterisks: EMEP) versus WASS observations (gray solid line): expected maximum over space-time as a function of area size. Observations are provided together with error bands (grey): the wider band (brighter gray) includes WASS error. (a) Non-normalized extremes $\overline{\eta}_{ST}$. (b) Normalized extremes $\overline{\xi}_{ST}$.

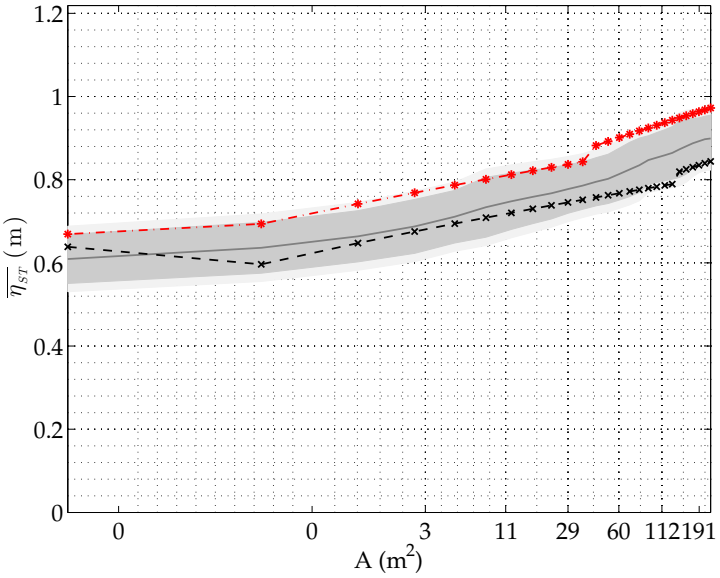

(a)

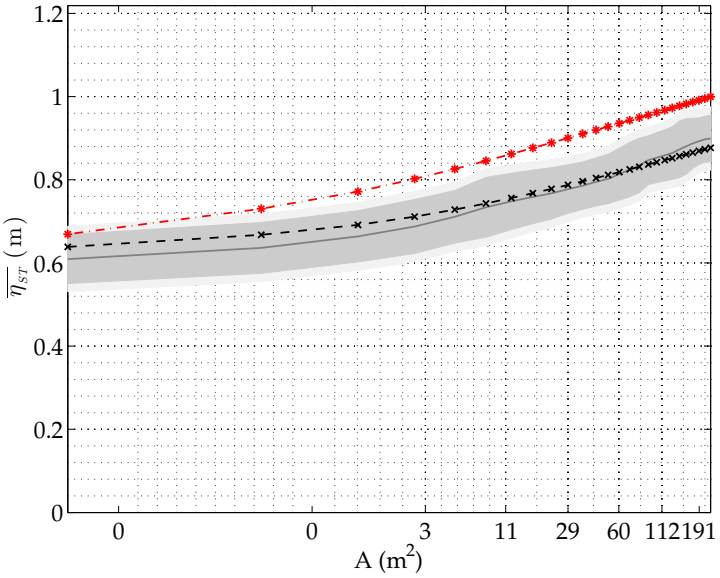

(b)

Figure 7.49: Stochastic models prediction (red crosses: SWAN-ST runs; black asterisks: EMEP) versus WASS observations (gray solid line): expected maximum over space-time as a function of area size. Observations are provided together with error bands (grey): the wider band (brighter gray) includes WASS error. SWAN-ST spectrum scaled by the ratio of zero-th moments r_{m0}. (a) Piterbarg's model. (b) Fedele's model.

7.4.4 Results

Space-time extremes $\overline{\xi}_{ST}$ and time extremes $\overline{\xi}_{T}$ calculated from Fedele's model after SWAN-ST results are depicted in the following Figures. We synthesized results by calculating the temporal mean ($< \cdot >$) and the absolute maximum ($max(\cdot)$) of each quantity at every grid node. Hence, mean and maximum $\overline{\xi}_{T}$ are plotted in Figure 7.50 and Figure 7.51, respectively, while mean and maximum $\overline{\xi}_{ST}$ are plotted in Figure 7.52 and Figure 7.53, respectively. To highlight the contribution of space domain in sea surface extremes prediction, the mean and the maximum ratio $r = \overline{\xi}_{ST}/\overline{\xi}_{T}$ over the 3 hindcasted years also are depicted in Figure 7.54 and Figure 7.55. In other words, these two Figures emphasize the mean and maximum underestimation that would have followed over 24000 m^2 areas if a time domain approach was used instead of a space-time approach.

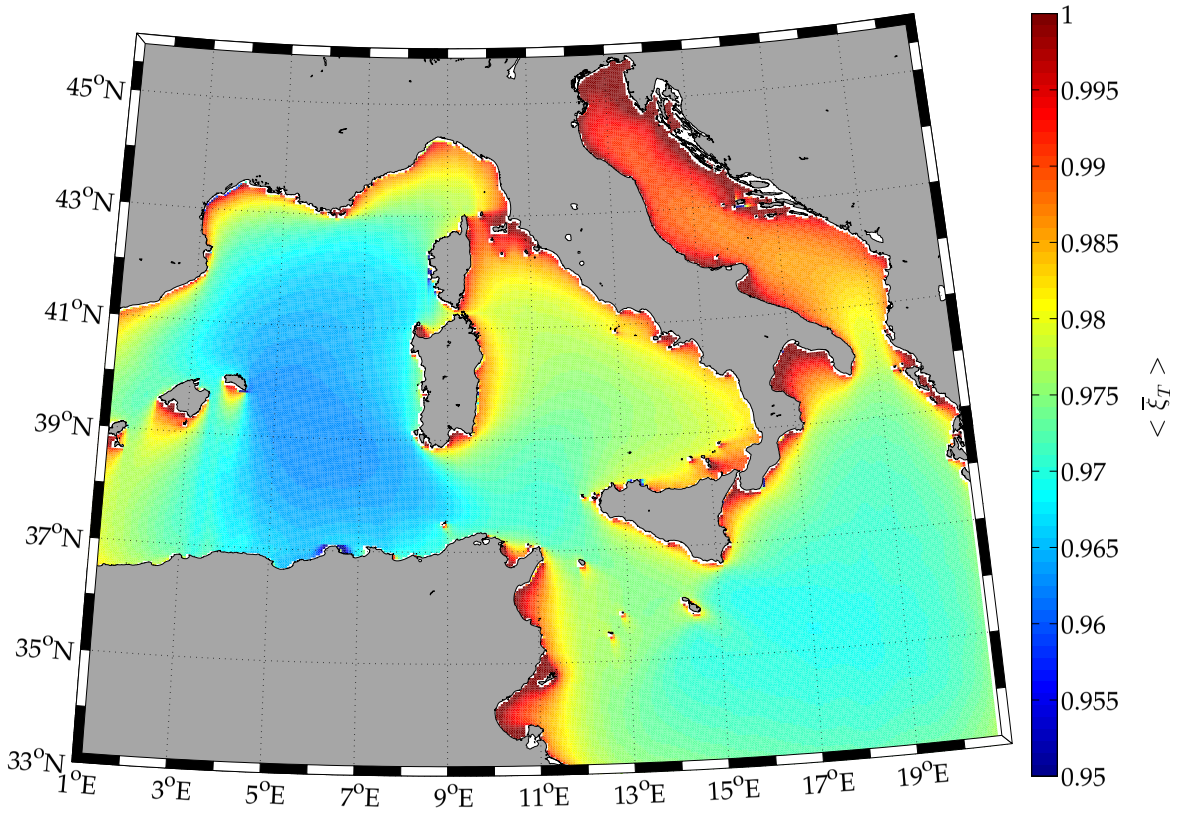

Figure 7.50: Mean $\overline{\xi}_T$ in the Mediterranean Sea over 2008-2010, according to Fedele's model (A=24000 m^2, D=1 hour) and SWAN-ST simulations.

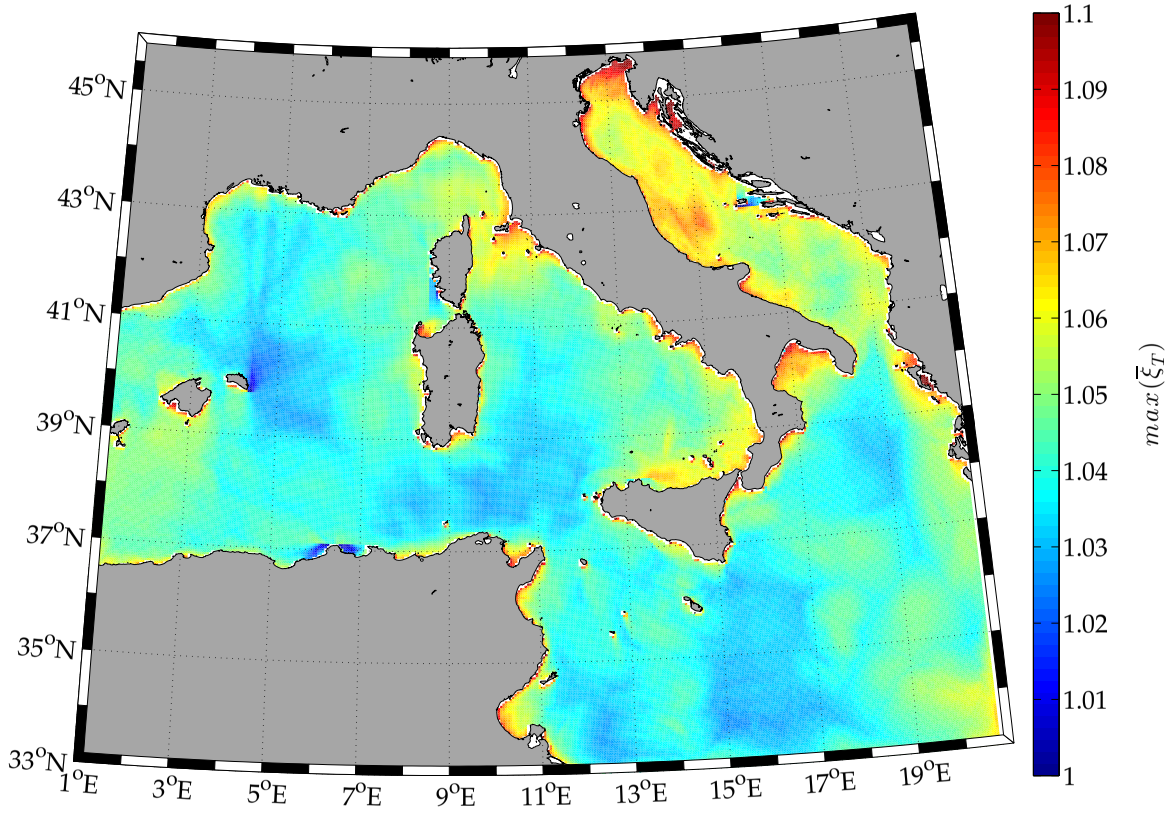

Figure 7.51: Maximum $\overline{\xi}_T$ in the Mediterranean Sea over 2008-2010, according to Fedele's model (A=24000 m^2, D=1 hour) and SWAN-ST simulations.

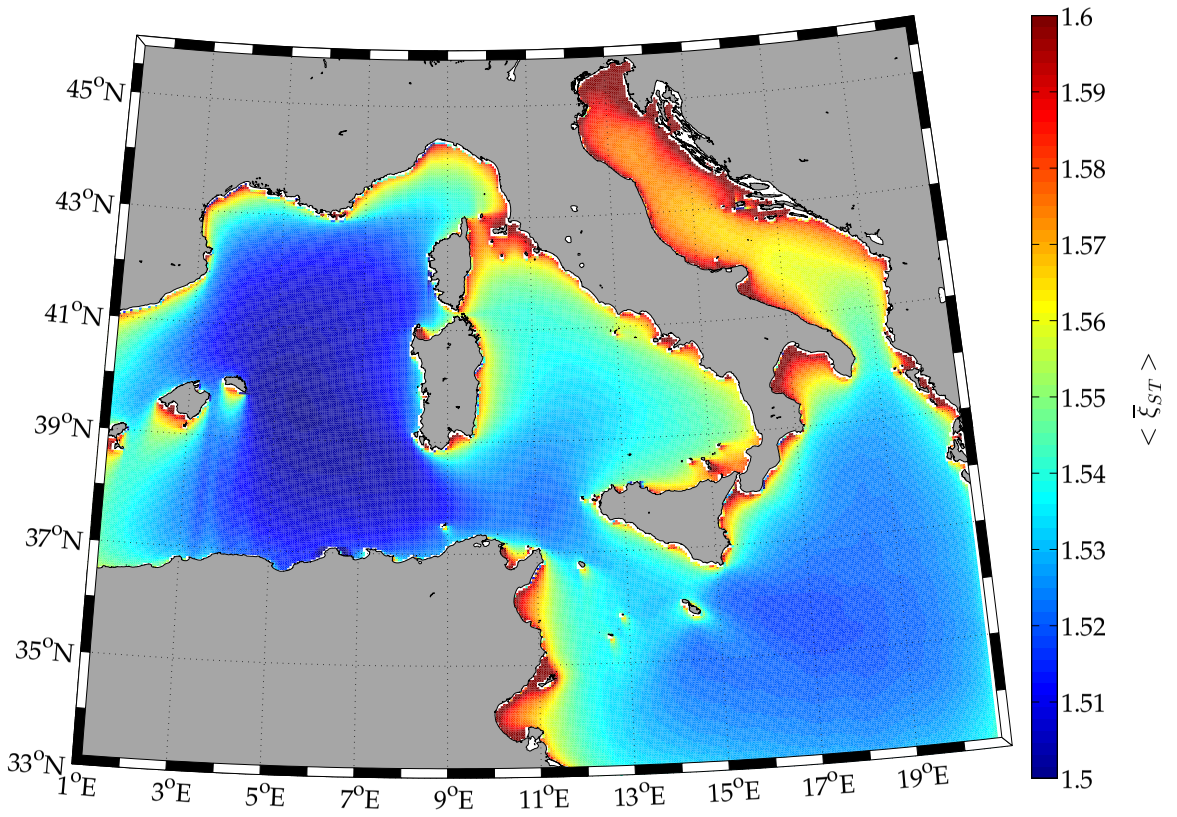

Figure 7.52: Mean $\overline{\xi}_{ST}$ in the Mediterranean Sea over 2008-2010, according to Fedele's model (A=24000 m^2, D=1 hour) and SWAN-ST simulations.

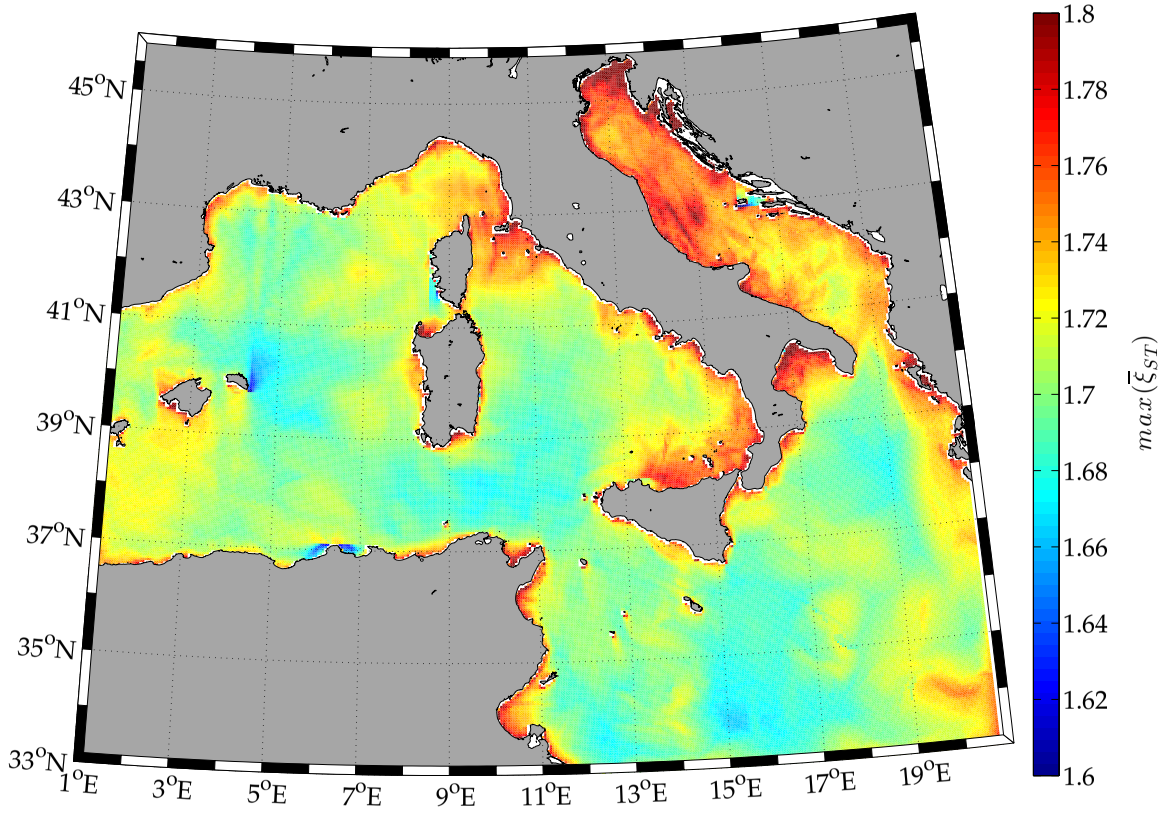

Figure 7.53: Maximum $\overline{\xi}_{ST}$ in the Mediterranean Sea over 2008-2010, according to Fedele's model (A=24000 m^2, D=1 hour) and SWAN-ST simulations.

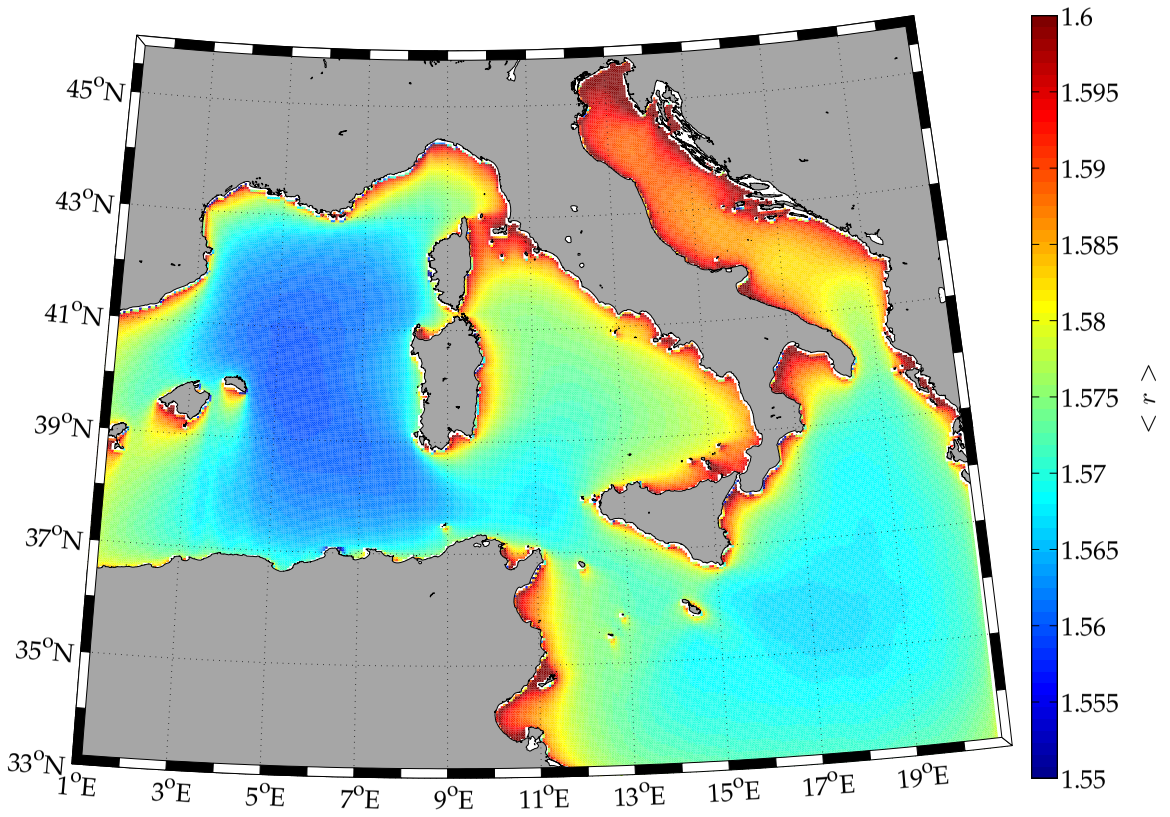

Figure 7.54: Mean ratio $r = \overline{\xi}_{ST}/\overline{\xi}_T$ in the Mediterranean Sea over 2008-2010, according to Fedele's model (A=24000 m^2, D=1 hour) and SWAN-ST simulations.

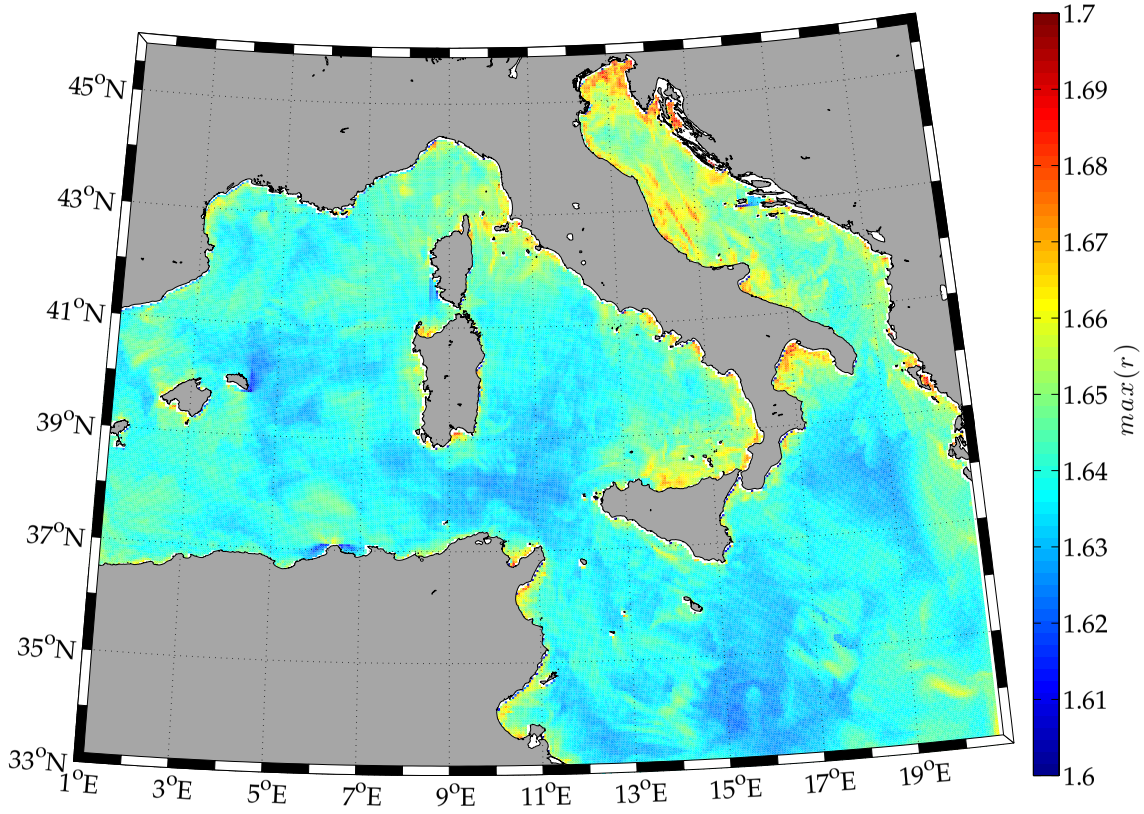

Figure 7.55: Maximum ratio $r = \overline{\xi}_{ST}/\overline{\xi}_T$ in the Mediterranean Sea over 2008-2010, according to Fedele's model (A=24000 m^2, D=1 hour) and SWAN-ST simulations.

For the 1 hour simulated sea states, time extremes were within 1.0 and 0.965 times the significant wave height (Figure 7.50). In the linear context assumed, this would lead to an average maximum wave height estimate of $H_{max} \sim 1.93 \div 2.00 H_s$, which is consistent with conventional predictions from the standard wave model, i.e. $H_{max} \sim 1.8 \div 2.2 H_s$. Highest $\overline{\xi}_{ST}$ were localized on shallower waters. Therefore, Adriatic Sea was featured by the highest values, especially in the northern part of the basin. This can be ascribed to the fact that in these regions the sea severity was lower than in deeper waters sea, hence mean wave periods $\overline{T}$ were shorter. Thus, according to (3.15) a larger average number of waves M_1 was expected within a fixed duration D, causing higher predicted $\overline{\xi}_T$ (3.20). Maximum time extremes were only slightly higher (Figure 7.51), reaching up to $1.1 H_s$, i.e. $H_{max} \sim 2.2 H_s$. Spatial distribution of maxima was more scattered than the distribution of mean values.

Space-time extremes exhibited similar mean and maximum patterns (Figure 7.52 and Figure 7.53, respectively). The reason for mean space-time extremes pattern is partially the same adduced to motivate time extremes mean pattern. As explained for M_1, according to (3.13) and (3.14), in lower sea severity regions also M_2 and M_3 were lower than in deeper waters regions. Hence, after (3.18), lower space-time maxima had to be expected, being space domain fixed. Thus, Adriatic Sea exhibited the highest values (up to 1.6 times the significant wave height) also for space-time extremes. In the context of a linear wave model, this would lead to an average maximum wave height estimate of $H_{max} \sim 3.00 \div 3.30 H_s$. In addition, we could argue that western Mediterranean Sea exhibited the lowest average values of $\overline{\xi}_{ST}$ because of the persistence of long-crested sea states, which developed in Mistral conditions (north-westerly wind).

Ratios r substantially reproduced the pattern of $\overline{\xi}_T$ and $\overline{\xi}_{ST}$ for mean pattern. They are included within 1.55 and 1.60 on average and within 1.60 and 1.65 at maximum, pointing out that a considerable underestimation of wave extremes would be done if only time domain approach was adopted.

7.5 Conclusions

In this Chapter, we applied a numerical approach to solve the problem of space-time extreme prediction. To this end, we developed a modified version of SWAN model, i.e. SWAN-ST. Thanks to this model, we widened the possibility of gathering directional spectra and thus performing space-time extremes analysis. In fact, we could calculate spectral parameters needed by stochastic models of Piterbarg and Fedele at each computational step (in

space and time) of an arbitrary domain.

As a first test case, we applied SWAN-ST on a simplified domain to investigate the dependence of $\overline{\eta}_{ST}$ from ambient current speed and shoaling. We found that following currents decreased $\overline{\eta}_{ST}$, while opposing currents increased $\overline{\eta}_{ST}$. Apart from these expected results, we observed a global maximum of $\overline{\xi}_{ST}$ at approximately -0.35 m/s, for every sea severity tested. We ascribed this behavior to the blocking effect higher frequency of the spectrum experienced for opposing current speeds stronger than -0.20 m/s. Dealing with shoaling, we observed an increase of $\overline{\eta}_{ST}$ while approaching the shoreline, which is however localized in areas where depth-induced breaking could occur. In fact, depth-induced breaking and bottom friction reduced the $\overline{\eta}_{ST}$ increase. Besides these results, consistent with the physics of wave propagation, we provided a tool to get quantitative estimates of wave-current interaction and shoaling effects on $\overline{\eta}_{ST}$.

As a second test case, we applied SWAN-ST on a complex domain to test its capability in predicting space-time extremes in realistic conditions. Hence, we hindcasted 3 years (2008-2010) of Mediterranean Sea states by forcing a 6x6 km^2 model with high-resolution wind fields. Prior to this, we verified the performance of SWAN-ST in prediction of $\overline{\eta}_{ST}$ by comparing model-based results with measurements-based results of "Acqua Alta" and "Urania" experiments. We found that $\overline{\xi}_{ST}$ were included within 1.5 and 1.6 times the significant wave height and 1.55 to 1.6 times the time extreme $\overline{\xi}_{T}$. Spatially, mean and maximum space-time and time extremes seemed to be correlated to bottom topography, being higher in the shallowest parts of the basin and lower in the deepest ones. In general, we observed low spatial and temporal variabilities of mean $\overline{\xi}_{ST}$ and $\overline{\xi}_{ST}$, meaning their estimates are rather robust. Although these results were obtained only in a fixed space-time domain condition, they reveal how numerical models forecasting could benefit from space-time extremes stochastic models.

Appendix A

Appendix to Chapter 5

A.1 Quality control

To avoid that some bugs in the measuring system and other unknown external sources of error could affect the data, in particular the maxima, a quality control was applied to the recorded sea surface elevation time series prior to the wave extremes analyses. Drawing upon the work of Casas-Prat and Holthuijsen (2010), we defined 4 criteria to check the quality of the data:

- *Completeness*: time series shorter than 30 minutes, i.e. 2304 data at 1.28 Hz, were discarded.

- *Bumping*: we observed unusual low frequency-high amplitude oscillations of the sea surface elevation (Figure A.1). Casas-Prat and Holthuijsen (2010) described them as bumpings caused by the hitting of external objects against the buoy, e.g. a ship. We observed them both in the time and in the frequency domain. As done by the cited authors we discarded the sea states when the omnidirectional spectrum $S(\sigma)$ showed energy above a certain threshold S_{lim} in the lower frequency components. We considered the same threshold of the paper, $S_{lim} = 0.004$ m^2/Hz:

$$S(\sigma_i) \leq S_{lim} \qquad i = 1, 2$$

- *Aliasing*: to avoid aliasing we discarded sea states when the peak frequency f_p was too close to the Nyquist frequency $\sigma_N = 2\pi f_s/2 = 2\ \pi\ 0.64 = 4.02$ rad/s.

$$\sigma_p \leq \frac{\sigma_N}{3}$$

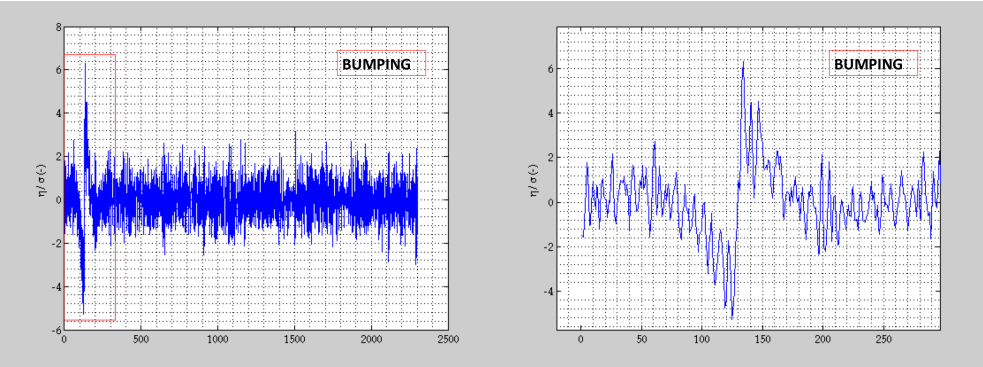

Figure A.1: Bumping observed in a time series.

Coefficient 1/3 was chosen in accordance to Casas-Prat and Holthuijsen (2010).

- *Peak period*: sometimes peak period T_p inconsistent with wind gravity waves in the Mediterranean Sea were observed, hence we discarded sea states showing peak period of the spectrum $S(\sigma)$ greater than 15 s

$$T_p \leq 15s \tag{A.1}$$

A.2 Spectral analysis

Analysis of each sea state in the frequency domain was done using Welch's method with a 50% overlapping and Hanning windowing (Bendat and Piersol, 2011). Spectral resolution is 0.0028 Hz. After the spectrum $S(\sigma)$ has been so obtained, exploiting its moments $m_i = \int_0^\infty \sigma^i S(\sigma) d\sigma$, we calculated

- spectral significant wave height H_{m0}

$$H_{m0} = 4\sqrt{m_0} \tag{A.2}$$

- peak period $T_p = 2\pi/\sigma_p$, σ_p being the peak frequency;
- spectral bandwidth parameter of Longuet-Higgins (1975) (Figure A.2-a)

$$\nu = \left(\frac{m_0 m_2}{m_1^2} - 1 \right) \tag{A.3}$$

- integral steepness of the sea state (Fedele and Tayfun, 2009) (Figure A.2-b)

$$\begin{aligned} \mu &= \mu_{nb}(1 - \nu + \nu^2) \\ \mu_{nb} &= \sqrt{m_0}(m_1/m_0)^2/g \end{aligned} \tag{A.4}$$

where μ_{nb} is the integral steepness of a sea state represented by a narrow-banded frequency spectrum.

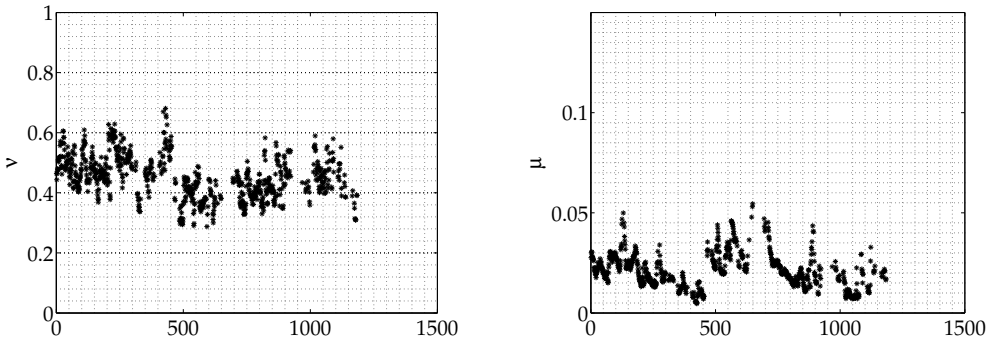

(a) (b)

Figure A.2: (a) Spectral bandwidth parameter of the sea states. (b) Integral steepness of the sea states. x-labels are measured sea states.

Spectral bandwidth parameter ν fill the range of values between 0.3 and 0.7 (Figure A.2-a). Integral steepness parameter μ is included between 0.005 and 0.055 (Figure A.2-b). Steepness we calculated was quite low if compared to typical values occurring during storms, i.e. approximately 0.1 (Casas-Prat and Holthuijsen, 2010). The reasons for this could be the linearization and sampling frequency effects described in Chapter 5. Both of them act more on the wave heights than on the periods, thus reducing the steepness.

Autocovariance function $\psi(T)$ was calculated from the spectrum $S(\sigma)$. The first minimum of $\psi(T)$, i.e. ψ^*, (Figure A.3) was stored to be used for Boccotti probability distribution (Tayfun and Fedele, 2007). Typical values for wind sea states are $-0.75 \leq \psi^* \leq -0.65$, while $-0.60 \leq \psi^*$ deal with wind waves superimposed on swells (Boccotti, 2000). We observed a huge number of sea states outside wind sea range, i.e. $-0.65 \leq \psi^* \leq -0.15$ (Figure A.3). Plotting ψ^* versus the spectral significant wave height (Figure A.3-a) we saw that as H_{m0} increases, the values seemed to converge, though dispersively, to a narrower range of values. Plotting ψ^* versus the spectral bandwidth parameter ν (Figure A.3-b), we observed a trend such that the values indicated by Boccotti seemed associated to the more narrow banded spectra while the high values of ψ^*, i.e. until -0.1, seemed associated with wider spectra. This is reasonable since $|\psi^*|$ is itself a narrow bandedness parameter, approaching 1 when the process is narrow-banded and 0 when it is wide-banded.

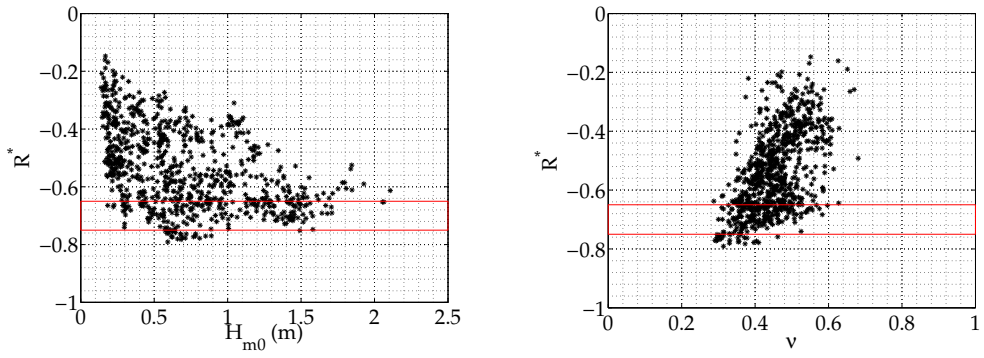

(a) (b)

Figure A.3: First minimum ψ^* of the autocovariance function $\psi(T)$ versus spectral significant wave height H_{m0} (a) and versus spectral bandwidth parameter ν (b). Red rectangle highlights the typical region for wind waves, i.e $-0.75 \leq \psi^* \leq -0.65$. Sea states with $-0.60 \leq \psi^*$ are probably dealing with wind waves superimposed on swells.

We can conclude that the data set was composed of both narrow-banded and wide-banded spectrum sea states; wide-banded spectra could either:

- be caused by errors in the measurements. The values of ψ^* outside the range indicated by Boccotti are much more frequent for low height sea states, i.e. the ones for which the error could be comparable to the measurement. E.g. for $H_{m0} > 1.5$ m, $-0.55 \leq \psi^* \leq -0.75$ (Figure A.3-a);
- indicate the presence of swell and/or bimodal sea states, as pointed out by Sánchez-Arcilla et al. (2008).

Appendix B

Appendix to Chapter 6

B.1 MATLAB script to compute $\Gamma(a, z)$

```
%%%%%%%%%%%%%%%%%%%%%%%%%%%%%%%%%%%%%%%%%%%%%%%%%%%%%%%%%%%%%%%%%%%%%%%%%%%%%%%%
%
%                                gammainc_fb(a,z)
%
%   MATLAB function to calculate upper incomplete gamma function, using
%    limiting function X (Abramowitz and Stegun, 1972), when a tends to 0.
%
%%%%%%%%%%%%%%%%%%%%%%%%%%%%%%%%%%%%%%%%%%%%%%%%%%%%%%%%%%%%%%%%%%%%%%%%%%%%%%%%

function X = gammainc_fb(a,z);
k = 1 : 10;
% limiting function to the upper incomplete gamma f. as a tends to 0
X = - 0.5772-log(z)-sum((-1).^k.*z.^k./(k.*factorial(k)));
```

B.2 Alternative spectral parameters formulations

In this Chapter, alternative formulations for the spectral parameters of directional spectra presented in Chapter 2 (i.e. Pierson-Moskowitz or JONSWAP spectra with $\cos^2$ function) are provided. For the Pierson-Moskowitz spectrum, the following formulae express spectral parameters as a function of either wind speed U or significant wave height H_s. For the JONSWAP spectrum, they highlight dependence of spectral parameters upon wind speed U and fetch length F, simultaneously. A formulation for JONSWAP depending on significant wave height has not been derived since there is not a relationship between H_s and σ_m or (F, U) for fetch limited conditions. To conclude, following equations complete the formulae provided in Chapter 6, which are expressed as a function of modal frequency σ_m.

B.2.1 Pierson-Moskowitz and $\cos^2$ function

Wind speed U

The wind speed U dependent spectral parameters of Pierson-Moskowitz and $\cos^2$ function directional spectrum can be obtained in a similar manner as in Section 6.2.1, using (2.25) instead of (2.26). Alternatively, they can be achieved from (6.13) through the universal relationship observed in fully developed seas between modal frequency σ_m and wind speed U, i.e. $\sigma_m = 0.87(g/U)$:

$$\begin{aligned}
\overline{T} &= 0.518U \\
\overline{L}_x &= \frac{0.859U^2}{\sqrt{\Gamma(0,s)}} \\
\overline{L}_y &= \frac{1.49U^2}{\sqrt{\Gamma(0,s)}} \\
\alpha_{xy} &= 0 \\
\alpha_{xt} &= \frac{2.68}{\sqrt{\Gamma(0,s)}} \\
\alpha_{yt} &= 0
\end{aligned} \tag{B.1}$$

Here, $s = \frac{g^4 B}{1.296 \cdot 10^7 U^4}$ and $\Gamma(0,s)$ is the upper incomplete Gamma function.

Significant wave height H_s

Spectral parameters of Pierson-Moskowitz and $\cos^2$ function directional spectrum can be also expressed as a function of significant wave height H_s by following procedure in Section 6.2.1 with (2.27) instead of (2.26). Alternatively, the same result can be obtained by substituting into (B.1) the universal relationship observed in fully developed seas between significant

wave height H_s and wind speed U, i.e. $H_s = 0.21(U^2/g)$:

$$\begin{aligned}
\overline{T} &= 3.56\sqrt{H_s} \\
\overline{L}_x &= \frac{40.6H_s}{\sqrt{\Gamma(0,s)}} \\
\overline{L}_y &= \frac{70.3H_s}{\sqrt{\Gamma(0,s)}} \\
\alpha_{xy} &= 0 \\
\alpha_{xt} &= \frac{2.68}{\sqrt{\Gamma(0,s)}} \\
\alpha_{yt} &= 0
\end{aligned} \tag{B.2}$$

where $s = \frac{g^2 Q}{1.296 \cdot 10^7 H_s^2}$.

B.2.2 JONSWAP and $\cos^2$ function

Dependence of spectral parameters of JONSWAP and $\cos^2$ directional spectrum upon wind speed U and fetch length F can be more explicit by using modal frequency formulation (2.31) of Lewis and Allos (1990) into (6.21):

$$\begin{aligned}
\overline{T} &= \frac{0.38}{(FU)^{-0.33}}\sqrt{\frac{\gamma + 5.0}{\gamma + 10.88}} \\
\overline{L}_x &= \frac{0.26}{(FU)^{-0.66}}\sqrt{\frac{\gamma + 5.0}{\gamma + 7.5\Gamma(0,s) - 1}} \\
\overline{L}_y &= \frac{0.45}{(FU)^{-0.66}}\sqrt{\frac{\gamma + 5.0}{\gamma + 7.5\Gamma(0,s) - 1}} \\
\alpha_{xy} &= 0 \\
\alpha_{xt} &= \frac{0.981(\gamma + 24.68)}{\sqrt{\gamma + 10.88}\sqrt{\gamma + 7.5\Gamma(0,s) - 1}} \\
\alpha_{yt} &= 0
\end{aligned} \tag{B.3}$$

where $s = \frac{g^4 B}{1.296 \cdot 10^7 U^4}$ and $\Gamma(0,s)$ is the upper incomplete Gamma function. Note that according to Lewis and Allos (1990), also peak parameter γ depends upon U and F. Nevertheless, often γ is fixed. Hence, herein it is not expressed as a function of wind speed and fetch length but in any case, (2.31) provides their relationship (Lewis and Allos, 1990).

Appendix C

Appendix to Chapter 7

C.1 SWAN-ST specific subroutines

C.1.1 Spectral parameters computation: fboexm

```
1  !
2  subroutine fboexm ( oqproc, bkc, mip, xc, yc, voqr, voq, ac2, &
3                      acloc, spcsig, spcdir, kgrpnt, depxy, cross)
4  !
5  !
6  !    Authors
7  !
8  !    40FB: Francesco Barbariol
9  !
10 !    Updates
11 !
12 !    Purpose
13 !
14 !    Subroutine for the space-time extreme analysis in SWAN model
15 !
16 !    Method
17 !
18 !    The sbrt is called by SWOUTP, when output variables are requested
19 !    and command
20 !    STEXTREMES is read in the command file .sw.
21 !    ---- Call FBSMOM, to calculate the spectral moments
22 !    ---- Call FBSPAR, to calculate spectral parameters
23 !
24 !    Modules used
25 !
26       use ocpcomm4
27       use swcomm1
28       use swcomm2
29       use swcomm3
30       use swcomm4
31       use outp_data
32 !
33       implicit none
34 !
35 ! number of variables to compute
```

```
36      integer, parameter                          :: nmom = 13
37  !
38  !   Argument variables
39  !
40  ! action density at one location
41      real, dimension(MDC,MSC)                    :: acloc
42  ! action density at one location
43      real, dimension(MDC,MSC,MCGRD), intent(in) :: ac2
44  ! x-coord of comp grid points
45      real, dimension(MIP), intent(in)            :: xc
46  ! y-coord of comp grid points
47      real, dimension(MIP), intent(in)            :: yc
48      real, dimension(MSC), intent(in)            :: spcsig   !
49      real, dimension(MDC,*), intent(in)          :: spcdir !
50      real, dimension(MCGRD), intent(in)          :: depxy
51      integer, dimension(MXC,MYC), intent(in)     :: kgrpnt
52      logical, dimension(4,mip), intent(in)       :: cross
53      integer, intent(in)                         :: bkc
54      integer, intent(in)                         :: mip
55      logical, dimension(*), intent(in)           :: oqproc
56      integer, dimension(*)                       :: voqr
57      real, dimension(MIP,*)                      :: voq
58  !
59  !   Local variables
60  !
61  ! number of entries in this subroutine
62      integer, save                       :: ient = 0
63  ! power of the pqr-th moment, kx
64      integer                             :: p
65  ! power of the pqr-th moment, ky
66      integer                             :: q
67  ! power of the pqr-th moment, sigma
68      integer                             :: r
69  ! counter on output points
70      integer                             :: ip
71  ! vector containing spec mom SWAN computes
72      integer, dimension(nmom)            :: ivoum(nmom)
73      logical                             :: eqreal
74  ! if true value in point is undefined          40.86
75      logical                             :: excpt
76      real                                :: pqrm
77      real                                :: e000
78      real                                :: e011
79      real                                :: e101
80      real                                :: e110
81      real                                :: e002
82      real                                :: e020
83      real                                :: e200
84      real                                :: stvar
85      real                                :: deploc
86      integer                             :: ii
87      integer                             :: ivtype
88      integer                             :: xp, yp
89      real, dimension(MSC)                :: wk
90      real, allocatable                   :: wkx(:)
91      real, allocatable                   :: wky(:)
92  !
93  !   Structure
94  !
95  !   Description of the pseudo code
96  !
97  !   Source text
```

```
98  !
99      data ivoum /72, 73, 74, 75, 76, 77, 78, 79, 80, 81, 82, 83, 84/
100
101 !     call strace (ient,'fboexm')
102 !
103     allocate(wkx(mdc*msc))
104     allocate(wky(mdc*msc))
105 !
106 !     loop over all output points
107 !
108     do 800 ip = 1, mip
109        deploc=voq(ip,voqr(4))
110 !
111 !      assign exception value if depth is negative or point is outside grid
112 !
113        if (deploc.le.0.)                      goto 700
114        if (eqreal(deploc,ovexcv(4)))          goto 700
115        if (optg.ne.5) then
116           if (kreptx.eq.0) then
117 !           non-repeating grid
118             if (xc(ip) .lt. -0.01)               goto 700
119             if (xc(ip) .gt. real(mxc-1)+0.01) goto 700
120           endif
121             if (yc(ip) .lt. -0.01)               goto 700
122             if (yc(ip) .gt. real(myc-1)+0.01) goto 700
123        endif
124 !
125 !       first the action density spectrum is interpolated
126 !
127        if (optg.ne.5) then
128           call swoina (xc(ip), yc(ip), ac2, acloc, kgrpnt, depxy, &
129                cross(1,ip), excpt)
130        else
131           if (.not.lcompgrd) then
132              if (.not.eqreal(voq(ip,1),ovexcv(1))) xp=voq(ip,1)-xoffs
133              if (.not.eqreal(voq(ip,2),ovexcv(2))) yp=voq(ip,2)-yoffs
134              call SwanInterpolateAc ( acloc, xp, yp, ac2, excpt )
135           else
136              acloc(:,:) = ac2(:,:,ip)
137           endif
138        endif
139 !
140 !      Calculate spectral moments
141 !
142 !      m000
143 !
144        ivtype = 72
145        if (oqproc(ivtype)) then
146           p = 0
147           q = 0
148           r = 0
149           pqrm = 0.
150           call fbsmom(p,q,r,acloc,spcdir,deploc,spcsig,wk,pqrm,wkx,wky)
151 !
152 !         write spectral moment to output vector
153 !
154           if (pqrm .ne. 0.) then
155              voq(ip,voqr(ivtype)) = pqrm
156           else
157              voq(ip,voqr(ivtype)) = 0.
158           endif
159           if (itest.ge.100) then
```

```
160                write(printf, 222) ip, ovsnam(ivtype), voq(ip,voqr(ivtype))
161  222           format(' FBOEXM: POINT ', i5, 2x, a, 1x, e12.4)
162              endif
163           endif
164  !
165  !
166  !
167  !        m101
168  !
169           ivtype = 73
170           if (oqproc(ivtype)) then
171              p = 1
172              q = 0
173              r = 1
174              pqrm = 0.
175              call fbsmom(p,q,r,acloc,spcdir,deploc,spcsig,wk,pqrm,wkx,wky)
176  !
177  !           write spectral moment to output vector
178  !
179              if (pqrm .ne. 0.) then
180                 voq(ip,voqr(ivtype)) = pqrm
181              else
182                 voq(ip,voqr(ivtype)) = 0.
183              endif
184              if (itest.ge.100) then
185                 write(printf, 222) ip, ovsnam(ivtype), voq(ip,voqr(ivtype))
186              endif
187           endif
188  !
189  !
190  !
191  !        m011
192  !
193           ivtype = 74
194           if (oqproc(ivtype)) then
195              p = 0
196              q = 1
197              r = 1
198              pqrm = 0.
199              call fbsmom(p,q,r,acloc,spcdir,deploc,spcsig,wk,pqrm,wkx,wky)
200  !
201  !           write spectral moment to output vector
202  !
203              if (pqrm .ne. 0.) then
204                 voq(ip,voqr(ivtype)) = pqrm
205              else
206                 voq(ip,voqr(ivtype)) = 0.
207              endif
208              if (itest.ge.100) then
209                 write(printf, 222) ip, ovsnam(ivtype), voq(ip,voqr(ivtype))
210              endif
211           endif
212  !
213  !
214  !
215  !        m110
216  !
217           ivtype = 75
218           if (oqproc(ivtype)) then
219              p = 1
220              q = 1
221              r = 0
```

```
222             pqrm = 0.
223             call fbsmom(p,q,r,acloc,spcdir,deploc,spcsig,wk,pqrm,wkx,wky)
224  !
225  !          write spectral moment to output vector
226  !
227             if (pqrm .ne. 0.) then
228                voq(ip,voqr(ivtype)) = pqrm
229             else
230                voq(ip,voqr(ivtype)) = 0.
231             endif
232             if (itest.ge.100) then
233                write(printf, 222) ip, ovsnam(ivtype), voq(ip,voqr(ivtype))
234             endif
235          endif
236  !
237  !
238  !
239  !       m002
240  !
241          ivtype = 76
242          if (oqproc(ivtype)) then
243             p = 0
244             q = 0
245             r = 2
246             pqrm = 0.
247             call fbsmom(p,q,r,acloc,spcdir,deploc,spcsig,wk,pqrm,wkx,wky)
248  !
249  !          write spectral moment to output vector
250  !
251             if (pqrm .ne. 0.) then
252                voq(ip,voqr(ivtype)) = pqrm
253             else
254                voq(ip,voqr(ivtype)) = 0.
255             endif
256             if (itest.ge.100) then
257                write(printf, 222) ip, ovsnam(ivtype), voq(ip,voqr(ivtype))
258             endif
259          endif
260  !
261  !
262  !
263  !       m020
264  !
265          ivtype = 77
266          if (oqproc(ivtype)) then
267             p = 0
268             q = 2
269             r = 0
270             pqrm = 0.
271             call fbsmom(p,q,r,acloc,spcdir,deploc,spcsig,wk,pqrm,wkx,wky)
272  !
273  !          write spectral moment to output vector
274  !
275             if (pqrm .ne. 0.) then
276                voq(ip,voqr(ivtype)) = pqrm
277             else
278                voq(ip,voqr(ivtype)) = 0.
279             endif
280             if (itest.ge.100) then
281                write(printf, 222) ip, ovsnam(ivtype), voq(ip,voqr(ivtype))
282             endif
283          endif
```

```
284 !
285 !
286 !
287 !       m200
288 !
289         ivtype = 78
290         if (oqproc(ivtype)) then
291            p = 2
292            q = 0
293            r = 0
294            pqrm = 0.
295            call fbsmom(p,q,r,acloc,spcdir,deploc,spcsig,wk,pqrm,wkx,wky)
296 !
297 !          write spectral moment to output vector
298 !
299            if (pqrm .ne. 0.) then
300               voq(ip,voqr(ivtype)) = pqrm
301            else
302               voq(ip,voqr(ivtype)) = 0.
303            endif
304            if (itest.ge.100) then
305               write(printf, 222) ip, ovsnam(ivtype), voq(ip,voqr(ivtype))
306            endif
307         endif
308 !
309 !
310 !
311 !       sttm
312 !
313         ivtype = 79
314         if (oqproc(ivtype)) then
315            p = 0
316            q = 0
317            r = 0
318            e000 = 0.
319            call fbsmom(p,q,r,acloc,spcdir,deploc,spcsig,wk,e000,wkx,wky)
320
321            p = 0
322            q = 0
323            r = 2
324            e002 = 0.
325            call fbsmom(p,q,r,acloc,spcdir,deploc,spcsig,wk,e002,wkx,wky)
326
327            stvar = 2*pi*sqrt(e000/e002)
328 !
329 !          write spectral moment to output vector
330 !
331            if (stvar .ne. 0.) then
332               voq(ip,voqr(ivtype)) = stvar
333            else
334               voq(ip,voqr(ivtype)) = 0.
335            endif
336            if (itest.ge.100) then
337               write(printf, 222) ip, ovsnam(ivtype), voq(ip,voqr(ivtype))
338            endif
339         endif
340 !
341 !
342 !
343 !       stlx
344 !
345         ivtype = 80
```

```
346           if (oqproc(ivtype)) then
347              p = 0
348              q = 0
349              r = 0
350              e000 = 0.
351              call fbsmom(p,q,r,acloc,spcdir,deploc,spcsig,wk,e000,wkx,wky)
352
353              p = 2
354              q = 0
355              r = 0
356              e200 = 0.
357              call fbsmom(p,q,r,acloc,spcdir,deploc,spcsig,wk,e200,wkx,wky)
358
359              stvar = 2*pi*sqrt(e000/e200)
360     !
361     !        write spectral moment to output vector
362     !
363              if (stvar .ne. 0.) then
364                 voq(ip,voqr(ivtype)) = stvar
365              else
366                 voq(ip,voqr(ivtype)) = 0.
367              endif
368              if (itest.ge.100) then
369                 write(printf, 222) ip, ovsnam(ivtype), voq(ip,voqr(ivtype))
370              endif
371           endif
372     !
373     !
374     !
375     !     stly
376     !
377           ivtype = 81
378           if (oqproc(ivtype)) then
379              p = 0
380              q = 0
381              r = 0
382              e000 = 0.
383              call fbsmom(p,q,r,acloc,spcdir,deploc,spcsig,wk,e000,wkx,wky)
384
385              p = 0
386              q = 2
387              r = 0
388              e020 = 0.
389              call fbsmom(p,q,r,acloc,spcdir,deploc,spcsig,wk,e020,wkx,wky)
390
391              stvar = 2*pi*sqrt(e000/e020)
392     !
393     !        write spectral moment to output vector
394     !
395              if (stvar .ne. 0.) then
396                 voq(ip,voqr(ivtype)) = stvar
397              else
398                 voq(ip,voqr(ivtype)) = 0.
399              endif
400              if (itest.ge.100) then
401                 write(printf, 222) ip, ovsnam(ivtype), voq(ip,voqr(ivtype))
402              endif
403           endif
404     !
405     !
406     !
407     !     staxy
```

```
!
      ivtype = 82
      if (oqproc(ivtype)) then
         p = 1
         q = 1
         r = 0
         e110 = 0.
         call fbsmom(p,q,r,acloc,spcdir,deploc,spcsig,wk,e110,wkx,wky)

         p = 2
         q = 0
         r = 0
         e200 = 0.
         call fbsmom(p,q,r,acloc,spcdir,deploc,spcsig,wk,e200,wkx,wky)

         p = 0
         q = 2
         r = 0
         e020 = 0.
         call fbsmom(p,q,r,acloc,spcdir,deploc,spcsig,wk,e020,wkx,wky)

         stvar = e110/sqrt(e200*e020)
!
!        write spectral moment to output vector
!
         if (stvar .ne. 0.) then
            voq(ip,voqr(ivtype)) = stvar
         else
            voq(ip,voqr(ivtype)) = 0.
         endif
         if (itest.ge.100) then
            write(printf, 222) ip, ovsnam(ivtype), voq(ip,voqr(ivtype))
         endif
      endif
!
!
!
!     staxt
!
      ivtype = 83
      if (oqproc(ivtype)) then
         p = 1
         q = 0
         r = 1
         e101 = 0.
         call fbsmom(p,q,r,acloc,spcdir,deploc,spcsig,wk,e101,wkx,wky)

         p = 2
         q = 0
         r = 0
         e200 = 0.
         call fbsmom(p,q,r,acloc,spcdir,deploc,spcsig,wk,e200,wkx,wky)

         p = 0
         q = 0
         r = 2
         e002 = 0.
         call fbsmom(p,q,r,acloc,spcdir,deploc,spcsig,wk,e002,wkx,wky)

         stvar = e101/sqrt(e200*e002)
!
!        write spectral moment to output vector
```

```
!
            if (stvar .ne. 0.) then
               voq(ip,voqr(ivtype)) = stvar
            else
               voq(ip,voqr(ivtype)) = 0.
            endif
            if (itest.ge.100) then
               write(printf, 222) ip, ovsnam(ivtype), voq(ip,voqr(ivtype))
            endif
         endif
!
!
!
!        staxy
!
         ivtype = 84
         if (oqproc(ivtype)) then
            p = 0
            q = 1
            r = 1
            e011 = 0.
            call fbsmom(p,q,r,acloc,spcdir,deploc,spcsig,wk,e011,wkx,wky)

            p = 0
            q = 2
            r = 0
            e020 = 0.
            call fbsmom(p,q,r,acloc,spcdir,deploc,spcsig,wk,e020,wkx,wky)

            p = 0
            q = 0
            r = 2
            e002 = 0.
            call fbsmom(p,q,r,acloc,spcdir,deploc,spcsig,wk,e002,wkx,wky)

            stvar = e011/sqrt(e020*e002)
!
!           write spectral moment to output vector
!
            if (stvar .ne. 0.) then
               voq(ip,voqr(ivtype)) = stvar
            else
               voq(ip,voqr(ivtype)) = 0.
            endif
            if (itest.ge.100) then
               write(printf, 222) ip, ovsnam(ivtype), voq(ip,voqr(ivtype))
            endif
         endif
!
         goto 800
!
!
!        points on land: assign exception value
!
700      do 730 ii = 1, nmom
            ivtype = ivoum(ii)
            if (oqproc(ivtype)) then
              voq(ip,voqr(ivtype)) = ovexcv(ivtype)
              if (ovsvty(ivtype).eq.3) then
                voq(ip,voqr(ivtype)+1) = ovexcv(ivtype)
              endif
            endif
```

```
532  730     enddo
533  800  enddo
534  !
535      deallocate(wkx)
536      deallocate(wky)
537  !
538  end subroutine fboexm
539  !
```

C.1.2 Spectral moments computation: fbsmom

```
1   !
2   subroutine fbsmom(p,q,r,acloc,spcdir,deploc,spcsig,wk,pqrm,wkx,wky)
3   !
4   !    Authors
5   !
6   !    40FB: Francesco Barbariol
7   !
8   !    Updates
9   !
10  !    Purpose
11  !
12  !    Subroutine for the spectral moments calculation
13  !
14  !    Method
15  !
16  !    The sbrt is called by FBOEXM.
17  !    --- Call KSCIP1, to calculate the wavenumbers from frequencies
18  !    --- Calculate kx and ky components of wavenumbers, for each
19  !        direction theta (SPCDIR)
20  !    --- Integrate the wave action densities and calculate the spectral
21  !        moments.
22  !        --- Numerical integration up to maximum frequency
23  !        --- Analytic intergration up to:
24  !            --- infinity, for moments up to 3rd order
25  !            --- qinf, for 4th order moments (
26  !                gravity-capillarity limit = 60 rad/s)
27  !
28  !
29  !    Modules used
30  !
31      use swcomm1
32      use swcomm2
33      use swcomm3
34      use swcomm4
35      use outp_data
36      use ocpcomm4
37  !
38      implicit none
39  !
40  !    Argument variables
41  !
42  !    SPCDIR: (*,1); spectral directions (radians)   30.82
43  !            (*,2); cosine of spectral directions   30.82
44  !            (*,3); sine of spectral directions     30.82
45  !
46  ! number of entries in this subroutine
47      integer, save                           :: ient = 0
48  ! power of the pqr-th moment, kx
49      integer, intent(in)                     :: p
50  ! power of the pqr-th moment, ky
```

```
51      integer, intent(in)                          :: q
52  ! power of the pqr-th moment, sigma
53      integer, intent(in)                          :: r
54  ! depth at one location
55      real, intent(in)                             :: deploc
56  ! action density at one location
57      real, dimension(MDC,MSC), intent(in)         :: acloc
58      real, dimension(MSC), intent(in)             :: spcsig   !
59      real, dimension(MDC,*), intent(in)           :: spcdir !
60  ! pqr-th moment of energy density spectrum
61      real, intent(out)                            :: pqrm
62      real, dimension(MDC,MSC)                     :: wkx
63      real, dimension(MDC,MSC)                     :: wky
64  !
65  !   Local variables
66  !
67  ! loop counter over direction bins
68      integer                                      :: id
69  ! loop counter over frequency bins
70      integer                                      :: is
71  ! power of the frequency for calculation, rr = r + 2
72      integer                                      :: rr
73      integer                                      :: istat
74      real                                         :: wkxp
75      real                                         :: wkyq
76      real                                         :: sigrr
77      real                                         :: eptail
78      real                                         :: pptail
79      real                                         :: mom
80      real                                         :: kks
81  ! upper bound for integration of 4th order moments in freq
82      real                                         :: qinf
83      real, dimension(*)                           :: wk
84      real, dimension(MSC)                         :: cg
85      real, dimension(MSC)                         :: n
86      real, dimension(MSC)                         :: nd
87  !
88  !   Structure
89  !
90  !   Description of the pseudo code
91  !
92  !   Source text
93  !
94      if (ltrace) call strace (ient,'fbsmom')
95  !
96  !   Calculate the wavenumbers from frequencies: kscip1
97  !
98      call kscip1 (msc, spcsig, deploc, wk, cg, n, nd)
99  !
100 !   Calculate kx and ky components of wavenumbers,
101 !   for each freq (SPCSIG) and direction theta (SPCDIR)
102 !
103     wkx = 0.
104     wky = 0.
105     do id = 1, mdc
106        do is = 1, msc
107           wkx(id,is) = wk(is)*cos(spcdir(id,1))
108           wky(id,is) = wk(is)*sin(spcdir(id,1))
109        enddo
110     enddo
111 !
112 !   Integrate the wave action densities and calculate
```

```
!    the spectral moments.
!
     mom = 0.
     wkxp = 0.
     wkyq = 0.
     rr = r + 2.
!    integration over [0,inf]                                    40.87
     do id=1, mdc
        do is=1, msc
           wkxp = wkx(id,is)**p
           wkyq = wky(id,is)**q
           sigrr = spcsig(is)**rr
           kks = wkxp*wkyq*sigrr
           mom = mom + kks*acloc(id,is)*ddir
        enddo
     enddo
     mom = mom*frintf
!       contribution of tail to total energy density
!       (frequency counter @ msc)
     if (msc .gt. 3) then
!       tail integral until infinity if p+q<2
        if (p+q .lt. 2) then
        pptail = pwtail(1) - r - 2*(p+q) - 1
        eptail = 1./(pptail*(1. + pptail*(frinth-1.)))
           do id=1, mdc
              wkxp = wkx(id,msc)**p
              wkyq = wky(id,msc)**q
              sigrr = spcsig(msc)**rr
              kks = wkxp*wkyq*sigrr
              mom = mom + eptail*kks*acloc(id,msc)*ddir
           enddo
!       tail integral until qinf=60 rad/s if p+q>=2,
!       otherwise integral diverges (gravity-capillarity limit)
        else
        qinf = 60
           do id=1, mdc
              wkxp = wkx(id,msc)**p
              wkyq = wky(id,msc)**q
              sigrr = spcsig(msc)**rr
              kks = wkxp*wkyq*sigrr
              mom = mom + kks*acloc(id,msc)* &
                    (log(qinf) - log(spcsig(msc)*frinth))*ddir
           enddo
        endif
     endif
     pqrm = mom
!
end subroutine fbsmom
!
```

C.1.3 Adaptation of existing subroutines

Output variables initialization: SWINIT

```
!
!      Spectral moments, step2 - 10.10.2012 - FB
!
       IVTYPE = 72
       OVKEYW(IVTYPE) = 'M000'                 ! 40.FB
       OVSNAM(IVTYPE) = 'm000'                 ! 40.FB
       OVLNAM(IVTYPE) = '000-th spec mom'
```

```
8         OVUNIT(IVTYPE) = 'm2'
9         OVSVTY(IVTYPE) = 1
10        OVLLIM(IVTYPE) = 0.
11        OVULIM(IVTYPE) = 1000.
12        OVLEXP(IVTYPE) = 0.
13        OVHEXP(IVTYPE) = 10.
14        OVEXCV(IVTYPE) = -99.
15 !
16        IVTYPE = 73
17        OVKEYW(IVTYPE) = 'M101'                ! 40.FB
18        OVSNAM(IVTYPE) = 'm101'                ! 40.FB
19        OVLNAM(IVTYPE) = '101-th spec mom'
20        OVUNIT(IVTYPE) = 'rad2*m/s'
21        OVSVTY(IVTYPE) = 1
22        OVLLIM(IVTYPE) = -1000.
23        OVULIM(IVTYPE) = 1000.
24        OVLEXP(IVTYPE) = -0.1
25        OVHEXP(IVTYPE) = 0.1
26        OVEXCV(IVTYPE) = -99.
27 !
28        IVTYPE = 74
29        OVKEYW(IVTYPE) = 'M011'                ! 40.FB
30        OVSNAM(IVTYPE) = 'm011'                ! 40.FB
31        OVLNAM(IVTYPE) = '011-th spec mom'
32        OVUNIT(IVTYPE) = 'rad2*m/s'
33        OVSVTY(IVTYPE) = 1
34        OVLLIM(IVTYPE) = -1000.
35        OVULIM(IVTYPE) = 1000.
36        OVLEXP(IVTYPE) = -0.1
37        OVHEXP(IVTYPE) = 0.1
38        OVEXCV(IVTYPE) = -99.
39 !
40        IVTYPE = 75
41        OVKEYW(IVTYPE) = 'M110'                ! 40.FB
42        OVSNAM(IVTYPE) = 'm110'                ! 40.FB
43        OVLNAM(IVTYPE) = '110-th spec mom'
44        OVUNIT(IVTYPE) = 'rad2'
45        OVSVTY(IVTYPE) = 1
46        OVLLIM(IVTYPE) = -1000.
47        OVULIM(IVTYPE) = 1000.
48        OVLEXP(IVTYPE) = -0.1
49        OVHEXP(IVTYPE) = 0.1
50        OVEXCV(IVTYPE) = -99.
51 !
52        IVTYPE = 76
53        OVKEYW(IVTYPE) = 'M002'                ! 40.FB
54        OVSNAM(IVTYPE) = 'm002'                ! 40.FB
55        OVLNAM(IVTYPE) = '002-th spec mom'
56        OVUNIT(IVTYPE) = 'rad2*m2/s2'
57        OVSVTY(IVTYPE) = 1
58        OVLLIM(IVTYPE) = 0.
59        OVULIM(IVTYPE) = 1000.
60        OVLEXP(IVTYPE) = 0.
61        OVHEXP(IVTYPE) = 10.
62        OVEXCV(IVTYPE) = -99.
63 !
64        IVTYPE = 77
65        OVKEYW(IVTYPE) = 'M020'                ! 40.FB
66        OVSNAM(IVTYPE) = 'm020'                ! 40.FB
67        OVLNAM(IVTYPE) = '020-th spec mom'
68        OVUNIT(IVTYPE) = 'rad2'
69        OVSVTY(IVTYPE) = 1
```

```
70          OVLLIM(IVTYPE) = 0.
71          OVULIM(IVTYPE) = 1000.
72          OVLEXP(IVTYPE) = 0.
73          OVHEXP(IVTYPE) = 10.
74          OVEXCV(IVTYPE) = -99.
75  !
76          IVTYPE = 78
77          OVKEYW(IVTYPE) = 'M200'                 ! 40.FB
78          OVSNAM(IVTYPE) = 'm200'                 ! 40.FB
79          OVLNAM(IVTYPE) = '020-th spec mom'
80          OVUNIT(IVTYPE) = 'rad2'
81          OVSVTY(IVTYPE) = 1
82          OVLLIM(IVTYPE) = 0.
83          OVULIM(IVTYPE) = 1000.
84          OVLEXP(IVTYPE) = 0.
85          OVHEXP(IVTYPE) = 10.
86          OVEXCV(IVTYPE) = -99.
87  !
88  !       Synthetic spectral quantities, step3 - 18.12.2012 - FB
89  !
90          IVTYPE = 79
91          OVKEYW(IVTYPE) = 'STTM'                 ! 40.FB
92          OVSNAM(IVTYPE) = 'sttm'                 ! 40.FB
93          OVLNAM(IVTYPE) = 'ST-mean per'
94          OVUNIT(IVTYPE) = UT
95          OVSVTY(IVTYPE) = 1
96          OVLLIM(IVTYPE) = 0.
97          OVULIM(IVTYPE) = 1000.
98          OVLEXP(IVTYPE) = 0.
99          OVHEXP(IVTYPE) = 100.
100         OVEXCV(IVTYPE) = -9.
101 !
102         IVTYPE = 80
103         OVKEYW(IVTYPE) = 'STLX'                 ! 40.FB
104         OVSNAM(IVTYPE) = 'stlx'                 ! 40.FB
105         OVLNAM(IVTYPE) = 'ST-mean Lx'
106         OVUNIT(IVTYPE) = UL
107         OVSVTY(IVTYPE) = 1
108         OVLLIM(IVTYPE) = 0
109         OVULIM(IVTYPE) = 1000.
110         OVLEXP(IVTYPE) = 0
111         OVHEXP(IVTYPE) = 200
112         OVEXCV(IVTYPE) = -9.
113 !
114         IVTYPE = 81
115         OVKEYW(IVTYPE) = 'STLY'                 ! 40.FB
116         OVSNAM(IVTYPE) = 'stly'                 ! 40.FB
117         OVLNAM(IVTYPE) = 'ST-mean Ly'
118         OVUNIT(IVTYPE) = UL
119         OVSVTY(IVTYPE) = 1
120         OVLLIM(IVTYPE) = 0
121         OVULIM(IVTYPE) = 1000.
122         OVLEXP(IVTYPE) = 0
123         OVHEXP(IVTYPE) = 200
124         OVEXCV(IVTYPE) = -9.
125 !
126         IVTYPE = 82
127         OVKEYW(IVTYPE) = 'STAXY'                ! 40.FB
128         OVSNAM(IVTYPE) = 'staxy'                ! 40.FB
129         OVLNAM(IVTYPE) = 'ST-xy corr'
130         OVUNIT(IVTYPE) = ' '
131         OVSVTY(IVTYPE) = 1
```

```
      OVLLIM(IVTYPE) = -10.
      OVULIM(IVTYPE) = 10.
      OVLEXP(IVTYPE) = -1.
      OVHEXP(IVTYPE) = 1.
      OVEXCV(IVTYPE) = -9.
!
      IVTYPE = 83
      OVKEYW(IVTYPE) = 'STAXT'              ! 40.FB
      OVSNAM(IVTYPE) = 'staxt'              ! 40.FB
      OVLNAM(IVTYPE) = 'ST-xt corr'
      OVUNIT(IVTYPE) = ' '
      OVSVTY(IVTYPE) = 1
      OVLLIM(IVTYPE) = -10.
      OVULIM(IVTYPE) = 10.
      OVLEXP(IVTYPE) = -1.
      OVHEXP(IVTYPE) = 1.
      OVEXCV(IVTYPE) = -9.
!
      IVTYPE = 84
      OVKEYW(IVTYPE) = 'STAYT'              ! 40.FB
      OVSNAM(IVTYPE) = 'stayt'              ! 40.FB
      OVLNAM(IVTYPE) = 'ST-yt corr'
      OVUNIT(IVTYPE) = ' '
      OVSVTY(IVTYPE) = 1
      OVLLIM(IVTYPE) = -10.
      OVULIM(IVTYPE) = 10.
      OVLEXP(IVTYPE) = -1.
      OVHEXP(IVTYPE) = 1.
      OVEXCV(IVTYPE) = -9.
!
```

Output requests processing: SWOUTP

```
!
!          call FBOEXM, to perform space-time extreme analysis
!
           CALL FBOEXM (OQPROC                ,BKC                ,
     &                  MIP                  ,VOQ(1+2*MIP)       ,
     &                  VOQ(1+3*MIP)         ,VOQR               ,
     &                  VOQ(1)               ,AC2                ,
     &                  ACLOC                ,SPCSIG             ,
     &                  SPCDIR               ,KGRPNT             ,
     &                  COMPDA(1,JDP2)       ,CROSS                )
!
```

Module with common variables: SWCOMM1

```
!     synthetic spectral parameters added (7), 18.12.2012-FB
      PARAMETER (NMOVAR = 84, MOUTPA=50)                          ! 40FB
!
```

Acknowledgements

While I was writing the present thesis, when I was reporting the work I did, I intentionally chose to use the plural "we". Indeed, at the end of my Ph.D. schools program, I feel obliged to thank all the people that supported me in different manners during the realization of my research.

First of all, I would like to thank dr. Alvise Benetazzo (ISMAR-CNR, Italy) that encouraged me to engage the doctoral program and shared with me the most of the work I did. He has given me a lot of motivations and the passion for studying ocean waves. Then, I thank my supervisor prof. Piero Ruol (University of Padua, Italy) for being very helpful and careful from the first moment I entered University of Padua as a potential Ph.D. student and for all these three years. Dr. Sandro Carniel and dr. Mauro Sclavo (ISMAR-CNR, Italy) offered me great opportunities by supporting me with publishing and travelling. Besides, they provided me computational resources to perform numerical simulations. I am very grateful to them. Prof. Francesco Fedele (GATECH, USA) provided very useful comments and introduced me into the world of space-time wave analysis. Prof. Agustin Sànchez-Arcilla and Joan Pau Sierra (UPC, Spain) were very kind to give me hospitality at UPC in Barcelona, sharing with me two months on buoy data analysis.

Finally, I wish to acknowledge ISMAR-CNR (Italy) for providing stereo-photogrammetric data, Filippo Bergamasco (University of Ca' Foscari-Venice, Italy) for processing them, XIOM network of the Catalan Government (Spain) for providing the buoy data and ARPA-EMR (Italy) for providing COSMO-I7 meteorological forcings.

Bibliography

M. Abramowitz and I. A. Stegun. *Handbook of Mathematical Functions with Formulas, Graphs, and Mathematical Tables*, volume 55 of *Applied Mathematics*. ERIC, 1972.

R. Adler. *The geometry of random fields*. John Wiley & Sons, Chichester, 1981.

R. J. Adler and J. E. Taylor. *Random fields and geometry*, volume 115. Springer, 2007.

J. Allender, T. Audunson, S. Barstow, S. Bjerken, H. Krogstad, P. Steinbakke, L. Vartdal, L. Borgman, and C. Graham. The wadic project: A comprehensive field evaluation of directional wave instrumentation. *Ocean engineering*, 16(5):505–536, 1989.

M. Banner, J. Trinder, and I. JONES. Wavenumber spectra of short gravity waves. *Journal of Fluid Mechanics*, 198:321–344, 1989.

J. Battjes, T. Zitman, and L. Holthuijsen. A re-analysis of the spectra observed in JONSWAP. *Coastal Engineering Proceedings*, 1(20), 1986.

A. Baxevani and I. Rychlik. Maxima for gaussian seas. *Ocean Engineering*, 33:895–911, 2006.

A. Baxevani, K. Podgórski, and I. Rychlik. Velocities for moving random surfaces. *Probabilistic Engineering Mechanics*, 18(3):251–271, 2003.

J. S. Bendat and A. G. Piersol. *Random data: analysis and measurement procedures*, volume 729. John Wiley & Sons, 2011.

A. Benetazzo. Measurements of short water waves using stereo matched image sequences. *Coastal engineering*, 53(12):1013–1032, 2006.

A. Benetazzo, F. Fedele, G. Gallego, P. Shih, and A. Yezzi. Offshore stereo measurements of gravity waves. *Coastal Engineering*, 64:127–138, 2012.

A. Benetazzo, F. Bergamasco, F. Barbariol, A. Torsello, S. Carniel, and M. Sclavo. Towards an operational stereo system for directional wave measurements from moving platforms. In *Proceedings of the 33rd International Offshore and Polar Engineering Conference, San Francisco, USA*, volume Submitted and accepted. American Society of Mechanical Engineers, 2014.

M. Benoit, F. Marcos, and F. Becq. Development of a third generation shallow-water wave model with unstructured spatial meshing. *Coastal Engineering Proceedings*, 1(25), 1996.

M. Benoit, P. Frigaard, H. A. Sch, et al. Analyzing multidirectional wave spectra: a tentative classification of available methods. 1997.

P. Boccotti. *Wave mechanics for ocean engineering*, volume 64. Elsevier Science, 2000.

N. Booij, R. Ris, and L. Holthuijsen. A third-generation wave model for coastal regions. I: model description and validation. *Journal of Geophysical Research*, 104(C4):7649–7666, 1999.

M. Casas-Prat and L. H. Holthuijsen. Short-term statistics of waves observed in deep water. *Journal of Geophysical Research: Oceans (1978–2012)*, 115 (C9), 2010.

L. Cavaleri, L. Bertotti, L. Torrisi, E. Bitner-Gregersen, M. Serio, and M. Onorato. Rogue waves in crossing seas: The louis majesty accident. *Journal of Geophysical Research: Oceans (1978–2012)*, 117(C11), 2012.

H. Dankert, J. Horstmann, S. Lehner, and W. Rosenthal. Detection of wave groups in SAR images and radar image sequences. *Geoscience and Remote Sensing, IEEE Transactions on*, 41(6):1437–1446, 2003.

Datawell. *Datawell Waverider Reference Manual*, October 2009.

K. Dysthe, H. E. Krogstad, and P. Müller. Oceanic rogue waves. *Annu. Rev. Fluid Mech.*, 40:287–310, 2008.

F. Fedele. Space–time extremes in short-crested storm seas. *Journal of Physical Oceanography*, 42(9):1601–1615, 2012.

F. Fedele and M. A. Tayfun. On nonlinear wave groups and crest statistics. *Journal of Fluid Mechanics*, 620:221–239, Feb. 2009. doi: DOI 10.1017/S0022112008004424.

F. Fedele, A. Benetazzo, and G. Forristall. Space-time waves and spectra in the northern Adriatic Sea via a Wave Acquisition Stereo System. In *Proc. 30th ASME International Conference on Offshore Mechanics and Arctic Engineering*, 2011.

F. Fedele, A. Benetazzo, G. Gallego Bonet, P. Shih, A. Yezzi, and F. Barbariol. Wave statistics and space-time extremes via stereo imaging. In *Proceedings of the 22nd International Offshore and Polar Engineering Conference, Rhodes*, volume 3, pages 762–769, 2012.

F. Fedele, A. Benetazzo, G. Gallego, P.-C. Shih, A. Yezzi, F. Barbariol, and F. Ardhuin. Space-time measurements of oceanic sea states. *Ocean Modelling*, 70:103–115, 2013.

G. Forristall. Understanding rogue waves: Are new physics really necessary. In *Proceedings of the 14 th'Aha Huliko'a Hawaiian Winter Workshop*, pages 29–35, 2005.

G. Forristall. Wave crest heights and deck damage in hurricanes ivan, katrina, and rita. In *Offshore Technology Conference*, 2007.

G. Z. Forristall. Measurements of a saturated range in ocean wave spectra. *Journal of Geophysical Research: Oceans (1978–2012)*, 86(C9):8075–8084, 1981.

G. Z. Forristall. Maximum wave heights over an area and the air gap problem. In *Proc. ASME 25th Inter. Conf. Off. Mech. Arc. Eng., Hamburg, OMAE2006-92022*, pages 11–15, 2006.

G. Z. Forristall. Maximum Crest Heights Under a Model TLP Deck. In *Proceedings of the ASME 2011 30th International Conference on Ocean, Offshore and Arctic Engineering*. ASME, 2011.

Y. Gōda. *Random seas and design of maritime structures*. World Scientific, 2010.

S. Gran. *A course in ocean engineering*, volume 8 of *Developments in Marine Technology*. Elsevier, 1992.

E. J. Gumbel. *Statistics of Extremes*. Columbia Univ. press, New York, 1958.

H. Günther, S. Hasselmann, and P. A. Janssen. *The WAM model, Cycle 4*. DKRZ, 1992.

N. Hashimoto, T. Nagai, and T. Asai. Extension of the maximum entropy principle method for directional wave spectrum estimation. In *Proceedings of the 24th Int. Conf. on Coastal Engineering, Kobe (Japan)*, volume 1, pages 232–246. ASCE, 1994.

K. Hasselmann, T. Barnett, E. Bouws, H. Carlson, D. Cartwright, K. Enke, J. Ewing, H. Gienapp, D. Hasselmann, P. Kruseman, et al. Measurements of wind-wave growth and swell decay during the Joint North Sea Wave Project (JONSWAP). 1973.

K. Hasselmann, D. Ross, P. Muller, and W. Sell. A parametric wave prediction model. 1976.

L. H. Holthuijsen. *Waves in oceanic and coastal waters*. Cambridge University Press, 2007.

M. Isobe, K. Kondo, and K. Horikawa. Extension of {MLM} for estimating directional wave spectrum. 1984.

D. Johnson. *DIWASP, a directional wave spectra toolbox for MATLAB®: User Manual. Research Report WP-1601-DJ (V1.3)*.

C. Kharif and E. Pelinovsky. Physical mechanisms of the rogue wave phenomenon. *European Journal of Mechanics-B/Fluids*, 22(6):603–634, 2003.

H. E. Krogstad, J. Liu, H. Socquet-Juglard, K. B. Dysthe, and K. Trulsen. Spatial extreme value analysis of nonlinear simulations of random surface waves. In *Proceedings of the ASME 2011 23rd International Conference on Ocean, Offshore and Arctic Engineering*. ASME, 2004.

A. Lewis and R. Allos. JONSWAP's parameters: Sorting out the inconsistencies. *Ocean engineering*, 17(4):409–415, 1990.

M. Longuet-Higgins. On the joint distribution of the periods and amplitudes of sea waves. *Journal of Geophysical Research*, 80(18):2688–2694, 1975.

M. S. Longuet-Higgins, D. Cartwright, and N. Smith. Observations of the directional spectrum of sea waves using the motions of a floating buoy. In *Ocean Wave Spectra*, pages 111–136. Prentice-Hall, 1963.

O. S. Madsen, Y.-K. Poon, and H. C. Graber. Spectral wave attenuation by bottom friction: Theory. *Coastal Engineering Proceedings*, 1(21), 1988.

MATLAB. version 7.14.0.739 (r2012a), 2012.

Maxima. Maxima, a computer algebra system. version 11.08.0, 2011. URL `http://maxima.sourceforge.net/`.

A. Miche. Mouvements ondulatoires de la mer en profondeur croissante ou décroissante. *Annales des ponts et chaussées*, 114:369–406, 1944.

H. Mitsuyasu, F. Tasai, T. Suhara, S. Mizuno, M. Ohkusu, T. Honda, and K. Rikiishi. Observation of the power spectrum of ocean waves using a cloverleaf buoy. *Journal of Physical Oceanography*, 10(2):286–296, 1980.

M. Ochi. *Ocean Waves: The Stochastic Approach*. Cambridge Ocean Technology Series. Cambridge University Press, 2005.

M. Onorato, A. R. Osborne, M. Serio, and S. Bertone. Freak waves in random oceanic sea states. *Physical Review Letters*, 86(25):5831, 2001.

M. Onorato, A. R. Osborne, and M. Serio. Extreme wave events in directional, random oceanic sea states. *Physics of Fluids*, 14:L25, 2002.

A. R. Osborne, M. Onorato, and M. Serio. The nonlinear dynamics of rogue waves and holes in deep-water gravity wave trains. *Physics Letters A*, 275 (5):386–393, 2000.

O. Phillips. The equilibrium range in the spectrum of wind-generated waves. *J. Fluid Mech*, 4(4):426–434, 1958.

O. M. Phillips. The dynamics of the upper ocean. 1977.

J. W. J. Pierson and L. Moskowitz. A proposed spectral form for fully developed wind seas based on the similarity theory of SA Kitaigorodskii. *Journal of Geophysical Research*, 69(24):5181–5190, 1964.

V. I. Piterbarg. *Asymptotic Methods in the Theory of Gaussian Processes and Fields*. AMS Transl. of Math Monographs, 1996.

W. Rosenthal and S. Lehner. Rogue waves: Results of the MaxWave project. *Journal of Offshore Mechanics and Arctic Engineering*, 130(2):020201–1, 2008.

A. Sánchez-Arcilla, D. González-Marco, and R. Bolaños. A review of wave climate and prediction along the spanish mediterranean coast. *Natural Hazards and Earth System Sciences*, 8:1217–1228, 2008.

S. E. Sand, N. O. Hansen, P. Klinting, O. T. Gudmestad, and M. J. Sterndorff. Freak wave kinematics. In *Water Wave Kinematics*, pages 535–549. Springer, 1990.

O. H. Shemdin, H. M. Tran, and S. Wu. Directional measurement of short ocean waves with stereophotography. *Journal of Geophysical Research: Oceans (1978–2012)*, 93(C11):13891–13901, 1988.

J. Skourup, N.-E. O. Hansen, and K. Andreasen. Non-gaussian extreme waves in the central north sea. *Journal of Offshore Mechanics and Arctic Engineering*, 119(3), 1997.

H. Socquet-Juglard. Spectral evolution and probability distributions of surface ocean gravity waves and extreme waves, 2005.

H. Socquet-Juglard, K. Dysthe, K. Trulsen, H. E. Krogstad, and J. Liu. Probability distributions of surface gravity waves during spectral changes. *Journal of Fluid Mechanics*, 542(1):195–216, 2005.

O. Sorensen, H. Kofoed-Hansen, M. Rugbjerg, and L. Sorensen. A third-generation spectral wave model using an unstructured finite volume technique. In *COASTAL ENGINEERING CONFERENCE*, volume 29, page 894. World Scientific, 2004.

J. Steppeler, G. Doms, U. Schättler, H. Bitzer, A. Gassmann, U. Damrath, and G. Gregoric. Meso-gamma scale forecasts using the nonhydrostatic model LM. *Meteorology and Atmospheric Physics*, 82(1):75–96, 2003.

M. A. Tayfun. Narrow-band nonlinear sea waves. *Journal of Geophysical Research*, 85(C3):1548–1552, 1980.

M. A. Tayfun. Distributions of envelope and phase in wind waves. *Journal of Physical Oceanography*, 38(12):2784–2800, 2008.

M. A. Tayfun and F. Fedele. Wave-height distributions and nonlinear effects. *Ocean Engineering*, 34:1631–1649, 2007.

The SWAN Team. SWAN cycle III, version 40.85: Scientific and Technical Documentation. *Delft, The Netherlands: Delft University of Technology, digital version available in http://www.fluidmechanics.tudelft.nl/swan/index.htm*, 2011.

The WAMDI Group. The wam model-a third generation ocean wave prediction model. *Journal of Physical Oceanography*, 18(12):1775–1810, 1988.

Y. Toba. Local balance in the air-sea boundary processes. *Journal of the Oceanographical Society of Japan*, 29(5):209–220, 1973.

H. Tolman. User manual and system documentation of WAVEWATCH III version 1.18. Technical report, Note 166, NOAA/NWS/NCEP/OMB, 1999.

M. J. Tucker and E. Pitt. *Waves in ocean engineering.* Number Volume 5. 2001.

M. Yamaguchi. Approximate expressions for integral properties of the JONSWAP spectrum. *Proc. Japanese Society of Civil Engineers*, 345:149–152, 1984.

L. Yan. *An improved wind input source term for third generation ocean wave modelling.* Koninklijk Nederlands Meteorologisch Instituut, 1987.

I. R. Young. *Wind generated ocean waves*, volume 2. Elsevier Science Limited, 1999.

Francesco Barbariol
Space-time extremes of sea wave states: field, analytical and numerical investigations
January 2014